

Searches for New Physics at the Compact Muon Solenoid  
Experiment and Precision Timing Calorimetry

Thesis by  
Cristián H. Peña

In Partial Fulfillment of the Requirements for the  
degree of  
Doctor of Philosophy

**Caltech**

CALIFORNIA INSTITUTE OF TECHNOLOGY  
Pasadena, California

2016  
Defended October 2016

© 2016

Cristián H. Peña  
ORCID: [Author ORCID]

All rights reserved

Choose one from  
the choices in the  
source code!! And  
delete this todo  
when you're done  
that. :-)

## ACKNOWLEDGEMENTS

To the two times Copa America Champions!!!

## ABSTRACT

[This abstract must provide a succinct and informative condensation of your work. Candidates are welcome to prepare a lengthier abstract for inclusion in the dissertation, and provide a shorter one in the CaltechTHESIS record.]

## TABLE OF CONTENTS

Acknowledgements . . . . .	iii
Abstract . . . . .	iv
Table of Contents . . . . .	v
List of Illustrations . . . . .	viii
List of Tables . . . . .	xxviii
<b>I Preliminaries, Supersymmetry, and Dark Matter</b>	<b>1</b>
Chapter I: Introduction . . . . .	2
Chapter II: The Standard Model in a Nutshell . . . . .	5
2.1 The Standard Model of Particle Physics . . . . .	5
2.2 The Higgs Boson and Electroweak Symmetry Breaking . . . . .	6
2.3 Fermion Masses . . . . .	9
Chapter III: Dark Matter and Weakly Interacting Particles . . . . .	11
3.1 The Evidence for Dark Matter . . . . .	11
3.2 Weakly Interacting Dark Matter Candidates . . . . .	15
3.3 Searches for Dark Matter . . . . .	15
<b>II The Large Hadron Collides and The Compact Muon Solenoid Experiment</b>	<b>17</b>
Chapter IV: The Large Hadron Collider . . . . .	18
4.1 The Large Hadron Collider . . . . .	18
Chapter V: The Compact Muon Solenoid Experiment . . . . .	23
5.1 The Superconducting Solenoid . . . . .	23
5.2 The Tracker System . . . . .	26
5.3 The Electromagnetic Calorimeter . . . . .	30
5.4 The Hadronic Calorimeter . . . . .	38
5.5 The Muon Chambers . . . . .	45
5.6 The Trigger System . . . . .	50
<b>III Searches for New Physics with the Compact Muon Solenoid Experiment</b>	<b>54</b>
Chapter VI: Razor Approach to Search for BSM Physics . . . . .	55
6.1 Introduction . . . . .	55
6.2 The Razor Variables . . . . .	56
6.3 Application of the Razor Variables to Search for BSM Physics . . . . .	59
Chapter VII: Searches for Dark Matter at the LHC with 8 TeV pp collisions . .	64

7.1	Introduction . . . . .	64
7.2	Data set and simulated samples . . . . .	66
7.3	Event selection . . . . .	67
7.4	Analysis Strategy . . . . .	69
7.5	Background estimation . . . . .	71
7.6	Systematic uncertainties . . . . .	79
7.7	Results and interpretation . . . . .	82
7.8	Summary . . . . .	90
	Acknowledgments . . . . .	93
7.9	Background estimation and observed yield . . . . .	95
	<b>Chapter VIII: Searches for Anomalous Higgs Boson Production . . . . .</b>	<b>97</b>
8.1	Introduction . . . . .	97
8.2	Summary of the 8 TeV Results . . . . .	98
8.3	Object Selection . . . . .	100
8.4	Event Selection and Analysis Strategy . . . . .	102
8.5	Background Estimation . . . . .	105
8.6	Nos-resonant Background Functional Form Selection: AIC Criterion and Bias Tests . . . . .	106
8.7	Systematic Uncertainties . . . . .	112
8.8	Results and Interpretations . . . . .	114
8.9	Summary . . . . .	116
	<b>IV Precision Timing Calorimetry . . . . .</b>	<b>126</b>
	<b>Chapter IX: Introduction . . . . .</b>	<b>127</b>
9.1	EM Calorimeter Preliminaries . . . . .	129
	<b>Chapter X: LYSO-based Calorimeters . . . . .</b>	<b>138</b>
10.1	Introduction . . . . .	138
10.2	Experimental Setup . . . . .	139
10.3	Event Selection and Data Analysis . . . . .	140
10.4	Timing in LYSO-based Calorimeters . . . . .	142
10.5	Results Discussion and Summary . . . . .	148
10.6	Acknowledgements . . . . .	150
	<b>Chapter XI: High-Granularity MCP-BASED Calorimeters . . . . .</b>	<b>152</b>
11.1	Introduction . . . . .	152
11.2	Experimental Setup . . . . .	154
11.3	Event Selection and Pulse Reconstruction . . . . .	155
11.4	Electromagnetic Shower Position Reconstruction and Resolution . . . . .	156
11.5	Electromagnetic Shower Time Resolution . . . . .	158
11.6	Summary . . . . .	160
11.7	Acknowledgements . . . . .	162
	<b>Chapter XII: Silicon-Based Sampling Calorimeters . . . . .</b>	<b>165</b>
12.1	Introduction . . . . .	165
12.2	General Properties of Silicon Timing and Bench Test Studies . . . . .	165
12.3	Test-beam Setup and Experimental Apparatus . . . . .	167

12.4 Test Beam Measurements and Results . . . . .	167
12.5 Discussion . . . . .	173
12.6 Conclusion . . . . .	175
Chapter XIII: CMS High-Granularity Calorimeter Timing Layer . . . . .	176
13.1 Introduction . . . . .	176
13.2 General Properties of Silicon Timing and Bench Test Studies . . . . .	176
13.3 Test-beam Setup and Experimental Apparatus . . . . .	177
13.4 Test Beam Measurement, Data Analysis, and Results . . . . .	178
13.5 Conclusions . . . . .	186
<b>V Summary and Conclusions</b>	<b>188</b>
13.6 Conclusion . . . . .	189
Bibliography . . . . .	190
Appendix A: Search for Massive Resonances Decaying into Two Photons . . . . .	210
A.1 Introduction . . . . .	210
A.2 The CMS detector . . . . .	211
A.3 Event simulation . . . . .	212
A.4 Event selection and diphoton mass spectrum . . . . .	213
A.5 Likelihood fit . . . . .	215
A.6 Systematic uncertainties . . . . .	217
A.7 Results for the 2016 data . . . . .	218
A.8 Combination with the 2012 and 2015 data . . . . .	219
A.9 Summary . . . . .	222
Appendix B: Phenomenology of Anomalous Higgs Production in SuperSymmetric models . . . . .	225
B.1 Introduction . . . . .	225
B.2 Benchmark signal models . . . . .	226
B.3 Event generation and detector simulation . . . . .	227
B.4 Emulation of the CMS search . . . . .	227
B.5 Bayesian Statistical Interpretation . . . . .	230
B.6 Correction and Validation . . . . .	231
B.7 Results . . . . .	231
B.8 Discussion and summary . . . . .	233

## LIST OF ILLUSTRATIONS

<i>Number</i>	<i>Page</i>
2.1 The catalog of particles in the standard model. . . . .	6
2.2 The shape of the Higgs potential (“Mexican hat”). The degeneracy of the potential is observed along the azimuthal angle . . . . .	8
3.1 The rotation curves for different galaxies as measured by Persic and Salucci [186]. . . . .	13
3.2 The rotation curve of the M33 galaxy. . . . .	13
3.3 BBN abundances as calculated by theory and measured by experiments in primordial-like areas of the universe with low concentration of Li. . . . .	14
3.4 The CMB anisotropy spectrum measured by WMAP. Different values of the baryonic matter are also shown with different curves. In the multipole expansion of the CMB anisotropies $l \approx \pi/\theta$ , where $\theta$ is the angular scale in radians. . . . .	16
4.1 The CERN accelerator complex. . . . .	19
4.2 The CERN Large Hadron Collider schematic layout. . . . .	20
4.3 An schematic cross sectional view of the LHC dipole magnet. . . . .	21
4.4 An 3D visualization of a LHC dipole magnet. . . . .	21
4.5 Intregated luminosity received by the CMS experiment during the LHC operation. . . . .	22
5.1 A perspective view of the CMS detector. . . . .	24
5.2 A cross-sectional-slice view of the CMS detector. The different components of the detector are clearly labeled and different particle detections are depicted. . . . .	24
5.3 Map of the magnetic field in the $y - z$ plane of the CMS detector. . . . .	25
5.4 A photograph of the steel-yoke in the early stages of assembly. The centermost wheel in the barrel support the superconducting coil. One of the endcaps yoke can be seen at the back. . . . .	25
5.5 A cross-sectional view of the silicon tracker layout. The different subsystems are clearly labeled. . . . .	27

5.6	Material budget of the CMS tracker in units of radiation length as a function of pseudorapidity $\eta$ for the (left) different subdetectors and (right) functional contributions. . . . .	27
5.7	BPix completed modules; (left) half-module, (center) an schematic of the different component forming the a full-module,(right) full-module. . . . .	28
5.8	FPix module; (left) an schematic of the two types of module, (right) a photograph of one of the completed FPix modules. . . . .	29
5.9	(Left) the layout of the silicon pixel tracker, (right) the pixel tracker detection efficiency as a function of the pseudorapidity. . . . .	29
5.10	Tracking efficiency for muons from Z decays using the tag-and - probe technique. The left panel and right panel show the efficiency as function of the muon $\eta$ and the number of reconstructed vertices, respectively. The black dots represent the measurement in 7 TeV data and the solid color represents the CMS simulation. . . . .	31
5.11	Resolution as a function of the pseudorapidity $\eta$ for muons of $p_T = 1$ , 10, and 100 GeV. The left panel shows the trasverse momentum resolution and the right panel the transverse impact parameter resolution. Both quantities are estimated from Simulation. . . . .	31
5.12	The layout of the CMS electromagnetic calorimenter. The left panel shows a projectional schematic layout including all the major parts while the left panel shows a geometric view of a quarter of the ECAL. . . . .	32
5.13	The PbWO <sub>4</sub> crystal of the CMS ECAL, (left) a EB crystal instrumented with an APD and (right) a EE crystal instrumented with a VPT. . . . .	33
5.14	A photograph of a EB module instrumented with crystals. . . . .	33
5.15	A photograph of a EE Dee instrumented with crystals. . . . .	34
5.16	The reconstructed Z invariant mass from $e^+e^-$ decays. The left and right panels show the reconstructed invariant mass for the EB and EE, repectively, with different algorithms to reconstructed electron energies. . . . .	35
5.17	The reconstructed Z invariant mass from $e^+e^-$ decays. The left and right panels show the reconstructed invariant mass for the EB and EE, repectively, with different algorithms to reconstructed electron energies. . . . .	36

5.18	The reconstructed Z invariant mass from $e^+e^-$ decays. The left and right panels show the reconstructed invariant mass for the EB and EE, repectively, with different algorithms to reconstructed electron energies. . . . .	36
5.19	The reconstructed Z invariant mass from $e^+e^-$ decays. The left and right panels show the reconstructed invariant mass for the EB and EE, repectively, with different algorithms to reconstructed electron energies. . . . .	37
5.20	The reconstructed Z invariant mass from $e^+e^-$ decays. The left and right panels show the reconstructed invariant mass for the EB and EE, repectively, with different algorithms to reconstructed electron energies. . . . .	38
5.21	The reconstructed Z invariant mass from $e^+e^-$ decays. The left and right panels show the reconstructed invariant mass for the EB and EE, repectively, with and without the IC and the LM corrections. . . . .	38
5.22	The reconstructed Z invariant mass from $e^+e^-$ decays. The left and right panels show the reconstructed invariant mass for the EB and EE, repectively, with different algorithms to reconstructed electron energies. . . . .	39
5.23	The CMS HCAL layout. . . . .	39
5.24	An schematic drawn of one of the wedges of the CMS HB. . . . .	41
5.25	A photograph of the finalized CMS HB. . . . .	41
5.26	An schematic of the HE geometry in the $\phi$ direction is presented in the left panel. The configuration of two adjacent scintillator trays is presented in the right panel. . . . .	42
5.27	A photograph of the one partially finalized CMS HE. . . . .	43
5.28	A photograph of a HO scintillating tile with the embedded WLS. . . .	44
5.29	An schematic drawing presenting the geometry of the HO. . . . .	44
5.30	A photograph of the HF steel wedges equipped with quartz fibers. . . .	45
5.31	A layout of the CMS muon system. Different subdetectors are labeled with different colors. . . . .	46
5.32	(Left) an schematic of a barrel chamber with DT and SL clearely labeled. (Right) an schematic of a drift cell. . . . .	47
5.33	A photograph of the a barrel wheel during construction. The DT chambers are gray while the steel return-yokes are painted in red. . . .	47
5.34	An schematic of a typical CSC. . . . .	48

5.35	A photograph of one of the endcaps wheels. . . . .	49
5.36	An schematic of one of the resistive plates in the CMS muon system. . . . .	50
5.37	Architecture and hierarchy of the CMS L1 Trigger. . . . .	51
5.38	An schematic respresentation of the HLT. The modular desing can seen tracing the vertical arrows while the independent paths are seen from left to right. The HLT final decision is the logical OR of all the existing paths. . . . .	52
5.39	A summary of the data streams recorded during (left) 2012 and (right) 2015. . . . .	53
6.1	Feynman diagram for squark pair-production. . . . .	56
6.2	An schematic of the different rest frames involved in deriving the razor variables. The lab frame is in the left panel, the CM frame is in the middle panel, and the squark rest frames are in the right panel.	57
6.3	Razor variables distributions for squark pair-production. $M_R$ is shown in the left panel and $R^2$ is shown in the right panel. The squark mass is set to 1150 GeV while the LSP mass is varied and shown with different color lines. . . . .	60
6.4	The 2-dimensional $R^2$ - $M_R$ distribution. The squark mass is set to 1150 GeV while the LSP mass is varied and shown with different color squares. The orange band represents the contour of constant SM background. . . . .	60
6.5	Razor analysis 95% CL. limit in the $m_0$ - $m_{1/2}$ plane of the CMSSM model using 7 TeV data. The model parameters have the following values: $\tan(\beta) = 10$ , $A_0 = 0$ , and $\text{sgn}(\mu) = +1$ . . . . .	61
6.6	Razor analysis 95% CL. limits for (left) gluino and (right) stop pair- production using 8 TeV data. The limits are shown for different branching ratios of the particles involved. . . . .	62
6.7	Razor analysis 95% CL. limits for gluino pair-production using 13 TeV data. The limits are shown for different branching ratios of the parti- cles involved. . . . .	62
7.1	Feynman diagrams for the pair production of DM particles corre- sponding to an effective field theory using a vector or axial-vector operator (left), and a scalar operator (right). . . . .	66
7.2	$R^2$ - $\Delta\phi(J_1, J_2)$ distribution for the QCD background in the $0\mu$ box. . . . .	72
7.3	(a) $R^2$ and (b) $M_R$ - $R^2$ razor distributions for the QCD background in the $0\mu$ box. . . . .	73

- 7.4 Comparison of observed yields in the  $1\mu$  control region and the data-driven background estimate derived from on the  $2\mu$  control region data in the four  $M_R$  categories: VL (top left), L (top right), H (bottom left), and VH (bottom right). The bottom panel in each plot shows the ratio between the two distributions. The observed bin-by-bin deviation from unity is interpreted as an estimate of the systematic uncertainty associated to the background estimation methodology for the  $0\mu$  search region. The dark and light bands represent the statistical and the total uncertainties in the estimates, respectively. The horizontal bars indicate the variable bin widths. . . . . 75
- 7.5 Comparison of the observed yield and the prediction from simulation as a function of  $R^2$  in the  $2\mu b$  control region. The uncertainties in the data and the simulated sample are represented by the vertical bars and the shaded bands, respectively. The horizontal bars indicate the variable bin widths. . . . . 76
- 7.6 Comparison of the observed yield in the zero b-tag control region and the background estimates in the four  $M_R$  categories: VL (top left), L (top right), H (bottom left), and VH (bottom right). The contribution of individual background processes is shown by the filled histograms. The bottom panels show the ratio between the observed yields and the total background estimate. For reference, the distributions from two benchmark signal models are also shown, corresponding to the pair production of DM particles of mass 1 GeV in the EFT approach with vector coupling to u or d quarks. The horizontal bars indicate the variable bin widths. . . . . 77
- 7.7 Comparison of the observed yield and the prediction from simulation in the  $Z(\mu\mu)b$  control sample (left) and of the observed yield in the  $1\mu b$  control sample and the background estimates from the  $2\mu b$  and  $Z(\mu\mu)b$  control samples (right), shown as a function of  $R^2$ . The bottom panel of each figure shows the ratio between the data and the estimates. The shaded bands represent the statistical uncertainty in the left plot, and the total uncertainty in the right plot. The horizontal bars indicate the variable bin widths. . . . . 78

7.8 Comparison of observed event yields and background estimates as a function of $R^2$ , for the one (left) and two (right) b-tag search regions. The shaded bands represent the total uncertainty in the estimate. The horizontal bars indicate the variable bin widths. . . . .	79
7.9 Total (estimated using the cross-check analysis) and JES systematic uncertainties. The green band corresponds to the systematic uncertainty associated with the background prediction method, while the red band corresponds to the JES systematic only. Panels (a) and (b) show the VL and L $M_R$ categories, respectively. Panels (c) and (d) show the H and VH $M_R$ categories, respectively. . . . .	80
7.10 Total (estimated using the cross-check analysis) and ISR systematic uncertainties. The green band corresponds to the systematic uncertainty associated with the background prediction method, while the red band corresponds to the ISR systematic only. Panels (a) and (b) show the VL and L $M_R$ categories, respectively. Panels (c) and (d) show the H and VH $M_R$ categories, respectively. . . . .	81
7.11 PDF systematic uncertainty for a vector mediated EFT signal model with DM mass = 700 GeV. The blue band corresponds to the systematic error associated with PDF uncertainty. Panels (a) and (b) show the VL and L $M_R$ categories, respectively. Panels (c) and (d) show the H and VH $M_R$ categories, respectively. . . . .	83
7.12 JES systematic uncertainty for a vector mediated EFT signal model with DM mass = 700 GeV. The blue band corresponds to the systematic error associated with JES uncertainty. Panels (a) and (b) show the VL and L $M_R$ categories, respectively. Panels (c) and (d) show the H and VH $M_R$ categories, respectively. . . . .	84
7.13 ISR systematic uncertainty for a vector mediated EFT signal model with DM mass = 700 GeV. The blue band corresponds to the systematic error associated with ISR uncertainty. Panels (a) and (b) show the VL and L $M_R$ categories, respectively. Panels (c) and (d) show the H and VH $M_R$ categories, respectively. . . . .	85

7.14 Lower limit at 90% CL on the cutoff scale $\Lambda$ as a function of the DM mass $M_\chi$ in the case of axial-vector (left) and vector (right) currents. The validity of the EFT is quantified by $R_\Lambda = 80\%$ contours, corresponding to different values of the effective coupling $g_{\text{eff}}$ . For completeness, regions forbidden by the EFT validity condition $\Lambda > 2M_\chi/g_{\text{eff}}$ are shown for two choices of the effective coupling: $g_{\text{eff}} = 1$ (light gray) and $g_{\text{eff}} = 4\pi$ (dark gray). . . . .	87
7.15 Upper limit at 90% CL on the DM-nucleon scattering cross section $\sigma_{N\chi}$ as a function of the DM mass $M_\chi$ in the case of spin-dependent axial-vector (left) and spin-independent vector (right) currents. A selection of representative direct detection experimental bounds are also shown. . . . .	89
7.16 Lower limit at 90% CL on the cutoff scale $\Lambda$ as a function of the DM mass $M_\chi$ in the case of axial-vector (left) and vector (right) currents. A selection of direct detection experimental bounds are also shown. . . . .	90
7.17 Lower limit at 90% CL on the cutoff scale $\Lambda$ for the scalar operator $\hat{O}_S$ as a function of the DM mass $M_\chi$ . The validity of the EFT is quantified by $R_\Lambda = 80\%$ (left) and $R_\Lambda = 25\%$ (right) contours, corresponding to different values of the effective coupling $g_{\text{eff}}$ . For completeness, regions forbidden by the EFT validity condition $\Lambda > 2M_\chi/g_{\text{eff}}$ are shown for two choices of the effective coupling: $g_{\text{eff}} = 1$ (light gray) and $g_{\text{eff}} = 4\pi$ (dark gray). . . . .	91
8.1 Diagram illustrating the SUSY benchmark simplified model of bottom squark decays to a Higgs boson, a b-jet, and the LSP. . . . .	98
8.2 Summary of the results in the HighRes category for the 8 TeV version of the analysis. . . . .	99
8.3 Summary of the results in the HighRes category for the 8 TeV version of the analysis. . . . .	99
8.4 Summary of the results in the HighRes category for the 8 TeV version of the analysis. . . . .	100
8.5 Summary of the results in the HighRes category for the 8 TeV version of the analysis. . . . .	100
8.6 Summary of the results in the HighRes category for the 8 TeV version of the analysis. . . . .	100
8.7 Diagram illustrating the event categorization used in the analysis. . . . .	103

8.8	Distribution of events in the $M_R$ and $R^2$ plane for the HighPt and H( $\gamma\gamma$ )-H/Z(bb) category for sbottom pair production with $m_{\tilde{b}} = 300$ GeV and $m_\chi = 1$ GeV. The signal expectation is shown in the color scale and the bin numbers show where each bin is located in the $M_R$ and $R^2$ plane. . . . .	104
8.9	Distribution of events in the $M_R$ and $R^2$ plane for the HighRes and LowRes categories for sbottom pair production with $m_{\tilde{b}} = 300$ GeV and $m_\chi = 1$ GeV. The signal expectation is shown in the color scale and the bin numbers show where each bin is located in the $M_R$ and $R^2$ plane. . . . .	105
8.10	sideband fits for the search region: HighPt, $M_R > 600$ GeV, $R^2 > 0.025$ . . . . .	107
8.11	sideband fits for the search region: HighRes, $150 < M_R < 250$ GeV, $R^2 > 0$ . . . . .	108
8.12	Sideband fits for the search region: LowRes, $150 < M_R < 250$ GeV, $R^2 > 0.175$ . . . . .	108
8.13	Sideband fits for the search region: H( $\gamma\gamma$ )-H/Z(bb), $M_R > 150$ GeV, $R^2 > 0$ . . . . .	111
8.14	Examples of the bias distribution for bin0 (HighPt, $M_R > 600$ , $R^2 > 0.025$ ). Left: $f_1$ (assumed parent function) = poly3, $f_2$ (tested function) = singleExp; right: $f_1 = \text{poly3}$ , $f_2 = \text{poly3}$ . From the left plot we can see that singleExp does not pass the bias test since it has large bias to fit poly3. . . . .	113
8.15	The diphoton mass distribution for various search region bins in the HighPt category are shown along with the background-only fit (left) and the signal plus background fit (right). The red curve represents the background prediction; the green curve represents the signal; and the blue curve represents the sum of the signal and background. The definition of the search bin is labeled above each pair of plots. . . . .	115
8.16	The diphoton mass distribution for various search region bins in the HighPt category are shown along with the background-only fit (left) and the signal plus background fit (right). The red curve represents the background prediction; the green curve represents the signal; and the blue curve represents the sum of the signal and background. The definition of the bin is labeled above each pair of plots. . . . .	116

- 8.17 The diphoton mass distribution for various search region bins in the HighPt category are shown along with the background-only fit (left) and the signal plus background fit (right). The red curve represents the background prediction; the green curve represents the signal; and the blue curve represents the sum of the signal and background. The definition of the bin is labeled above each pair of plots. . . . . 117
- 8.18 The diphoton mass distribution for various search region bins in the  $H(\gamma\gamma)$ -H/Z(bb) category are shown along with the background-only fit (left) and the signal plus background fit (right). The red curve represents the background prediction; the green curve represents the signal; and the blue curve represents the sum of the signal and background. The definition of the bin is labeled above each pair of plots. . . . . 117
- 8.19 The diphoton mass distribution for the search region bin 9 are shown along with the background-only fit (left) and the signal plus background fit (right). The top row shows the HighRes category, while the bottom row shows the LowRes category. The red curve represents the background prediction; the green curve represents the signal; and the blue curve represents the sum of the signal and background. The definition of the bin is labeled above each pair of plots. . . . . 118
- 8.20 The diphoton mass distribution for the search region bin 10 are shown along with the background-only fit (left) and the signal plus background fit (right). The top row shows the HighRes category, while the bottom row shows the LowRes category. The red curve represents the background prediction; the green curve represents the signal; and the blue curve represents the sum of the signal and background. The definition of the bin is labeled above each pair of plots. . . . . 119
- 8.21 The diphoton mass distribution for the search region bin 11 are shown along with the background-only fit (left) and the signal plus background fit (right). The top row shows the HighRes category, while the bottom row shows the LowRes category. The red curve represents the background prediction; the green curve represents the signal; and the blue curve represents the sum of the signal and background. The definition of the bin is labeled above each pair of plots. . . . . 120

8.22	The diphoton mass distribution for the search region bin 12 are shown along with the background-only fit (left) and the signal plus background fit (right). The top row shows the HighRes category, while the bottom row shows the LowRes category. The red curve represents the background prediction; the green curve represents the signal; and the blue curve represents the sum of the signal and background. The definition of the bin is labeled above each pair of plots. . . . .	121
8.23	The diphoton mass distribution for the search region bin 13 are shown along with the background-only fit (left) and the signal plus background fit (right). The top row shows the HighRes category, while the bottom row shows the LowRes category. The red curve represents the background prediction; the green curve represents the signal; and the blue curve represents the sum of the signal and background. The definition of the bin is labeled above each pair of plots. . . . .	122
8.24	The observed significance in units of standard deviations is plotted for each search bin. The significance is computed using the profile likelihood, where the sign reflects whether an excess (positive sign) or deficit (negative sign) is observed. The categories that the bins belong to are labeled at the bottom. The yellow and green bands represent the $1\sigma$ and $2\sigma$ regions, respectively. . . . .	124
8.25	The observed 95% confidence level (C.L.) upper limits on the production cross section for sbottom pair production decaying to a bottom quark, a Higgs boson, and the LSP are shown. The solid and dotted black contours represent the observed exclusion region and its $1\sigma$ bands, while the analogous blue contours represent the expected exclusion region and its $1\sigma$ bands. . . . .	124
8.26	The observed significance scan for sbottom pair production decaying to a bottom quark, a Higgs boson, and the LSP is shown. . . . .	125
9.1	Cross section as a function of the incoming photon energy in lead. . . .	130
9.2	Fractional energy loss per radiation length in lead as a function of the electron/positron energy. . . . .	131
9.3	Graphical definition of the critical energy ( $E_c$ ). The intersection of the solid lines is the definition used in this thesis. The intersection between the solid (ionization) and dashed line is alternative definition.	132

9.4	Electron critical energy ( $E_c$ ) for the chemical elements. Experimental data is shown for gases (red circles) and solids (magenta crosses). Fits are shown for gases (dashed red line) and solids (solid magenta line) .	133
9.5	Shower profile in the longitudinal direction for a 30 GeV electron in iron from an EGS4 simulation. The solid line histogram shows the fractional energy per radiation length, and the solid line curve is a fit to the distribution using a gamma function. The number of electrons (solid circles) and photons (hollowed squares) with energies larger than 1.5 MeV and crossing planes at $X_0/2$ intervals (scale on the right) is also shown. The number of photons has been scaled down to have the same area as the number of electrons distribution. . . . .	134
9.6	Shower profile in the longitudinal direction for electrons in copper. The different curves and points represent different electron energies ranging from 1 GeV-1 TeV. . . . .	135
9.7	Energy deposited per unit length in the transverse direction for 10 GeV electrons in copper. The shower has been sample in three different places; at $2X_0$ (red circles), $6X_0$ (black dots), and $15X_0$ (blue crosses).	136
10.1	Timing measurement schematic breakdown using a monolithic, large scintillating crystal. The incident particle impinges on the crystal face from the left. The characteristic time intervals are discussed in the text. . . . .	139
10.2	The basic schematic diagram of the experimental setup for a typical TOF measurement is shown to illustrate the basic detector elements. One photodetector is used as a time reference and the second measures energy and time simultaneously. . . . .	140
10.3	Sample pulses as digitized by the DRS4 board. On the left a pulse is shown from the reference Hamamatsu R3809 MCP-PMT, and on the right is a pulse from the Hamamatsu R3809 MCP-PMT optically coupled to a $(1.7 \text{ cm})^3$ LYSO crystal cube recorded using 8 GeV electron beam. . . . .	141
10.4	Sample fits used to assign timestamps to digitized MCP-PMT pulses. On the left is a pulse from the reference Hamamatsu R3809 MCP-PMT, and on the right is a pulse from the Hamamatsu R3809 MCP-PMT optically coupled to a $(1.7 \text{ cm})^3$ LYSO crystal recorded during an 8 GeV electron run.	141
10.5	A schematic diagram of the experimental setup for the TOF measurement using the LYSO sampling calorimeter is shown on the left, along with a picture of the experimental setup shown on the right. . . . .	143

10.6	TOF distributions for the LYSO cube sampling calorimeter for 4 GeV (top left), 8 GeV (top right), 16 GeV (bottom left), 32 GeV (bottom right) electron beam energy. . . . .	144
10.7	The shashlik configuration based upon interleaved W and LYSO layers. Twenty-eight LYSO crystal plates and twenty-seven W plates comprise the module. Four WLS fibers are used to read out the scintillation light from the tiles. . . . .	145
10.8	A schematic diagram of the experimental setup for the TOF measurement using the LYSO-tungsten shashlik calorimeter with fiber signal extraction, along with a photograph of the experimental setup. . . . .	145
10.9	(a) Pulse shapes digitized by the DRS4 board and averaged over several hundred events obtained from the LYSO-tungsten shashlik calorimeter with light extracted using DSB1 (blue) and Y11 (red) WLS fibers. (b) DSB1(blue) shashlik average light pulse shape compared with the averaged pulse shape obtained from direct optical coupling of the photodetector to one edge of a LYSO tile in the shashlik calorimeter. (green) . . . . .	146
10.10	(Left) Histogram of the pulse integral which is proportional to the total collected charge is shown for events recorded using the LYSO cube sampling calorimeter for a 32 GeV electron beam. (Right) Histogram of the pulse integral for events recorded using the LYSO-tungsten shashlik calorimeter using DSB1 fibers, for a 32 GeV electron beam. The background is included due to a misconfiguration of the Cherenkov counter. . . . .	147
10.11	TOF distributions for the LYSO-tungsten shashlik calorimeter using DSB1 fibers for electron beams with varying beam energies. . . . .	147
10.12	A schematic diagram of the experimental setup for the TOF measurement using the LYSO-tungsten shashlik calorimeter with signal extraction from the edges of two LYSO plates, along with a picture of the experimental setup.	148
10.13	A photograph of the two exposed LYSO layers in the shashlik cell. The scintillation light signal is extracted by optically coupling the edges of these two exposed LYSO layers to MCP-PMT photodetectors. . . . .	148
10.14	TOF distributions for the LYSO-tungsten shashlik calorimeter with signal extracted from the edges of two LYSO layers. . . . .	149
10.15	. . . . .	149

10.16	Timing resolution measurement as a function of the electron beam energy for (left) the LYSO cube sampling calorimeter (middle) the LYSO-tungsten shashlik calorimeter read-out with DSB1 fibers (right) the LYSO-tungsten shashlik calorimeter read-out directly by optically coupling to the edges of two LYSO layers. In all cases we fit the data with a function of $1/\sqrt{E}$ and a constant term. . . . .	149
10.17	Comparison of time resolutions obtained with the $(1.7 \text{ cm})^3$ LYSO cube (blue), and the LYSO-tungsten shashlik calorimeter with light extracted using DSB1 fibers (red). The x-axis in this figure displays the amplitude of the signal, corrected for the attenuation factors. . . . .	150
11.1	The experimental setup inside of the dark box is shown. The beam direction is from the bottom of the photograph to the top. The detector elements shown in the order from upstream to downstream of the beam are: the tungsten absorber, the Photonis XP85011 MCP-PMT located on the motorized stage, and the Photek 240 MCP-PMT used as a time reference detector. The DRS4 waveform digitizers are also shown on the lower right side. . . . .	154
11.2	The external view of the Photonis XP85011 MCP-PMT is shown on the left, and the schematic diagram is shown on the right. The red square indicates the pixels used for the experiment and data analysis. .	155
11.3	Example of a digitized signal from a single Photonis pixel (left) and Photek (right) MCP-PMT following a high-energy electron shower, via DRS4. . . .	156
11.4	The mean charge measured for each pixel for one example run is shown. During this run, the Photonis MCP-PMT was held in the same location. Based on the distribution of the mean charge among the pixels, we can infer that the beam center is located in the upper half of the center pixel. Pixel 44 is not shown as it was found to be not operational. . . . .	157
11.5	The distribution of reconstructed shower positions is shown for three runs with the beam centered near the top, center, and bottom of the central pixel. . . . .	158
11.6	The distributions of reconstructed shower position in the y axis is shown for the three runs corresponding to the distributions shown in Figure 11.5. The measured beam displacements are compared to the known displacements as recorded by the motorized stage. . . . .	159

11.7	The distributions of the measured $x$ (left) and $y$ (right) coordinates are shown along with the fit to the resolution model. The position resolution of the EM shower as measured by the MCP-PMT detector is determined from the fit to the resolution model. . . . .	160
11.8	The time distributions obtained using the highest energy pixel (left) and the energy weighted algorithm (right) are shown for one example run. The distributions are fitted with Gaussian models, and the width parameter of the Gaussian is displayed on the plot. . . . .	161
11.9	Time resolution found for each run. The time-stamp obtained using the energy weighting method yields time resolutions consistently below 60 ps. The time resolution measured using the single pixel with the largest signal is significantly worse. . . . .	162
11.10	The correlation between the time measurement and the measured integrated charge is shown on the left for one example pixel. The same correlation after performing the time measurement correction is shown on the right. . . . .	163
11.11	The time resolution of the electromagnetic shower for various runs is shown after performing the time measurement correction based on the measured integrated charge. . . . .	163
11.12	The time resolution is plotted as a function of the number of pixels included in the energy-weighted algorithm for one example run. . . .	164
12.1	The measured capacitance as a function of the applied bias voltage. .	166
12.2	The electric diagram for the silicon diode connections (left). External view of the box with silicon diode, and the bias voltage connection is shown below it (right). . . . .	166
12.3	A schematic diagram of the test-beam setup is shown. The $t_0$ and $t_1$ are defined in Section B.7. . . . .	168
12.4	Test beam setup. . . . .	168
12.5	Examples of the signal pulse waveform for the silicon sensor (left) and the Photek MCP-PMT (right) digitized by CAEN V1742 digitizer board. The bias voltage applied to the silicon pad sensor is 500 V. .	169
12.6	The distribution of charge integrated in the silicon sensor is shown for data events with no beam and random trigger. . . . .	170

- 12.7 The distribution of charge integrated in the silicon sensor is shown for a beam of 120 GeV protons (left) and 8 GeV electrons (right) without any absorber upstream of the silicon sensor. These conditions mimic the response of the silicon sensor to a minimum-ionizing particle. All triggered events were used in these distributions. . . . . 171
- 12.8 Left: An example of the distribution of integrated charge in the silicon sensor for 32 GeV electrons and 6  $X_0$  absorber shown in units of  $Q_{MIP}$ . Right: The integrated charge in the silicon sensor expressed in units of  $Q_{MIP}$  is shown for the same 6  $X_0$  absorber as a function of the electron beam energy. The uncertainty bands show the RMS of the measured charge distribution. The red line is the best fit to a linear function. . . . . 171
- 12.9 The dependence of  $\Delta t$  on the integrated charge in the silicon sensor is shown on the left. The red curve represents the fit to the profile plot of the two dimensional distribution, and is used to correct  $\Delta t$  for this effect. On the right, we show the corresponding two dimensional distribution after performing the correction. A 16 GeV electron beam is used, and the silicon sensor is placed after 6  $X_0$  of tungsten absorber. 173
- 12.10 Left: The distribution of  $\Delta t$  between the silicon sensor and the Photek MCP-PMT. A 32 GeV electron beam is used, and the silicon sensor is placed after 6  $X_0$  of tungsten absorber. Right: The measured time resolution between the silicon sensor and the Photek MCP-PMT reference is shown as a function of the electron beam energy. The silicon sensor is placed after 6  $X_0$  of tungsten absorber. . . . . 174
- 12.11 On the left, the integrated charge in the silicon sensor expressed in units of  $Q_{MIP}$  is shown as a function of the absorber ( $W$ ) thickness measured in units of radiation lengths ( $X_0$ ). The electron beam energy was 8 GeV. The uncertainty bands show the RMS of the measured charge distribution. On the right, the time resolution between the silicon sensor and the Photek MCP-PMT reference is shown as a function of the absorber thickness. . . . . 174
- 12.12 The time resolution between the silicon sensor and the Photek MCP-PMT reference is shown as a function of bias voltage applied on the silicon sensor. The electron beam energy was 16 GeV, and the silicon sensor is placed after 6  $X_0$  of tungsten absorber. . . . . 175

13.1	An HGC sensor schematic geometry with 7 pixels (left), and a s CAD schematic of the entire sensor (right) are shown. . . . .	177
13.2	The implemented HGC timing layer is shown. 25 pixels with full analog electronics were implemented. The silicon sensor is at the back of the PCB. . . . .	177
13.3	A schematic diagram of the test-beam setup is shown. The $t_0$ and $t_1$ are defined in Section B.7. . . . .	178
13.4	HGC timing layer test beam setup. . . . .	179
13.5	Examples of the signal pulse waveform for one the pixels of the HGC timing layer (left) and the Photek MCP-PMT (right) digitized by CAEN V1742 digitizer board. The bias voltage applied to the HGC silicon sensor is $-300$ V. . . . .	179
13.6	Examples of the timestamps extraction for a pulse waveform in one the pixels of the HGC timing layer (left) and the Photek 240 MCP-PMT (right) digitized by CAEN V1742 digitizer board. The timestamp on the HGC pixel is extracted by intersecting the linear fit (solid red line) with the horizontal line corresponding to 45% of the pulse maximum. The timestamp for the Photek 240 is the mean parameter of the Gaussian fit (solid blue line). . . . .	180
13.7	Examples of the shower transverse profile sampled by the HGC layer for a 32 GeV (left) and 16 GeV (right) electron beam. There is $6X_0$ of tungsten right upstream of the HGC layer. . . . .	181
13.8	TOF distributions for (left) the pixel with the highest and (right) the the pixel with the second highest charge in the HGC layer using a 32 GeV electron beam and $6X_0$ of tungsten. The TOF resolutions are estimated by the standard deviation parameter of the Gaussian fit (red solid curve) to the TOF distribution. . . . .	182
13.9	TOF distributions of the HGC layer using a 32 GeV electron beam and $6X_0$ of tungsten, where the pixels are combined with (left) the default algorithm and (right) the mpv of the charge distribution as the weight. The TOF resolutions are estimated by the standard deviation parameter of the Gaussian fit (red solid curve) to the TOF distribution .	182
13.10	HGC layer TOF resolution as a function of the number of pixels combined. The distance between the absorber and the HGC layer was varied to sample the shower at different location. . . . .	183

13.11	$R_7$ distribution for different separations between the HGC layer and the $6X_0$ of tungsten. . . . .	183
13.12	HGC layer TOF resolution as a function of the beam energy using $6X_0$ of tungsten. The functional form $A/\sqrt{E} + B$ was fitted to the data points (red solid curve). . . . .	184
13.13	TOF distributions for (left) the Photonis MCP-PMT and (right) the final two-layer combination using a 32 GeV electron beam and $6X_0$ of tungsten. The TOF resolutions are estimated by the standard deviation parameter of the Gaussian fit (red solid curve) to the TOF distribution . . . . .	185
13.14	TOF distributions after a 50 ps Gaussian smearing for (left) the pixel with the highest and (right) the pixel with the second highest charge in the HGC layer using a 32 GeV electron beam and $6X_0$ of tungsten. The TOF resolutions are estimated by the standard deviation parameter of the Gaussian fit (red solid curve) to the TOF distribution. . . . .	185
13.15	TOF distributions after a 50 ps Gaussian smearing for (left) the HGC layer and (right) the final two-layer combination using a 32 GeV electron beam and $6X_0$ of tungsten. The TOF resolutions are estimated by the standard deviation parameter of the Gaussian fit (red solid curve) to the TOF distribution. . . . .	186
13.16	HGC layer TOF resolution after a 50 ps Gaussian smearing as a function of the number of pixels combined. . . . .	186
13.17	TOF distributions as a function of the beam energy after a 50 ps Gaussian smearing for (left) the HGC layer and (right) the final two-layer combination using $6X_0$ of tungsten. The functional form $A/\sqrt{E} + B$ was fitted to the data points (red solid curve). . . . .	187
A.1	The observed invariant mass spectra $m_{\gamma\gamma}$ for selected events in the (left) EBEB and (right) EBEE categories. There are no selected events with $m_{\gamma\gamma} > 2000$ GeV. The solid lines and the shaded bands show the results of likelihood fits to the data together with the associated 1 and 2 standard deviation uncertainty bands. The ratio of the difference between the data and the fit to the statistical uncertainty in the data is given in the lower plots. . . . .	215

- A.2 The 95% CL upper limits on the production of diphoton resonances as a function of the resonance mass  $m_X$ , from the analysis of data collected in 2016. Exclusion limits for the scalar and RS graviton signals are given by the grey (darker) and green (lighter) curves, respectively. The observed limits are shown by the solid lines, while the median expected limits are given by the dashed lines together with their associated 1 standard deviation uncertainty bands. The leading-order production cross section for diphoton resonances in the RS graviton model is shown for three values of the dimensionless coupling parameter  $\tilde{k}$  together with the exclusion upper limits calculated for the corresponding three values of the width relative to the mass,  $\Gamma_X/m_X$ . Shown are the results for (upper) a narrow width, (middle) an intermediate-width, and (lower) a broad resonance. . . . . 218
- A.3 Observed background-only  $p$ -values for resonances with (upper left)  $\Gamma_X/m_X = 1.4 \times 10^{-4}$ , (upper right)  $1.4 \times 10^{-2}$ , and (bottom)  $5.6 \times 10^{-2}$  as a function of the resonance mass  $m_X$ , from the analysis of data collected in 2016. The solid black and dashed blue lines correspond to spin-0 and spin-2 resonances, respectively. . . . . 219
- A.4 The 95% CL upper limits on the production of diphoton resonances as a function of the resonance mass  $m_X$ , from the combined analysis of data collected in 2015 and in 2016. Exclusion limits for the scalar and RS graviton signals are given by the grey (darker) and green (lighter) curves, respectively. The observed limits are shown by the solid lines, while the median expected limits are given by the dashed lines together with their associated 1 standard deviation uncertainty bands. The leading-order production cross section for diphoton resonances in the RS graviton model is shown for three values of the dimensionless coupling parameter  $\tilde{k}$  together with the exclusion upper limits calculated for the corresponding three values of the width relative to the mass,  $\Gamma_X/m_X$ . Shown are the results for (upper) a narrow width, (middle) an intermediate-width, and (lower) a broad resonance. . . . . 221

A.5 Observed background-only $p$ -values for resonances with (upper) $\Gamma_X/m_X = 1.4 \times 10^{-4}$ and (lower) $5.6 \times 10^{-2}$ as a function of the resonance mass $m_X$ , from the combined analysis of data recorded in 2015 and 2016. The results obtained for the two individual data sets are also shown. The curves corresponding to the scalar and RS graviton hypotheses are shown in left and right columns, respectively. The insets show an expanded region around $m_X = 750$ GeV. . . . .	222
A.6 The 95% CL upper limits on the production of diphoton resonances as a function of the resonance mass $m_X$ , from the combined analysis of the 8 and 13 TeV data. The 8 TeV results are scaled by the ratio of the 8 to 13 TeV cross sections. Exclusion limits for the scalar and RS graviton signals are given by the grey (darker) and green (lighter) curves, respectively. The observed limits are shown by the solid lines, while the median expected limits are given by the dashed lines together with their associated 1 standard deviation uncertainty bands. The leading-order production cross section for diphoton resonances in the RS graviton model is shown for three values of the dimensionless coupling parameter $\tilde{k}$ together with the exclusion upper limits calculated for the corresponding three values of the width relative to the mass, $\Gamma_X/m_X$ . Shown are the results for (upper) a narrow width, (middle) an intermediate-width, and (lower) a broad resonance. . . . .	223
A.7 Observed background-only $p$ -values for resonances with (upper) $\Gamma_X/m_X = 1.4 \times 10^{-4}$ and (lower) $5.6 \times 10^{-2}$ as a function of the resonance mass $m_X$ , from the combined analysis of the 8 and 13 TeV data. The results obtained for the two individual center-of-mass energies are also shown. The curves corresponding to the scalar and RS graviton hypotheses are shown in left and right columns, respectively. The insets show an expanded region around $m_X = 750$ GeV. . . . .	224
B.1 Pictorial representation of the decay chains and event topologies associated with model A (left) and model B (right), as described in the text. . . . .	227
B.2 Comparison between the CMS result (red) and our emulation (black). Note, this scan assumes $m_{\tilde{\chi}_1^0} = 1$ GeV and $m_{\tilde{\chi}_1^\pm} = m_{\tilde{\chi}_2^0}$ . . . . .	232

- B.3 (Top) The expected background and uncertainty (multiplied by a factor of two as explained in the text) compared to the best-fit signal distribution in the HighRes box for two particular mass points,  $m_{\tilde{b}_2} = 500 \text{ GeV}$  and  $m_{\tilde{b}_2} = 800 \text{ GeV}$ , in model A. (Bottom) The expected background and uncertainty (multiplied by a factor of two as explained in the text) compared to the best-fit signal distribution in the HighRes box for two particular mass points,  $m_{\tilde{b}_1} = 500 \text{ GeV}$  and  $m_{\tilde{b}_1} = 800 \text{ GeV}$ , in model B. The bin numbers correspond to the order of the signal regions in the yield tables in Ref. [208] and are reproduced in Tab. B.2. . . . . 233
- B.4 (Top) The 95% CL upper limit on the cross section on  $\tilde{b}_1 \tilde{b}_2$  production in model A as a function of  $m_{\tilde{b}_2}$  (black). (Bottom) The 95% CL upper limit on the cross section on  $\tilde{b}_1 \tilde{b}_1$  production in model B as a function of  $m_{\tilde{b}_1}$  (black) compared to the NLO+NLL predicted cross section (yellow). Note, these scans assume  $m_{\tilde{\chi}_1^0} = 100 \text{ GeV}$ ,  $m_{\tilde{\chi}_2^0} = 230 \text{ GeV}$ , and for model A  $m_{\tilde{b}_1} = 130 \text{ GeV}$ . . . . . 234
- B.5 (Top) The maximum significance  $Z(\sigma)$  for a given  $m_{\tilde{b}_2}$  in the top panel and the “best fit” signal cross section  $\sigma$  in the bottom panel for model A. (Bottom) The maximum significance  $Z(\sigma)$  for a given  $m_{\tilde{b}_1}$  in the top panel and the “best fit” signal cross section  $\sigma$  in the bottom panel for model B. Note, these scans assume  $m_{\tilde{\chi}_1^0} = 100 \text{ GeV}$ ,  $m_{\tilde{\chi}_2^0} = 230 \text{ GeV}$ , and for model A  $m_{\tilde{b}_1} = 130 \text{ GeV}$ . . . . . 235

## LIST OF TABLES

<i>Number</i>	<i>Page</i>
2.1 Group representation of the matter fields in the SM. . . . .	7
7.1 Measured trigger efficiency for different $M_R$ regions. The selection $R^2 > 0.35$ is applied. The uncertainty shown represents the statistical uncertainty in the measured efficiency. . . . .	67
7.2 Observed yield in each in events with $0\mu$ and no b-tagged jets for each $M_R$ category. The number overlapping events between the razor and monojet seaches is also presented. . . . .	70
7.3 Analysis regions for events with zero identified b-tagged jets. The definition of these regions is based on the muon multiplicity, the output of the CSV b-tagging algorithm, and the value of $M_R$ . For all the regions, $R^2 > 0.5$ is required. . . . .	71
7.4 Analysis regions for events with identified b-tagged jets. The definition of these regions is based on the muon multiplicity, the output of the CSV b-tagging algorithm, and the value of $M_R$ . For all the regions, $R^2 > 0.5$ is required. . . . .	71
7.5 Comparison of the observed yield in the $1\mu$ control region in each $M_R$ category and the corresponding data-driven background estimate obtained by extrapolating from the $2\mu$ control region. The uncertainty in the estimates takes into account both the statistical and systematic components. The contribution of each individual background process is also shown, as estimated from simulated samples, as well as the total MC predicted yield. . . . .	74
7.6 Comparison of the observed yield for the $2\mu$ control region in each $M_R$ category and the corresponding prediction from background simulation. The quoted uncertainty in the prediction reflects only the size of the simulated sample. The contribution of each individual background process is also shown, as estimated from simulated samples. .	74
7.7 Observed yield and predicted background from simulated samples in the $2\mu b$ control region. The quoted uncertainty in the prediction only reflects the size of the simulated sample. The contribution of each individual background process is also shown, as estimated from simulated samples. . . . .	75

7.8 Comparison of the observed yields for for the zero b-tag search region in each $M_R$ category and the corresponding background estimates. The uncertainty in the background estimate takes into account both the statistical and systematic components. The contribution of each individual background process is also shown, as estimated from simulated samples, as well as the total MC predicted yield. . . . .	76
7.9 Comparison of the observed yields in the $Z(\mu\mu)b$ and $1\mu b$ samples, the corresponding predictions from background simulation, and (for $1\mu b$ only) the cross-check background estimate. The contribution of each individual background process is also shown, as estimated from simulated samples. . . . .	78
7.10 Comparison of the observed yield for events in the one and two b-tag search regions and the corresponding background estimates. The uncertainty in the estimates takes into account both the statistical and systematic components. The contribution of each individual background process is also shown, as estimated from simulated samples, as well as the total MC predicted yield. . . . .	79
7.11 Systematic uncertainties associated with the description of the DM signal. The values indicated represent the typical size. The dependence of these systematic uncertainties on the $R^2$ and $M_R$ values is taken into account in the determination of the results. . . . .	82
7.12 The 90% CL limits on DM production in the case of axial-vector couplings. Here, $\sigma_{UL}^u$ and $\sigma_{UL}^d$ are the observed upper limits on the production cross section for u and d quarks, respectively; $\Lambda_{LL}$ is the observed cutoff energy scale lower limit; and $\sigma_{N\chi}$ is the observed DM-nucleon scattering cross section upper limit. . . . .	89
7.13 The 90% CL limits on DM production in the case of vector couplings. Here, $\sigma_{UL}^u$ and $\sigma_{UL}^d$ are the observed upper limits on the production cross section for u and d quarks, respectively; $\Lambda_{LL}$ is the observed cutoff energy scale lower limit; and $\sigma_{N\chi}$ is the observed DM-nucleon scattering cross section upper limit. . . . .	89
7.14 The 90% CL limits on DM production in the case of scalar couplings. Here, $\sigma_{UL}^{obs}$ is the observed upper limit on the production cross section, $\Lambda_{LL}^{obs}$ and $\Lambda_{LL}^{exp}$ are the observed and expected cutoff energy scale lower limit, respectively. . . . .	91

7.15	Background estimates and observed yield for each $R^2$ bin in the VL $M_R$ category. . . . .	95
7.16	Background estimates and observed yield for each $R^2$ bin in the L $M_R$ category. . . . .	95
7.17	Background estimates and observed yield for each $R^2$ bin in the H $M_R$ category. . . . .	96
7.18	Background estimates and observed yield for each $R^2$ bin in the VH $M_R$ category. . . . .	96
7.19	Background estimates and observed yield for each bin in the $0\mu b$ signal region. . . . .	96
7.20	Background estimates and observed yield for each bin in the $0\mu bb$ signal region. . . . .	96
8.1	A summary of the search region bins in each category is presented. The functional form used to model the non-resonant background is also listed. An exponential function of the form $e^{-ax}$ is denoted as “singleExp”; a modified exponential function of the form $e^{-ax^b}$ is denoted as “modExp”; and an N’th order Bernstein polynomial is denoted by “polyN”. . . . .	104
8.2	The predicted yields for the standard model Higgs background processes are shown for an integrated luminosity corresponding to $15.2 \text{ fb}^{-1}$ for each search region considered in this analysis. The contributions from each standard model Higgs process is shown separately, and the total is shown on the rightmost column along with its full uncertainty.	109
8.3	Full list of p.d.f (function) used in the AIC test. . . . .	110
8.4	AIC results summary for the search region: HighPt, $M_R > 600 \text{ GeV}$ , $R^2 > 0.025$ . . . . .	110
8.5	AIC results summary for the search region: HighRes, $150 < M_R < 250 \text{ GeV}$ , $R^2 > 0$ . . . . .	110
8.6	AIC results summary for the search region: LowRes, LowRes, $150 < M_R < 250 \text{ GeV}$ , $R^2 > 0.175$ . . . . .	111
8.7	AIC results summary for the search region: H( $\gamma\gamma$ )-H/Z(bb), $M_R > 150 \text{ GeV}$ , $R^2 > 0$ . . . . .	111

8.8 Examples of the bias estimate for different function pairs passing the AIC test for bin0 (HighPt, $M_R > 600$ , $R^2 > 0.025$ ). Functions in the first column are the assumed parent functions ( $f_1$ ), while functions in the first row are the ones being tested ( $f_2$ ). In the first row, the numbers in brackets are the AIC weights. . . . .	113
8.9 List of the selected background functions for different search regions. . . . .	114
8.10 Summary of systematic uncertainties and their size. . . . .	114
8.11 The non-resonant background yields, SM Higgs background yields, best fit signal yields, and observed local significance are shown for the signal plus background fit in each search region bin. The uncertainties include both statistical and systematic components. The non-resonant background yields shown correspond to the yield within the window between 122 GeV and 129 GeV and is intended to better reflect the background under the signal peak. The observed significance for the bins in HighRes and LowRes categories are identical because they are the result of a simultaneous fit. The significance is computed using the profile likelihood, where the sign reflects whether an excess (positive sign) or deficit (negative sign) is observed. . . . .	123
9.1 Tabulated values for $L_{\text{rad}}$ and $L'_{\text{rad}}$ from Y. S Tsai. . . . .	131
B.1 Photon isolation requirements, as in Ref [157]. The photon isolation variables, $I_\gamma$ , $I_h$ , and $I_\pi$ , are computed by summing the transverse momenta of photons, neutral hadrons, and charged hadrons, respectively, inside an isolation cone of radius $\Delta R = 0.3$ around the selected photon. . . . .	228
B.2 HighRes bin numbering scheme as in Ref. [208]. . . . .	232

## **Part I**

# **Preliminaries, Supersymmetry, and Dark Matter**

## Chapter 1

### INTRODUCTION

Particle physics is perhaps facing one of the biggest crossroads since the discovery of the electron in 1987. The subject evolved from having just one particle to have a catalog of particles and their possible interactions, and even explain the origin of the particles masses. This knowledge is encoded in what we today know as the Standard Model (SM) of particle physics, the most precise and perhaps the most successful theory that mankind has ever had. The SM is a quantum field theory that sets the rules by which the particles that we have observed interact with each other, these interactions comprise three of the four fundamental forces we know: the strong, weak, and electromagnetic interactions; leaving gravity aside. Most of the predictions since its formulation, mostly during the 1960s, have been experimentally observed: we have measured the W and Z bosons, the top quark, and recently the discovery of the last piece of the puzzle by the ATLAS and CMS collaborations [89, 17], the Higgs boson. Despite the success and completeness of the SM, both experimentally and theoretically motivated, we are now faced with fundamental questions that are unfortunately not answered:

- What is the nature of the *dark matter* whose existence has only been inferred by astrophysical measurement?
- Is there a unification of the gauge coupling at the Planck scale?
- Why is Higgs boson mass at the weak scale since its mass is sensitive to a high energy scale through radiative corrections (fine tuning)?
- What's the nature of the matter/anti-matter asymmetry observed in the universe?
- What is the nature of *dark energy* whose existence provides an explanation for the expansion of the universe?
- Is there a quantum theory of gravity?

This thesis is more concerned with the first three bullets, which can actually be answered with a single theory: *supersymmetry*, a quantum field theory that relates

fermions and bosons[xx], which tackles these questions by adding a dark matter candidate to the particle spectrum, unifying the gauge couplings at the Planck scale, and alleviating the fine tuning of the Higgs mass.

Although supersymmetry is a very compelling theoretical framework, it is not needed for having a suitable dark matter candidate. In fact, in order to match the observed dark matter relic density, there are just two conditions that need to be satisfied. These are, the strength of the interaction of the dark matter (DM) candidate – here it is assumed that the DM candidate is a fundamental particle – with the SM particles is at the level of the weak interaction, and the mass of the DM candidate is about 100 GeV. This realization is called the *weakly interacting massive particle (wimp) miracle*. This led to the idea that DM candidates can be produced at particle colliders by just inverting the direction of interaction, i.e. two SM particles annihilating into two DM candidates. Unfortunately, this event topology will leave no trace on the particle detectors due to the weakly interacting nature of the DM candidate, and therefore another particle must be produced in the event; the latter is easily resolved by the production of additional particles via initial-state radiation (ISR) off the incoming SM particles. All of the above, led to collider searches in events with one highly-energetic jet or photon and substantial momentum imbalance, these searches became to be known as *monojet* [24, 90] and *monophoton* [159, 23], respectively.

Another line of thought, one might say, more experimentally driven, is the fact that there has to be new phenomena since the SM falls short on explaining some of the current observations. This realization gives ground to what is called *model-independent* searches, in which the events are selected based on interesting topologies rather than a particular theoretical model. Examples of such data analyses are dijet and diphoton resonance searches at relatively high masses. Another way to probe new physics is to search for anomalous production of Higgs bosons, where new phenomena could enhance the SM Higgs production or decay rates. These searches have recently been enabled by the measurements of the Higgs boson properties.

The broad experimental programs established by the ATLAS and CMS collaborations rely on the good performance of the particle detectors, reconstruction algorithms, as well as the large datasets provided by the large Hadron Collider (LHC). The High-Luminosity upgrade of the LHC will significantly boost the sensitivity to rare processes but at the cost of increasing the pileup interactions to about 200. This high pileup environment will deteriorate particle reconstruction and identification due to the large occupancy in the detector. One solution to alleviate this detrimental

effect is to have a calorimetric device capable of delivering a time stamp for particle detection with a resolution of about 30 ps (approximately 1 cm in the z-axis). Detector research and development (R&D) is crucial in order to make precision timing calorimetry a reality that could enhance the potential discovery and characterization of new physics.

This thesis is organized in five parts, the first part gives a brief introduction to the main theoretical and phenomenological considerations covered by the experimental searches in the following parts, the second part provides an introduction to the Large Hadron Collider and the Compact Muon Solenoid Experiment where the searches presented in this thesis are carried out, the third part covers in detail two searches for beyond the SM (BSM) physics with *razor variables* using data collected by the CMS experiment at a center-of-mass-energy of 8 TeV and 13 TeV, the fourth part presents the research and development on precision timing calorimetry that we carried out at Fermilab, the last part – the appendices – presents another search for new resonances in high-mass diphotons using 13 TeV data collected by the CMS experiment as well as a reinterpretation of the excess observed by CMS in events with SM Higgs produced in association with jets at 8 TeV.

## C h a p t e r ~ 2

# THE STANDARD MODEL IN A NUTSHELL

### 2.1 The Standard Model of Particle Physics

The Standard Model (SM) of particle physics is a renormalizable quantum field theory based on symmetries and the gauge principle [137, 221]. The SM explains the electromagnetic, weak, and strong interactions, as well as having a complete catalog of all subatomic particles known. The interactions between the fermions (spin 1/2 particles) is realized by the exchange of force carriers (spin-1 particle).

The SM is represented by the symmetry group  $SU(3)_C \times SU(2)_L \times U(1)_Y$ , where each of the fundamental forces, represented by gauge fields, corresponds to one of symmetry groups. This is better understood by the following diagrammatic representation:

$$\begin{array}{ccc}
 SU(3)_C & \times & SU(2)_L & \times & U(1)_Y \\
 \downarrow & & \downarrow & & \downarrow \\
 G_\mu^\alpha & & W_\mu^a & & B_\mu \\
 \alpha = 1, \dots, 8 & & a = 1, 2, 3
 \end{array}$$

Where  $G_\mu^\alpha$  represents the eight bosons, the gluons, that take part in the strong interaction and are associated with the  $SU(3)_C$  term;  $W_\mu^a$  represents the three bosons that take part in the weak interaction and are associated with the  $SU(2)_L$ ; while  $B_\mu$  represents the boson associated with the hypercharge  $U(1)_Y$  term. The latter four bosons mix to form the most commonly known  $W^\pm$  and  $Z$  bosons of the weak interaction, and the photon ( $\gamma$ ) of the electromagnetic interaction.

The particles that make up matter are represented by fermion fields in the form of left- and right-handed Weyl spinors. These fermions are divided into two categories, quarks (u, d, c, s, t, and b), and leptons (e,  $\mu$ ,  $\tau$ ,  $\nu_e$ ,  $\nu_\mu$ , and  $\nu_\tau$ ). Quarks are the only fermions that experience the strong interaction. Both, quarks and fermions, are further categorized into three generations of matter – where e, u, and d are in the first generation and  $\tau$ , t and b are in the third generation –, with particles masses increasing in the same order as the generations. Figure 2.1 shows the whole catalog of particles and interactions in the standard model, including their categorization, and the Higgs boson which will be discussed in the following section.

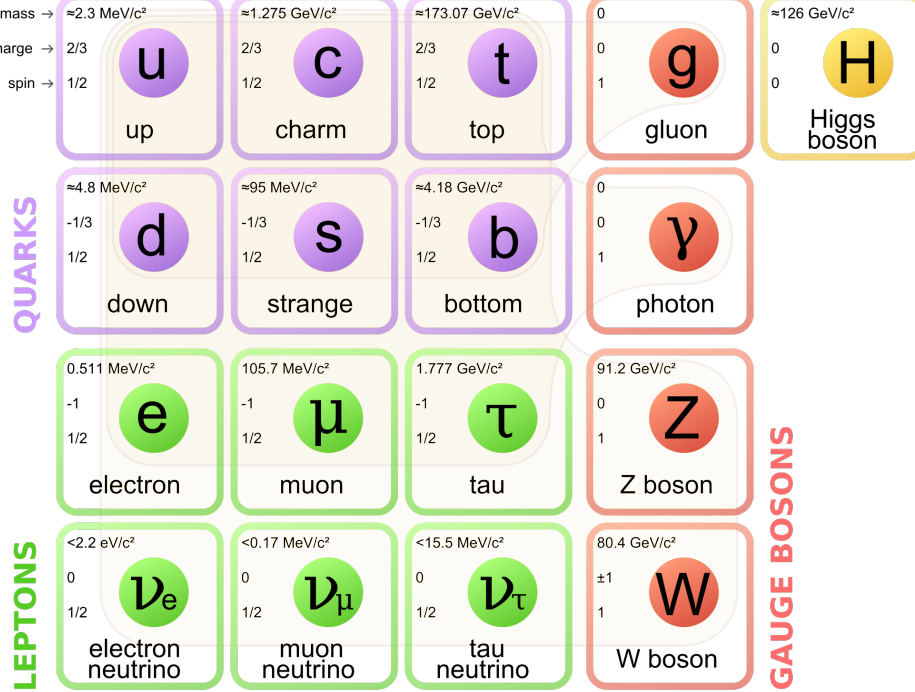


Figure 2.1: The catalog of particles in the standard model.

The dynamics and kinematics of the SM are controlled by the Lagrangian density, which in conjunction with the particle content and force carriers completes the theory. The lagrangian density is presented below in compact formulation:

$$\begin{aligned}
\mathcal{L}_{\text{SM}} = & -\frac{1}{4}B_{\mu\nu}B^{\mu\nu} - \frac{1}{4}W_a^aW_a^{\mu\nu} - \frac{1}{4}G_{\mu\nu}^\alpha G_\alpha^{\mu\nu} & \text{gauge terms} \\
& + \bar{\ell}_L \tilde{\sigma}^\mu iD_\mu \ell_L + \bar{e}_R \sigma^\mu iD_\mu e_L + \bar{\nu}_R \sigma^\mu iD_\mu \nu_L & \text{lepton kinetic terms} \\
& + \bar{q}_L \tilde{\sigma}^\mu iD_\mu q_L + \bar{u}_R \sigma^\mu iD_\mu u_L + \bar{d}_R \sigma^\mu iD_\mu d_L & \text{quark kinetic terms} \\
& + \mathcal{L}_{\text{Higgs}} + \mathcal{L}_{\text{Yukawa}} & \text{Higgs and Yukawa terms}
\end{aligned} \tag{2.1}$$

Where  $\ell_L = \begin{pmatrix} e_L \\ \nu_L \end{pmatrix}$  is the lepton  $SU(2)_L$  doublet,  $q_L = \begin{pmatrix} u_L \\ d_L \end{pmatrix}$  is the quark  $SU(2)_L$  doublet,  $D_\mu$  is the corresponding covariant derivative, and  $\sigma_{\mu u}$  is the identity and the pauli matrices ( $\sigma_\mu = 1, \sigma^i$ ). The  $\mathcal{L}_{\text{Higgs}}$  and  $\mathcal{L}_{\text{Yukawa}}$  are presented in sections 2.2 and 2.3, respectively. Table 2.1 presents the matter field representation in the SM gauge group.

## 2.2 The Higgs Boson and Electroweak Symmetry Breaking

Gauge theories prohibit – in order to maintain the local symmetries – explicit mass terms for the gauge bosons in the SM, therefore all gauge bosons are massless. Since

field	SU(3) <sub>C</sub>	SU(2) <sub>L</sub>	U(1) <sub>Y</sub>
$q_L$	<b>3</b>	<b>2</b>	1/6
$\ell_L$	<b>1</b>	<b>2</b>	-1/2
$u_R$	<b><math>\bar{3}</math></b>	<b>1</b>	-2/3
$d_R$	<b><math>\bar{3}</math></b>	<b>1</b>	1/3
$e_R$	<b>1</b>	<b>1</b>	1
$h$	<b>1</b>	<b>1</b>	1/2

Table 2.1: Group representation of the matter fields in the SM.

some of gauge boson in the SM are massive ( $W^\pm, Z$ ) there should be a mechanism by which gauge boson acquire mass. The gauge boson masses in the SM are realized by the *spontaneous symmetry breaking* of the  $SU(2)_L \times U(1)_Y$  symmetry which induced by the nature of the Higgs potential [116, 135, 133, 132, 134, 163]. The best way to understand this mechanism (the Higgs mechanism) is to closely look at the lagrangian density:

$$\mathcal{L}_{\text{Higgs}} = (D^\mu \Phi)^\dagger (D^\mu \Phi) + V(\Phi); \quad V(\Phi) = -\mu^2 \Phi^\dagger \Phi + \lambda (\Phi^\dagger \Phi)^2, \quad (2.2)$$

where  $D^\mu$  is the covariant derivative;  $\Phi$  is a spin-0 complex field, and a  $SU(2)_L$  doublet with weak hypercharge  $Y = 1/2$ . The field is more easily represented as a  $SU(2)_L$  doublet in the following fashion:

$$\Phi = \begin{pmatrix} \phi^+ \\ \phi^0 \end{pmatrix}. \quad (2.3)$$

When  $\mu^2 > 0$  the potential ( $V(\Phi)$ ) has the commonly known ‘‘Mexican hat’’ shape, shown in Figure 2.2, which a minimum which does not preserve the original  $SU(2)_L \times U(1)_Y$  symmetry. Therefore the scalar field acquires a non-zero *vacuum expectation value (vev)*:

$$\langle \Phi \rangle \equiv \langle 0 | \Phi | 0 \rangle = \frac{1}{\sqrt{2}} U(x) \begin{pmatrix} 0 \\ v \end{pmatrix}; \quad v = \sqrt{\frac{\mu^2}{\lambda}}, \quad (2.4)$$

where  $U(x)$  is a unitary transformation that transforms the field into the degenerate solution. An important consequence is that the *vev* of field preserves a  $U(1)$  symmetry from the original  $SU(2)_L \times U(1)_Y$  symmetry of the lagrangian. Therefore the full electroweak symmetry of the SM ( $SU(2)_L \times U(1)_Y$ ) is spontaneously broken to  $U(1)_{\text{EM}}$ .

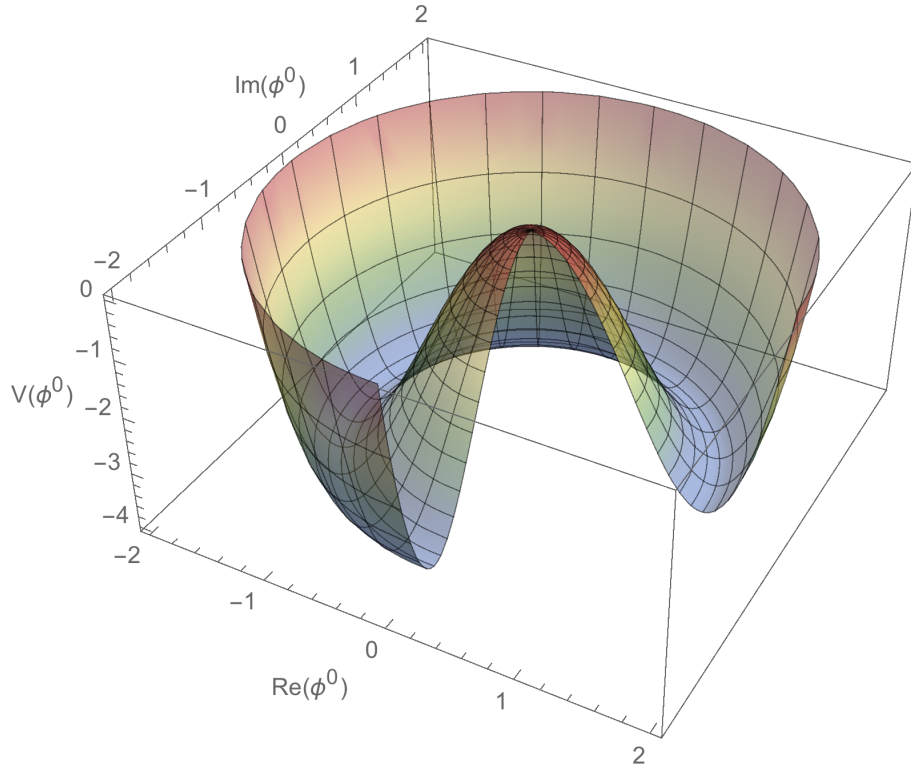


Figure 2.2: The shape of the Higgs potential (“Mexican hat”). The degeneracy of the potential is observed along the azimuthal angle

This spontaneous breaking of the  $SU(2)_L \times U(1)_Y$  symmetry is responsible for the appearance of masses to 3 of the four gauge bosons in the electroweak sector, this is called: the Higgs mechanism. The masses become apparent when replacing the  $v_{ev}$  into the Higgs kinetic term in the lagrangian:

$$(D^\mu \Phi)^\dagger (D^\mu \Phi) \rightarrow \Delta \mathcal{L} = \frac{1}{2} \begin{pmatrix} 0 & v \end{pmatrix} (g A_\mu^a \tau^a + g' B_\mu) (g A^{b\mu} \tau^b + g' B^\mu) \begin{pmatrix} 0 \\ v \end{pmatrix}. \quad (2.5)$$

Evaluating the matrix products, using  $\tau^a = \sigma^a/2$  and  $\{\tau^a, \tau^b\} = \delta^{ab}/2$ , we find

$$\Delta \mathcal{L} = \frac{v^2}{8} \left[ g^2 (A_\mu^1)^2 + g^2 (A_\mu^2)^2 + (-g A_\mu^3 + g' B_\mu)^2 \right]. \quad (2.6)$$

This forms the mass matrix squared for the gauge boson in the  $(A_\mu^i, B_\mu)$  basis

$$m^2 = \left(\frac{v}{2}\right)^2 \begin{pmatrix} g^2 & 0 & 0 & 0 \\ 0 & g^2 & 0 & 0 \\ 0 & 0 & g^2 & -gg' \\ 0 & 0 & -gg' & g^2 \end{pmatrix}, \quad (2.7)$$

by diagonalizing this matrix, it is clearly observed that there are three massive and one massless gauge boson, the linear combination of the gauge fields and their respective masses are the following:

$$\begin{aligned} W_\mu^\pm &= \frac{1}{\sqrt{2}}(A_\mu^1 \mp A_\mu^2) && \text{with mass} && m_W = g \frac{v}{2} \\ Z_\mu^0 &= \frac{1}{\sqrt{g^2 + g'^2}}(g A_\mu^3 - g'^2 B_\mu) && \text{with mass} && m_Z = \sqrt{g^2 + g'^2} \frac{v}{2} \\ A_\mu &= \frac{1}{\sqrt{g^2 + g'^2}}(g' A_\mu^3 + g B_\mu) && \text{with mass} && m_A = 0 \end{aligned} \quad (2.8)$$

Besides providing the Higgs mechanism, the inclusion of the  $SU(2)_L$  field in the SM predicts the presence of a self-interacting massive spin-0 boson, this is realized by the fluctuation of the field around the *vev*, i.e.

$$\Phi = \frac{1}{\sqrt{2}} \begin{pmatrix} 0 \\ v + h(x) \end{pmatrix}, \quad (2.9)$$

now collecting the higgs-related terms in the lagrangian, we obtain the following:

$$\mathcal{L}_{\text{Higgs}} \supset \frac{1}{2} (\partial_\mu h)^2 - \lambda v^2 h^2 - \lambda v h^3 - \frac{\lambda}{4} h^4. \quad (2.10)$$

Where the first term is the standard kinetic term, the second term is the mass term ( $m_h = \sqrt{2\lambda}v$ ), and the last two are the higgs self-interaction terms.

### 2.3 Fermion Masses

Fermion masses in the standard model arise from the inclusion of interaction terms between the fermions and the  $\Phi$  field [221], when the latter is at the *vev*. These interactions are called Yukawa terms, they have different strength depending on the particle type and generation. The corresponding part of the lagrangian in Eq. 2.1 is

$$\mathcal{L}_{\text{Yukawa}} = -y_e \bar{\ell}_L \Phi e_R - y_u \bar{q}_L \Phi u_R - y_d \bar{q}_L \tilde{\Phi} d_R + (h.c.), \quad (2.11)$$

where  $y_{e,u,d}$  are the Yukawa couplings to the leptons, up-type quarks, and down-type quarks, respectively;  $\tilde{\Phi} = i\sigma^2\Phi^*$  with weak hypercharge  $Y = -1/2$  is used in the third term to generate the down-type quark masses. After the  $\Phi$  field acquires its  $v_{ev}$  we can identify the fermion mass terms as

$$\begin{aligned} m_e &= \frac{y_e v}{2} & m_u &= \frac{y_u v}{2} & m_\mu &= \frac{y_d v}{2} \\ m_\mu &= \frac{y_\mu v}{2} & m_c &= \frac{y_c v}{2} & m_s &= \frac{y_s v}{2} \\ m_\tau &= \frac{y_\tau v}{2} & m_t &= \frac{y_t v}{2} & m_b &= \frac{y_b v}{2}. \end{aligned} \quad (2.12)$$

The Yukawa terms give mass to all the fermions in the SM, provide decay modes of the physical higgs boson – with  $h \rightarrow b\bar{b}$  having the highest branching fraction –, and allow the fermions to modify the observed mass of the Higgs boson through loop corrections – the most important correction comes from the top-quark, which has the largest Yukawa coupling.

### *Chapter 3*

## DARK MATTER AND WEAKLY INTERACTING PARTICLES

Different measurements during the twentieth century indicate that baryonic matter is not the dominant form of matter in the universe. In fact, recent measurements constraint the amount of baryonic matter to be about 5% of the total energy density, while the rest is comprise of dark matter and dark energy, accounting for approximately 27% and 68%, respectively. The existence of dark matter has been inferred by several astronomical and astrophysical measurements since the 1930s, as well as the recent success of the standard model of Big Bang cosmology (commonly known as the  $\Lambda$ CDM). Nowadays, the existence of dark matter is widely accepted but little is known about its nature. Dark energy is perhaps the least understood component of our Universe, currently, we infer its existence based on the missing energy density in conjunction with the measured flatness of the universe, as well as the accelerated expansion of the universe.

This chapter is intended to briefly summarize the evidence supporting the existence of dark matter and to introduce the concepts needed to understand the basis of the current searches for dark matter in direct detection experiments, indirect detection experiments, and the experiments at the Large Hadron Collider.

### **3.1 The Evidence for Dark Matter**

#### **Early evidence**

Perhaps the first convincing evidence of the existence of dark matter was the measurements carried out in the Coma cluster by F. Zwicky in 1933 – Oort also had measured earlier inconsistencies between the velocities of stars near the galactic center and the luminous mass. Zwicky measured the velocities of the galaxies in the cluster by observing the doppler shifts in their emission spectra and by employing the virial theorem he was able to calculate the cluster’s total mass [228, 226]. The cluster mass was  $M_{\text{cluster}} = 4.5 \times 10^{13} M_{\odot}$ , since there are approximately 1,000 galaxies in the cluster the average galactic mass is  $M_{\text{galaxy}} = 4.5 \times 10^{13} M_{\odot}$ . The mass of the galaxies were also measured using the standard mass-to-light ratio which yielded a galactic mass approximately 2% of that measured by Zwicky. Therefore most of the mass in the Coma cluster was missing, or at least did not interact electromagnetically and thus dubbed “dark matter”.

In the 1970s Vera Rubin and others set to measure the rotation curves of about 100 isolated galaxies [201]. What they found was that the rotation velocities reached a plateau at radii of about 10 kpc, which blatantly contradicted the observations from the luminous matter profile in the galaxies. The measured rotation curves measured by Persic and Salucci [186] are shown in Figure 3.1, and a rotation curve from the spiral galaxy M33 is shown in Figure 3.2. The fact that the luminous matter decays exponentially with the radius of the galaxy implies that the velocity of gas and stars in the outskirts of the galaxy should start to decrease at around the optical radius  $R_{\text{opt}} = 10 \text{ kpc}$  – the radius such that 83% of the light is contained in it. As observed in Figures 3.1 and 3.2, this is not the case, since the velocities tend to be flat or even increase as a function of the galactic radius. To solve this conundrum one can introduce a dark matter halo with an spherically symmetric profile to account for the apparent missing mass that would explain the observed rotation curves. The most pedagogical way to visualize this effect is by considering the rotation velocity to be constant (at large radius), assuming circular trajectories in the galactic disk, and using a spherically symmetric density profile. Thus one finds

$$\begin{aligned} \frac{GM(r)}{r^2} &= \frac{v_c^2}{r} \quad \text{and} \quad M(r) = \int_0^r 4\pi\rho(r)r^2 dr \\ \Rightarrow \quad \frac{v_c^2 r}{G} &= 4\pi \int_0^r \rho(r)r^2 dr \\ \Rightarrow \quad \rho(r) &= \frac{v_c^2}{4\pi G r^2}, \end{aligned} \tag{3.1}$$

where  $\rho(r)$  is the density profile of the dark matter halo,  $v_c$  is the constant rotational velocity (about 220 km/s),  $G$  is the gravitational constant, and  $r$  is the galactic radius. A more accurate density profile, which fits the observed galaxy rotation data, was proposed by Navarro, Frenk, and White [181]

$$\rho(r) = \frac{\rho_0}{\left(\frac{r}{R_s} \left(1 + \frac{r}{R_s}\right)\right)^2}, \tag{3.2}$$

where the central density ( $\rho_0$ ) and the scale radius ( $R_s$ ) are parameters that vary from galaxy to galaxy.

### Cosmological evidence

Cosmological evidence arise later by comparing the measurements of light elements (H, D, He, and Li) – produced at the early stages of the universe in what is called the Big Bang Nucleosynthesis – abundances with the theoretical calculations of nuclear

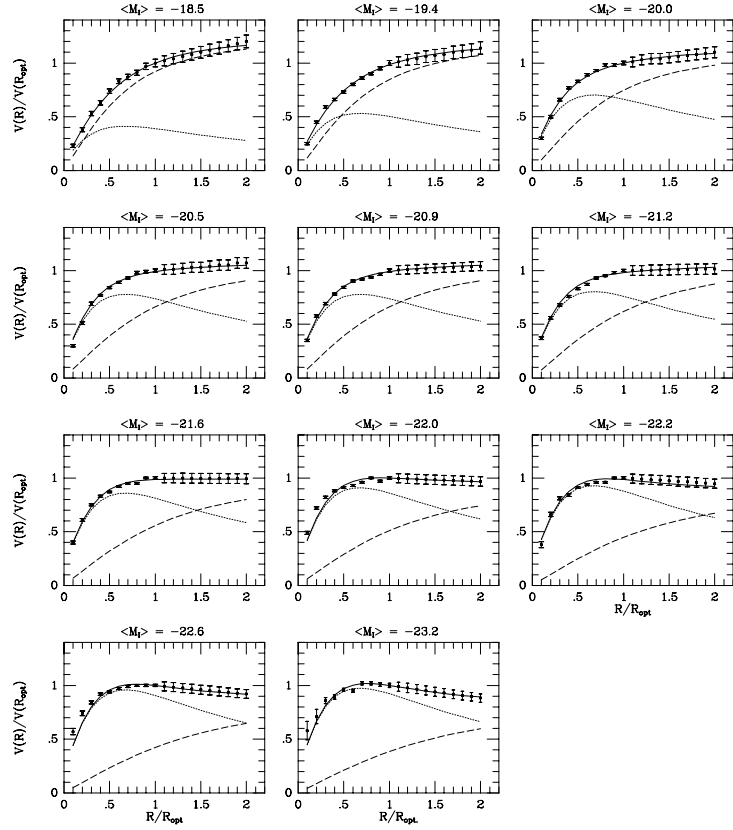


Figure 3.1: The rotation curves for different galaxies as measured by Persic and Salucci [186].

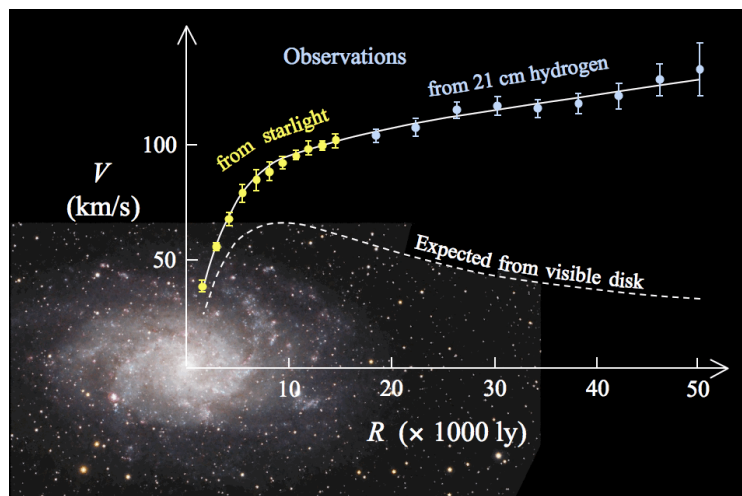


Figure 3.2: The rotation curve of the M33 galaxy.

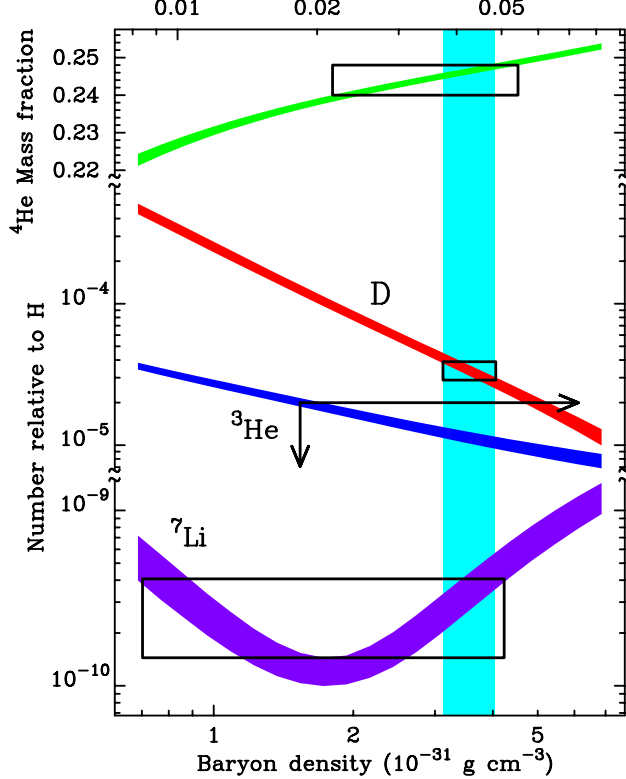


Figure 3.3: BBN abundances as calculated by theory and measured by experiments in primordial-like areas of the universe with low concentration of Li.

physics and known reaction rates. The results are shown in Figure 3.3, where the colored widths in the abundances represent the uncertainties in the calculations, the rectangular boxes represent the experimental measurements, and the vertical band indicates the region allowed by the deuterium observation. R. H Cyburt calculated possible values of the baryon relative density ( $\Omega_b$ ) by using two deuterium measurements [107]

$$\Omega_b h^2 = 0.0229 \pm 0.0013 \quad \text{and} \quad \Omega_b h^2 = 0.0216_{-0.0021}^{+0.0020}, \quad (3.3)$$

where  $h$  is the reduced Hubble parameter. Again, the baryon density is found to be very low compared to the energy budget of the universe, thus indicating the presence of dark matter – and later, dark energy.

The Cosmic Microwave Background (CMB) discovered by Penzias and Wilson in 1964 as an excess of background temperature of about 3.5 K at a wavelength of 7.5 cm [108], has undoubtedly revolutionized the realm of precision cosmology. Later the CMB has been measured to be consistent with an almost perfect black-body spectrum with a temperature of  $2.72548 \pm 0.00057$  K, and thus consistent

with compatible with the expected relic radiation in the form of photons from the epoch of recombination (380,000 years after the Big Bang). Although, the CMB is very much isotropic and uniform, there are fluctuation of about 1 part in  $10^5$  in the temperature of the CMB as measured by the COBE satellite. These fluctuations are attributed to two different effects, first, the Sachs-Wolfe effect: where photons with lower energy today came from denser areas at the time of recombination as they lost energy on their way out (these are associated with large angular scales). Second, the acoustic oscillations of the photon-baryon fluid that underwent compression and rarefaction and thus imprinted temperature fluctuations in the photons released when the baryons became electrically neutral and the CMS photons were released (these fluctuation are associated with small angular scales). The Wilkinson Microwave Anisotropy Probe (WMAP) measured the temperature fluctuations in the CMB with unprecedented precision and allowed the measurement of different cosmological parameters including the density of baryonic dark matter. The spectrum of the CMB anisotropies is shown in Figure 3.4, where a multipole expansion has been performed in order to clearly see the intensity of each mode. The features of CMB anisotropies are directly related to the cosmological parameters such as baryonic matter and dark matter, this is clearly shown in Figure 3.4, where different values of the baryonic density are overlaid with the real data from WMAP; as observed, the incorrect baryonic density clearly mismodels the observations. Finally a global fit can be performed to the CMB power spectrum and thus obtain the cosmological parameters. The Plank satellite – current state of the art CMB experiment – has measured the relative densities to be [188]

$$\begin{aligned} \Omega_b h^2 &= 0.02230 \pm 0.00014 & \text{and} & \Omega_{DM} h^2 = 0.1188 \pm 0.0010 \\ \Omega_m &= 0.6911 \pm 0.0062 & \text{and} & \Omega_\Lambda = 0.3089 \pm 0.0062, \end{aligned} \quad (3.4)$$

where  $\Omega_{DM}$  is the dark matter relative density,  $\Omega_m$  is the total matter density (baryonic and dark), and  $\Omega_\Lambda$  is the dark energy relative density.

## **Recent evidence**

### **3.2 Weakly Interacting Dark Matter Candidates**

### **3.3 Searches for Dark Matter**

#### **Direct detection**

#### **Indirect detection**

#### **Searches for dark matter production at the LHC**

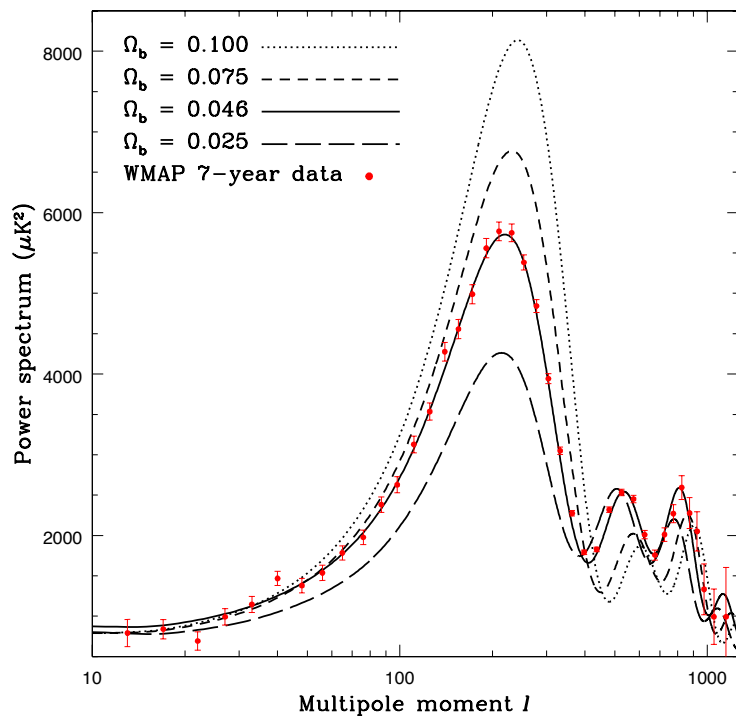


Figure 3.4: The CMB anisotropy spectrum measured by WMAP. Different values of the baryonic matter are also shown with different curves. In the multipole expansion of the CMB anisotropies  $l \approx \pi/\theta$ , where  $\theta$  is the angular scale in radians.

## **Part II**

# **The Large Hadron Collides and The Compact Muon Solenoid Experiment**

## C h a p t e r ~ 4

# THE LARGE HADRON COLLIDER

### 4.1 The Large Hadron Collider

The CERN Large Hadron Collider (LHC) is a two-ring superconducting accelerator and collider with 27 km of circumference, which is located in the tunnel constructed for the CERN Large Electron-Positron Collider (LEP). The tunnel lies between 45 m and 170 m below the surface on an inclind plane (1.41% slope) towards Lake Lèman and spans between the French and Swiss border close to Geneva. The layout of the tunnel is such that contains 8 arc sections that spans most of the circumference and 8 straight sections where the experimental halls are located.

The LHC is a particle-particle collider – in its most common configuration it collides protons – with a designed center-of-mass energy of 14 TeV. In order to achieve such high energies, the LHC uses the existing CERN facilities to gradually increase the energy of the protons. Everything starts with a bottle of compressed hydrogen gas, then, hydrogen atoms are fed into the source chamber of the linear accelerator, where an electric field strips off their electrons. The resulting protons are then injected into the linear accelaretor, Linac 2, which is the first step in the accelerator chain and boosts the protons energy up to 50 MeV. The accelerated proton beam is then divided into 4 (to increase its intensity) and enters the second stage of acceleration, this occurs in the Proton Synchrotron Booster (PSB), where protons are now accelerated to 1.4 GeV. Subsequently, the proton beam is recombined and sent to the Proton Synchrotron (PS), which increases the energy to 25 GeV, followed by the Super Proton Synchrotron (SPS), which brings the beam energy to 450 GeV.

Finally, the proton beam is transferred to the two beam pipes of the LHC. The beams circulate in opposite directions. The LHC filling time is 4 minutes and 20 seconds, but it takes around 20 minutes for the protons to reach their maximum energy. Figure 4.1 shows the CERN accelerator complex just described. At this point, the two beams are brought to collide at the four interaction points (IP) in the straight sections where the LHC’s experiments are located. There are two main purpose experiments located in diametrical opposite locations, the ATLAS experiment is located at point 1 and the CMS experiment is located at point 1. There are also two specialized experiments; the LHCb experiment, which studies B-hadron physics, and

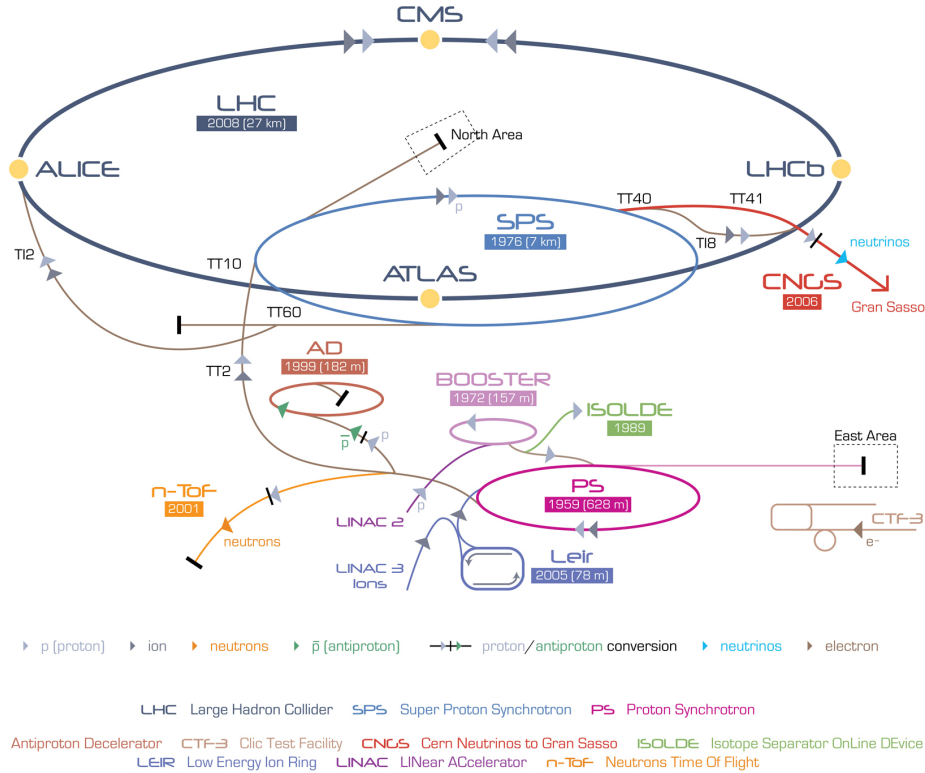


Figure 4.1: The CERN accelerator complex.

the ALICE experiment, which specializes in studying heavy ion collisions (another type of collision possible at the LHC). Figure 4.2 shows an schematic layout of the LHC. Due to the small diameter of the tunnel in the arcs (3.7 m), which complicates the installation of two separate proton rings, the LHC uses a twin-bore magnet design, proposed in 1971 by John Blewett at the Brookhaven National Laboratory (BNL) [**JBlewett**] as a cost-saving alternative.

Since the usage of superconducting magnets at the Intersecting Storage Rings at CERN, particle colliders have used them as the default technology for their operation. However, the main difference is that the LHC's superconducting magnets operate at a temperature lower (below 2 K) than the standard superconducting magnets in other particle colliders (4-5 K). The LHC ring accommodates 1,232 NbTi main dipole magnets, cooled down to 1.9 K by using superfluid helium; they operate at fields above 8 T. The twin-bore design allows for a common nonmagnetic collar and iron yoke, as well as common cryogenic system. The core of the dipole magnet system is enclosed by a cylindrical alloyed low-carbon steel vacuum vessel with an outer diameter of 914 mm and a wall thickness of 12 mm. Figures 4.3 and 4.4 show a cross sectional view and a 3-dimensional visualization of the main dipole magnet

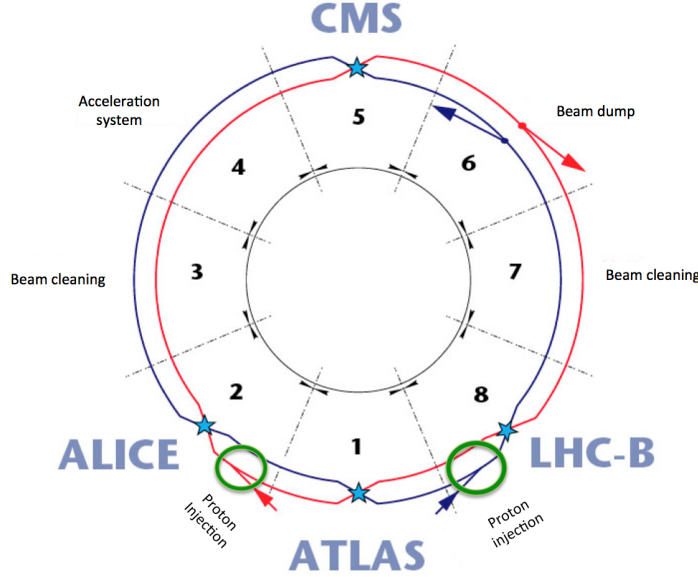


Figure 4.2: The CERN Large Hadron Collider schematic layout.

system, respectively.

The goal of the LHC program is to reveal the nature of new physics. The high-energy collision (14 TeV) are a key ingredient to probe new physics, since new physics could just be present at that energy scale. However, it is by no means the only ingredient; new physics will likely have smaller cross sections than that of the known SM processes and therefore a large number of proton-proton collision is needed. The number of events for a particular physics process  $N_{exp}$  generated in the LHC is the product of the experimental cross section  $\sigma_{exp}$  and the integrated luminosity, i.e.

$$N_{exp} = \sigma_{exp} \int \mathcal{L}(t) dt. \quad (4.1)$$

Where  $\mathcal{L}(t)$  is the instantaneous luminosity, which depends on the LHC beam parameters and can be written as [LHCbeamParam]:

$$\mathcal{L}(t) = \frac{N_b^2 n_b f_{rev} \gamma_r}{4\pi \epsilon_n \beta^*}, \quad (4.2)$$

where  $N_b$  is the number of particles per bunch,  $n_b$  is the number of bunches per beam,  $f_{rev}$  is the revolution frequency,  $\gamma_r$  is the relativistic factor,  $\epsilon_n$  is the normalized transverse beam emittance,  $\beta^*$  is the transverse size of the beam at the IP, and  $F$  is

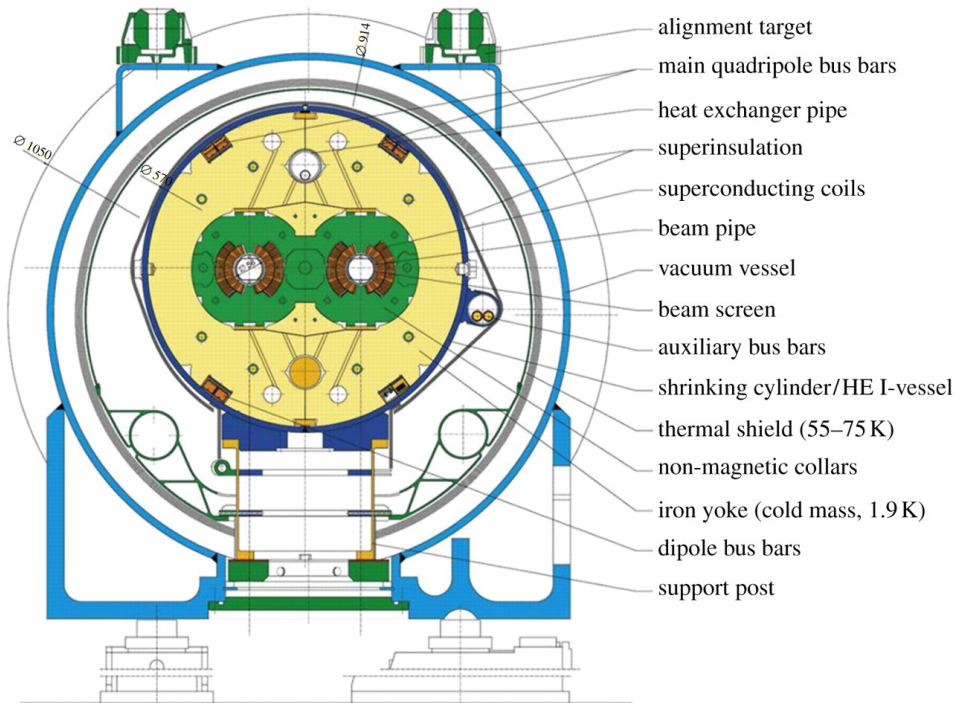


Figure 4.3: An schematic cross sectional view of the LHC dipole magnet.

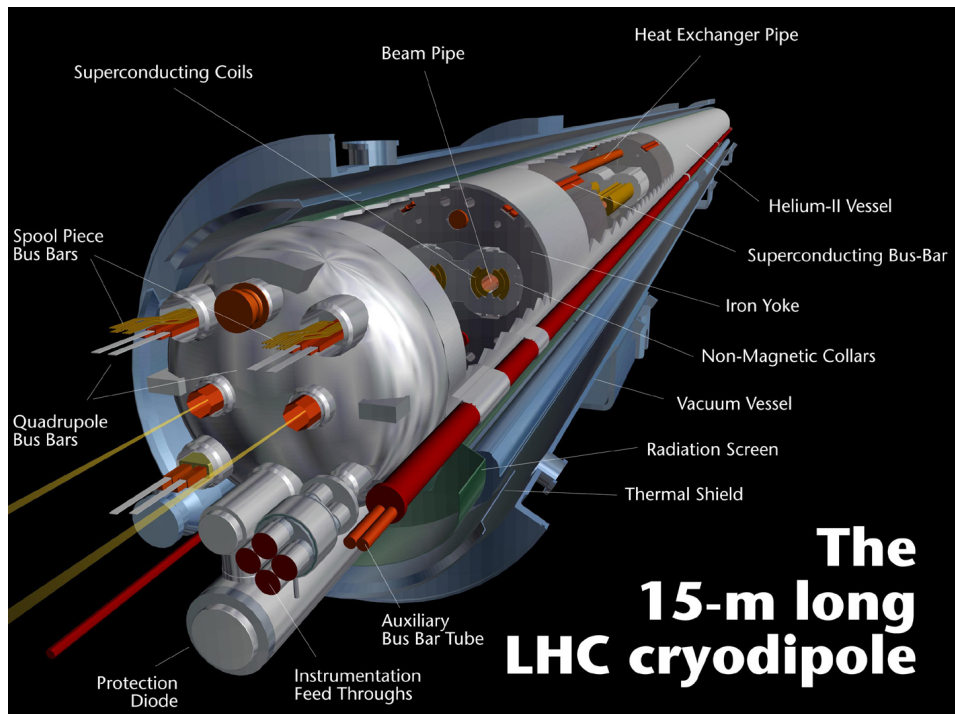


Figure 4.4: An 3D visualization of a LHC dipole magnet.

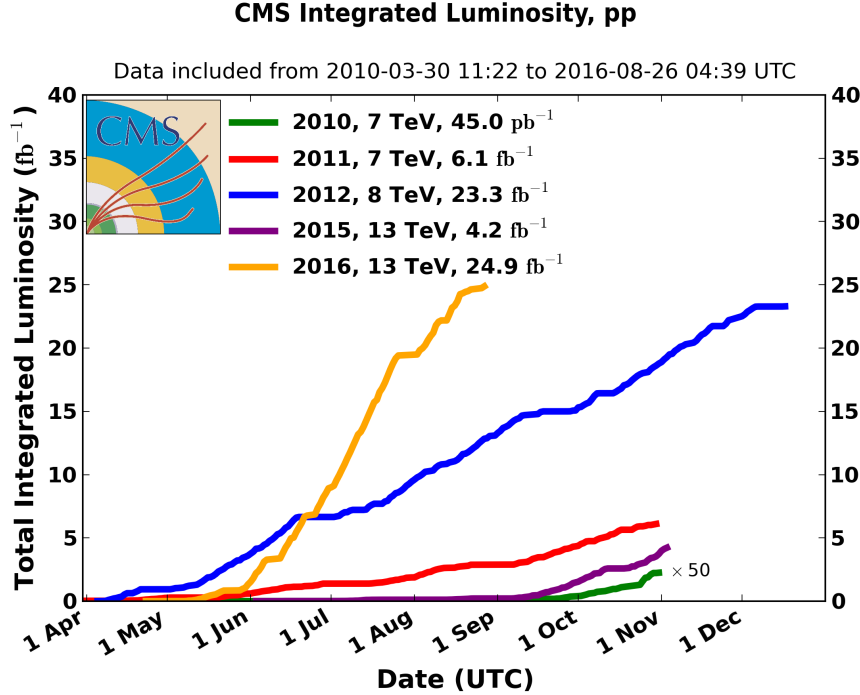


Figure 4.5: Intregated luminosity received by the CMS experiment during the LHC operation.

the geometric luminosity reduction factor due to the crossing angle at the IP:

$$F = \left( 1 + \left( \frac{\theta_c \sigma_z}{2\sigma^*} \right) \right)^{-1/2} \quad (4.3)$$

In the last expression,  $\theta_c$  is the full crossing angle at the IP,  $\sigma_z$  is the rms bunch length, and  $\sigma^*$  is the transverse rms beam size at the IP. The designed peak luminosity to be delivered the ATLAS and CMS is  $\mathcal{L}(t) = 10^{34} \text{ cm}^{-2} \text{ s}^{-1}$ . Figure 4.5 shows the integrated luminosity received by the CMS experiment from 2007 to 2016.

## Chapter 5

### THE COMPACT MUON SOLENOID EXPERIMENT

The Compact Muon Solenoid (CMS) detector operates at the LHC at CERN. It was designed to operate in proton-proton (and lead-lead) collisions at a center-of-mass energy of 14 TeV (5.5 TeV) and at luminosities up to  $10^{34}\text{cm}^{-2}\text{s}^{-1}$  ( $10^{27}\text{cm}^{-2}\text{s}^{-1}$ ). The CMS has cylindrical geometry and its dimensions are a length of 21.5 m, a diameter of 14.6, and a total weight of 12,500 tons. At the heart of the CMS detector system lies a 4 T magnetic field produced by a large-bore superconducting solenoid which encloses a silicon – pixel and strips – tracker, a homogeneous lead-tungstate crystal electromagnetic calorimeter, and a brass-scintillator sampling hadron calorimeter. Outside the superconducting solenoid lies an steel yoke for magnetic flux-return instrumented with four stations for muon detection. Forward sampling calorimeters extend the rapidity coverage up to  $\eta < 5$  and thus ensure good hemicity. Figure 5.1 shows an schematic representation of the CMS detector and Figure 5.2 shows a cartoon with a cross-sectional-slice view of the CMS detector along with different particle detections.

This chapter presents an introduction to the CMS detector systems and reconstruction algorithms. It is by no means a complete picture of the CMS detector and its mostly based on Ref. [83].

#### 5.1 The Superconducting Solenoid

The superconducting solenoid magnet is at the heart of the CMS detector and the rest of the detector systems are build around it. The superconducting magnet is 6 m in diameter and 12.5 m in length. It is comprised of 4 layer of winding made from reinforced NbTi conductors. Creating a cold mass of about 220 tons. The magnitude of the magnetic field is 3.8 T – produced by a current of 19.1 kA running through the conductors – along the  $z$ -direction in the barrel sector. The magnetic flux is return by means of a 10,000 tons steel-yoke which is designed in modular fashion: there are 5 wheels in the barrel, each divided in 12 sectors in the transverse plane, and 2 endcaps, each composed of three disks along the  $z$ -axis. Figure 5.3 shows a map of the magnetic field produced by the CMS superconducting solenoid magnet. A view of the steel-yokes in the early stages of assembly is presented in Figure 5.4

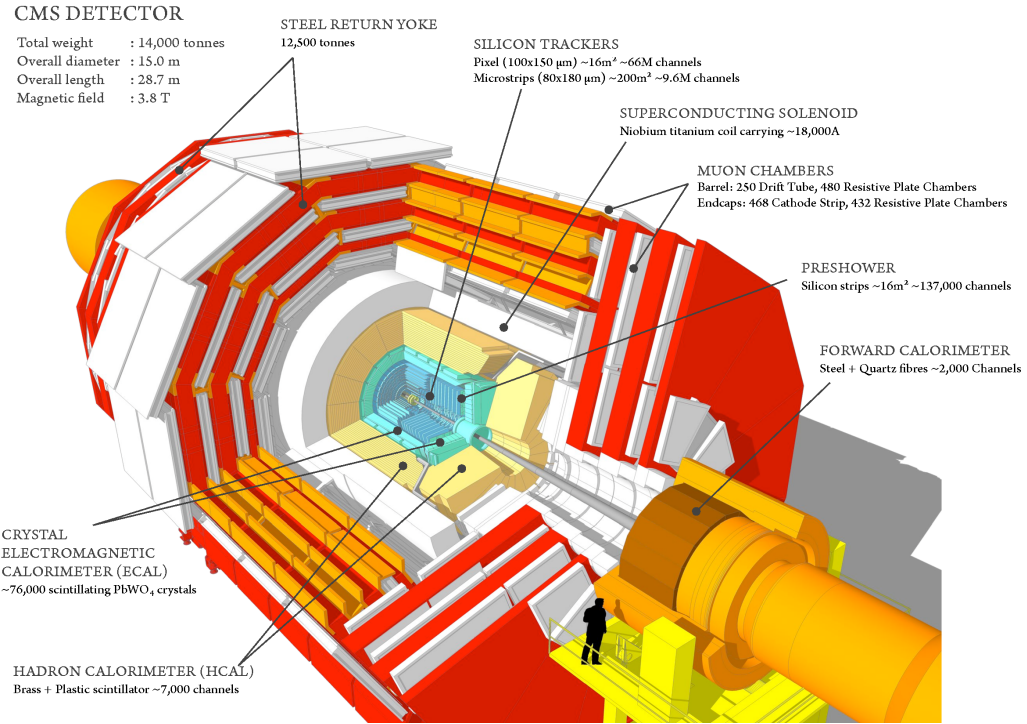


Figure 5.1: A perspective view of the CMS detector.

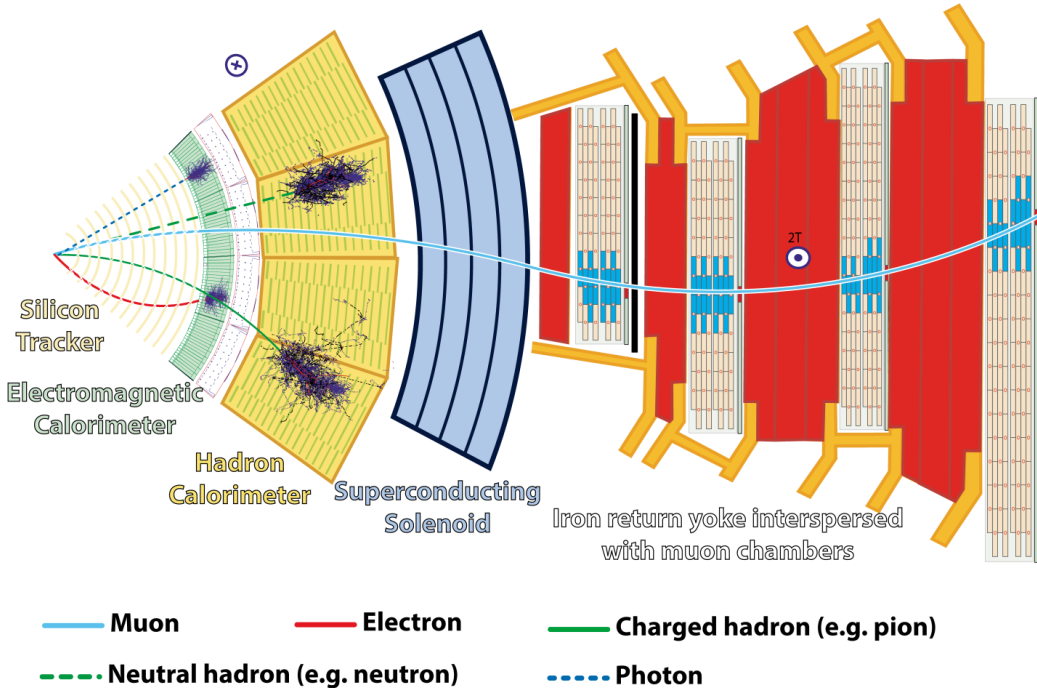


Figure 5.2: A cross-sectional-slice view of the CMS detector. The different components of the detector are clearly labeled and different particle detections are depicted.

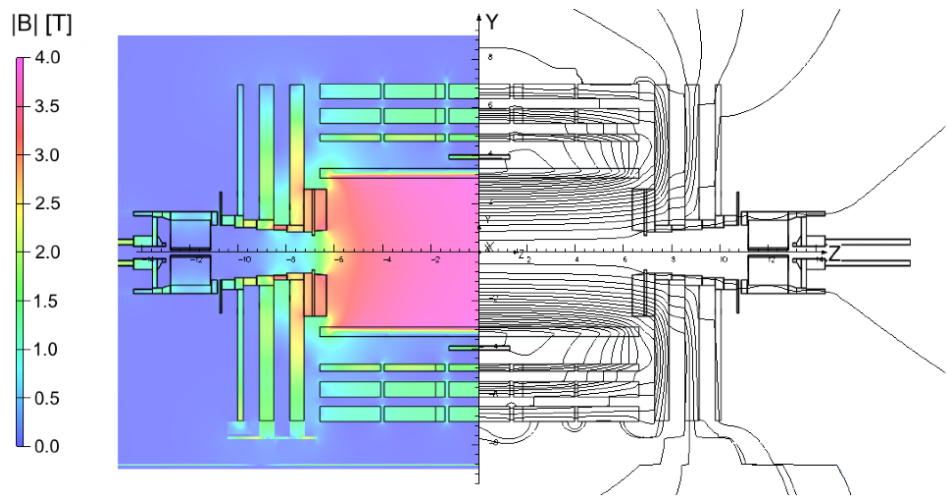


Figure 5.3: Map of the magnetic field in the  $y - z$  plane of the CMS detector.

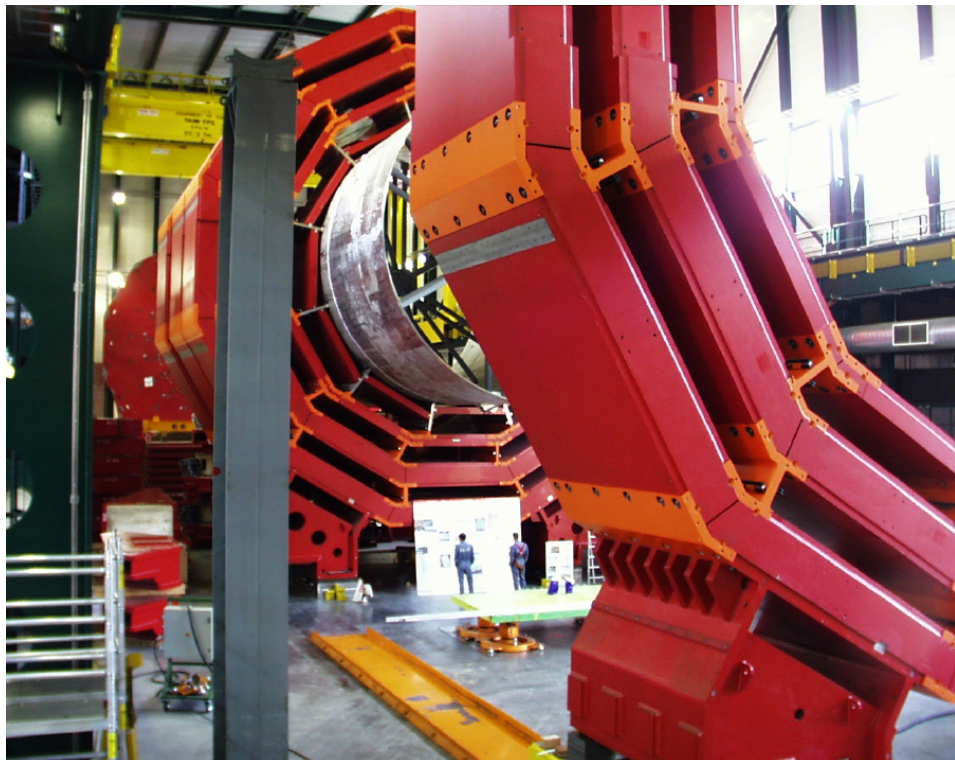


Figure 5.4: A photograph of the steel-yoke in the early stages of assembly. The centermost wheel in the barrel support the superconducting coil. One of the endcaps yoke can be seen at the back.

## 5.2 The Tracker System

The tracker is the innermost system of the CMS detector. It was designed to measure efficiently and precisely the trajectories of charged particles coming from the interaction points, as well as to provide a precise reconstruction of the secondary vertices at each bunch crossing. When running at the LHC designed conditions, every bunch crossing, i.e 25 ns, the number of proton-proton collision will be about 20 and they will produce an average number of particles of about 1000. These conditions and the above requirements implied a highly granular and fast response design. That being said, this design due to its high power consumption requires an efficient cooling system which in turn is in conflict with the goal of minimizing the material budget and thus reduce unwanted interactions. In addition, the harsh radiation environment that will deteriorate the detector performance posed further challenges in its construction. Therefore, the system – silicon sensors, readout, mechanical structures, granularity, etc – was designed to operate for 10 year and satisfying the considerations listed above. The CMS tracker is composed of three layers of pixels detectors up to a radius of 10.2 cm, a 10-layer silicon strip tracker up to a radius of 1.1 m, two endcap disks at each side of the barrel pixel detectors, 3 endcap disks at each side of the inner region of the strips (up to a radius of 55 cm), and finally 9 disks covering the  $|z| > 120$  cm regions starting a radius of 55 cm. More details about the tracker layout will be given below and are summarized in Figure 5.5. The tracker covers up to pseudorapidities of  $|\eta| < 2.5$  with a about 200 m<sup>2</sup> of active silicon area implemented. The material budget of the CMS tracker is shown in Figure 5.6. As it can be seen the most heavily implemented pseudorapidity is found to be at  $|\eta| \approx 1.4$ .

### Pixel Tracker

The inner pixel detector is composed of three 53-cm-long cylindrical layers at a radii of 4.4, 7.3, and 10.2 cm – which is called BPix. It is finalized by two disks of pixel modules at each side extending from approximately 6 to 15 cm in radius – which is called FPix. The barrel is composed of 672 full and 96 half modules, a full (half) module is composed of 16 (8) read-out chips equipped with 52×80 pixels of size 100×150  $\mu\text{m}$ . A completed full-module has the dimensions of 66 mm×26 mm and is provided with readout and power. Figure 5.7 shows a completed full- and half- module as well as an schematic of the different component integrated in the module. The two disks at each side of the pixel barrel (see Figure 5.5) is composed 24 modules – with a trapezoidal geometry. Each disk is composed of

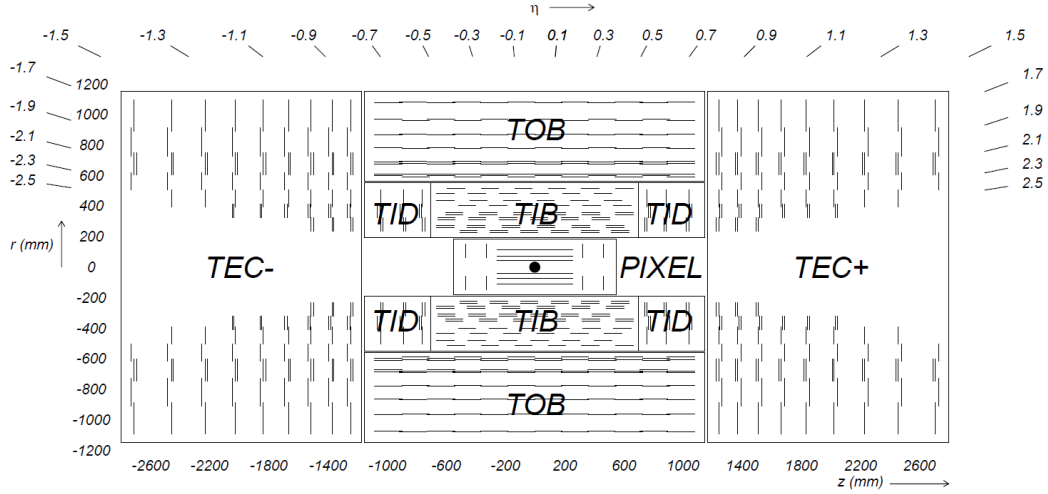


Figure 5.5: A cross-sectional view of the silicon tracker layout. The different subsystems are clearly labeled.

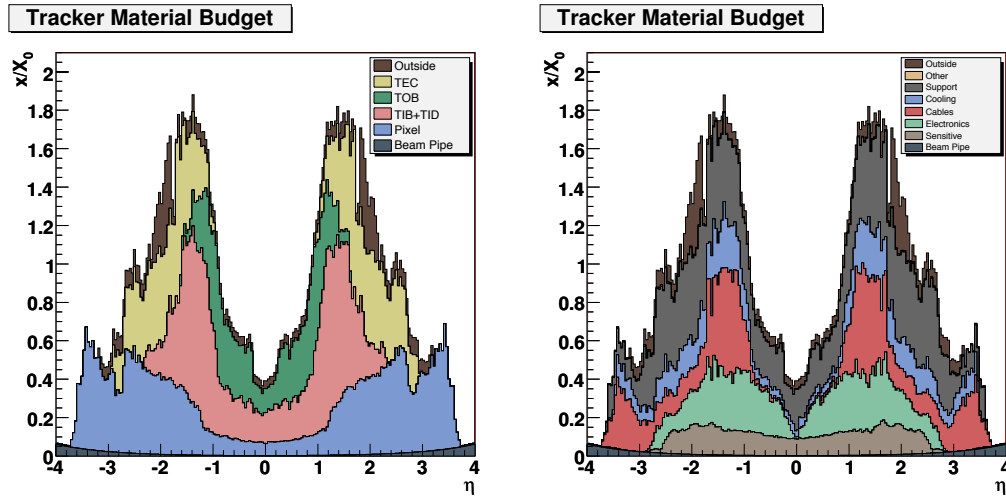


Figure 5.6: Material budget of the CMS tracker in units of radiation length as a function of pseudorapidity  $\eta$  for the (left) different subdetectors and (right) functional contributions.

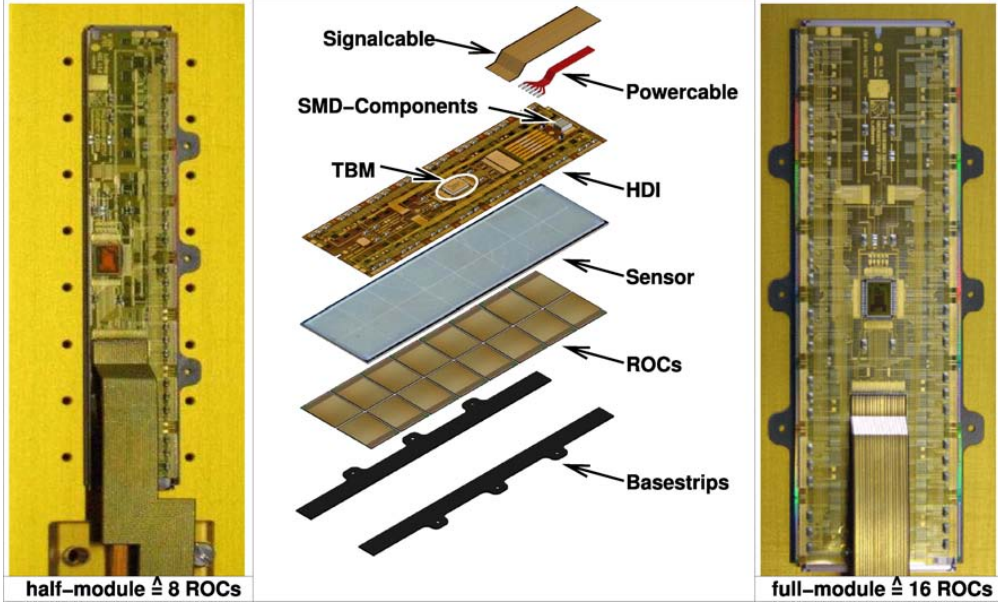


Figure 5.7: BPix completed modules; (left) half-module, (center) an schematic of the different component forming the a full-module,(right) full-module.

two different panel types; the first and closest to the interaction point is formed by a  $1 \times 2$ ,  $2 \times 3$ ,  $2 \times 4$ , and  $1 \times 5$  plaquettes amounting to a total of 21 read-out chips; the second and furthest from the interaction point is formed by a  $2 \times 3$ ,  $2 \times 4$ , and  $2 \times 5$  plaquettes amounting to a total of 24 read-out chips. A plaquette is the basic unit of the FPix and consist of a single pixel sensor bump-bonded to the read-out chip and wired-bonded to a very-high-density-interconnect (VHDI) that provides data connections, power, and control. Figure 5.8 show an schematic of these two different panels as well as a photograph of a finalized panel. Finally, a layout of the pixel traker system is given in Figure 5.9 as well as the a detection efficiency as a function of the pseudorapidity. The total number of pixels in the pixel tracker is about 66 millions and they are equivalent to an area of about  $1 \text{ m}^2$ .

### Strip Tracker

The silicon tracker is located outside the inner pixel tracker and is composed of three subsystems that extend from 20 cm to 116 cm in the radial direction. The Tracker Inner Barrel and Disks (TIB/TID) are the innermost subsystem extending up to a radius of 55 cm, it includes 4 barrel layers and 3 disks at each side. The TIB/TID with their  $320 \mu\text{m}$  thick silicon micro-strip sensor oriented along the  $z$ -axis records up to 4  $r$ - $\phi$  measurements on a particle's trajectory. The strips pitch in the TIB – the distance between each strip – varies between  $80 \mu\text{m}$  and  $120 \mu\text{m}$  in layers 1-2

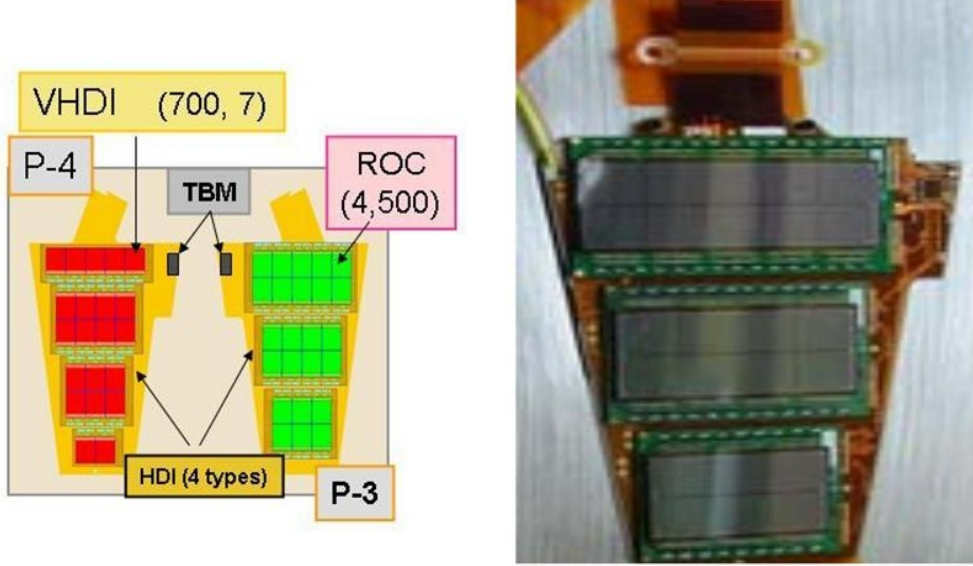


Figure 5.8: FPix module; (left) an schematic of the two types of module, (right) a photograph of one of the completed FPix modules.

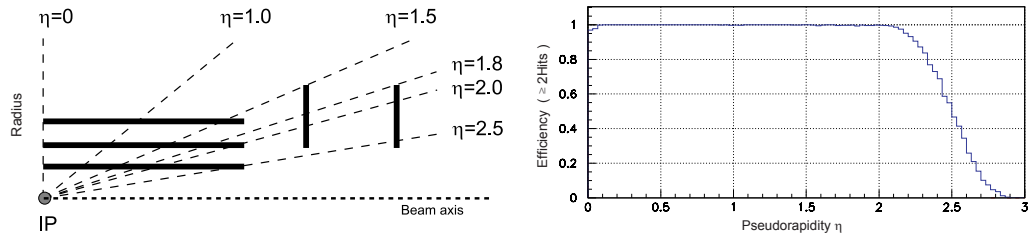


Figure 5.9: (Left) the layout of the silicon pixel tracker, (right) the pixel tracker detection efficiency as a function of the pseudorapidity.

and 3-4, respectively. The resulting single point resolution is therefore  $23 \mu\text{m}$  and  $35 \mu\text{m}$  for the 1-2 and 3-4 layers, respectively. The TID has strip pitches between  $100 - 140 \mu\text{m}$  – resulting in single point resolution between  $29 - 41 \mu\text{m}$ . The TIB/TID is completely surrounded by the Tracker Outer Barrel (TOB) which with its 6 barrel layer extends up to a radius of 116 cm. The layers are composed of  $500 \mu\text{m}$  thick micro-strips sensor with pitches of  $183 \mu\text{m}$  and  $122 \mu\text{m}$  for the first 4 and last 2 layer, respectively – recording up to 6  $r - \phi$  measurements on a particle's trajectory with single point resolutions of  $53 \mu\text{m}$  and  $\mu\text{m}$ , respectively. The TIB/TID and the TOB cover the region with  $|z| < 113 \text{ cm}$ , beyond this point (see Figure 5.5) the Tracker EndCaps ( $\text{TEC}^{\pm}$ ) – where the sign, obviously, represents the position on the  $z$ -axis – extend from 124 cm  $|z| < 282 \text{ cm}$  and  $22.5 \text{ cm} |r| < 113.5 \text{ cm}$ . The TEC consists of 9 disks which contain up to 7 rings of silicon micro-strips, the

latter are 320  $\mu\text{m}$  and 500  $\mu\text{m}$  thick in the inner 4 and outer 3 rings, respectively. Additionally, modules in the two innermost layers in the TIB and TOB, the two inner most rings of the TID, as well as rings 1,2 and 5 of the TECs are equipped with a second micro-strip detector module that is mounted back-to-back allowing measurements on the perpendicular coordinate – i.e.  $z$  and  $r$  in the barrel and the disks, respectively. In this fashion at least  $\approx 9$  hits in the silicon strip tracker in the  $|\eta| < 2.4$  range are ensured, with at least  $\approx 4$  two-dimensional measurements. The full strip tracker amounts to a total of 9.3 million strips and covers an active area of silicon equal to 198  $\text{m}^2$ .

### Performance of the CMS Tracker

The tracker efficiency for single muons is measured in 7 TeV data as a function of the muon pseudorapidity  $\eta$  and the number of reconstructed vertices using the tag-and-probe technique on muons decaying from Z bosons. The results are shown in Figure 5.10, where the muon efficiency is above 99% within the tracker acceptance and up to 20 reconstructed vertices. The muon transverse momentum and transverse impact parameter resolution as a function of  $\eta$  are estimated from the CMS full simulation, the results are shown in left and right panel of Figure 5.11, respectively. The muon transverse momentum resolution is about 1-3% for  $|\eta| < 1.5$  for muons of different energies. The transverse impact parameter is estimated to be between  $\sim 10\text{-}20 \mu\text{m}$  for a 100 GeV muon while for 1 GeV muons the resolution is between  $\sim 80\text{-}250 \mu\text{m}$ .

### 5.3 The Electromagnetic Calorimeter

The CMS electromagnetic calorimeter (ECAL) is a granular and homogeneous calorimeter built out of 61,200 lead tungstate ( $\text{PbWO}_4$ ) crystals in the barrel and closed by 7,324  $\text{PbWO}_4$  crystals in each of the two endcaps. Additionally, a preshower detector is placed in front of the endcaps – i.e. closer to the interaction point. The scintillating light is collected by silicon avalanche photodiodes (APDs) in the ECAL barrel (EB) and by vacuum phototriodes (VPTs) in the ECAL endcaps (EE). Figure 5.12 shows a projectional schematic layout as well as a geometric view of a quarter of the CMS ECAL. The ECAL excellent performance is one of the keystones of the physics results of the CMS experiment, perhaps, best exemplified by the Higgs boson search and characterization in the  $H \rightarrow \gamma\gamma$  and  $H \rightarrow ZZ^*$  decay channels [154, 86].

The  $\text{PbWO}_4$  crystals with a density of 8.28 g/cm<sup>3</sup> provided a good candidate because

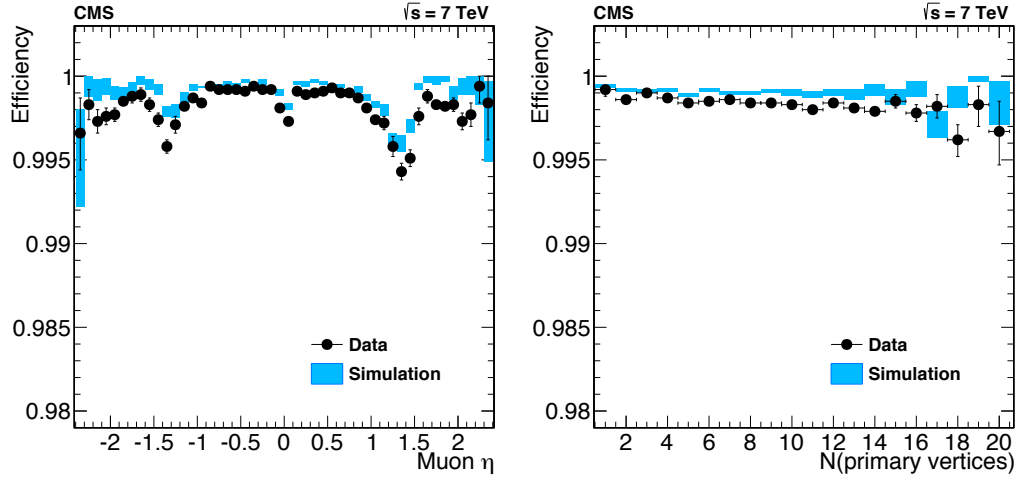


Figure 5.10: Tracking efficiency for muons from  $Z$  decays using the tag-and -probe technique. The left panel and right panel show the efficiency as function of the muon  $\eta$  and the number of reconstructed vertices, respectively. The black dots represent the measurement in 7 TeV data and the solid color represents the CMS simulation.

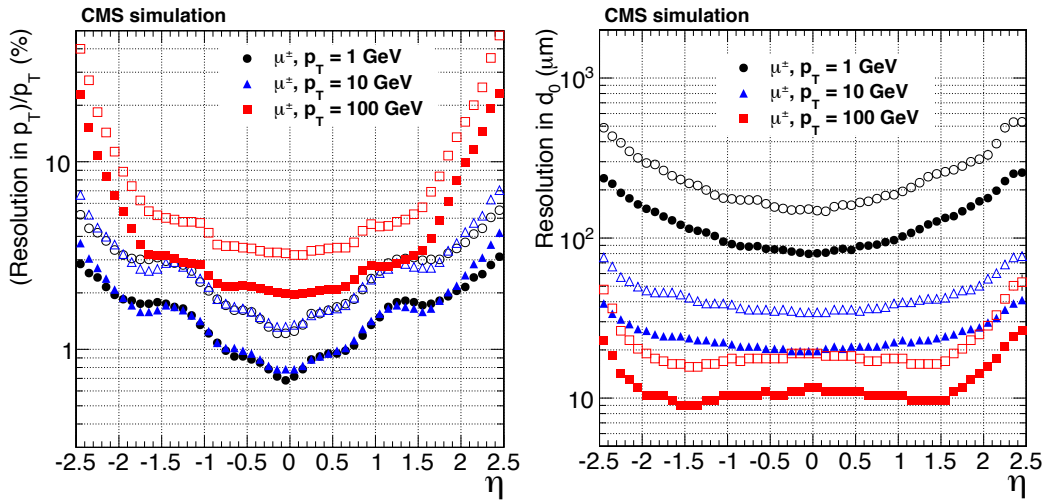


Figure 5.11: Resolution as a function of the pseudorapidity  $\eta$  for muons of  $p_T = 1$ , 10, and 100 GeV. The left panel shows the transverse momentum resolution and the right panel the transverse impact parameter resolution. Both quantities are estimated from Simulation.

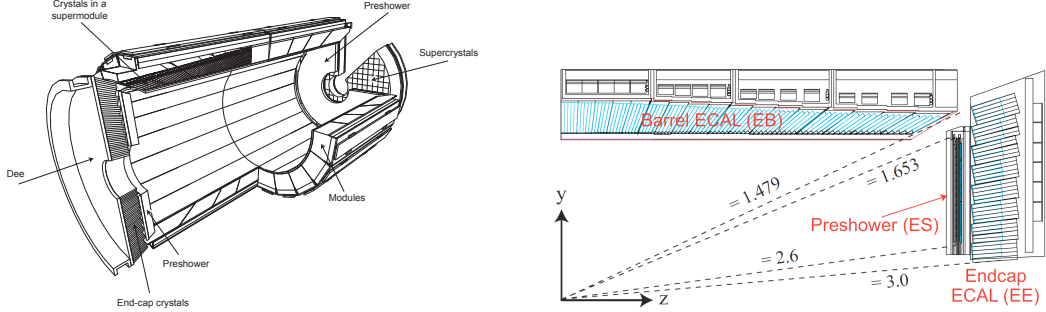


Figure 5.12: The layout of the CMS electromagnetic calorimenter. The left panel shows a projectional schematic layout including all the major parts while the left panel shows a geometric view of a quarter of the ECAL.

of its small radiation length ( $X_0 = 0.89$  cm), small molière radius (2.19 cm), and fast response. PbWO<sub>4</sub> crystals have a relatively low light yield of about 10 photo-electrons/MeV and therefore they required to be read out by sensors with internal amplification inside the 3.8 T magnetic field. The crystals in the EB are 23 cm long and have a cross-sectional area of  $2.2 \times 2.2$  cm<sup>2</sup> (equivalent to  $0.0174 \times 0.0174$  in  $\eta, \phi$ ), they are located at radius of 1.29 m and arranged in a quasi-projective geometry with 170 crystals – 85 at each side – covering up to a pseudorapidity range  $|\eta| < 1.48$ . With 360 crystals in the  $\phi$  direction the EB is fully hermetic. The EE crystals are located at  $z = \pm 315.4$  cm, they have a cross-sectional area of  $2.86 \times 2.86$  cm<sup>2</sup> and  $3.0 \times 3.0$  cm<sup>2</sup> at the front and rear faces, respectively, and a length of 22 cm. They are grouped in mechanical structure of  $5 \times 5$  crystals and arranged in the traditional  $x$ - $y$  directions. Each endcap is divided into halves or *Dees*, holding 3,662 crystals. The EE extends the ECAL coverage up to the range  $1.479 < |\eta| < 3.0$ . The left and right panels of Figure 5.13 show the EB crystal instrumented with an APD and the EE crystal instrumented with a VPT, respectively. Real photographs of an EB module equipped with crystal is presented in Figure 5.14 while an EE Dee fully instrumented with crystals is shown in Figure 5.15.

### ECAL Performance

The EB has been extensively tested using electron beams, in this test beam setup – with no magnetic field or material in front – the energy resolution has been measured to be:

$$\frac{\sigma_E}{E} = \frac{2.8\%}{\sqrt{E(\text{GeV})}} \oplus \frac{12\%}{E(\text{GeV})} \oplus 0.3\%, \quad (5.1)$$

where E is the electron beam energy in units of GeV. The terms in the right-hand side of the Eq. 5.1 are the so called stochastic, noise, and constant terms. The first

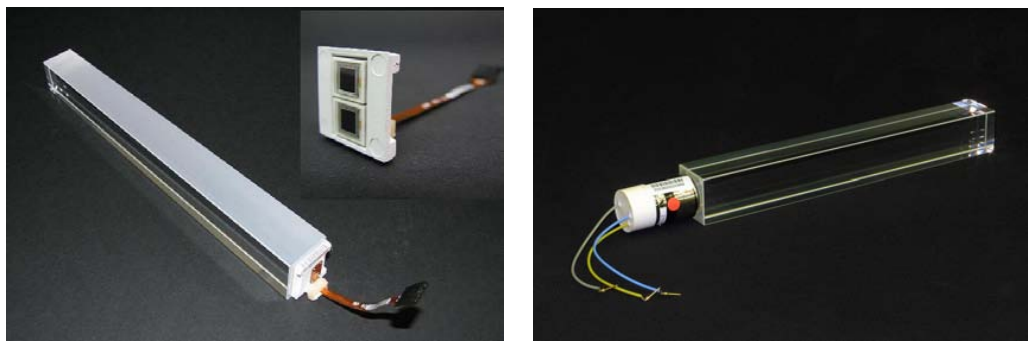


Figure 5.13: The PbWO<sub>4</sub> crystal of the CMS ECAL, (left) a EB crystal instrumented with an APD and (right) a EE crystal instrumented with a VPT.

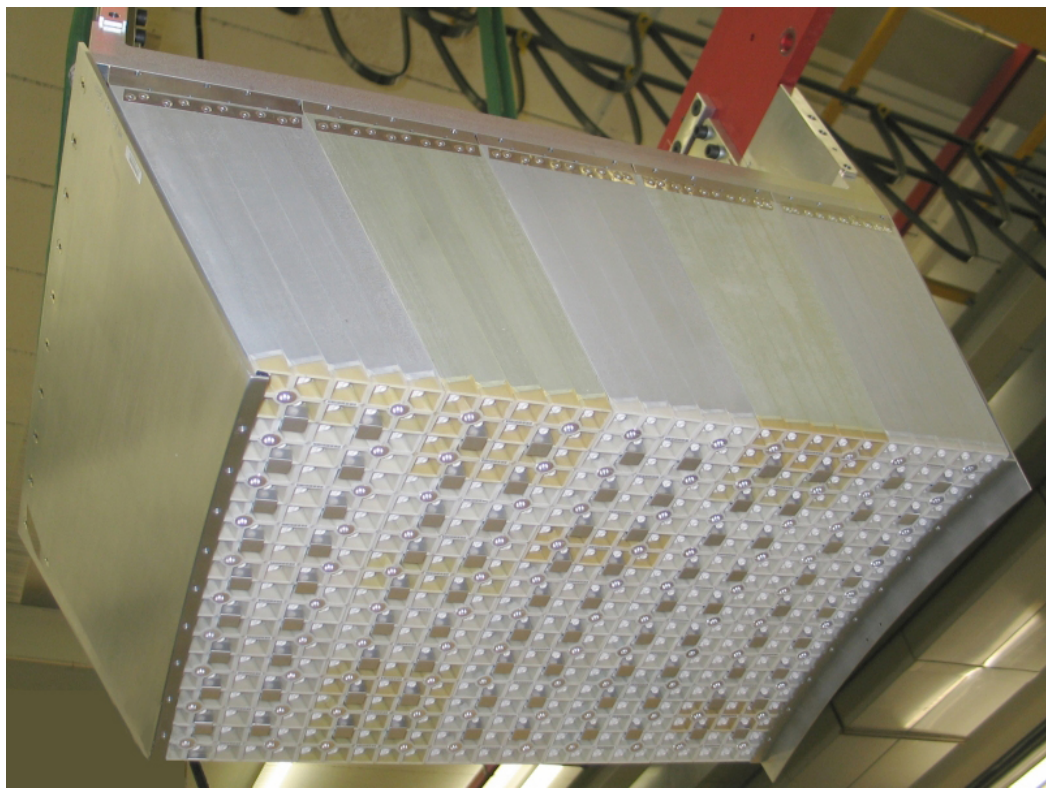


Figure 5.14: A photograph of a EB module instrumented with crystals.



Figure 5.15: A photograph of a EE Dee instrumented with crystals.

is due to the fluctuations related to the development of the electromagnetic shower inside the calorimeter crystals, the second is due to electronic noise of the readout chain, and the last is related to the instrumental effect such as non-linear response, radiation damage, shower leakage among others.

The test beam ideal conditions clearly differ from those at the CMS experiment and therefore in situ measurements of the performance of the ECAL have been performed during the data-taking period at 7 and 8 TeV. One key measurement is the trigger efficiency for electron/photon ( $e/\gamma$ ) candidates, the Level-1 trigger was operated with a threshold of  $E_T = 20$  GeV (provided by  $5 \times 5$  crystals) in 2012 and found to be above 99% efficient for  $E_T > 40$  GeV, thus enabling a fully efficient  $H \rightarrow \gamma\gamma$  search.

The  $e/\gamma$  energy measurement depends upon the correct reconstruction of electromagnetic showers in the ECAL. Some  $e/\gamma$  candidates interact – by bremsstrahlung or photon conversion – with the silicon tracker prior reaching the ECAL or their trajectories are modified due to the 3.8 T magnetic field causing the showers to spread on the azimuthal direction and thus their energy is shared by multiple crystals. In order to account for these effects and ensure a more accurate  $e/\gamma$  reconstruction a

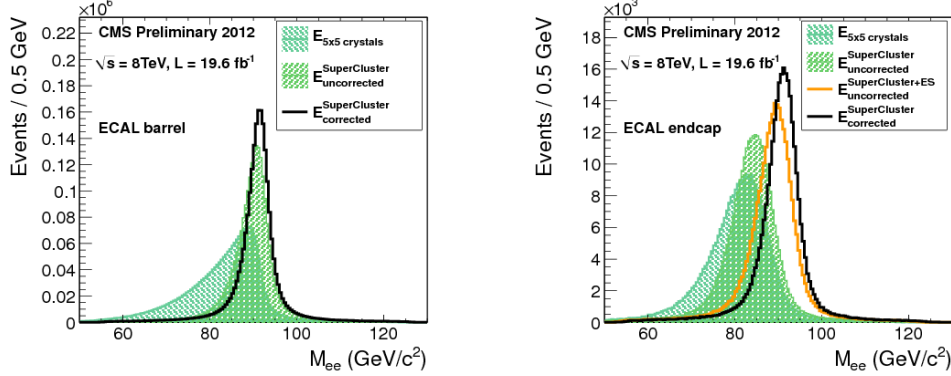


Figure 5.16: The reconstructed Z invariant mass from  $e^+e^-$  decays. The left and right panels show the reconstructed invariant mass for the EB and EE, respectively, with different algorithms to reconstruct electron energies.

dynamic clustering algorithm is used to merge clusters of energy deposited that belong to the same electromagnetic shower into the so-called *superclusters* (SCs). Once the SC is formed, the  $e/\gamma$  candidate energy ( $E_{e/\gamma}$ ) is reconstructed using the following expression:

$$E_{e/\gamma} = F_{e/\gamma} \cdot (G \cdot \sum S_i(t) C_i A_i + E_{\text{ES}}) \quad (5.2)$$

where  $F_{e/\gamma}$  is a correction accounting for the imperfect clustering, material, and geometric effect;  $G$  is the ADC-to-GeV conversion;  $S_i(t)$  is the time-dependent correction to account for the response variations of the  $i$ -th crystal;  $C_i$  is the inter-calibration coefficient of the  $i$ -th crystal;  $A_i$  is the amplitude of the  $i$ -th crystal in ADC counts; finally,  $E_{\text{ES}}$  is the pre-shower energy – only relevant for  $e/\gamma$ s in the EE. Figure 5.16 shows the effect of the clustering process and the application of the  $F_{e/\gamma}$  correction by comparing the invariant mass of  $e^+e^-$  pairs coming from a Z boson with respect to the usage of the simple fixed  $5\times 5$  cluster energy.

The inter-calibration coefficient is responsible for correcting the channel-to-channel variation in response. The main sources for such variations are the crystal light yield variations (up to  $\sim 15\%$ ) and the spread on the gain of the photodetectors (up to  $\sim 25\%$ ). An inter-calibration is carried out in situ by methods that exploit the time- and  $\phi$ -invariance of the energy flow in the crystals at a given  $\eta$  in minimum-bias events, as well as the  $\pi^0/\text{eta}$  mass constraint to the photons pair from its decay, and the momentum constraint of isolated electrons from W and Z boson decays. The precision of these methods as a function of  $\eta$  is shown in Figure 5.17. The invariant

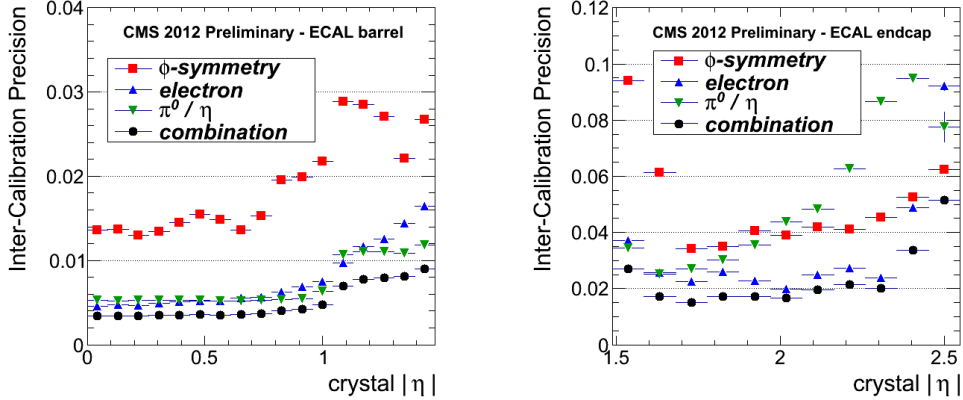


Figure 5.17: The reconstructed Z invariant mass from  $e^+e^-$  decays. The left and right panels show the reconstructed invariant mass for the EB and EE, respectively, with different algorithms to reconstructed electron energies.

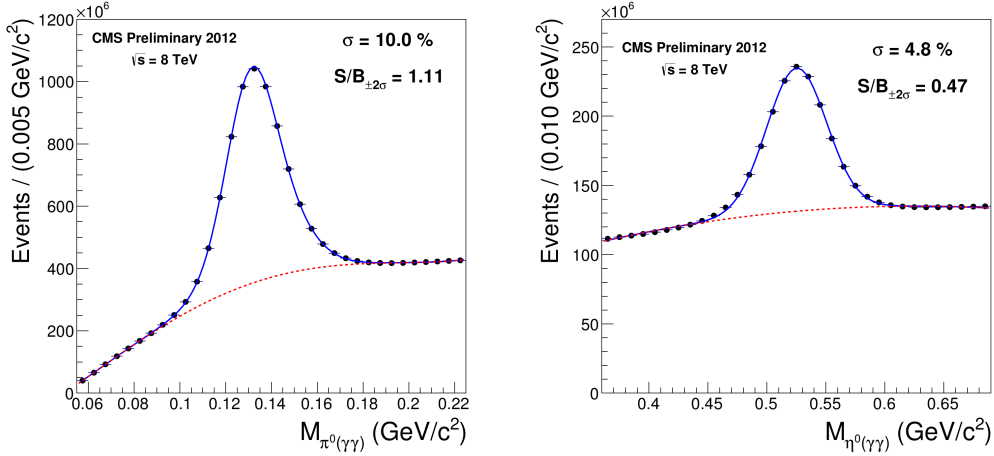


Figure 5.18: The reconstructed Z invariant mass from  $e^+e^-$  decays. The left and right panels show the reconstructed invariant mass for the EB and EE, respectively, with different algorithms to reconstructed electron energies.

mass of diphotons consistent with a  $\pi^0$  and  $\eta$  used in the inter-calibration is shown in the left and right panels of Figure 5.18, respectively.

Another important ingredient to the precise measurement of the electromagnetic shower energy is the time dependent corrections, at CMS the ECAL crystals undergo changes in transparency due to the radiation received while collisions occur, while during downtime the transparency is recovered. In order to correct for the transparency changes a laser monitoring system is installed and run every  $\sim 40$  minutes. Laser light ( $\lambda = 440$  nm) close to the emission peak of PbWO<sub>4</sub> is impinge into all the crystals, thus, tracking their response variations. The variations on

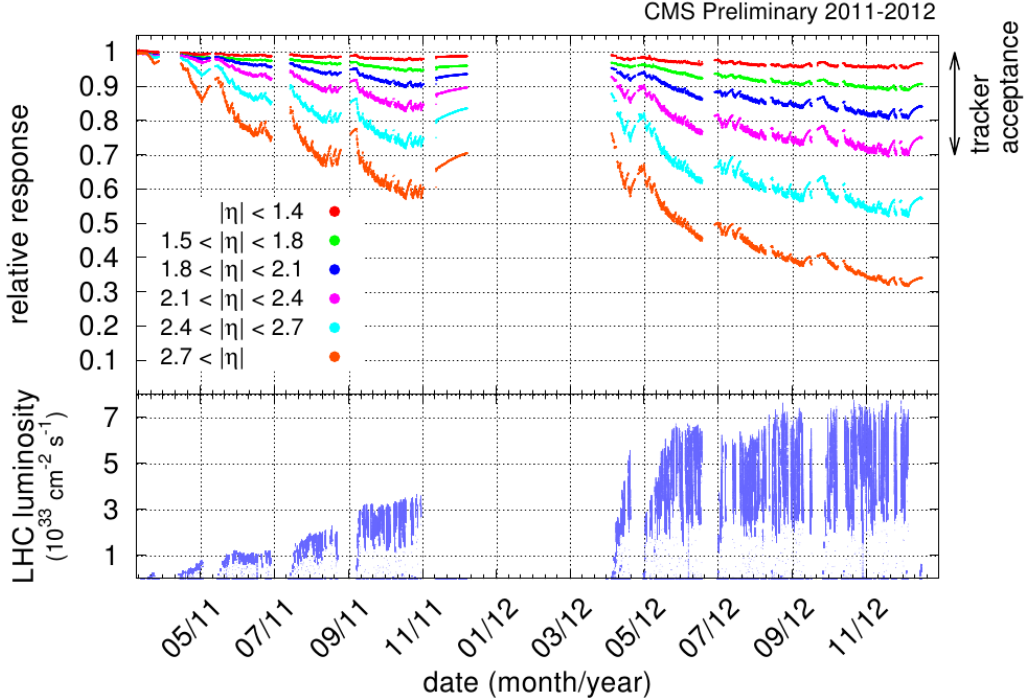


Figure 5.19: The reconstructed  $Z$  invariant mass from  $e^+e^-$  decays. The left and right panels show the reconstructed invariant mass for the EB and EE, respectively, with different algorithms to reconstruct electron energies.

transparency as a function of time for different  $\eta$  ranges is shown in the left panel of Figure 5.19, where it is observed that the transparency variations are more severe at large pseudorapidities. The validity of the laser monitoring (LM) correction is checked using electrons from  $W$  decays. The stability of the LM correction is estimated by the rms of the  $E/p$  ratio in these events and found to be about 0.1% and 0.3% for the EB and EE, respectively. The right panel of Figure 5.19 shown the LM correction effect on electron from  $W$  events in the EE. The effect of the inter-calibration and LM corrections is shown Figure 5.21, where the invariant mass of  $e^+e^-$  pairs from  $Z$  decays is reconstructed with and without such corrections being applied.

Finally, the overall energy resolution of the CMS ECAL has been measured and compared to simulation, this is shown in the right panel of Figure 5.22. The energy resolution is found to be between 1-2% for  $|\eta| < 1$  and between 3-5% in the EE, it is also observed that the simulation and measurement do not agree and that an extra constant term as a function of  $\eta$  should be added to the simulation. The performance of the ECAL can also be observed in the width of the invariant mass of the Higgs

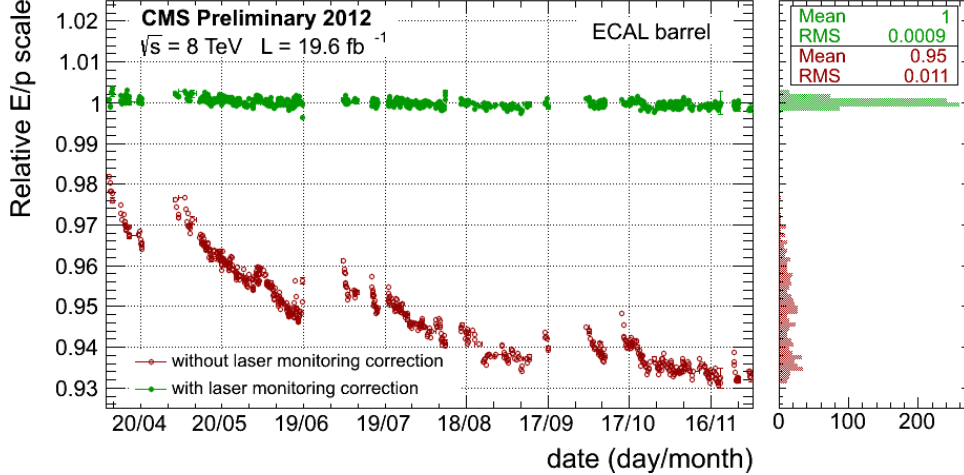


Figure 5.20: The reconstructed Z invariant mass from  $e^+e^-$  decays. The left and right panels show the reconstructed invariant mass for the EB and EE, respectively, with different algorithms to reconstructed electron energies.

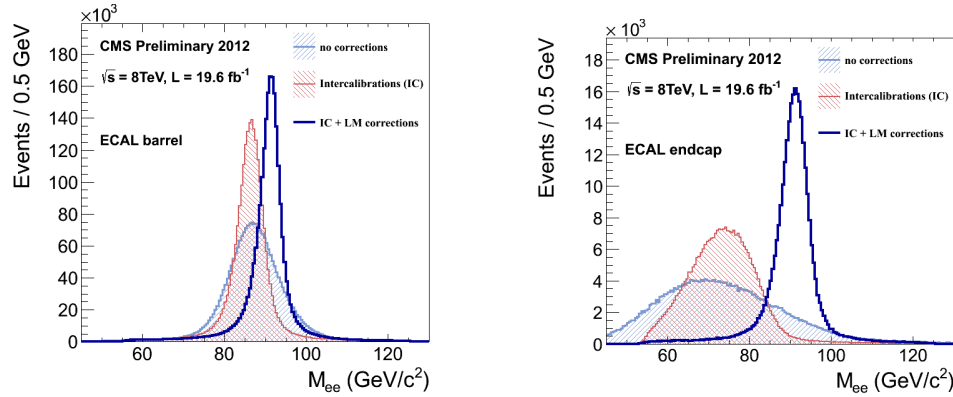


Figure 5.21: The reconstructed Z invariant mass from  $e^+e^-$  decays. The left and right panels show the reconstructed invariant mass for the EB and EE, respectively, with and without the IC and the LM corrections.

boson, this is shown in the left panel of Figure 5.22, where a  $\sigma_{eff} = 1.36 \text{ GeV}$  is observed.

#### 5.4 The Hadronic Calorimeter

The CMS Hadron Calorimeter (HCAL) surrounds the silicon tracker and the electromagnetic calorimeter. It is composed of four different subsystems: the barrel (HB), endcaps (HEs), the outer (HO), and the forward (HF) calorimeters. The HB and HE are located inside the cryostat of the superconducting solenoid and both are sampling calorimeters with brass as the absorber and plastic scintillator as the active medium. The HO is plastic scintillator calorimeter located outside the

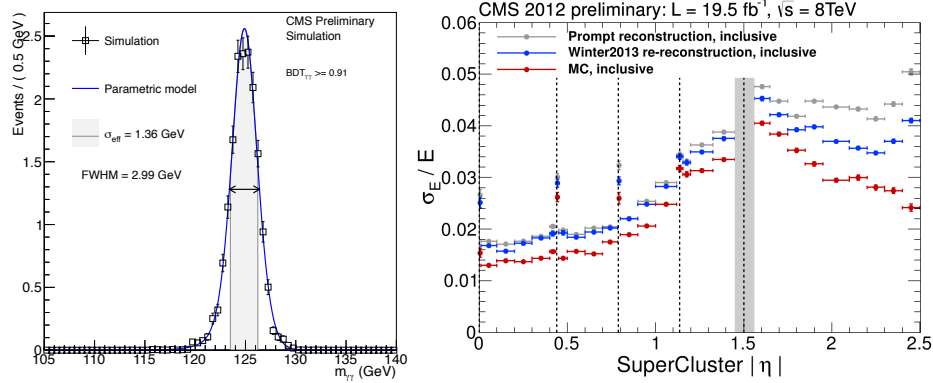


Figure 5.22: The reconstructed  $Z$  invariant mass from  $e^+e^-$  decays. The left and right panels show the reconstructed invariant mass for the EB and EE, respectively, with different algorithms to reconstructed electron energies.

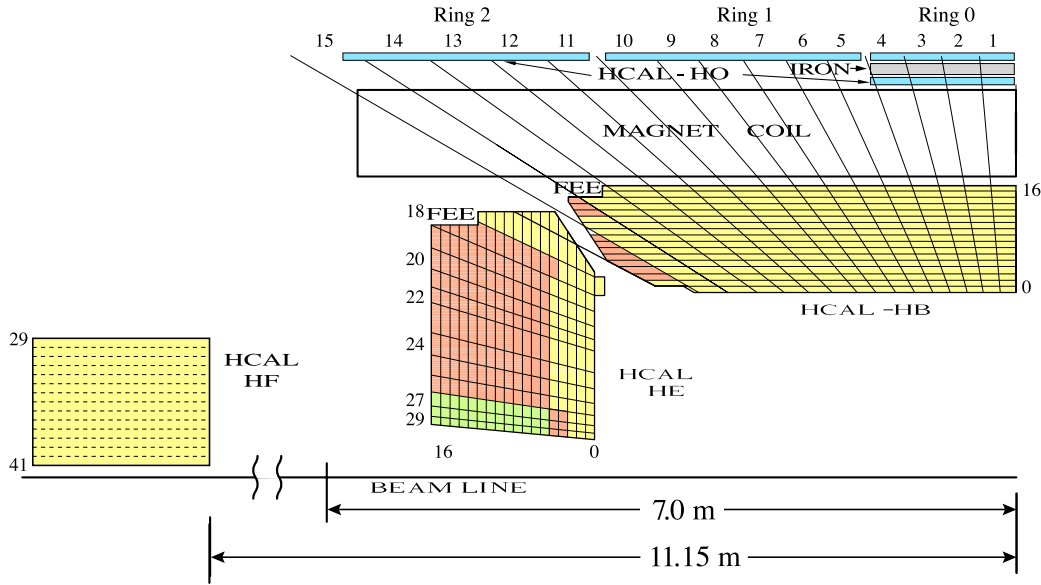


Figure 5.23: The CMS HCAL layout.

superconducting solenoid cryostat and is designed to catch the energy leakage from the HB. The HF is a quartz fiber and steel calorimeter located at  $z = \pm 11.15 \text{ m}$ , thus, extending the pseudorapidity coverage up to  $|\eta| = 5$ . The layout of the HCAL is presented in Figure 5.23.

The hadronic energy resolution for the barrel HCAL and ECAL combination was measured in beam test using pions and protons and found to be:

$$\frac{\sigma_E}{E} = \frac{0.847 \pm 0.016 \text{ GeV}^{\frac{1}{2}}}{\sqrt{E(\text{GeV})}} \oplus 0.074 \pm 0.008. \quad (5.3)$$

The energy resolution in the endcaps is similar to that of the barrel.

The following passages are aimed to give a more detailed description of the four HCAL subsystems.

### **The Barrel Hadronic Calorimeter**

The HB is a sampling calorimeter made of brass absorber and plastic scintillator as the active medium. The whole EB is build out of two identical cylindrical structures, each of which is composed of 18 brass wedges. The pseudorapidity coverage of the HB reaches approximately  $|\eta| = 1.4$  while the  $\phi$  covarage is  $360^\circ$ . The segmentation of the HB is provided by the plastic scintillator tiles inserted in the layers of the brass wedges, the latter are segmented into four  $\phi$  sector, while there are 16 scintillator tiles along the  $\eta$  direction, thus providing the HB with an equivalent segmentation of  $0.087 \times 0.087$  in  $\eta, \phi$ . Each wedge calorimeter is composed of 16 layers of absorber and 17 layers of plastic scintillator, the intermediate layer are made of brass absorber and 3 mm plastic scintillator while the first and last layers are made of stainless steel and thicker 9 mm plastic scintillator tiles. The very first layer is scintillator in order to detect showers developed in the electromagnetic calorimeter material. Figure 5.24 shows an schematic of a HB wedge. The 16 scintillator tiles of each layer are laid in a tray in order to facilitate their insertion and removal. Each tile's scintillating light is collected by a green double-cladded wavelength-shinting (WLS) fibers from Kuraray (Y-11) placed in groove in the scintillator. Upon exiting the scintillating tile, each WLS is splice into a clear fiber which subsequently ends in an optical connector at the back of the tray. At this point, optical cables take the light from the clear fiber into a 19 pixel hybrid photodiode (HPD), which is designed to work inside the 3.8 T magnetic field. The total interaction lengths ( $\lambda_I$ ) of the HB varies with pseudorapidity, there are  $5.8 \lambda_I$  at  $\eta = 0$ , increasing up to  $10.6 \lambda_I$  at  $|\eta| = 1.3$ . The finalized HB is shown in Figure 5.25.

### **The Endcap Hadronic Calorimeter**

The HE is a brass/platic-scintillator sampling calorimeter that extend the pseudo-rapidity coverage from  $1.3 < |\eta| < 3$ . It is composed of 79-mm-thick brass plates with 9 mm gaps to accomodate the scintillator. The total material, including the crystals in the EE, is about  $10 \lambda_I$ . There are 18 layers – along the  $z$ -direction – of plastic scintillators, the first layer, right after the EE, is 9-mm-thick, while the rest are 3-mm-thick. The scintillators are segmented in the radial direction and their light is collected by embedded WLS fiber. The scintillator tiles and the WLS are

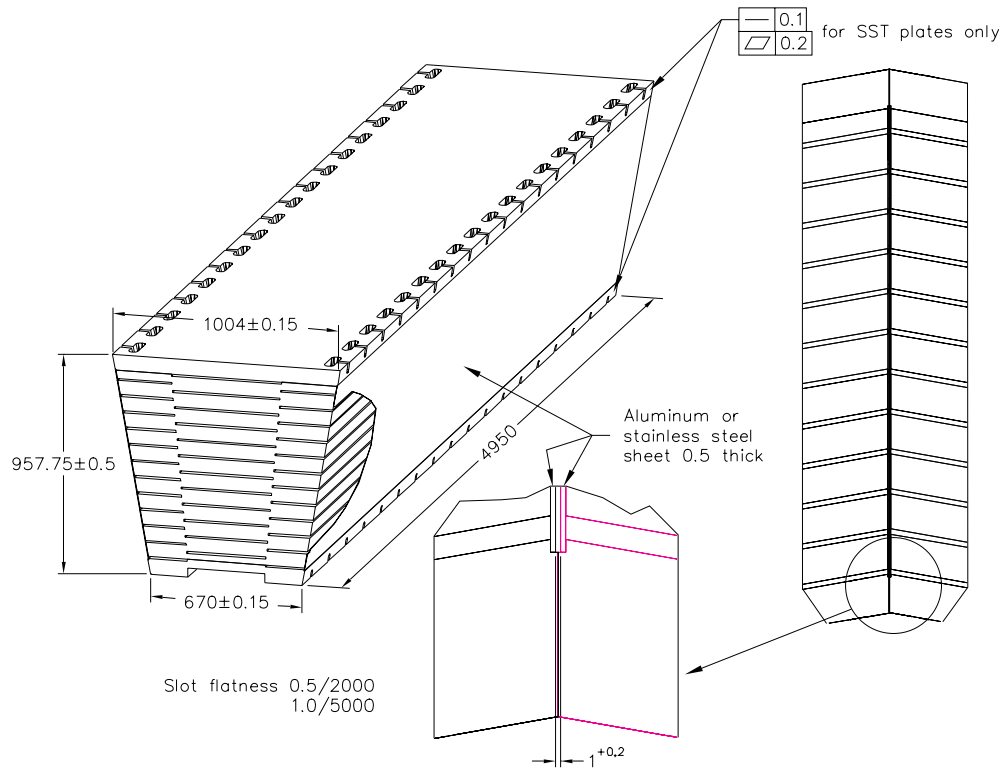


Figure 5.24: An schematic drawn of one of the wedges of the CMS HB.

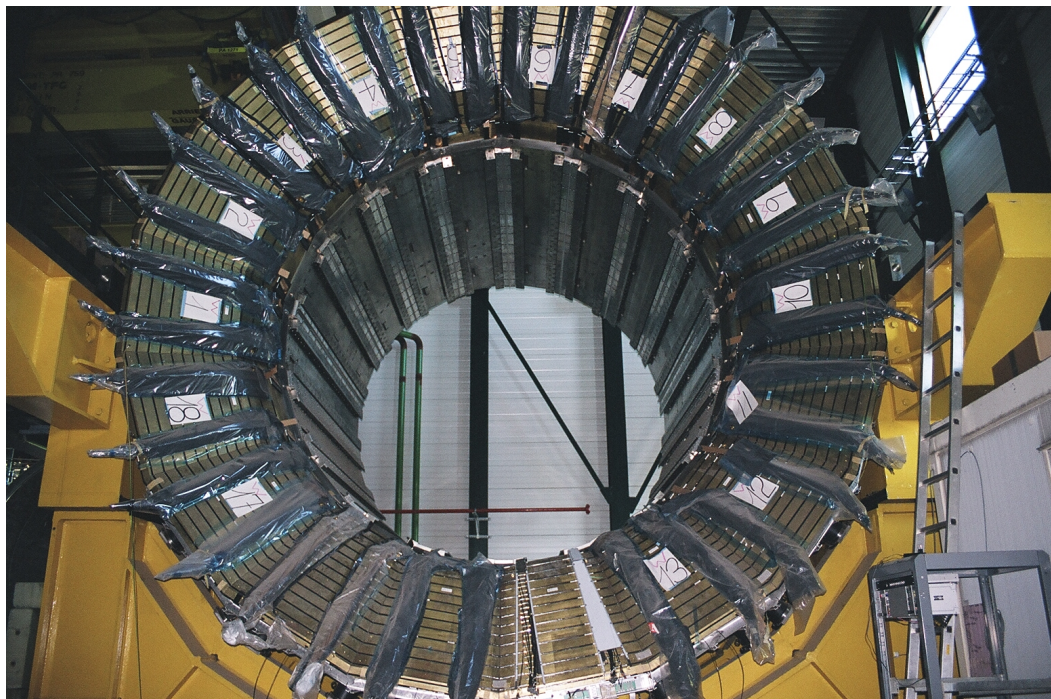


Figure 5.25: A photograph of the finalized CMS HB.

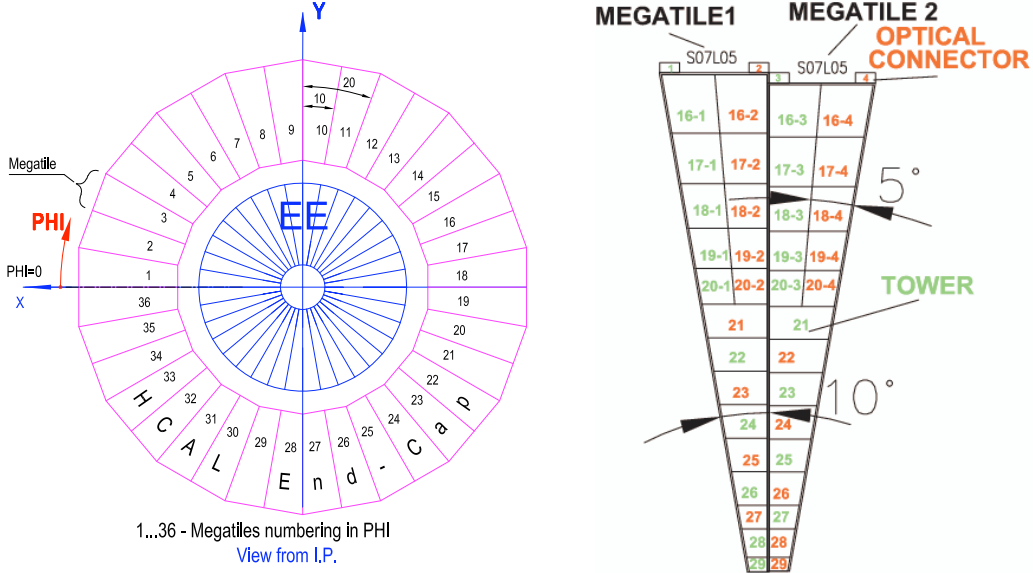


Figure 5.26: An schematic of the HE geometry in the  $\phi$  direction is presented in the left panel. The configuration of two adjacent scintillator trays is presented in the right panel.

laid in trays with a trapezoidal geometry. Figure 5.26 shows an schematic of the trays. The WLS are spliced to clear fibers which are susequently terminated in an optical connector. Optical cables transport the light from the optical connector the HPDs, which, as mentioned earlier, could operate in the presense of a magnetic field. This design results in a granularity of  $0.087 \times 0.087$  ( $\eta \times \phi$ ) for  $|\eta| < 1.6$  and  $0.17 \times 0.17$  for  $|\eta| > 1.6$ . Figure 5.27 shows one partially finalized HE, where only some of the scintillator trays have been inserted.

### The Outer Hadronic Calorimeter

The space constraints posed by the superconducting solenoid limited the stopping power of the combined EB and HB and therefore their ability to fully contain hadronic showers. In order to overcome this limitation, another calorimeter layer, the HO, is located just outside the cryostat of the superconducting solenoid in the central region ( $|\eta| < 1.3$ ) of the detector. The HO uses the solenoid coil as an additional absorber layer equivalent to  $1.4/\sin(\theta) \lambda_I$ . The active layer are 10-cm-thick plastic scintillator. The geometry of the HO is constraint to that of the muons system and therefore is composed of 5 rings along the  $z$ -direction (each ring is about 2.52 m). The HO rings are label with number -2, -1, 0, 1, and 2 which are located at  $z$ -positions of -5.342 m, -2.686 m, 0, +2.686 m, and +5.342 m, respectively. The central ring (ring-0) has two 10 cm thick layers of plastic scintillator at each side of



Figure 5.27: A photograph of the one partially finalized CMS HE.

a 19.5 cm iron slab located  $r = 3.82$  m and  $r = 4.07$  m. The rest of the rings contain only one 10 cm thick scintillator layer and no extra absorber. This brings the total calorimeter depth to a minimum of about  $12 \lambda_I$  except at the boundary between the HB and the HE. Each ring is divided into 12 identical  $\phi$ -sectors, additionally, each sector has six scintillating tiles in the  $\phi$  direction. The two layers in ring-0 have 8 tiles in the  $\eta$  direction, rings 1 and -1 have 6 tiles, and rings 2 and -2 have 6 tiles. This design provides a granularity of  $0.087 \times 0.087$  in  $\eta \times \phi$ , thus matching the granularity of the HB. The light from the scintillating tiles is transported by embedded WLS which are subsequently spliced into clear fiber – which have a  $\sim 4$  time longer attenuation length– that finally transport the light into a photodetector outside the muon rings. Figure 5.28 shows the photograph of one of the HO tiles with the embedded WLS. Finally, the geometry of the HO is presented in Figure 5.29

### The Forward Hadronic Calorimeter

The HF cover the forward region,  $3 < |\eta| < 5.2$ , thus receiving a substantial amount of radiation. This harsh radiation environment was the principal reason to use quartz fibers, due to its radiation hardness properties, as the active medium of a sampling

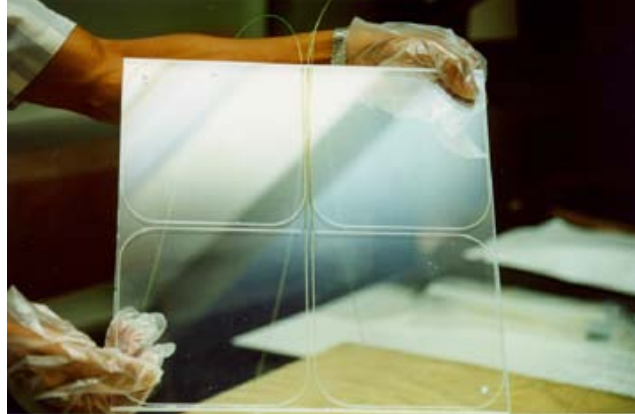


Figure 5.28: A photograph of a HO scintillating tile with the embedded WLS.

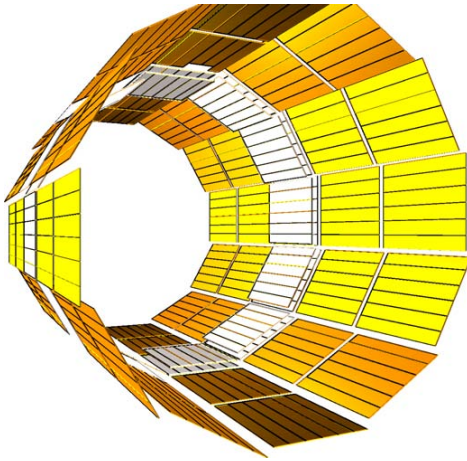


Figure 5.29: An schematic drawing presenting the geometry of the HO.

calorimeter with steel absorber. The HF is a cylindrical structure –with inner and outer radii of 12.5 cm and 130 cm, respectively – composed of 18 steel wedges that are divided into two sectors, each wedge has quartz fiber embedded along the  $z$ -direction. The quartz fibers propagate the Cherenkov light that the secondary particle of a shower produce when traversing through them. In order to separate electromagnetic showers, that tend to be produced closer to the front face of the HF, from hadronic showers; two different types of fiber are embedded in the steel, half of the fibers cover the whole length of the HF ( $165 \text{ cm} \approx 10\lambda_I$ ) while the other half start to run 22 cm from the front face of the HF, these two groups are read out separately by PMTs with a borosilicate glass window. The fiber are grouped in such a way that the effective granularity of the HF is  $0.175 \times 0.175$  in  $\eta \times \phi$ . Figure 5.30 shows a photograph of some of the HF steel wedges equipped with quartz fibers.



Figure 5.30: A photograph of the HF steel wedges equipped with quartz fibers.

## 5.5 The Muon Chambers

The CMS muon system is designed to trigger, identify, and measure the momenta of muons over a large kinematic range. Good muon momentum resolution is provided by the high granularity of the muon system and the relatively high magnetic field provided by the superconducting solenoid and its steel flux-return yoke. The muon system design requirements are the following:

- Trigger on single- and multi-muon event with thresholds from a few to 100 GeV
- Muon momentum (muon system only) resolution of 8-15% at 10 GeV, and 20-40% at 1 TeV
- Muon momentum (muon & tracker system) resolution of 1-1.5% at 10 GeV, and 6-17% at 1 TeV
- Charge missassignment < 0.1% at muon  $p_T$  of 100 GeV

The muon system detector is based in gas ionization chambers. In order to achieve the physics requirement and comply with the geometry constraints, three different technologies are used: drift tubes (DT) chambers, cathode strip chambers (CSCs), and resistive plate chambers (RPCs). There are 250 DT chambers, 540 CSCs, and 610 RPCs; each chamber operates independently and is assembled into the muon detector system. In order to match the cylindrical geometry of the CMS detector,

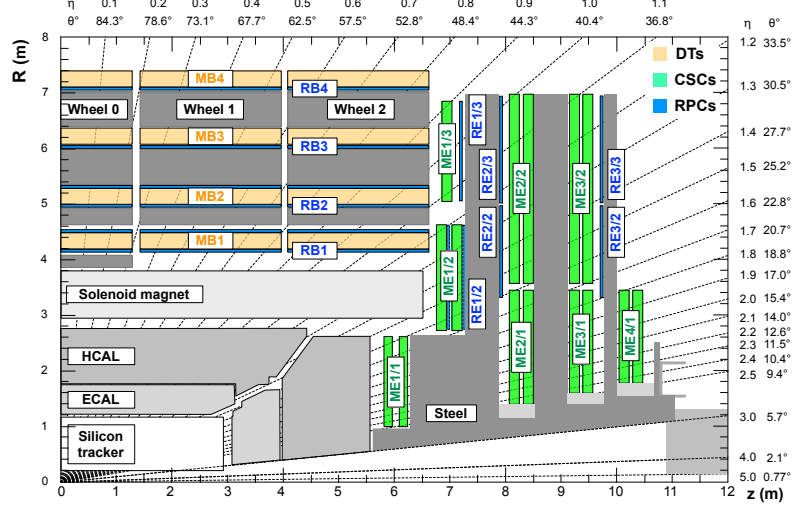


Figure 5.31: A layout of the CMS muon system. Different subdetectors are labeled with different colors.

a barrel region – covering up to  $|\eta| = 1.2$  – and 2 endcaps regions – covering the  $0.9 < |\eta| = 2.4$  region – are used. The barrel is equipped with DT chambers, the endcaps consists of CSCs, while the RPCs are used in both the barrel and endcap regions. The muon stations are collections of chambers around fixed  $r$  and  $z$  in the barrel and endcap regions, repectively. There are 4 stations in the barrel and endcaps, they are labeled MB1-MB4 and ME1-ME4, respectively. The barrel is divided into 5 “wheels” along the  $z$ -direction, wheel-0 (W0) is centered at  $z = 0$ , W+1 and W+2 are located in the positive  $z$ -region, while W-1 and W-2 are located in the negative  $z$ -region. The endcaps are divided in the  $r$ -direction forming rings of CSCs and RPCs. Thus, the former are labeled ME1/n-ME4/n, where n is an index that increments radially outwards. Figure 5.31 show a layout of the muon system with its different detectors as well as the other systems of the CMS detector.

### The Drift Tube Chambers

The DTs are composed of standard rectangular cells filled with a gas mixture of 85% Ar and 15% CO<sub>2</sub>, the latter are called drift cells. Each cell has a transverse size of 42×13 mm<sup>2</sup>, they are equipped with a gold-plated stainless-steel anode wire of 50  $\mu\text{m}$  diameter at the center, and four electrodes – including two cathode strips – at each side of the cell to shape the electric field. The anode wire operates at +3,600 V while the top/bottom electrodes and the electrodes on the side are operated at +1,800 V and -1,800 V, respetively. The gas mixture in the drift cell provide a drift velocity of 55  $\mu\text{m}/\text{s}$  and good quenching properties. The maximum drift time was measured

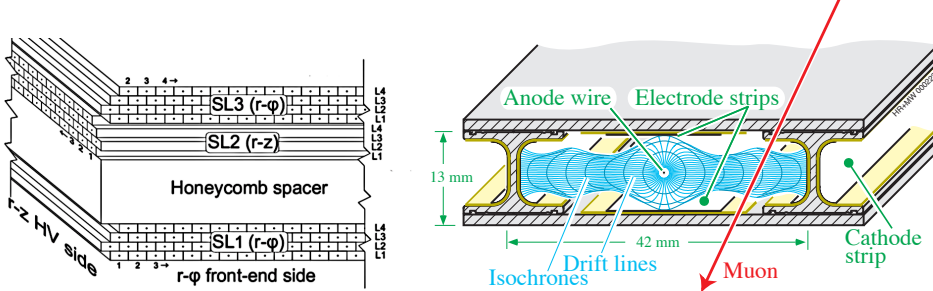


Figure 5.32: (Left) an schematic of a barrel chamber with DT and SL clearly labeled. (Right) an schematic of a drift cell.

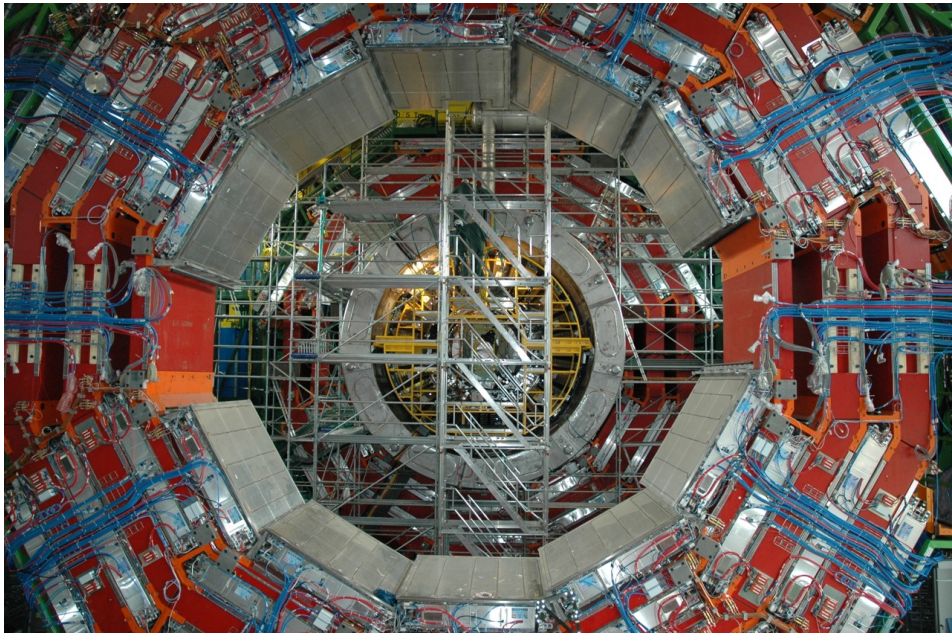


Figure 5.33: A photograph of the a barrel wheel during construction. The DT chambers are gray while the steel return-yokes are painted in red.

to be around 400 ns. Drift cells are grouped in 4 parallel and staggered layers – each layer at different  $r$  – to form a superlayer (SL). All DTs chambers – except those in MB4 – are formed by 2 SLs with wires along the  $z$ -direction, thus measuring  $r - \phi$  coordinates, and one SL with wires running perpendicular to the  $z$ -axis at fixed distance from the beam pipe, and therefore measuring  $r - z$  coordinates. The MB4 chambers have only an  $r - \phi$  SL. The left and right panels of Figure 5.32 show schematics of a barrel chamber and a DT, respectively . The chambers are 2.5 m long in the  $z$ -direction, and their transverse size varies with the station, ranging from 1.9 for MB1 and 4.1 for MB4. Figure 5.33 shows a photograph of a barrel wheel during construction.

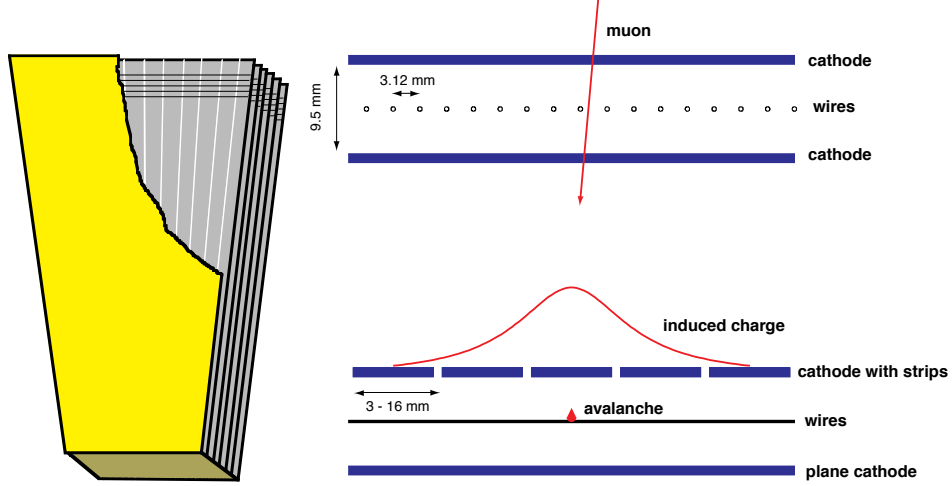


Figure 5.34: An schematic of a typical CSC.

### The Cathode Strips Chambers

Due to the higher rate of particles and the non-uniformities of the magnetic field in the endcap regions standard DTs are not a good candidate to detect muons in this region. Therefore, the muon endcap system is comprised of cathode strip chambers; which have a fast response, can be finely segmented, and can be operated in the presence of a non-uniform magnetic field – Figure 5.3 shows the magnetic field lines and intensity in the CMS detector. Each endcap region has four disk-shaped stations perpendicular to the  $z$ -axis. The endcap stations are formed by different sizes of CSC. The CSC units have 6 layers – again, along the  $z$ -axis –, each of which has cathode strips along the  $r$ -direction and wires running perpendicular to the strips. Thus, the CSC units provide a 2-dimensional measurement in the  $r - \phi$  plane. All CSC are filled with a gas mixture composed of 50% CO<sub>2</sub>, 40% Ar, and 10% CF<sub>4</sub>; the ME1/1 chambers are operated at an anode voltage of 2,900 V while the rest of them at 3,600 V. Each chamber has 80 cathode strips subtending an angle between 2.2 and 4.7 mrad. The ME1/1 anode wires are 30  $\mu\text{m}$  in diameter and placed 2.5 mm apart, while the rest of the chambers wire's are 50  $\mu\text{m}$  in diameter and placed 3.12 or 3.16 mm apart. Alternative layers are shifted in order to minimize gaps between chambers. An schematic of one the CSC is shown in Figure 5.34 while a photograph of one of the endcaps during construction is shown in Figure 5.35.

### The Resistive Plate Chambers

The resistive plate chambers of the muon system are a complementary and dedicated trigger system with excellent time resolution in order to correctly identify the correct

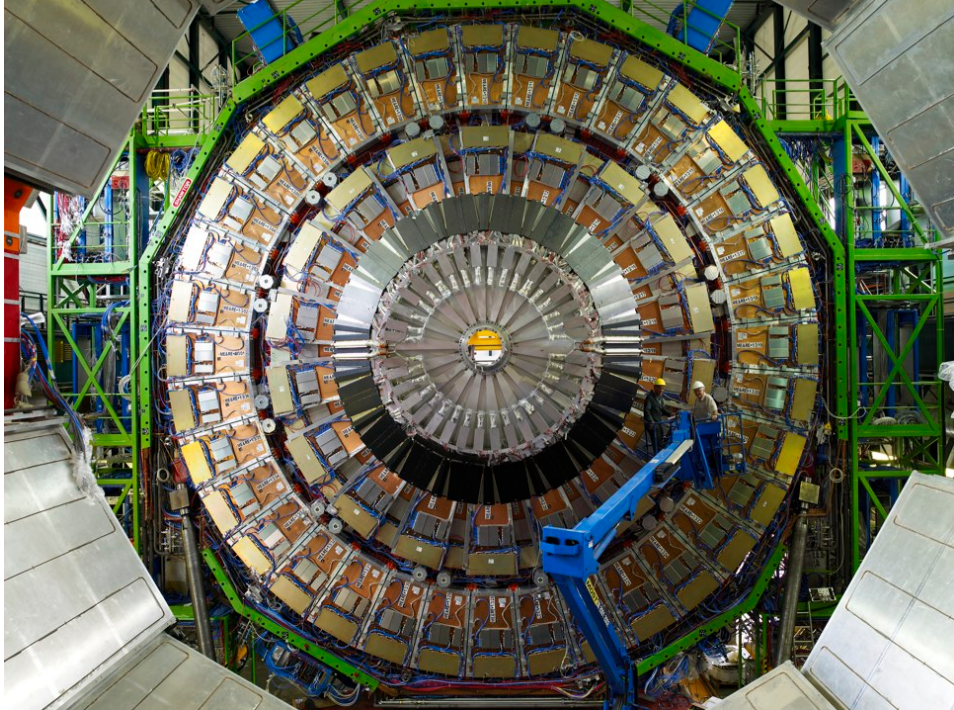


Figure 5.35: A photograph of one of the endcaps wheels.

bunch crossing when the LHC is operating at high luminosities. The barrel and endcaps of the muon systems are equipped – in addition to the main their main tracking systems, DT chambers and CSCs, respectively – with RPCs, which provide an independent trigger with lower  $p_T$  thresholds up to  $|\eta| = 1.6$ . The resistive plates are double-gap chambers consisting of two 2-mm-thick resistive Bakelite plates separated by a 2-mm-thick gas gap. The gas mixture is 95.2% Freon, 4.5% isobutane, and 0.3% sulphur hexafluoride. The outer surface of the resistive plates is coated with a conductive graphite layer and operated at 9,600 V. Figure 5.36 shows an schematic layout of a resistive plate. The geometry of the RPCs follows closely that of the DT chambers and the CSCs, thus, there are organized in 4 and 3 stations in the barrel and each of the endcaps, respectively. In the barrel, there are two RPCs at each side of the DT chambers in the first two stations while only one in the front of the DT chamber in stations 3 and 4. In the endcaps each station is divided into 3 rings at different radial distances. The RPCs are divided into 2 or 3 partitions in  $\eta$ . Figure 5.31 shows the locations of the RPCs in the muon system, labeled with blue color.

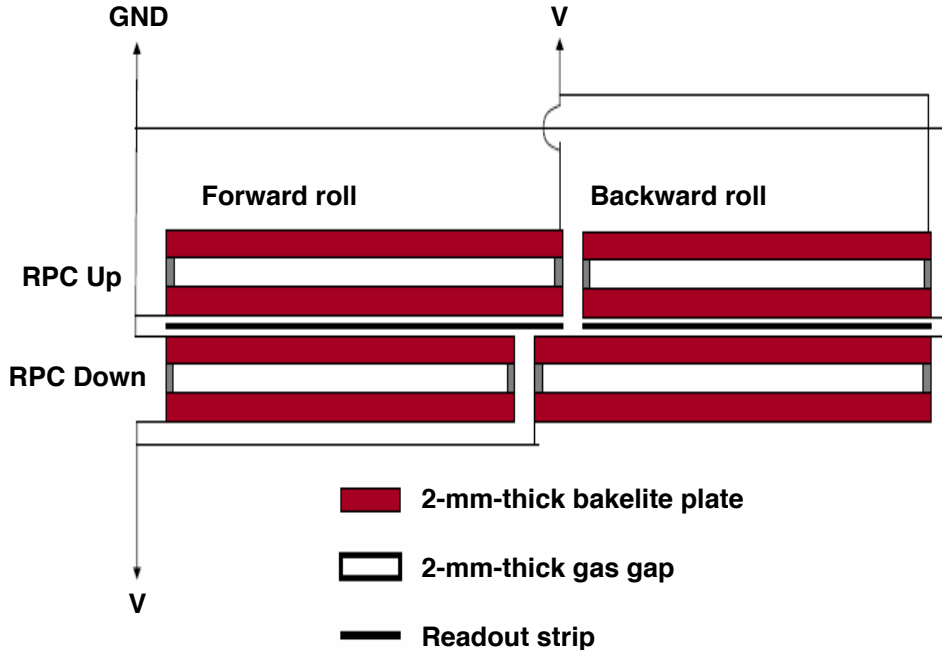


Figure 5.36: An schematic of one of the resistive plates in the CMS muon system.

## 5.6 The Trigger System

Due to the large rate of proton-proton collisions, the large amount of data needed to be recorded in order to reconstruct an event, and the constraints posed by the DAQ and computing systems, a selection mechanism that significantly reduces the rate of events needed to be deployed. This task is carried out by the CMS trigger system, thus starting the event selection process. The CMS trigger is a two stage system, composed of two sequential but independent trigger systems. The first is the Level-1 (L1) trigger, which is largely based in FPGAs and ASICs, and therefore uses coarse and crude information to reduce the rate from 40 MHz to 100 kHz. The second is the High-Level Trigger (HLT), which is a software based system, implemented in computing farm with approximately 16,000 CPU cores, that reduces the L1 trigger rate to a viable level for storage of about 1 kHz.

The L1 trigger has different components. First, the Local Triggers, also called Trigger Primitive Generators (TPG), are based in the calorimeter trigger towers, track segments, and hit patterns in the muon chambers. Second, the Regional Triggers combine the information from the TPGs to rank and sort trigger objects such as electron or muon candidates in limited spatial regions. Ranking is assigned based on the energy/momentum and quality of the parameters measured by the L1 trigger system. Third, The Global Calorimeter and Global Muon Triggers determin

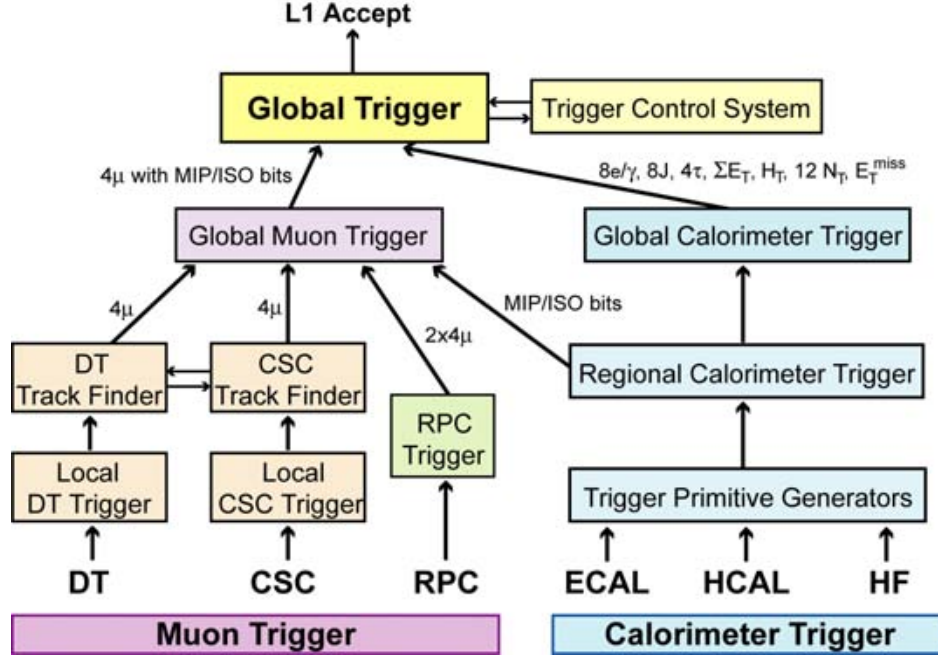


Figure 5.37: Architecture and hierarchy of the CMS L1 Trigger.

the highest-ranked calorimeter and muon object in the entire CMS detector and they transfer this information to the last step in the L1 hierarchy, the Global Trigger. The latter decides whether to reject or accept to event to be further analyze at the HLT. This decision is based on various algorithms and the readiness of the subdetectors and the DAQ system, which is in turn determined by the Trigger Control System (TCS). The latency of the L1 trigger is about  $4 \mu\text{s}$ . An schematic of the architecture and hierarchy of the L1 Trigger is presented in Figure 5.37.

The High-Level Trigger is software based and constructed in a modular fashion. The time of the HLT decision is fundamentally constraint by the computing power of the HLT farm and the L1 output rate, this requires the HLT decisions to be made in about 300 ms; surpassing this limit will result in the inability to effeciently collect data. The HLT modular design is such that allows logically independent trigger paths, which to a large extent could be run in parallel – thus better using the computing resources. Each trigger path is sequence of software modules and classified based on their function, there are reconstruction modules (producers) and filtering modules (filters). The latters usually accept or reject events based on the properties of physics object or kinematic variables, such as the new physics sensitive  $M_R$  and  $R^2$ , described in Section 6.2. The HLT modules are organized in ascending complexity, such that the faster algorithms are executed first and thus the filters could

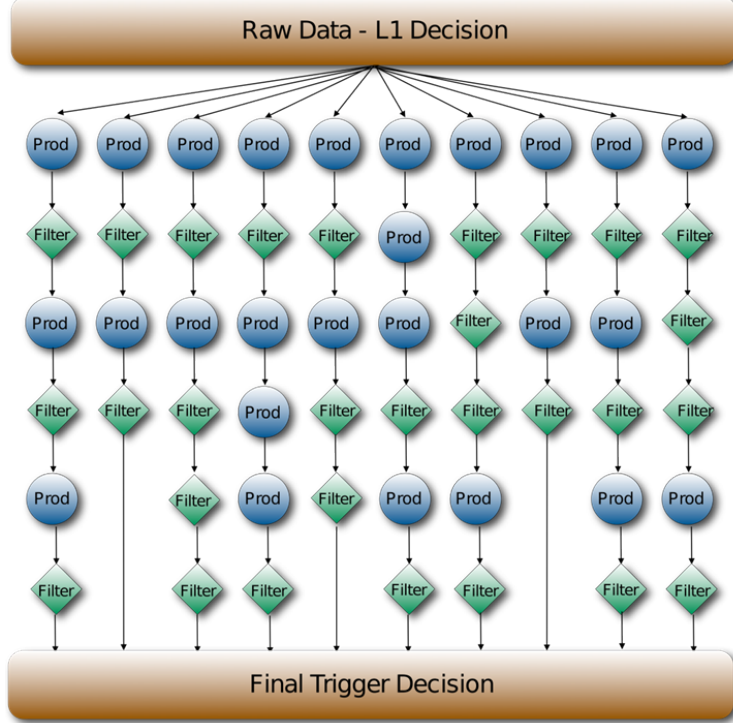


Figure 5.38: An schematic representation of the HLT. The modular desing can seen tracing the vertical arrows while the independent paths are seen from left to right. The HLT final decision is the logical OR of all the existing paths.

reject events at an earlier stage. The online HLT reconstruction is kept as similar as possible to that of the offline reconstruction, taking into account the computation and time constraints. An schematic diagram of the HLT is provided in Figure 5.38.

At the LHC the data processing is limited by the bandwidth at which the events are stored on disk, usually resulting in an increment on the trigger thresholds (physics objects  $p_T$ , missing transverse energy, etc.). In order to overcome this limitation, the CMS experiment has implemented special trigger paths were the event datasize is kept small, and thus more events – in other words triggers paths with lowers thresholds – can be recorded without stressing the allocated bandwidth. The latter solution has been adopted for the alignment and calibration of the detector and to increase the acceptance to certain event topologies interesting to probe new physics. The left and right panels of Figure 5.39 show a summary of the data streams recorded by the CMS experiment during 2012 and 2015, respectively.

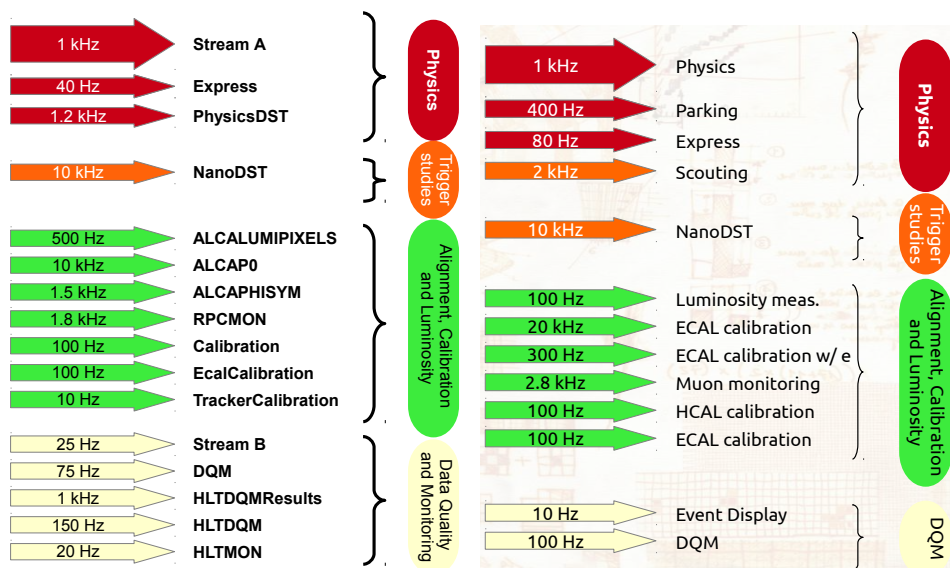


Figure 5.39: A summary of the data streams recorded during (left) 2012 and (right) 2015.

## **Part III**

# **Searches for New Physics with the Compact Muon Solenoid Experiment**

## Chapter 6

# RAZOR APPROACH TO SEARCH FOR BSM PHYSICS

### 6.1 Introduction

The challenges at hadron collider experiments are many, one of the most well known is the fact the the energy and momentum of the parton-parton (hard) interaction is not known. This limitation, in addition with the fact that a large number of the proposed extensions of the SM (e.g. SUSY) predict new particles that are weakly interacting and therefore escape the detector systems without a trace, have made events with large momentum imbalance in the plane transverse to the beam a key signature to search for BSM physics. The momentum imbalance is the transverse plane (missing energy) is quantified by  $\vec{p}_T^{\text{miss}}$  which is defined as

$$\vec{p}_T^{\text{miss}} = - \sum_{i=0}^{n_{pf}} \vec{p}_T^i, \quad (6.1)$$

where  $\vec{p}_T^i$  is the measured transverse momentum of a PF candidate, and  $n_{pf}$  is the total number of PF candidates reconstructed.

Additionally, in SUSY models with R-parity conservation the originally pair produced super-partners undergo a cascade decay and at least two particles (the LSPs) will escape detection and therefore further reduce the ability to fully reconstruct the event kinematics due to the lost information. Subsequently, all these effects result in loss of sensitivity as the discrimination power between a possible signal and the SM background processes is reduced. In order to recover sensitivity, different kinematic variables are employed which are functions of the visible objects momenta and the  $\vec{p}_T^{\text{miss}}$ . These kinematic variables have been shown to improve signal to background discrimination but are often model dependent. One example of such variables are the razor variables [196, 85], which have been widely used by the CMS collaboration to search for SUSY [93, 205] and recently shown to have good sensitivity for DM direct production at hadron colliders [124]. The razor variables:  $M_R$  and  $R^2$  provide an estimate of the underlying mass scale of the event and a handle to significantly suppress SM backgrounds – particularly QCD multijet –, respectively.

Since the two searches for BSM physics presented in this thesis are based on the razor variables, this Chapter describes its derivation (see Section 6.2) and their main features when searching for new physics (see Section 6.3).

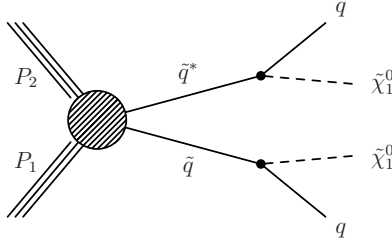


Figure 6.1: Feynman diagram for squark pair-production.

## 6.2 The Razor Variables

The razor variables were originally derived [196, 85] for squark pair-production in the context of SUSY; this topology is represented by the Feynman diagram shown in Figure 6.1, where the proton-proton collision pair produces two squarks ( $\tilde{q}_1 \tilde{q}_2$ ) which subsequently decay into a SM quark and the LSP ( $\tilde{q}_i \rightarrow q_i \tilde{\chi}_1^0$ ).

One interesting quantity that provides access to the mass scale of the SUSY particles is the magnitude of the 3-momentum of the quark in the rest frame of the squark, it is actually more convenient to write down twice this quantity:

$$2|\vec{p}^{q_i}| = 2|\vec{p}^{\tilde{\chi}_1^0}| = \frac{\sqrt{m_{\tilde{q}}^4 - 2m_{\tilde{q}}^2 m_{\tilde{\chi}_1^0}^2 + m_{\tilde{\chi}_1^0}^4 - 2m_{\tilde{q}}^2 m_{\tilde{\chi}_1^0}^2 - 2m_{\tilde{q}}^2 m_{\tilde{q}}^2 + m_q^4}}{m_{\tilde{q}}}, \quad (6.2)$$

where  $m_{\tilde{q}}$  is the squark mass,  $m_{\tilde{\chi}_1^0}$  is the LSP mass, and  $m_q$  is the SM quark mass. Eq. 6.2 can be simplified if the SM quarks are assumed massless – which is mostly accurate with the exception of the top-quark. This simplification is also useful to define:

$$M_\Delta = 2|\vec{p}^{q_i}| = \frac{m_{\tilde{q}}^2 - m_{\tilde{\chi}_1^0}^2}{m_{\tilde{q}}}. \quad (6.3)$$

$M_\Delta$  is sensitive to the mass-splitting between the squark and the LSP and therefore is usually refer to as the characteristic mass scale of the event. For example, in the case of the  $W \rightarrow \ell\nu$  decay,  $M_\Delta$  is simply the mass of the W boson.

The razor variable  $M_R$  provides an estimate of  $M_\Delta$  by approximating the boosts needed – since the actual boosts are impossible to reconstruct due to the missing particles, which can be viewed as an undetermined system of equations with not enough constraints – to go from the laboratory frame (lab frame) to the squark rest frame. This approximation is done in two steps, first , there is a common boost to go from the lab frame to the center-of-momentum (CM) frame, and then, an equal and oposite boost applied to each squark to go from the CM frame to their respective

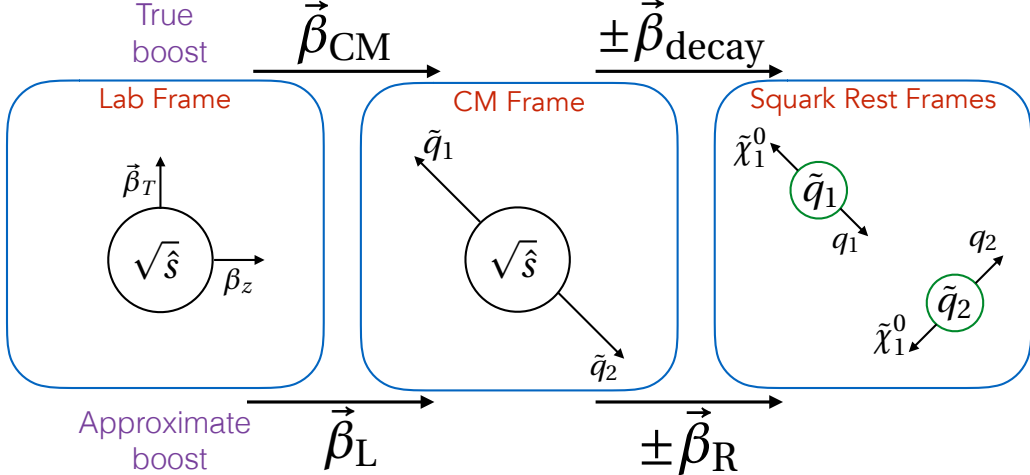


Figure 6.2: An schematic of the different rest frames involved in deriving the razor variables. The lab frame is in the left panel, the CM frame is in the middle panel, and the squark rest frames are in the right panel.

rest frame. Figure 6.2 depicts the three frames and the boosts needed to move from the lab frame to the squark rest frames.

The approximate boost relating the CM frame and the rest frames of each of the squarks ( $\vec{\beta}_R$ ) is assymetric since the two squarks are recoiling against each other in the CM frame.  $\vec{\beta}_R$  is obtained by adding the condition that in their respective squark rest frame the magnitud of each quark momentum is the same, this is to say that the two decays are identical up to the decay angle. Since the quarks are assumed to be massless the condition is:

$$E_s^{q_1} = E_s^{q_2} \quad (6.4)$$

$$\Rightarrow \gamma_R(E_{CM}^{q_1} - \vec{\beta}_R \cdot \vec{p}_{CM}^{q_1}) = \gamma_R(E_{CM}^{q_2} + \vec{\beta}_R \cdot \vec{p}_{CM}^{q_2}) \quad (6.5)$$

$$\Rightarrow \vec{\beta}_R \cdot (\vec{p}_{CM}^{q_1} + \vec{p}_{CM}^{q_2}) = E_{CM}^{q_1} - E_{CM}^{q_2}, \quad (6.6)$$

where  $E_s^{q_i}$  is the energy of the  $i$ -th quark on its respective squark rest frame,  $E_{CM}^{q_i}$  is the energy of the  $i$ -th quark in the CM frame,  $\vec{p}_{CM}^{q_i}$  is the momentum of the  $i$ -th quark in the CM frame, and  $\gamma_R$  is the gamma factor corresponding to  $\vec{\beta}_R$ . This symmetry constraint is not enough to uniquely determine  $\vec{\beta}_R$  and therefore an external condition is required; this external condition is such that the boost minimizes the sum of the quarks enegies, i.e.

$$\frac{\partial(E_s^{q_1} + E_s^{q_2})}{\partial \vec{\beta}_R} = 0. \quad (6.7)$$

With the addition of this extremal condition, the boost is now found to be

$$\vec{\beta}_R = \frac{\vec{p}_{CM}^{q_1} - \vec{p}_{CM}^{q_2}}{E_{CM}^{q_1} + E_{CM}^{q_2}}. \quad (6.8)$$

Now, let's turn to the boost that relates the CM and the lab frames. The later is approximated by a purely longitudinal boost ( $\vec{\beta}_L = \beta_L \cdot \hat{z}$ ). Again, the assumption that the boost is in the longitudinal direction only is not enough to uniquely determine  $\beta_L$  and therefore an additional constraint is needed. We require that the longitudinal momentum of the visible system in the CM frame ought to be zero – only resembling the true constraint: that the sum of the visible and invisible systems is indeed zero. This additional constraint,

$$p_{CM}^{1z} + p_{CM}^{2z} = 0, \quad (6.9)$$

is sufficient to find the magnitude of the boost :

$$\vec{\beta}_L = \frac{p_\ell^{1z} + p_\ell^{2z}}{E_\ell^{q_1} + E_\ell^{q_2}}. \quad (6.10)$$

With both boost now found, the only remaining task is to transform the quantities in the squark rest frame to the lab frame to be able to use them in a realistic environment. We define the characteristic mass estimator ( $M_R$ ), which is related to  $M_\Delta$ , in the following fashion:

$$M_R \equiv \gamma_R(E_s^{q_1} + E_s^{q_2}) = \gamma_R M_\Delta. \quad (6.11)$$

When expressed in the corresponding lab frame quantities by applying the boosts just found above,  $M_R$  takes the form:

$$M_R = \sqrt{(E_\ell^{q_1} + E_\ell^{q_2})^2 - (p_\ell^{1z} + p_\ell^{2z})^2}. \quad (6.12)$$

We now proceed to construct another variable purely from the transverse information in the detector. Inspired by the ideal back-to-back topology of QCD dijet events we define the razor transverse mass variable:

$$M_T^R = \sqrt{\frac{E_T^{\text{miss}}(p_T^{q_1} + p_T^{q_2}) - \vec{p}_T^{\text{miss}} \cdot (\vec{p}_T^{q_1} + \vec{p}_T^{q_2})}{2}}. \quad (6.13)$$

This variable estimates the transverse momentum imbalance in the event and therefore is useful to discriminate between signal and background. Additionally,  $M_T^R$  is strictly smaller than  $M_R$  ( $M_R < M_T^R$ ), with this in mind we define de dimensionless razor variable:

$$R^2 = \left( \frac{M_T^R}{M_R} \right)^2. \quad (6.14)$$

Background events with no missing energy will tend to have values of  $R^2$  close to zero, while signal events will have values of  $R^2$  that are on average larger than zero.

The razor variables have been also generalized to topologies which include more than two visible objects in the detector. In order to achieve this, a simple approach has been taken. Whenever more than two visible objects are present, the event is forced into a dijet-like topology by clustering all visible objects into two *megajets*. All possible permutations of these *megajets* are formed by adding the 4-momenta of the visible objects; we choose the configuration that minimizes  $M_1^2 + M_2^2$ , where  $M_i$  is the mass of the  $i$ -th *megajet*.

### 6.3 Application of the Razor Variables to Search for BSM Physics

The razor variables have been employed in canonical searches for SUSY at the LHC [85, 205, 141] and have been shown to have good sensitivity in a variety of final states. In this section a review of the main properties of this variables and a summary of the main results of the searches in references [85, 205, 141] is given.

Let's first examine if the expected behavior of the razor variables for the canonical squark pair production (see Figure 6.1) is indeed observed. Figure 6.3 shows the  $M_R$  and  $R^2$  for squark pair production in the left and right panel, respectively. The mass of the squark was fixed to 1150 GeV and the LSP mass was varied between 50-900 GeV. As expected,  $M_R$  peaks a characteristic value related to  $M_\Delta$ . For example,  $M_\Delta$  is approximately 930 GeV when the LSP mass is 500 GeV – this can be calculated by just plugging in the appropriate mass values into Equation 6.3 – and for this case  $M_R$  peaks at around  $\sim 1000$  GeV. Additionally,  $R^2$  exhibits a falling distribution that on average are much higher than the expected values for the SM processes – again, specially the daunting QCD dijet production. Finally, Figure 6.4 shows the 2-dimensional  $M_R$ - $R^2$  distribution for the same model, but adding contours of constant SM background. It is observed that the signals populates very clear regions on this 2-dimensional plane and that the SM background is reduced significantly (around 5

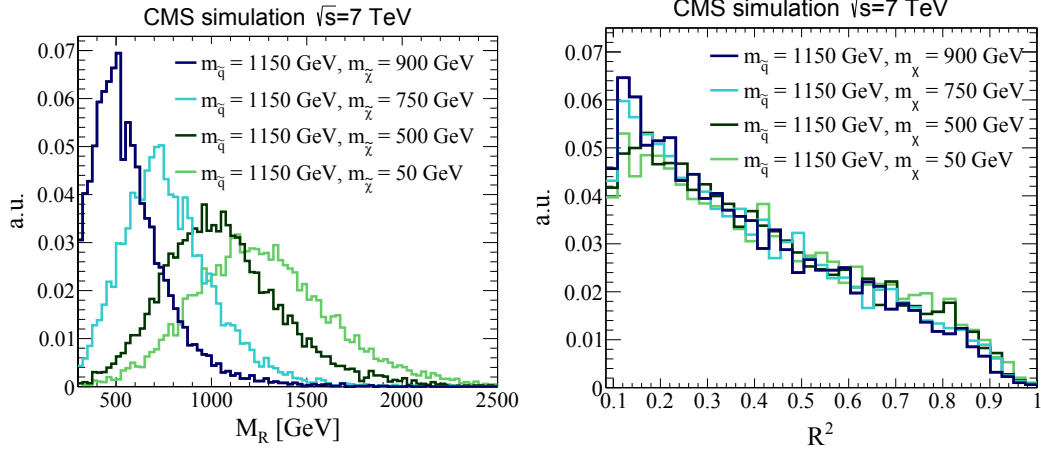


Figure 6.3: Razor variables distributions for squark pair-production.  $M_R$  is shown in the left panel and  $R^2$  is shown in the right panel. The squark mass is set to 1150 GeV while the LSP mass is varied and shown with different color lines.

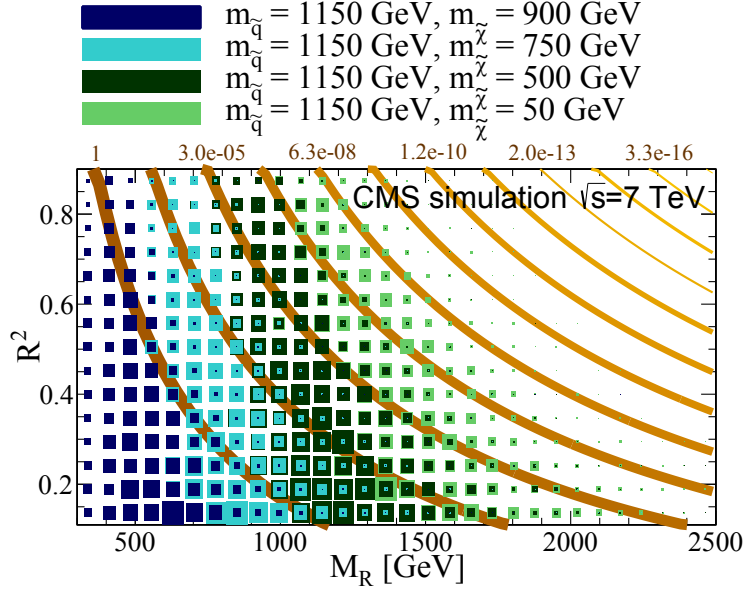


Figure 6.4: The 2-dimensional  $R^2$ - $M_R$  distribution. The squark mass is set to 1150 GeV while the LSP mass is varied and shown with different color squares. The orange band represents the contour of constant SM background.

orders of magnitude between the first and third contour) when more extreme values of the razor variables are required.

The first result using razor variables was carried out by CMS using data collected a center-of-mass energy of 7 TeV where an inclusive final state approach was adopted selecting jets, b-jets, and also leptons in the final state. There was no deviation from the SM background estimation and 95% confidence level (CL) limits on the CMSSM

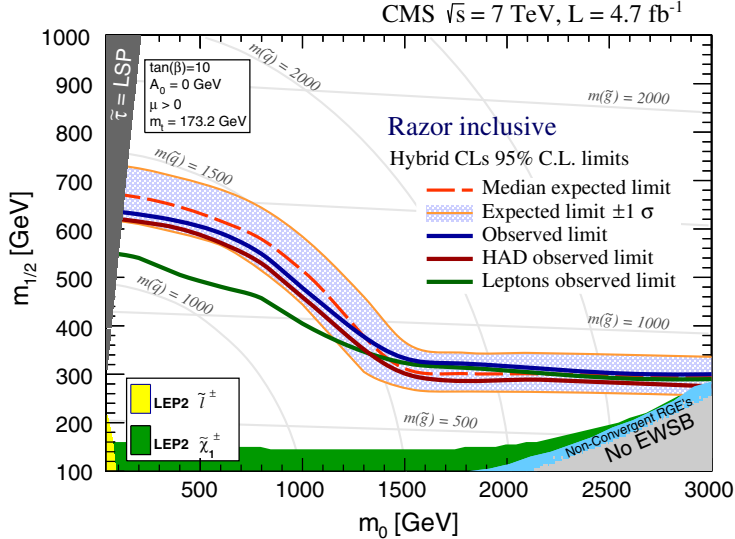


Figure 6.5: Razor analysis 95% CL. limit in the  $m_0$ - $m_{1/2}$  plane of the CMSSM model using 7 TeV data. The model parameters have the following values:  $\tan(\beta) = 10$ ,  $A_0 = 0$ , and  $\text{sgn}(\mu) = +1$ .

model were placed. Figure 6.5 shows the combine limit. CMS released another search for SUSY with razor variables using the full dataset ( $\sim 20 \text{ fb}^{-1}$ ) collected at 8 TeV, again, with no observed significant deviations from the SM background estimation. It is of note that the background estimation, which employs a fit to the sidebands of the data using an analytical functional form, was much improved with respect to the 7 TeV counterpart. The results were interpreted in the context of SUSY simplified models of gluino and top-squark (stop) pair production where the branching ratios (BRs) of the particles involved were varied in order to produce a more general result. Figure 6.6 shows the 95% CL. limits for gluino and stop pair-production in the left and right panels, respectively. It is observed that the gluino is excluded around 1200-1400 GeV depending on the exact values of the BRs, and the stop is excluded at about 700 GeV regardless of its BRs. Recently, an updated search using the first portion of 13 TeV data ( $\sim 2.1 \text{ fb}^{-1}$ ) was realeased following greatly the approach taken in the 8 TeV counterpart but adding an additional and totally independent background estimation based on scale factors derived in data control regions. Figure 6.7 show the 95% CL. limits for gluino pair-production. It is observed that the gluino is excluded around 1400-1600 GeV depending on the exact values of the BRs. It is of note that with only 10% of the integrated luminosity the 13 TeV result surpasses the corresponding 8 TeV result.

The razor approach has been taken beyond squark and gluino pair-production to

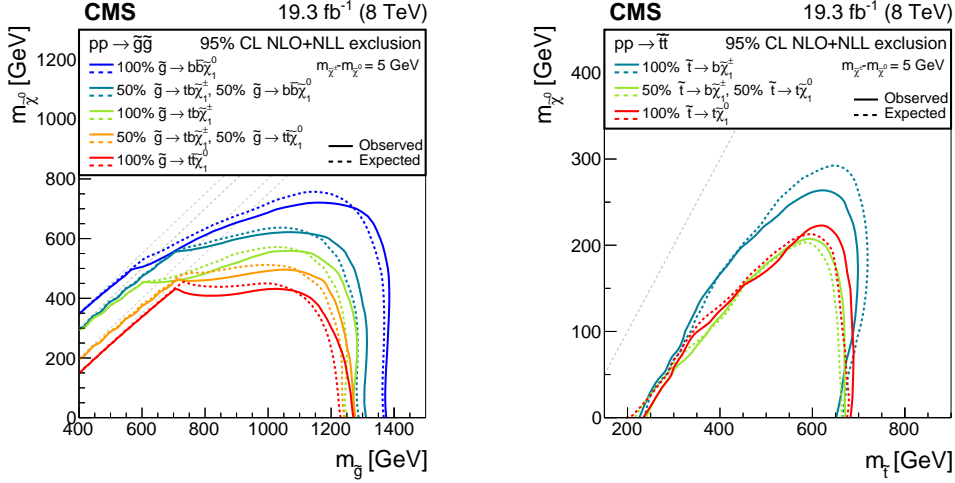


Figure 6.6: Razor analysis 95% CL. limits for (left) gluino and (right) stop pair-production using 8 TeV data. The limits are shown for different branching ratios of the particles involved.

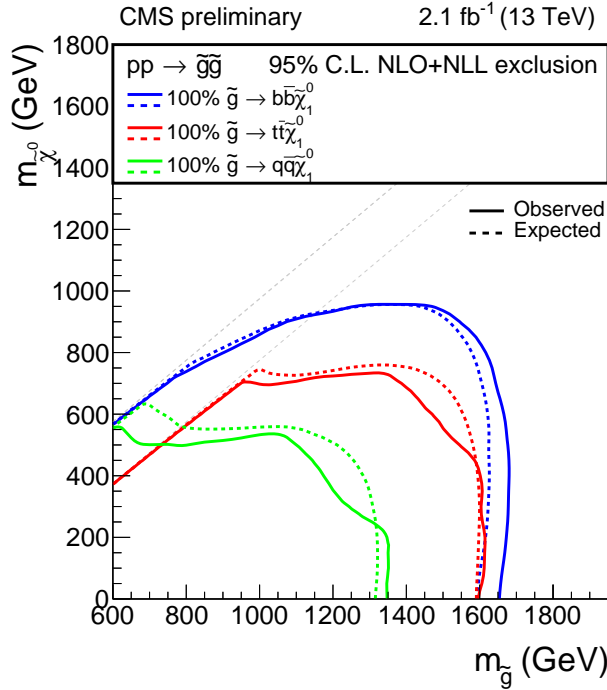


Figure 6.7: Razor analysis 95% CL. limits for gluino pair-production using 13 TeV data. The limits are shown for different branching ratios of the particles involved.

probe dark matter direct production and also to look for possible anomalous production of Higgs bosons. Searches for dark matter direct production have been a very hot topic at the LHC where the most common final state includes a single high- $p_T$  jet. It was suggested that the razor variables could have comparable sensitivity to dark matter direct production [124] using a different kinematic phase-space, since they require at least two jets, and therefore increase the overall sensitivity to such a signal. Chapter 7 presents the CMS search that carries out this idea, confirming the good sensitivity to direct dark matter production. Additionally, the razor variables have been also used to search for anomalous Higgs production by selecting events with jets and a diphoton pair whose invariant mass is consistent with the Higgs mass. The first search of this kind was carried out using the entire 8 TeV dataset [207] where an interesting excess of events was observed at high values of  $M_R$  and the results interpreted in the context of electroweak SUSY (see Section 8.2). Chapter 8 presents an updated result of this search with an entirely different background estimation technique and using  $15.3 \text{ fb}^{-1}$  of 13 TeV data.

## Chapter 7

# SEARCHES FOR DARK MATTER AT THE LHC WITH 8 TEV PP COLLISIONS

### 7.1 Introduction

The existence of dark matter (DM) in the universe, originally proposed [227] to reconcile observations of the Coma galaxy cluster with the prediction from the virial theorem, is commonly accepted as the explanation of many experimental phenomena in astrophysics and cosmology, such as galaxy rotation curves [140, 202], large structure formation [223, 72, 217], and the observed spectrum [214, 58, 215, 26] of the cosmic microwave background [53]. A global fit to cosmological data in the  $\Lambda$ CDM model (also known as the standard model of cosmology) [75] suggests that approximately 85% of the mass of the universe is attributable to DM [26]. To accommodate these observations and the dynamics of colliding galaxy clusters [95], it has been hypothesized that DM is made mostly of weakly interacting massive particles (WIMPs), sufficiently massive to be in nonrelativistic motion following their decoupling from the hot particle plasma in the early stages of the expansion of the universe.

While the standard model (SM) of particle physics does not include a viable DM candidate, several models of physics beyond the SM, e.g., supersymmetry (SUSY) [191, 129, 218, 222, 118] with  $R$ -parity conservation, can accommodate the existence of WIMPs. In these models, pairs of DM particles can be produced in proton-proton (pp) collisions at the CERN LHC. Dark matter particles would not leave a detectable signal in a particle detector. When produced in association with high-energy quarks or gluons, they could provide event topologies with jets and a transverse momentum ( $p_T$ ) imbalance ( $\vec{p}_T^{\text{miss}}$ ). The magnitude of  $\vec{p}_T^{\text{miss}}$  is referred to as missing transverse energy ( $E_T^{\text{miss}}$ ). The ATLAS and CMS collaborations have reported searches for events with one high- $p_T$  jet and large  $E_T^{\text{miss}}$  [24, 90], which are sensitive to such topologies. In this paper, we refer to these studies as monojet searches. Complementary studies of events with high- $p_T$  photons [159, 23];  $W$ ,  $Z$ , or Higgs bosons [18, 19, 21, 20];  $b$  jets [7] and top quarks [7, 148, 209]; and leptons [22, 160] have also been performed.

This paper describes a search for dark matter particles  $\chi$  in events with at least

two jets of comparable transverse momenta and sizable  $E_T^{\text{miss}}$ . The search is based on the razor variables  $M_R$  and  $R^2$  [196, 85]. Given a dijet event, these variables are computed from the two jet momenta  $\vec{p}^{j_1}$  and  $\vec{p}^{j_2}$ , according to the following definition:

$$\begin{aligned} M_R &= \sqrt{(|\vec{p}^{j_1}| + |\vec{p}^{j_2}|)^2 - (p_z^{j_1} + p_z^{j_2})^2}, \\ R &= \frac{M_T^R}{M_R}, \end{aligned} \quad (7.1)$$

with

$$M_T^R = \sqrt{\frac{E_T^{\text{miss}}(p_T^{j_1} + p_T^{j_2}) - \vec{p}_T^{\text{miss}} \cdot (\vec{p}_T^{j_1} + \vec{p}_T^{j_2})}{2}}. \quad (7.2)$$

In the context of SUSY,  $M_R$  provides an estimate of the underlying mass scale of the event, and quantity  $M_T^R$  is a transverse observable that includes information about the topology of the event. The variable  $R^2$  is designed to reduce QCD multijet background; it is correlated with the angle between the two jets, where co-linear jets have large  $R^2$  while back-to-back jets have small  $R^2$ . These variables have been used to study the production of non-interacting particles in cascade decays of heavier partners, such as squarks and gluinos in SUSY models with  $R$ -parity conservation [93, 205]. The sensitivity of these variables to direct DM production was suggested in Ref. [124], where it was pointed out that the dijet event topology provides good discrimination against background processes, with a looser event selection than that applied in the monojet searches. Sensitivity to DM production is most enhanced for large values of  $R^2$ , while categorizing events based on the value of  $M_R$  improves signal to background discrimination and yields significantly improved search sensitivity to a broader and more inclusive class of DM models. The resulting sensitivity is expected to be comparable to that of monojet searches [124, 184]. This strategy also offers the possibility to search for DM particles that couple preferentially to b quarks [30], as proposed to accommodate the observed excess of photons with energies between 1 and 4 GeV in the gamma ray spectrum of the galactic center data collected by the Fermi-LAT gamma-ray space telescope [138]. The results are interpreted using an effective field theory approach and the Feynman diagrams for DM pair production are shown in Fig. 7.1.

Unlike the SUSY razor searches [205, 85], which focus on events with large values of  $M_R$ , this study also considers events with small values of  $M_R$ , using  $R^2$  to

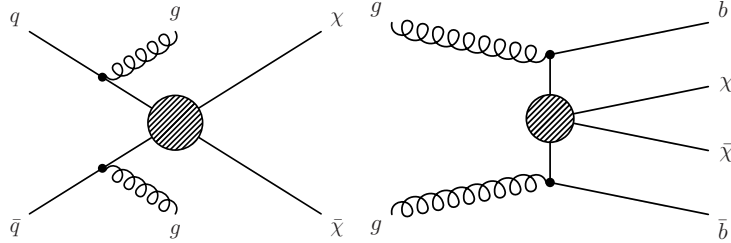


Figure 7.1: Feynman diagrams for the pair production of DM particles corresponding to an effective field theory using a vector or axial-vector operator (left), and a scalar operator (right).

discriminate between signal and background, in a kinematic region ( $R^2 > 0.5$ ) excluded by the baseline selection of Refs. [205, 85].

A data sample corresponding to an integrated luminosity of  $18.8 \text{ fb}^{-1}$  of pp collisions at a center-of-mass energy of 8 TeV was collected by the CMS experiment with a trigger based on a loose selection on  $M_R$  and  $R^2$ . This and other special triggers were operated in 2012 to record events at a rate higher than the CMS computing system could process during data taking. The events from these triggers were stored on tape and their reconstruction was delayed until 2013, to profit from the larger availability of processing resources during the LHC shutdown. These data, referred to as “parked data” [98], enabled the exploration of events with small  $M_R$  values, thereby enhancing the sensitivity to direct DM production.

This paper is organized as follows: the CMS detector is briefly described in Section ???. Section 7.2 describes the data and simulated samples of events used in the analysis. Sections 7.3 and 7.4 discuss the event selections and categorization, respectively. The estimation of the background is described in Section 8.5. The systematic uncertainties are discussed in Section 7.6, while Section 7.7 presents the results and the implications for several models of DM production. A summary is given in Section 7.8.

## 7.2 Data set and simulated samples

The analysis is performed on events with two jets reconstructed at L1 in the central part of the detector ( $|\eta| < 3.0$ ). The L1 jet triggers are based on the sums of transverse energy in regions  $\Delta\eta \times \Delta\phi$  approximately  $1.05 \times 1.05$  in size [83] (where  $\phi$  is the azimuthal angle in the plane transverse to the LHC beams.). At the HLT, energy deposits in ECAL and HCAL are clustered into jets and the razor variables  $R^2$  and  $M_R$  are computed. In the HLT, jets are defined using the FASTJET [69]

implementation of the anti- $k_{\mathrm{T}}$  [70] algorithm, with a distance parameter equal to 0.5. Events with at least two jets with  $p_{\mathrm{T}} > 64 \text{ GeV}$  are considered. Events are selected with  $R^2 > 0.09$  and  $R^2 \times M_{\mathrm{R}} > 45 \text{ GeV}$ . This selection rejects the majority of the background, which tends to have low  $R^2$  and low  $M_{\mathrm{R}}$  values, while keeping the events in the signal-sensitive regions of the  $(M_{\mathrm{R}}, R^2)$  plane. The trigger efficiency, measured using a pre-scaled trigger with very loose thresholds, is shown in Table 7.1. The requirements described above correspond to the least stringent event selection, given the constraints on the maximum acceptable rate.

Table 7.1: Measured trigger efficiency for different  $M_{\mathrm{R}}$  regions. The selection  $R^2 > 0.35$  is applied. The uncertainty shown represents the statistical uncertainty in the measured efficiency.

$M_{\mathrm{R}}$ region (GeV)	200–300	300–400	400–3500
Trigger efficiency (%)	$91.1 \pm 1.5$	$90.7 \pm 2.3$	$94.4 \pm 2.4$

Monte Carlo (MC) simulated signal and background samples are generated with the leading order matrix element generator `MADGRAPH v5.1.3` [38, 39] and the CTEQ6L parton distribution function set [189]. The generation includes the `PYTHIA 6.4.26` [211] Z2\* tune, which is derived from Z1 tune [119] based on the CTEQ5L set. Parton shower and hadronization effects are included by matching the generated events to `PYTHIA`, using the MLM matching algorithm [136]. The events are processed with a `GEANT4` [29] description of the CMS apparatus to include detector effects. The simulation samples for SM background processes are scaled to the integrated luminosity of the data sample ( $18.8 \text{ fb}^{-1}$ ), using calculations of the inclusive production cross sections at the next-to-next-to-leading order (NNLO) in the perturbative QCD expansion [127, 126, 109]. The signal processes corresponding to pair production of DM particles are simulated with up to two additional partons with  $p_{\mathrm{T}} > 80 \text{ GeV}$ .

### 7.3 Event selection

Events are selected with at least one reconstructed interaction vertex within  $|z| < 24 \text{ cm}$ . If more than one vertex is found, the one with the highest sum of the associated track momenta squared is used as the interaction point for event reconstruction. Events containing calorimeter noise, or large missing transverse momentum due to beam halo and instrumental effects (such as jets near non-functioning channels in the ECAL) are removed from the analysis [77].

A particle-flow (PF) algorithm [99, 96] is used to reconstruct and identify individual particles with an optimized combination of information from the various elements of the CMS detector. The energy of photons is directly obtained from the ECAL measurement, corrected for zero-suppression effects. The energy of electrons is determined from a combination of the electron momentum at the primary interaction vertex as measured by the tracker, the energy of the corresponding ECAL cluster, and the energy sum of all bremsstrahlung photons (or emissions) spatially compatible with originating from the electron track. The energy of muons is obtained from the curvature of the associated track. The energy of charged hadrons is determined from a combination of their momentum measured in the tracker and the matching ECAL and HCAL energy deposits, corrected for zero-suppression effects and for the response function of the calorimeters to hadronic showers. Finally, the energy of neutral hadrons is obtained from the corresponding corrected ECAL and HCAL energies. Contamination of the energy determinations from other pp collisions is mitigated by discarding the charged PF candidates incompatible with originating from the main vertex. Additional energy from neutral particles is subtracted on average when computing lepton (electron or muon) isolation and jet energy. This contribution is estimated as the per-event energy deposit per unit area, in the cone  $\Delta R = \sqrt{(\Delta\eta)^2 + (\Delta\phi)^2} = 0.3$ , times the considered jet size or isolation cone area.

Electrons (muons) are required to have  $p_T > 15\text{ GeV}$  and  $|\eta| < 2.5$  (2.4). In order to reduce the background from hadrons misidentified as leptons, additional requirements based on the quality of track reconstruction and isolation are applied. Lepton isolation is defined as the scalar  $p_T$  sum of all PF candidates other than the lepton itself, within a cone of size  $\Delta R = 0.3$ , and normalized to the lepton  $p_T$ . A candidate is identified as a lepton if the isolation variable is found to be smaller than 15%. For electrons [155], a characteristic of the shower shape of the energy deposit in the ECAL (the shower width in the  $\eta$  direction) is used to further reduce the contamination from hadrons. PF candidates with  $p_T > 10\text{ GeV}$  that are not consistent with muons and satisfy the same isolation requirements as those used for electrons are also identified to increase the lepton selection efficiency as well as to identify single-prong tau decays.

Jets are formed by clustering the PF candidates, using the anti- $k_T$  algorithm with distance parameter 0.5. Jet momentum is determined as the vectorial sum of all particle momenta in the jet, and is found from simulation to be within 5% to 10% of the generated hadron level jet momentum over the whole  $p_T$  spectrum and

detector acceptance. Jet energy corrections are derived from simulation, and are confirmed with in situ measurements of the energy balance in dijet and photon+jet events. Additional selection criteria are applied to each event to remove spurious jet-like features originating from isolated noise patterns in certain HCAL regions. We select events containing at least two jets with  $p_T > 80 \text{ GeV}$  and  $|\eta| < 2.4$ , for which the corresponding L1 and HLT requirements are maximally efficient. The combined secondary vertex (CSV) b-tagging algorithm [185, 84] is used to identify jets originating from b quarks. The loose and tight working points of the CSV algorithm, with 85% (10%) and 50% (0.1%) identification efficiency (misidentification probability) respectively, are used to assign the selected events to categories based on the number of b-tagged jets, as described below.

In order to compute the razor variables inclusively, the event is forced into a two-jet topology, by forming two *megajets* [93] out of all the reconstructed jets with  $p_T > 40 \text{ GeV}$  and  $|\eta| < 2.4$ . All possible assignments of jets to the megajets are considered, with the requirement that a megajet consist of at least one jet. The sum of the four-momenta of the jets assigned to a megajet defines the megajet four-momentum. When more than two jets are reconstructed, more than one megajet assignment is possible. We select the assignment that minimizes the sum of the invariant masses of the two megajets. In order to reduce the contamination from multijet production, events are rejected if the angle between the two selected megajets in the transverse plane  $|\Delta\phi(j_1, j_2)|$  is larger than 2.5 radians. The momenta of the two megajets are used to compute the razor variables, according to Eq. (7.1, 7.2). Events are required to have  $M_R > 200 \text{ GeV}$  and  $R^2 > 0.5$ .

## 7.4 Analysis Strategy

To enhance the DM signal and suppress background contributions from the  $W+\text{jets}$  and  $t\bar{t}$  processes, we veto events with selected electrons, muons, or isolated charged PF candidates. We define three different search regions based on the number of b-tagged jets. The zero b-tag search region contains events where no jets were identified with the CSV loose b-tagging criterion; the one b-tag search region contains events where exactly one jet passed the CSV tight criterion; and the two b-tag search region contains events where two or more jets passed the CSV tight criterion. Events in the zero b-tag search region are further classified into four categories based on the value of  $M_R$ , to enhance signal to background discrimination for a broad class of DM models: (i) *very low*  $M_R$  (VL), defined by  $200 < M_R \leq 300 \text{ GeV}$ ; (ii) *low*  $M_R$  (L), with  $300 < M_R \leq 400 \text{ GeV}$ ; (iii) *high*  $M_R$  (H), with  $400 <$

Table 7.2: Observed yield in each in events with  $0\mu$  and no b-tagged jets for each  $M_R$  category. The number overlapping events between the razor and monojet searches is also presented.

$M_R$ category	Observed	Monojet & Razor
VL	11623	0
L	3785	3
H	1559	57
VH	261	92

$M_R \leq 600$  GeV; and (iv) *very high*  $M_R$  (VH), including events with  $M_R > 600$  GeV. Because of the limited size of the data sample, no further categorization based on  $M_R$  is made for the one and two b-tag search regions. Within each category, the search is performed in bins of the  $R^2$  variable, with the binning chosen such that the expected background yield in each bin is larger than one event, as estimated from Monte Carlo simulation. In the H and VH categories, 3% and 35% respectively of the selected events were also selected in the monojet search [91], which used data from the same running period. The overlap in the L and VL categories is negligible, while the overlapping events in the H and VH categories were shown not to have an impact on the final sensitivity. Consequently, the results from this analysis and from the monojet analysis are largely statistically independent. Table 7.2 shows the events selected by this analysis and the overlapping events with the monojet search.

The main backgrounds in the zero b-tag search region are from the  $W(\ell\nu)$ +jets and  $Z(\nu\bar{\nu})$ +jets processes, while the dominant background in the one and two b-tag search regions is the  $t\bar{t}$  process. To estimate the contribution of these backgrounds in the search regions, we use a data-driven method that extrapolates from appropriately selected control regions to the search region, assisted by Monte Carlo simulation. A detailed description of the background estimation method is discussed in Section 8.5.

To estimate the  $W(\ell\nu)$ +jets and  $Z(\nu\bar{\nu})$ +jets background in the zero b-tag search region, we define the  $1\mu$  control region by selecting events using identical requirements to those used in the search region, with the exception of additionally requiring one selected muon. Events in this control region are extrapolated to the search region in order to estimate the background. In addition, we define the  $2\mu$  control region, enhanced in the  $Z$ +jets process, by requiring two selected muons with invariant mass between 80 GeV and 100 GeV. The  $2\mu$  control region is used to perform a cross-check prediction for the  $1\mu$  control region, and the systematic uncertainties in

Table 7.3: Analysis regions for events with zero identified b-tagged jets. The definition of these regions is based on the muon multiplicity, the output of the CSV b-tagging algorithm, and the value of  $M_R$ . For all the regions,  $R^2 > 0.5$  is required.

analysis region	purpose	b-tagging selection	$M_R$ category
$0\mu$	signal search region		$200 < M_R \leq 300$ GeV (VL)
$1\mu$	$W(\ell\nu)$ control region	no CSV loose jet	$300 < M_R \leq 400$ GeV (L) $400 < M_R \leq 600$ GeV (H)
$2\mu$	$Z(\ell\ell)$ control region		$M_R > 600$ GeV (VH)

Table 7.4: Analysis regions for events with identified b-tagged jets. The definition of these regions is based on the muon multiplicity, the output of the CSV b-tagging algorithm, and the value of  $M_R$ . For all the regions,  $R^2 > 0.5$  is required.

analysis region	purpose	b-tagging selection	$M_R$ category
$0\mu bb$		$\geq 2$ CSV tight jets	
$0\mu b$	signal serach region	$= 1$ CSV tight jet	
$1\mu b$	$t\bar{t}$ control region		
$2\mu b$	$t\bar{t}$ control region	$\geq 1$ CSV tight jets	$M_R > 200$ GeV
$Z(\mu\mu)b$	$Z(\ell\ell)$ control region	$\geq 1$ CSV loose jets	

background prediction are estimated based on this comparison.

To estimate the  $t\bar{t}$  background in the one and two b-tag search regions, we define the  $1\mu b$  and  $2\mu b$  control regions, by requiring at least one jet satisfying the CSV tight b-tagging criterion along with one and two selected muons respectively. Both of these control regions are dominated by the  $t\bar{t}$  process. The  $t\bar{t}$  background prediction is estimated by extrapolating from the  $2\mu b$  control region, while the  $1\mu b$  control region is used as a cross-check to estimate systematic uncertainties. Finally, we define the  $Z(\mu\mu)b$  control region by requiring two muons with invariant mass between 80 GeV and 100 GeV. This is used to estimate the  $Z(\nu\bar{\nu})+jets$  background in the one and two b-tag search regions.

The definitions of the search and control regions, and their use in this analysis are summarized in Tables 7.3 and 7.4.

## 7.5 Background estimation

The largest background contribution to the zero b-tag search region is from events in which a W or Z boson is produced, in association with jets, decaying to final states with one or more neutrinos. These background processes are referred to

as  $W(\ell\nu)$ +jets and  $Z(\nu\bar{\nu})$ +jets events. Additional backgrounds arise from events involving the production of top quark pairs, and from events in which a Z boson decays to a pair of charged leptons. These processes are referred to as  $t\bar{t}$  and  $Z(\ell\ell)$ +jets, respectively. Using simulated samples, the contribution from other SM processes, such as diboson and single top production, is found to be negligible.

The main background in the one and two b-tag search regions comes from  $t\bar{t}$  events. The use of the tight working point of the CSV algorithm reduces the  $Z(\nu\bar{\nu})$ +jets and  $W(\ell\nu)$ +jets contribution as shown in Table 7.8. Multijet production, which is the most abundant source of events with jets and unbalanced  $p_T$ , contributes to the search region primarily due to instrumental mismeasurement of the energy of jets. As a result the  $E_T^{\text{miss}}$  direction tends to be highly aligned in the azimuthal coordinate with the razor megajets. The requirement on the razor variables and  $|\Delta\phi(j_1, j_2)|$  reduces the multijet background to a negligible level, which is confirmed by checking data control regions with looser cuts on the razor variables. Figure 7.2 shows the 2-dimensional  $R^2 - |\Delta\phi(j_1, j_2)|$  distribution, where it is observed that for  $R^2 > 0.5$  and  $|\Delta\phi(j_1, j_2)| < 2.5$ , the multijet contribution is indeed negligible. Other relevant distributions for the multijet background are shown in Figure 7.3.

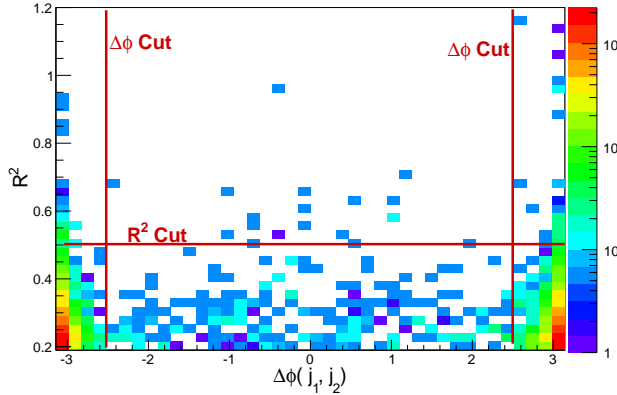


Figure 7.2:  $R^2 - \Delta\phi(J_1, J_2)$  distribution for the QCD background in the  $0\mu$  box.

### Background estimation for the zero b-tag search region

To predict the background from  $W(\ell\nu)$ +jets and  $Z(\nu\bar{\nu})$ +jets in the zero b-tag search region, we use a data-driven method that extrapolates the observed data yields in the  $1\mu$  control region to the search region. Similarly, the observed yield in the  $2\mu$  control region allows the estimation of the contribution from  $Z(\ell\ell)$ +jets background process. Each  $M_R$  category is binned in  $R^2$ .

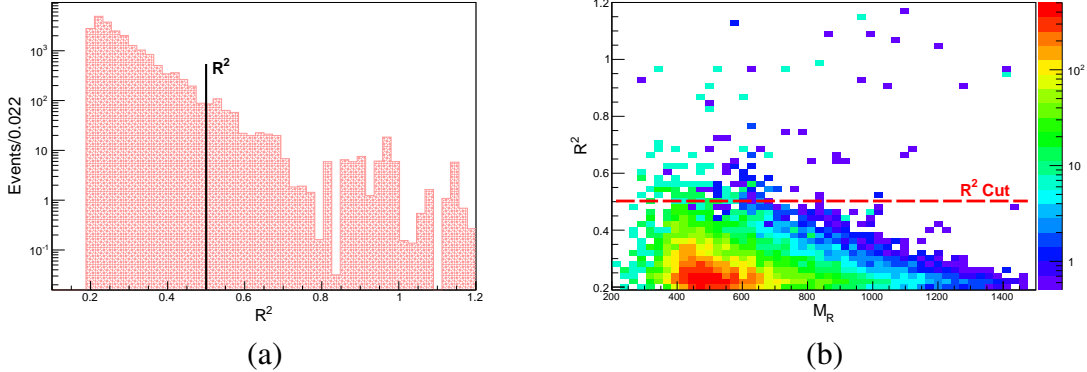


Figure 7.3: (a)  $R^2$  and (b)  $M_R$ - $R^2$  razor distributions for the QCD background in the  $0\mu$  box.

The background expected from  $W$  and  $Z$  boson production, in each  $R^2$  bin and in each  $M_R$  category of the  $0\mu$  sample, is computed as

$$n_i^{0\mu} = \left( n_i^{1\mu} - N_i^{\bar{t}\bar{t},1\mu} - N_i^{Z(\ell\ell)+\text{jets},1\mu} \right) \frac{N_i^{W(\ell\nu)+\text{jets},0\mu} + N_i^{Z(\nu\bar{\nu})+\text{jets},0\mu}}{N_i^{W(\ell\nu)+\text{jets},1\mu}} + \left( n_i^{2\mu} - N_i^{\bar{t}\bar{t},2\mu} \right) \frac{N_i^{Z(\ell\ell)+\text{jets},0\mu}}{N_i^{Z(\ell\ell)+\text{jets},2\mu}}, \quad (7.3)$$

where  $n_i^{k\mu}$  labels the data yield in bin  $i$  for the sample with  $k$  muons, and  $N_i^{X,k\mu}$  indicates the corresponding yield for process  $X$ , derived from simulations. This background estimation method relies on the assumption that the kinematic properties of events in which  $W$  and  $Z$  bosons are produced are similar.

To estimate the accuracy of the background estimation method, we perform a cross-check by predicting the background in the  $1\mu$  control region using the observed data yield in the  $2\mu$  control region. The Monte Carlo simulation is used to perform this extrapolation analogous to the calculation in Equation 7.3. The small contribution from the  $\bar{t}\bar{t}$  background process is also estimated using the simulated samples. In Tables 7.5 and 7.6, the observed yields in the  $1\mu$  and  $2\mu$  control regions respectively are compared to the estimate derived from data. In Tables 7.5-7.10, the contribution of each process as predicted directly by simulated samples are also given.

Figure 7.4 shows the comparison of the  $R^2$  distributions between the observed yield and the data-driven background estimate in the  $1\mu$  control region. The observed bin-by-bin difference is propagated as a systematic uncertainty in the data-driven background method, and accounts for the statistical uncertainty in the event yield in the  $2\mu$  control region data as well as potential differences in the modeling of the recoil spectra between  $W+\text{jets}$  and  $Z+\text{jets}$  processes. Some bins exhibit relatively large uncertainties primarily due to statistical fluctuations in the  $2\mu$  control region

Table 7.5: Comparison of the observed yield in the  $1\mu$  control region in each  $M_R$  category and the corresponding data-driven background estimate obtained by extrapolating from the  $2\mu$  control region. The uncertainty in the estimates takes into account both the statistical and systematic components. The contribution of each individual background process is also shown, as estimated from simulated samples, as well as the total MC predicted yield.

$M_R$ category	$Z(\nu\bar{\nu})$ +jets	$W(\ell\nu)$ +jets	$Z(\ell\ell)$ +jets	$t\bar{t}$	MC predicted	Estimated	Observed
VL	$0.7 \pm 0.3$	$4558 \pm 32$	$133 \pm 3$	$799 \pm 9$	$5491 \pm 33$	$5288 \pm 511$	5926
L	$0.5 \pm 0.3$	$1805 \pm 17$	$44 \pm 2$	$213 \pm 4$	$2063 \pm 18$	$1840 \pm 233$	2110
H	$0.1 \pm 0.1$	$915 \pm 11$	$16 \pm 1$	$66 \pm 2$	$997 \pm 11$	$629 \pm 240$	923
VH	<0.1	$183 \pm 5$	$2.6 \pm 0.2$	$8.5 \pm 0.8$	$194 \pm 5$	$166 \pm 93$	143

Table 7.6: Comparison of the observed yield for the  $2\mu$  control region in each  $M_R$  category and the corresponding prediction from background simulation. The quoted uncertainty in the prediction reflects only the size of the simulated sample. The contribution of each individual background process is also shown, as estimated from simulated samples.

$M_R$ category	$Z(\nu\bar{\nu})$ +jets	$W(\ell\nu)$ +jets	$Z(\ell\ell)$ +jets	$t\bar{t}$	MC predicted	Observed
VL	<0.1	<0.1	$214 \pm 4$	$1.9 \pm 0.3$	$215 \pm 4$	207
L	<0.1	$0.4 \pm 0.3$	$88 \pm 2$	$0.5 \pm 0.2$	$89 \pm 2$	78
H	<0.1	$0.1 \pm 0.1$	$48 \pm 1$	$0.1 \pm 0.1$	$48 \pm 1$	30
VH	<0.1	<0.1	$10 \pm 1$	$0.1 \pm 0.1$	$10 \pm 1$	7

from which the background is prediction estimated. Though the uncertainties are rather large in fractional terms, sensitivity to DM signal models is still obtained, because of the enhanced signal to background ratio for the bins at large values of  $M_R$  and  $R^2$ .

The  $t\bar{t}$  background is estimated using an analogous data-driven method, where we derive corrections to the Monte Carlo simulation prediction scaled to the  $t\bar{t}$  production cross-section computed to NNLO accuracy [127, 126, 109] using data in the  $2\mu b$  control region for each bin in  $R^2$ . The correction is then applied to the simulation prediction for the  $t\bar{t}$  background contribution to the zero b-tag search region. This correction factor reflects potential mismodeling of the recoil spectrum predicted by the Monte Carlo simulation. The contribution of each background process to the  $2\mu b$  sample, predicted from simulated samples, is given in Table 7.7. The fraction of  $t\bar{t}$  events in the  $2\mu b$  control sample is  $\approx 95\%$ . Figure 7.5 shows the comparison of the observed yield and the prediction from simulation, as a function of  $R^2$ . We observe no significant deviations between the observed data and the simulation prediction. The uncertainty derived from the data-to-simulation correction factor is propagated to the systematic uncertainty of the  $t\bar{t}$  prediction in

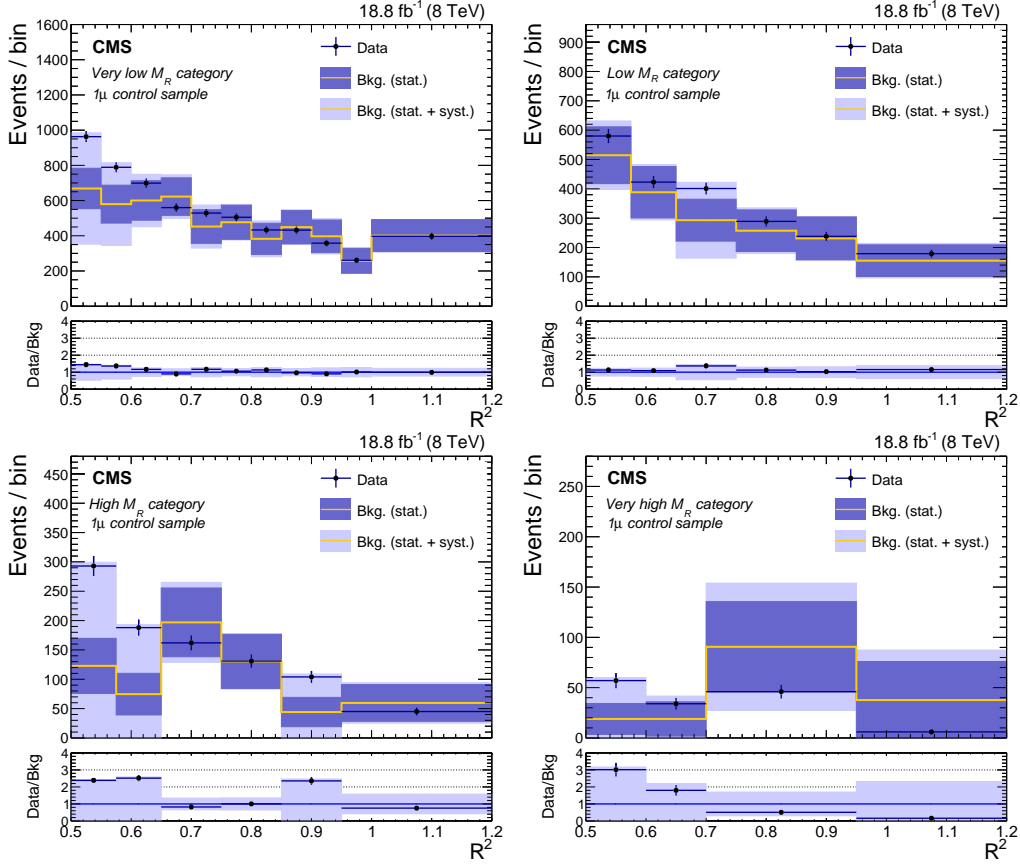


Figure 7.4: Comparison of observed yields in the  $1\mu$  control region and the data-driven background estimate derived from the  $2\mu$  control region data in the four  $M_R$  categories: VL (top left), L (top right), H (bottom left), and VH (bottom right). The bottom panel in each plot shows the ratio between the two distributions. The observed bin-by-bin deviation from unity is interpreted as an estimate of the systematic uncertainty associated to the background estimation methodology for the  $0\mu$  search region. The dark and light bands represent the statistical and the total uncertainties in the estimates, respectively. The horizontal bars indicate the variable bin widths.

Table 7.7: Observed yield and predicted background from simulated samples in the  $2\mu b$  control region. The quoted uncertainty in the prediction only reflects the size of the simulated sample. The contribution of each individual background process is also shown, as estimated from simulated samples.

Sample	$Z(\nu\bar{\nu})+\text{jets}$	$W(\ell\nu)+\text{jets}$	$Z(\ell\ell)+\text{jets}$	$t\bar{t}$	MC predicted	Observed
$2\mu b$	$<0.1$	$0.1 \pm 0.1$	$2.2 \pm 0.3$	$58 \pm 2$	$60 \pm 2$	60

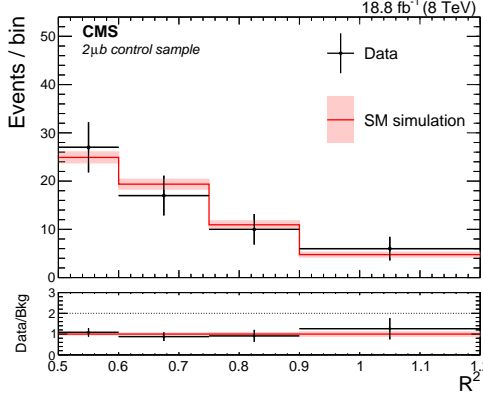


Figure 7.5: Comparison of the observed yield and the prediction from simulation as a function of  $R^2$  in the  $2\mu b$  control region. The uncertainties in the data and the simulated sample are represented by the vertical bars and the shaded bands, respectively. The horizontal bars indicate the variable bin widths.

Table 7.8: Comparison of the observed yields for the zero b-tag search region in each  $M_R$  category and the corresponding background estimates. The uncertainty in the background estimate takes into account both the statistical and systematic components. The contribution of each individual background process is also shown, as estimated from simulated samples, as well as the total MC predicted yield.

$M_R$ category	$Z(\nu\bar{\nu}) + \text{jets}$	$W(\ell\nu) + \text{jets}$	$Z(\ell\ell) + \text{jets}$	$t\bar{t}$	MC predicted	Estimated	Observed
VL	$6231 \pm 37$	$4820 \pm 33$	$49 \pm 2$	$555 \pm 7$	$11655 \pm 50$	$12770 \pm 900$	11623
L	$2416 \pm 19$	$1513 \pm 16$	$11 \pm 1$	$104 \pm 3$	$4044 \pm 25$	$4170 \pm 270$	3785
H	$1127 \pm 7$	$625 \pm 9$	$2.9 \pm 0.3$	$24 \pm 1$	$1779 \pm 12$	$1650 \pm 690$	1559
VH	$229 \pm 2$	$103 \pm 3$	$0.2 \pm 0.1$	$3.1 \pm 0.5$	$335 \pm 3$	$240 \pm 160$	261

the zero b-tag search region.

The result of the background estimation in the zero b-tag search region is given in Table 7.8, where it is compared to the observed yields in data. The uncertainty in the background estimates takes into account both the statistical and systematic components. The comparison of the data-driven background estimates and the observations for each  $M_R$  category is shown in Fig. 7.6, as a function of  $R^2$ . The expected event distribution is shown for two signal benchmark models, corresponding to the pair production of DM particles of mass 1 GeV in the effective field theory (EFT) approach with vector coupling to u or d quarks. Details on the signal benchmark models are given in Section 7.7.

### Background estimation for the $0\mu b$ and $0\mu bb$ samples

A similar data-driven technique is used to determine the expected background for the one and two b-tag search regions. The background from  $t\bar{t}$  events for each  $R^2$

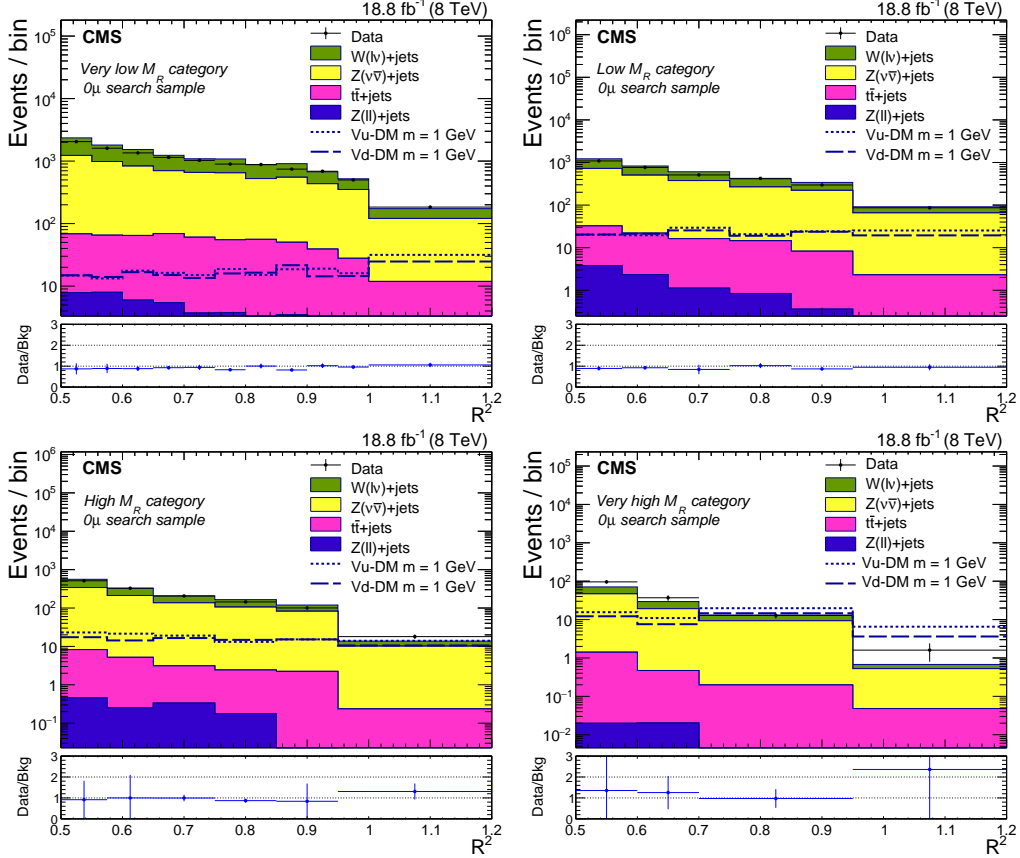


Figure 7.6: Comparison of the observed yield in the zero b-tag control region and the background estimates in the four  $M_R$  categories: VL (top left), L (top right), H (bottom left), and VH (bottom right). The contribution of individual background processes is shown by the filled histograms. The bottom panels show the ratio between the observed yields and the total background estimate. For reference, the distributions from two benchmark signal models are also shown, corresponding to the pair production of DM particles of mass 1 GeV in the EFT approach with vector coupling to u or d quarks. The horizontal bars indicate the variable bin widths.

bin in the one b-tag search region,  $n(\bar{t}t)_i^{0\mu b}$ , is computed as:

$$n(\bar{t}t)_i^{0\mu b} = (n(\bar{t}t)_i^{2\mu b} - N_i^{Z(\ell\ell)+jets,2\mu b} - N_i^{W(\ell\nu)+jets,2\mu b}) \frac{N(\bar{t}t)_i^{0\mu b}}{N(\bar{t}t)_i^{2\mu b}} \quad (7.4)$$

where  $n(\bar{t}t)_i^{2\mu b}$  is the observed yield in the  $i$ th  $R^2$  bin in the  $2\mu b$  control region, while  $N(\bar{t}t)_i^{0\mu b}$  and  $N(\bar{t}t)_i^{2\mu b}$  are the  $\bar{t}t$  yields in the  $i$ th  $R^2$  bin predicted by the simulation for the one b-tag search region and the  $2\mu b$  control region respectively. Similarly, the  $\bar{t}t$  background in the two b-tag search region is derived from Eq. (7.4), replacing  $N(\bar{t}t)_i^{0\mu b}$  with  $N(\bar{t}t)_i^{0\mu bb}$ , the  $\bar{t}t$  background yield in the  $i$ th bin of the two b-tag search region predicted by the simulation. The data yield in the  $2\mu b$  control region is

Table 7.9: Comparison of the observed yields in the  $Z(\mu\mu)b$  and  $1\mu b$  samples, the corresponding predictions from background simulation, and (for  $1\mu b$  only) the cross-check background estimate. The contribution of each individual background process is also shown, as estimated from simulated samples.

Sample	$Z(\nu\bar{\nu})+\text{jets}$	$W(\ell\nu)+\text{jets}$	$Z(\ell\ell)+\text{jets}$	$t\bar{t}$	MC predicted	Estimated	Observed
$Z(\mu\mu)b$	$<0.1$	$<0.1$	$134 \pm 3$	$17 \pm 1$	$151 \pm 3$	—	175
$1\mu b$	$0.2 \pm 0.1$	$279 \pm 7$	$11 \pm 1$	$3038 \pm 17$	$3328 \pm 18$	$3410 \pm 540$	2920

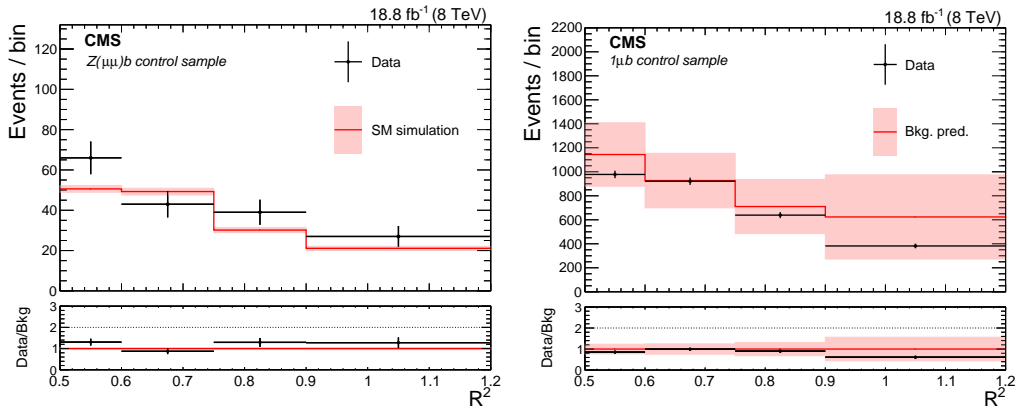


Figure 7.7: Comparison of the observed yield and the prediction from simulation in the  $Z(\mu\mu)b$  control sample (left) and of the observed yield in the  $1\mu b$  control sample and the background estimates from the  $2\mu b$  and  $Z(\mu\mu)b$  control samples (right), shown as a function of  $R^2$ . The bottom panel of each figure shows the ratio between the data and the estimates. The shaded bands represent the statistical uncertainty in the left plot, and the total uncertainty in the right plot. The horizontal bars indicate the variable bin widths.

corrected to account for the small contamination from  $Z+\text{jets}$  and  $W+\text{jets}$ , predicted with the simulated yields  $N_i^{Z(\ell\ell)+\text{jets},2\mu b}$  and  $N_i^{W(\ell\nu)+\text{jets},2\mu b}$ , respectively.

The background contribution from  $W(\ell\nu)+\text{jets}$  and  $Z(\nu\bar{\nu})+\text{jets}$  events is predicted using the  $Z(\mu\mu)b$  control region, and summarized in Table 7.9. The  $Z+\text{jets}$  purity of this control region is  $\approx 89\%$ . The observed yield in the  $Z(\mu\mu)b$  control region is shown in the left plot of Fig. 7.7, as a function of  $R^2$ , along with the Monte Carlo simulation prediction. The uncertainty on the simulation prediction accounts only for the statistical uncertainty of the simulated sample. This contribution, scaled by the ratio of the predicted  $V+\text{jets}$  background in the search regions to that in the control region, obtained from simulation, provides an estimate for each  $R^2$  bin.

We perform a cross-check of the method on the  $1\mu b$  control region by predicting the background from the  $2\mu b$  control region data. The data and prediction are compared on the right of Fig. 7.7, where we observe reasonable agreement. The

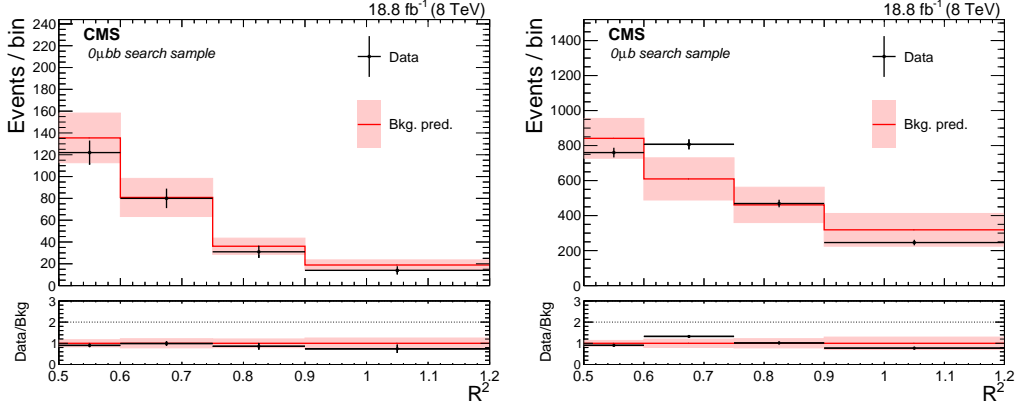


Figure 7.8: Comparison of observed event yields and background estimates as a function of  $R^2$ , for the one (left) and two (right) b-tag search regions. The shaded bands represent the total uncertainty in the estimate. The horizontal bars indicate the variable bin widths.

Table 7.10: Comparison of the observed yield for events in the one and two b-tag search regions and the corresponding background estimates. The uncertainty in the estimates takes into account both the statistical and systematic components. The contribution of each individual background process is also shown, as estimated from simulated samples, as well as the total MC predicted yield.

Sample	$Z(\nu\bar{\nu}) + \text{jets}$	$W(\ell\nu) + \text{jets}$	$Z(\ell\ell) + \text{jets}$	$t\bar{t}$	MC predicted	Estimated	Observed
$0\mu bb$	$44 \pm 3$	$14 \pm 2$	$0.2 \pm 0.1$	$204 \pm 4$	$262 \pm 5$	$271 \pm 37$	247
$0\mu b$	$417 \pm 8$	$216 \pm 7$	$2.4 \pm 0.4$	$1480 \pm 12$	$2115 \pm 16$	$2230 \pm 280$	2282

difference between the prediction and the observed data in this cross-check region is propagated as a systematic uncertainty of the method.

The estimated background in the one and two b-tag search regions is given in Table 7.10 and shown in Fig. 7.8, where it is compared to the observed yields in data. The uncertainty in the estimates take into account both the statistical and systematic components.

## 7.6 Systematic uncertainties

For each  $R^2$  bin in each  $M_R$  category, the difference between the observed and estimated yields in the crosscheck analysis (see Section 8.5) is taken as the estimate of the uncertainty associated with the method. The uncertainty is found to be typically  $\approx 20\text{--}40\%$ , depending on the considered bin in the  $(M_R, R^2)$  plane. Other sources of systematic uncertainties such as the modeling of the jet energy scale correction, and the initial-state radiation in the event are found to be negligible compared to the systematic from the cross-check. Figures 7.9 and 7.10 show the

indivial systematic uncertainties just mentioned and the systematic uncertainty from the cross-check.

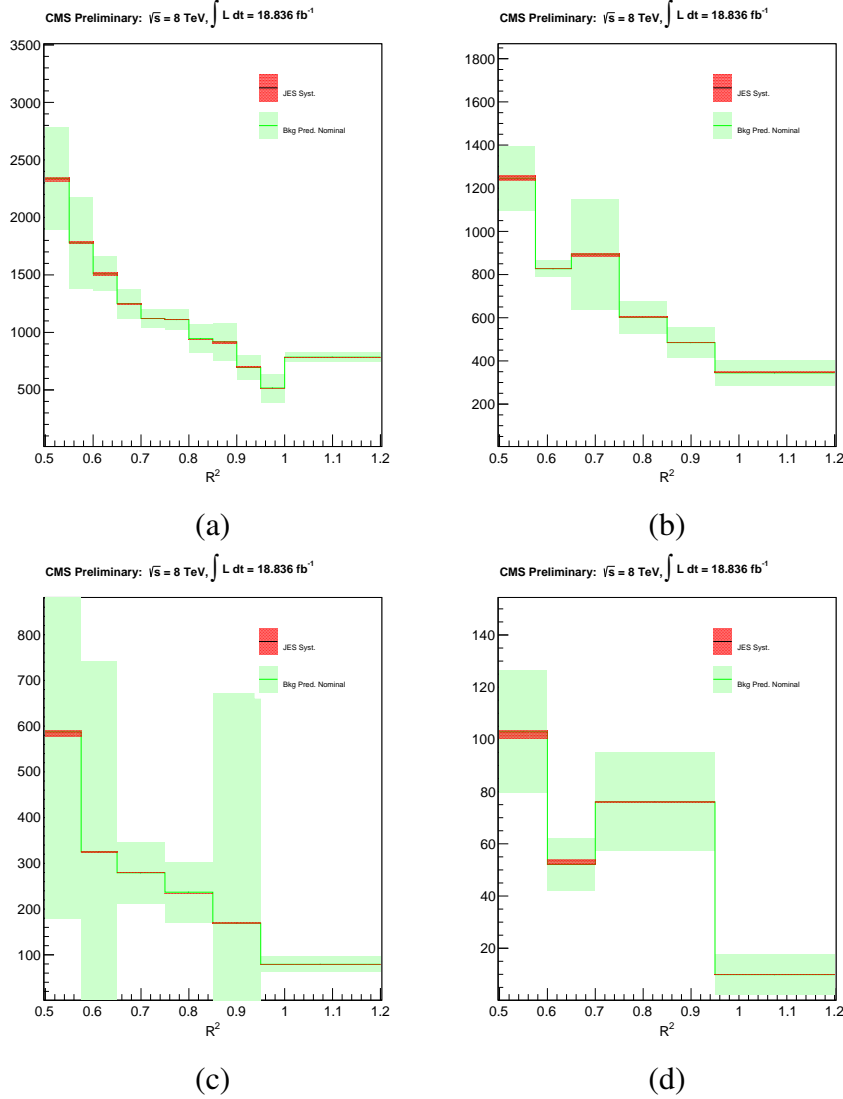


Figure 7.9: Total (estimated using the cross-check analysis) and JES systematic uncertainties. The green band corresponds to the systematic uncertainty associated with the background prediction method, while the red band corresponds to the JES systematic only. Panels (a) and (b) show the VL and L  $M_R$  categories, respectively. Panels (c) and (d) show the H and VH  $M_R$  categories, respectively.

The largest systematic uncertainty arises from the crosscheck analysis. This uncertainty is affected by statistical fluctuations from the limited number of selected events in the  $2\mu$  control region. This uncertainty covers the differences in the modeling of the recoil spectra between  $W+jets$  and  $Z+jets$  processes as well as the cross section uncertainties.

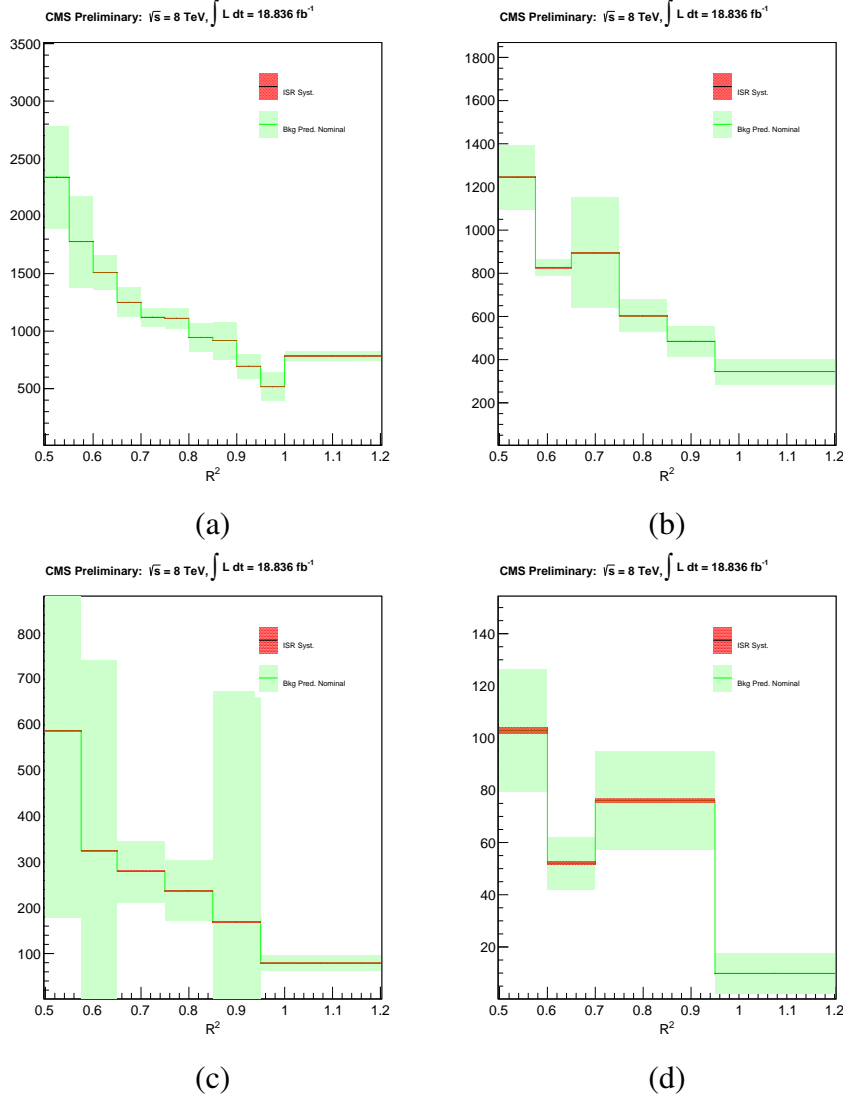


Figure 7.10: Total (estimated using the cross-check analysis) and ISR systematic uncertainties. The green band corresponds to the systematic uncertainty associated with the background prediction method, while the red band corresponds to the ISR systematic only. Panels (a) and (b) show the VL and L  $M_R$  categories, respectively. Panels (c) and (d) show the H and VH  $M_R$  categories, respectively.

For the  $0\mu$  analysis, differences between the kinematic properties of  $W+jets$  and  $Z+jets$  events are additional sources of systematic uncertainty. These differences arise from the choice of the PDF set, jet energy scale corrections,  $b$  tagging efficiency corrections, and trigger efficiency. These effects largely cancel when taking the ratio of the two processes, and the resulting uncertainty is found to be smaller than one fifth of the total uncertainty. The quoted uncertainty is an upper estimate of the total systematic uncertainty.

Table 7.11: Systematic uncertainties associated with the description of the DM signal. The values indicated represent the typical size. The dependence of these systematic uncertainties on the  $R^2$  and  $M_R$  values is taken into account in the determination of the results.

Effect	Uncertainty
Jet energy scale	3–6%
Luminosity	2.6%
Parton distribution functions	3–6%
Initial-state radiation	8–15%

For the  $0\mu b$  and  $0\mu bb$  samples, both the signal and control samples are dominated by  $t\bar{t}$  events. The cancellation of the systematic uncertainties is even stronger in this case, since it does not involve different processes, and different PDFs. The remaining uncertainty is dominated by the contribution arising from the small size of the control sample.

Systematic uncertainties in the signal simulation originate from the choice of the PDF set, the jet energy scale correction, the modeling of the initial-state radiation in the event generator, and the uncertainty in the integrated luminosity. The luminosity uncertainty changes the signal normalization while the other uncertainties also modify the signal shape. These effects are taken into account by propagating these uncertainties into the  $M_R$  category and the  $R^2$  bin. Figures 7.11, 7.12, and 7.13 show the PDF, jet energy scale, and the initial-state radiation systematic uncertainties for a vector-mediated EFT signal model with DM mass of 700 GeV, respectively. These uncertainties are considered to be fully correlated across  $M_R$  categories and  $R^2$  bins. Typical values for the individual contributions are given in Table 7.11. The total uncertainty in the signal yield is obtained by propagating the individual effects into the  $M_R$  and  $R^2$  variables and comparing the bin-by-bin variations with respect to the central value of the prediction based on simulation. In the particular case of the uncertainties due to the choice of the PDF set we have followed the PDF4LHC [62, 35, 61] prescription, using the CTEQ-6.6[180] and MRST-2006-NNLO [177] PDF sets.

## 7.7 Results and interpretation

In Figs. 7.6 and 7.8 the estimated backgrounds are compared to the observed yield in each  $M_R$  region, for events without and with b-tagged jets, respectively. The background estimates agree with the observed yields, within the uncertainties. This result is interpreted in terms of exclusion limits for several models of DM production.

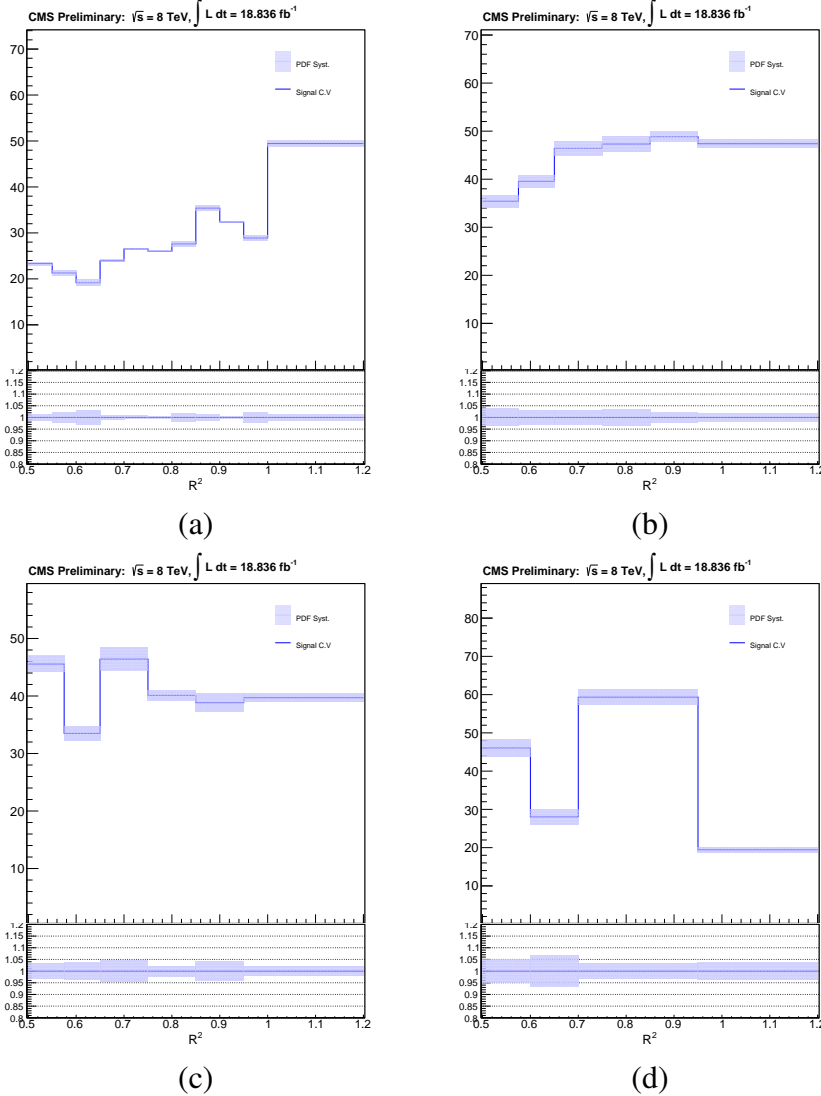


Figure 7.11: PDF systematic uncertainty for a vector mediated EFT signal model with DM mass = 700 GeV. The blue band corresponds to the systematic error associated with PDF uncertainty. Panels (a) and (b) show the VL and L  $M_R$  categories, respectively. Panels (c) and (d) show the H and VH  $M_R$  categories, respectively.

### Limits on dark matter production from the $0\mu$ sample

The result is interpreted in the context of a low-energy effective field theory, in which the production of DM particles is mediated by six or seven dimension operators [57, 48]. This choice allows the results be compared with those of previous analyses [24, 90], and shows that a similar sensitivity is achieved.

Operators of dimension six and seven are generated assuming the existence of a heavy particle, mediating the interaction between the DM and SM fields. To describe DM

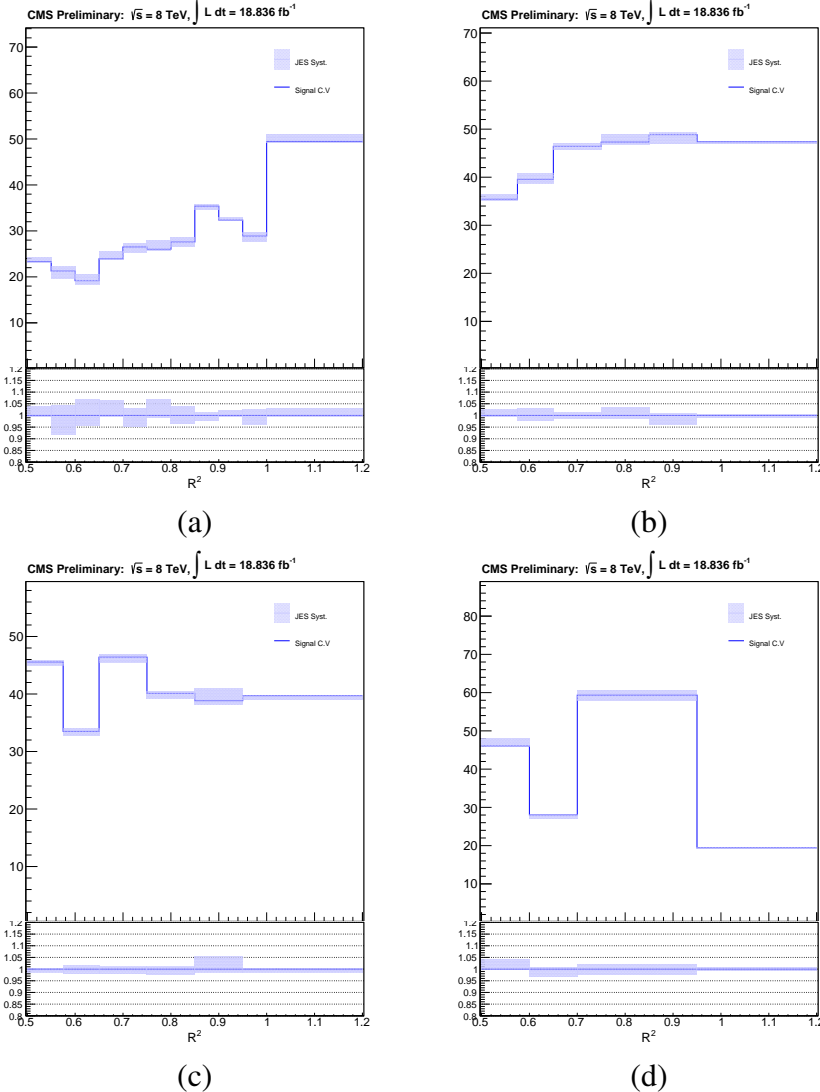


Figure 7.12: JES systematic uncertainty for a vector mediated EFT signal model with DM mass = 700 GeV. The blue band corresponds to the systematic error associated with JES uncertainty. Panels (a) and (b) show the VL and L  $M_R$  categories, respectively. Panels (c) and (d) show the H and VH  $M_R$  categories, respectively.

production as a local interaction, the propagator of the heavy mediator is expanded through an operator product expansion. The nature of the mediator determines the nature of the effective interaction. Two benchmark scenarios are considered in this study, axial-vector (AV), and vector (V) interactions [123], described by the following operators:

$$\hat{O}_{AV} = \frac{1}{\Lambda^2} (\bar{\chi} \gamma^\mu \gamma_5 \chi) (\bar{q} \gamma_\mu \gamma_5 q) ; \quad \hat{O}_V = \frac{1}{\Lambda^2} (\bar{\chi} \gamma^\mu \chi) (\bar{q} \gamma_\mu q) . \quad (7.5)$$

Here  $\gamma_\mu$  and  $\gamma_5$  are the Dirac matrices,  $\chi$  is the DM field, and  $q$  is an SM quark

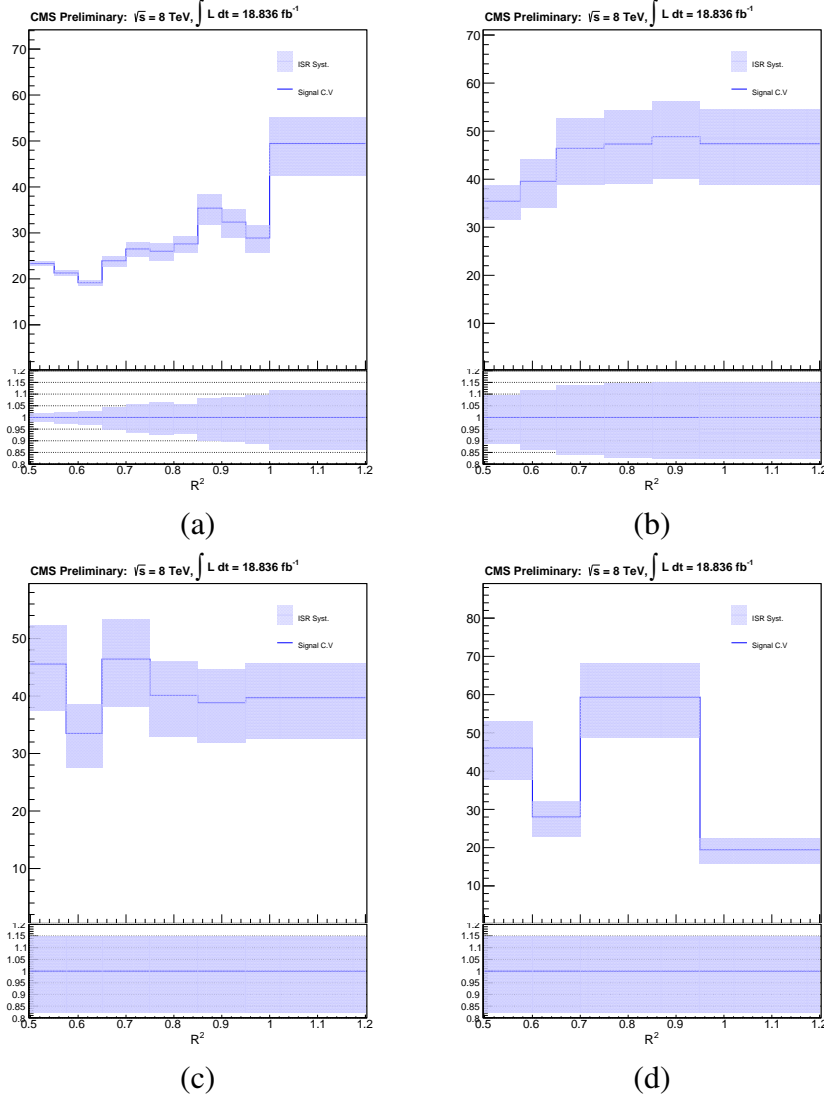


Figure 7.13: ISR systematic uncertainty for a vector mediated EFT signal model with DM mass = 700 GeV. The blue band corresponds to the systematic error associated with ISR uncertainty. Panels (a) and (b) show the VL and L  $M_R$  categories, respectively. Panels (c) and (d) show the H and VH  $M_R$  categories, respectively.

field. The DM particle is assumed to be a Dirac fermion where both operators will contribute in the low-energy theory, while in the case of a Majorana DM particle the vector coupling  $\hat{O}_V$  will vanish in the low-energy theory. Below the cutoff energy scale  $\Lambda$ , DM production is described as a contact interaction between two quarks and two DM particles. In the case of  $s$ -channel production through a heavy mediator, the energy scale  $\Lambda$  is identified with  $M/g_{\text{eff}}$ , where  $M$  is the mediator mass and  $g_{\text{eff}} = \sqrt{g_q g_\chi}$  is an effective coupling, determined by the coupling of the mediator to quark and DM fields,  $g_q$  and  $g_\chi$ , respectively.

The results in Tables 7.15-7.18 in the Appendix are used to obtain an upper limit at 90% confidence level (CL) on the DM production cross section,  $\sigma_{\text{UL}}^i$  (where the superscript denotes the coupling to an up or down quark). The limits are obtained using the LHC CL<sub>s</sub> procedure [47, 102] and a global likelihood determined by combining the likelihoods of the different search categories. Each systematic uncertainty (see Section 7.6) is incorporated in the likelihood with a dedicated nuisance parameter, whose value is not known a priori but rather must be estimated from the data.

Subsequently, the cross section ( $\sigma_{\text{UL}}^i$ ) limit is translated into a lower limit  $\Lambda_{\text{LL}}$  on the cutoff scale, through the relation:

$$\Lambda_{\text{LL}} = \Lambda_{\text{GEN}} \left( \frac{\sigma_{\text{GEN}}}{\sigma_{\text{UL}}} \right)^{\frac{1}{4}}. \quad (7.6)$$

Here  $\Lambda_{\text{GEN}}$  and  $\sigma_{\text{GEN}}$  are the cutoff energy scale and cross section of the simulated sample, respectively. The derived values of  $\Lambda_{\text{LL}}$  as a function of the DM mass, shown in Fig. 7.14, are comparable to those derived for the CMS monojet search [91]. The exclusion limits on  $\Lambda$  weaken at large DM masses since the cross section for DM production is reduced. The analysis has been repeated removing the events also selected by the monojet search. The reduction in background yields due to this additional requirement compensates for the reduction in signal efficiency, resulting in a negligible difference in the exclusion limit on  $\Lambda$ .

The EFT framework provides a benchmark scenario to compare the sensitivity of this analysis with that of previous searches for similar signatures. However, the validity of an EFT approach is limited at the LHC because a fraction of events under study are generated at a  $\sqrt{s}$  comparable to the cutoff scale  $\Lambda$  [130, 48, 125, 64]. For theories to be perturbative,  $g_{\text{eff}}$  is typically required to be smaller than  $4\pi$ , and this condition is unlikely to be satisfied for the entire region of phase space probed by the collider searches. In addition, the range of values for the couplings being probed within the EFT may be unrealistically large. Following the study presented in Refs. [65, 66, 67], we quantify this effect through two EFT validity measures. The first is a minimal kinematic constraint on  $\Lambda$  obtained by requiring  $Q_{\text{tr}} < g_{\text{eff}}\Lambda$  and  $Q_{\text{tr}} > 2M_\chi$ , where  $Q_{\text{tr}}$  is the momentum transferred from the mediator to the DM particle pair, which yields  $\Lambda > 2M_\chi/g_{\text{eff}}$ . The second is more stringent and

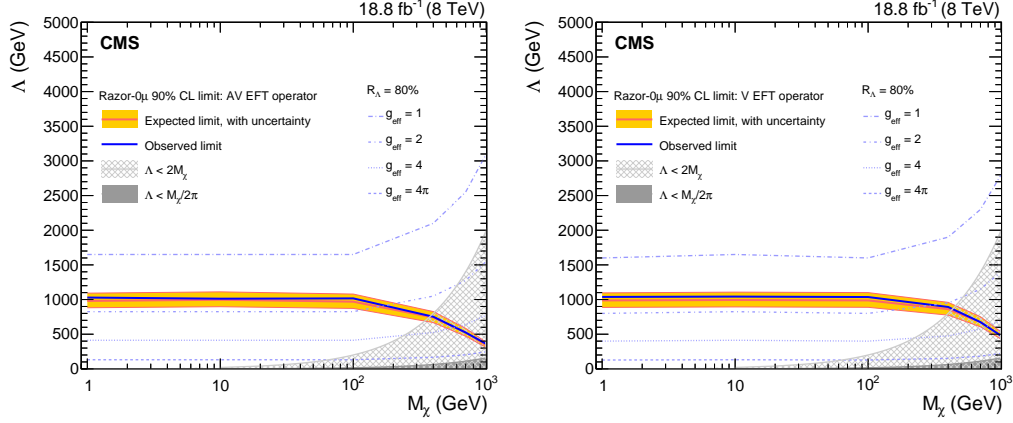


Figure 7.14: Lower limit at 90% CL on the cutoff scale  $\Lambda$  as a function of the DM mass  $M_\chi$  in the case of axial-vector (left) and vector (right) currents. The validity of the EFT is quantified by  $R_\Lambda = 80\%$  contours, corresponding to different values of the effective coupling  $g_{\text{eff}}$ . For completeness, regions forbidden by the EFT validity condition  $\Lambda > 2M_\chi/g_{\text{eff}}$  are shown for two choices of the effective coupling:  $g_{\text{eff}} = 1$  (light gray) and  $g_{\text{eff}} = 4\pi$  (dark gray).

uses the quantity:

$$R_\Lambda = \frac{\int dR^2 \int dM_R \frac{d^2\sigma}{dR^2 dM_R} \Big|_{Q_{\text{tr}} < g_{\text{eff}}\Lambda}}{\int dR^2 \int dM_R \frac{d^2\sigma}{dR^2 dM_R}}. \quad (7.7)$$

Values of  $R_\Lambda$  close to unity indicate a regime in which the assumptions of the EFT approximation hold, while a deviation from unity quantifies the fraction of events for which the EFT approximation is still valid. We consider the case of  $s$ -channel production, and we compute  $R_\Lambda$  as a function of the effective coupling  $g_{\text{eff}}$  in the range  $0 < g_{\text{eff}} \leq 4\pi$ . The contours corresponding to  $R_\Lambda = 80\%$  for different values of  $g_{\text{eff}}$  are shown in Fig. 7.14. For values of  $g_{\text{eff}} \gtrsim 2$ , the limit set by the analysis lies above the  $R_\Lambda = 80\%$  contour.

The exclusion limits on  $\Lambda$  for the axial-vector and vector operators are transformed into upper limits on the spin-dependent ( $\sigma_{N\chi}^{\text{SD}}$ ) [41, 179, 121, 120, 40, 46, 45] and spin-independent ( $\sigma_{N\chi}^{\text{SI}}$ ) [120, 121, 111, 203, 110, 122, 44, 43] DM-nucleon scattering cross section, respectively; using the following expressions [123]:

$$\sigma_{N\chi}^{\text{SD}} = 0.33 \frac{\mu^2}{\pi \Lambda_{\text{LL}}^4}, \quad (7.8)$$

$$\sigma_{N\chi}^{\text{SI}} = 9 \frac{\mu^2}{\pi \Lambda_{\text{LL}}^4}, \quad (7.9)$$

where

$$\mu = \frac{M_\chi M_p}{M_\chi + M_p}, \quad (7.10)$$

with  $M_p$  and  $M_\chi$  indicating the proton and DM masses, respectively. The numerical values of the derived limits are given in Tables 7.12 and 7.13. The bound on  $\sigma_{N\chi}$  as a function of  $M_\chi$  is shown in Fig. 7.15 for spin-dependent and spin-independent DM-nucleon scattering. A summary of the observed limits for the axial-vector and vector operators can be found in Tables 7.12 and 7.13 respectively. It is observed that the spin-independent bounds obtained by direct detection experiments are more stringent than those obtained by the present result for masses above  $\simeq 5$  GeV. Such an effect is expected since the spin-independent DM-nucleus cross section is enhanced by the coherent scattering of DM off nucleons in the case of spin-independent operators. We note that the present result is more sensitive for small DM mass because the recoil energy in direct detection experiments is lower in this region and therefore more difficult to detect. In the case of spin-dependent DM-nucleus scattering, the present results are more stringent than those obtained by direct detection experiments because the DM-nucleus cross section does not benefit from the coherent enhancement. A summary of the observed limits for the axial-vector and vector operators can be found in Tables 7.12 and 7.13 respectively.

In order to compare our results with those from direct detection experiments, the experimental bounds in [120, 121, 111, 203, 110, 122, 41, 179, 121, 120] are translated into bounds on  $\Lambda$ . This comparison is shown in Fig. 7.16. This translation is well defined since the momentum transfer in most direct detection experiments is low compared to the values of  $\Lambda$  being probed, and thus the EFT approximations in question are mostly valid.

### Limits on dark matter production from the $0\mu b$ and $0\mu bb$ samples

The results from the  $0\mu b$  and  $0\mu bb$  samples are interpreted in an EFT scenario, following a methodology similar to that of Section 7.7. In this case, a heavy scalar mediator is considered [175], generating an operator:

$$\hat{O}_S = \frac{M_q}{\Lambda^3} \bar{\chi} \chi \bar{q} q. \quad (7.11)$$

The dependence on the mass, induced by the scalar nature of the mediator, implies a stronger coupling to third-generation quarks, enhancing the sensitivity of the  $0\mu b$  and  $0\mu bb$  samples to this scenario. Unlike the case of V and AV operators, the

Table 7.12: The 90% CL limits on DM production in the case of axial-vector couplings. Here,  $\sigma_{\text{UL}}^u$  and  $\sigma_{\text{UL}}^d$  are the observed upper limits on the production cross section for u and d quarks, respectively;  $\Lambda_{\text{LL}}$  is the observed cutoff energy scale lower limit; and  $\sigma_{N\chi}$  is the observed DM-nucleon scattering cross section upper limit.

$M_\chi$ (GeV)	$\sigma_{\text{UL}}^u$ (pb)	$\sigma_{\text{UL}}^d$ (pb)	$\Lambda_{\text{LL}}$ (GeV)	$\sigma_{N\chi}$ ( $\text{cm}^2$ )
1	0.39	0.45	1029	$8.5 \times 10^{-42}$
10	0.43	0.45	1012	$2.9 \times 10^{-41}$
100	0.30	0.37	1017	$3.3 \times 10^{-41}$
400	0.25	0.26	752	$1.1 \times 10^{-40}$
700	0.21	0.26	524	$4.7 \times 10^{-40}$
1000	0.17	0.22	360	$2.1 \times 10^{-39}$

Table 7.13: The 90% CL limits on DM production in the case of vector couplings. Here,  $\sigma_{\text{UL}}^u$  and  $\sigma_{\text{UL}}^d$  are the observed upper limits on the production cross section for u and d quarks, respectively;  $\Lambda_{\text{LL}}$  is the observed cutoff energy scale lower limit; and  $\sigma_{N\chi}$  is the observed DM-nucleon scattering cross section upper limit.

$M_\chi$ (GeV)	$\sigma_{\text{UL}}^u$ (pb)	$\sigma_{\text{UL}}^d$ (pb)	$\Lambda_{\text{LL}}$ (GeV)	$\sigma_{N\chi}$ ( $\text{cm}^2$ )
1	0.41	0.38	1038	$2.3 \times 10^{-40}$
10	0.36	0.45	1043	$6.9 \times 10^{-40}$
100	0.33	0.44	1036	$8.3 \times 10^{-40}$
400	0.23	0.35	893	$1.5 \times 10^{-39}$
700	0.22	0.27	674	$4.7 \times 10^{-39}$
1000	0.22	0.27	477	$1.8 \times 10^{-38}$

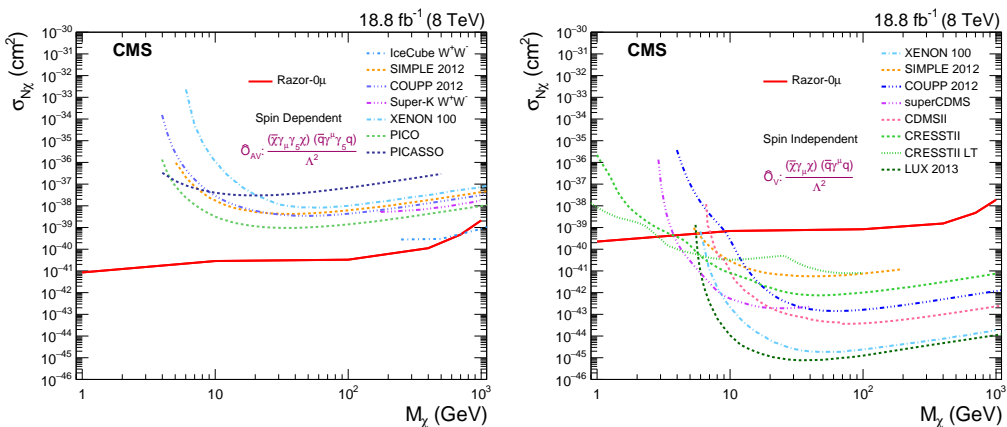


Figure 7.15: Upper limit at 90% CL on the DM-nucleon scattering cross section  $\sigma_{N\chi}$  as a function of the DM mass  $M_\chi$  in the case of spin-dependent axial-vector (left) and spin-independent vector (right) currents. A selection of representative direct detection experimental bounds are also shown.

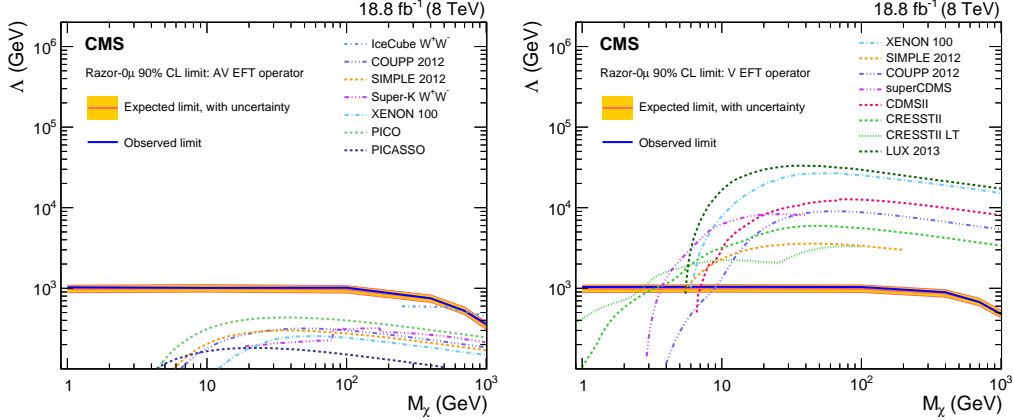


Figure 7.16: Lower limit at 90% CL on the cutoff scale  $\Lambda$  as a function of the DM mass  $M_\chi$  in the case of axial-vector (left) and vector (right) currents. A selection of direct detection experimental bounds are also shown.

production cross section for this process is proportional to  $1/\Lambda^6$ . The value of  $\Lambda_{\text{LL}}$  is then derived as

$$\Lambda_{\text{LL}} = \Lambda_{\text{GEN}} \left( \frac{\sigma_{\text{GEN}}}{\sigma_{\text{UL}}} \right)^{\frac{1}{6}}. \quad (7.12)$$

Given the results of Table 7.10 we proceed to set limits at 90% CL on the cutoff scale (see Table 7.14) using the LHC  $\text{CL}_s$  procedure. To quantify the validity of the EFT we follow the discussion in Section 7.7, considering an interaction mediated by an  $s$ -channel produced particle. The operator of Eq. (7.11) is suppressed by an additional factor  $m_b/\Lambda$  with respect to the operators in Eq. (7.5). As a result, for a given value of the coupling  $g_{\text{eff}}$ , smaller values of  $\Lambda$  are probed in this case. The observed limit stays below the contours derived for  $R_\Lambda = 80\%$ , even when the coupling is fixed to the largest value considered,  $g_{\text{eff}} = 4\pi$ , as shown in the left plot of Fig. 7.17. For the same choice of coupling, the derived limit on  $\Lambda$  would correspond to  $R_\Lambda \approx 25\%$ , as shown in the right plot of Fig. 7.17. Only for  $g_{\text{eff}} > 4\pi$  does the observed limit correspond to values of  $R_\Lambda > 80\%$ . This requirement implies a UV completion of the EFT beyond the perturbative regime. For this reason, this result is not interpreted in terms of an exclusion limit on  $\sigma_{N\chi}$ .

## 7.8 Summary

A search for dark matter has been performed studying proton-proton collisions collected with the CMS detector at the LHC at a center-of-mass energy of 8 TeV. The data correspond to an integrated luminosity of  $18.8 \text{ fb}^{-1}$ , collected with a dedicated high-rate trigger in 2012, made possible by the creation of parked data,

Table 7.14: The 90% CL limits on DM production in the case of scalar couplings. Here,  $\sigma_{\text{UL}}^{\text{obs}}$  is the observed upper limit on the production cross section,  $\Lambda_{\text{LL}}^{\text{obs}}$  and  $\Lambda_{\text{LL}}^{\text{exp}}$  are the observed and expected cutoff energy scale lower limit, respectively.

$M_\chi$ (GeV)	$\sigma_{\text{UL}}^{\text{obs}}$ (pb)	$\Lambda_{\text{LL}}^{\text{obs}}$ (GeV)	$\Lambda_{\text{LL}}^{\text{exp}}$ (GeV)
0.1	5.4	43.0	48.2
1	3.8	45.3	49.9
10	6.3	43.2	48.4
100	0.8	53.7	55.1
200	0.7	47.2	48.3
300	2.8	32.5	35.8
400	2.8	28.3	30.8
1000	1.7	13.2	13.8

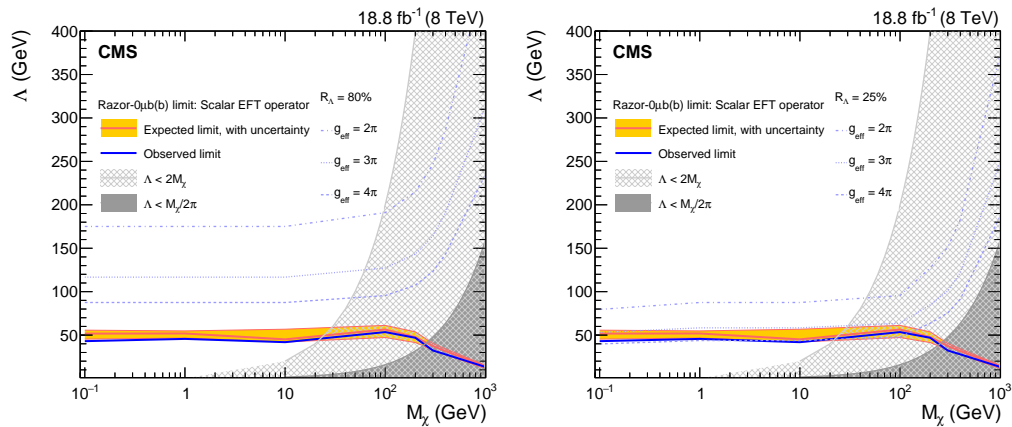


Figure 7.17: Lower limit at 90% CL on the cutoff scale  $\Lambda$  for the scalar operator  $\hat{O}_S$  as a function of the DM mass  $M_\chi$ . The validity of the EFT is quantified by  $R_\Lambda = 80\%$  (left) and  $R_\Lambda = 25\%$  (right) contours, corresponding to different values of the effective coupling  $g_{\text{eff}}$ . For completeness, regions forbidden by the EFT validity condition  $\Lambda > 2M_\chi/g_{\text{eff}}$  are shown for two choices of the effective coupling:  $g_{\text{eff}} = 1$  (light gray) and  $g_{\text{eff}} = 4\pi$  (dark gray).

and processed during the LHC shutdown in 2013.

Events with at least two jets are analyzed by studying the distribution in the ( $M_R$ ,  $R^2$ ) plane, in an event topology complementary to that of monojet searches. Events with one or two muons are used in conjunction with simulated samples, to predict the expected background from standard model processes, mainly  $Z+jets$  and  $W+jets$ . The analysis is performed on events both with and without b-tagged jets, originating from the hadronization of a bottom quark, where in the latter case the dominant background comes from  $t\bar{t}$ .

No significant excess is observed. The results are presented as exclusion limits on dark matter production at 90% confidence level for models based on effective operators and for different assumptions on the interaction between the dark matter particles and the colliding partons. Dark matter production at the LHC is excluded for a mediator mass scale  $\Lambda$  below 1 TeV in the case of a vector or axial vector operator. While the sensitivity achieved is similar to those of previously published searches, this analysis complements those results since the use of razor variables provides more inclusive selection criteria and since the exploitation of parked data allows events with small values of  $M_R$  to be included.

## ACKNOWLEDGMENTS

We congratulate our colleagues in the CERN accelerator departments for the excellent performance of the LHC and thank the technical and administrative staffs at CERN and at other CMS institutes for their contributions to the success of the CMS effort. In addition, we gratefully acknowledge the computing centers and personnel of the Worldwide LHC Computing Grid for delivering so effectively the computing infrastructure essential to our analyses. Finally, we acknowledge the enduring support for the construction and operation of the LHC and the CMS detector provided by the following funding agencies: the Austrian Federal Ministry of Science, Research and Economy and the Austrian Science Fund; the Belgian Fonds de la Recherche Scientifique, and Fonds voor Wetenschappelijk Onderzoek; the Brazilian Funding Agencies (CNPq, CAPES, FAPERJ, and FAPESP); the Bulgarian Ministry of Education and Science; CERN; the Chinese Academy of Sciences, Ministry of Science and Technology, and National Natural Science Foundation of China; the Colombian Funding Agency (COLCIENCIAS); the Croatian Ministry of Science, Education and Sport, and the Croatian Science Foundation; the Research Promotion Foundation, Cyprus; the Ministry of Education and Research, Estonian Research Council via IUT23-4 and IUT23-6 and European Regional Development Fund, Estonia; the Academy of Finland, Finnish Ministry of Education and Culture, and Helsinki Institute of Physics; the Institut National de Physique Nucléaire et de Physique des Particules / CNRS, and Commissariat à l'Énergie Atomique et aux Énergies Alternatives / CEA, France; the Bundesministerium für Bildung und Forschung, Deutsche Forschungsgemeinschaft, and Helmholtz-Gemeinschaft Deutscher Forschungszentren, Germany; the General Secretariat for Research and Technology, Greece; the National Scientific Research Foundation, and National Innovation Office, Hungary; the Department of Atomic Energy and the Department of Science and Technology, India; the Institute for Studies in Theoretical Physics and Mathematics, Iran; the Science Foundation, Ireland; the Istituto Nazionale di Fisica Nucleare, Italy; the Ministry of Science, ICT and Future Planning, and National Research Foundation (NRF), Republic of Korea; the Lithuanian Academy of Sciences; the Ministry of Education, and University of Malaya (Malaysia); the Mexican Funding Agencies (CINVESTAV, CONACYT, SEP, and UASLP-FAI); the Ministry of Business, Innovation and Employment, New Zealand; the Pakistan Atomic Energy Commission; the Ministry of Science and Higher Education and

the National Science Center, Poland; the Fundação para a Ciência e a Tecnologia, Portugal; JINR, Dubna; the Ministry of Education and Science of the Russian Federation, the Federal Agency of Atomic Energy of the Russian Federation, Russian Academy of Sciences, and the Russian Foundation for Basic Research; the Ministry of Education, Science and Technological Development of Serbia; the Secretaría de Estado de Investigación, Desarrollo e Innovación and Programa Consolider-Ingenio 2010, Spain; the Swiss Funding Agencies (ETH Board, ETH Zurich, PSI, SNF, UniZH, Canton Zurich, and SER); the Ministry of Science and Technology, Taipei; the Thailand Center of Excellence in Physics, the Institute for the Promotion of Teaching Science and Technology of Thailand, Special Task Force for Activating Research and the National Science and Technology Development Agency of Thailand; the Scientific and Technical Research Council of Turkey, and Turkish Atomic Energy Authority; the National Academy of Sciences of Ukraine, and State Fund for Fundamental Researches, Ukraine; the Science and Technology Facilities Council, UK; the US Department of Energy, and the US National Science Foundation.

Individuals have received support from the Marie-Curie programme and the European Research Council and EPLANET (European Union); the Leventis Foundation; the A. P. Sloan Foundation; the Alexander von Humboldt Foundation; the Belgian Federal Science Policy Office; the Fonds pour la Formation à la Recherche dans l'Industrie et dans l'Agriculture (FRIA-Belgium); the Agentschap voor Innovatie door Wetenschap en Technologie (IWT-Belgium); the Ministry of Education, Youth and Sports (MEYS) of the Czech Republic; the Council of Science and Industrial Research, India; the HOMING PLUS programme of the Foundation for Polish Science, cofinanced from European Union, Regional Development Fund; the OPUS programme of the National Science Center (Poland); the Compagnia di San Paolo (Torino); MIUR project 20108T4XTM (Italy); the Thalis and Aristeia programmes cofinanced by EU-ESF and the Greek NSRF; the National Priorities Research Program by Qatar National Research Fund; the Rachadapisek Sompot Fund for Postdoctoral Fellowship, Chulalongkorn University (Thailand); the Chulalongkorn Academic into Its 2nd Century Project Advancement Project (Thailand); and the Welch Foundation, contract C-1845; and the Weston Havens Foundation (USA).

## Appendix

### 7.9 Background estimation and observed yield

In this section, we provide the background estimate and the observed yield for each bin of the ( $M_R$ ,  $R^2$ ) plane.

Tables 7.15-7.18 show the expected and observed yields in each  $R^2$  bin of each  $M_R$  category for the  $0\mu$  sample. Tables 7.19 and 7.20 show the corresponding values for the  $0\mu b$  and the  $0\mu bb$  samples, respectively.

Table 7.15: Background estimates and observed yield for each  $R^2$  bin in the VL  $M_R$  category.

$R^2$ range	0.5–0.55	0.55–0.6	0.6–0.65	0.65–0.7
Observed	2049	1607	1352	1147
Estimated	$2350 \pm 720$	$1810 \pm 450$	$1530 \pm 180$	$1240 \pm 110$
$R^2$ range	0.7–0.75	0.75–0.8	0.8–0.85	0.85–0.9
Observed	1026	896	880	744
Estimated	$1090 \pm 140$	$1081 \pm 76$	$876 \pm 97$	$909 \pm 63$
$R^2$ range	0.9–0.95	0.95–1.0	1.0–2.5	
Observed	688	499	735	
Estimated	$674 \pm 67$	$521 \pm 43$	$694 \pm 62$	

Table 7.16: Background estimates and observed yield for each  $R^2$  bin in the L  $M_R$  category.

$R^2$ range	0.5–0.575	0.575–0.65	0.65–0.75
Observed	1088	765	682
Estimated	$1220 \pm 120$	$828 \pm 65$	$810 \pm 210$
$R^2$ range	0.75–0.85	0.85–0.95	0.95–2.5
Observed	565	395	290
Estimated	$551 \pm 59$	$454 \pm 32$	$304 \pm 43$

Table 7.17: Background estimates and observed yield for each  $R^2$  bin in the H  $M_R$  category.

$R^2$ range	0.5–0.575	0.575–0.65	0.65–0.75
Observed	513	328	279
Estimated	$560 \pm 550$	$330^{+360}_{-330}$	$275 \pm 41$
$R^2$ range	0.75–0.85	0.85–0.95	0.95–2.5
Observed	203	151	85
Estimated	$242 \pm 18$	$171^{+173}_{-171}$	$74 \pm 17$

Table 7.18: Background estimates and observed yield for each  $R^2$  bin in the VH  $M_R$  category.

$R^2$ range	0.5–0.6	0.6–0.7	0.7–0.95	0.95–2.5
Observed	117	58	75	11
Estimated	$100^{+150}_{-100}$	$59 \pm 36$	$75 \pm 30$	$9 \pm 7$

Table 7.19: Background estimates and observed yield for each bin in the  $0\mu b$  signal region.

$R^2$ range	0.5–0.6	0.6–0.75	0.75–0.9	0.9–2.5
Observed	760	807	469	246
Estimated	$850 \pm 170$	$620 \pm 120$	$470 \pm 110$	$320 \pm 160$

Table 7.20: Background estimates and observed yield for each bin in the  $0\mu bb$  signal region.

$R^2$ range	0.5–0.6	0.6–0.75	0.75–0.9	0.9–2.5
Observed	122	80	31	14
Estimated	$135 \pm 30$	$81 \pm 18$	$36 \pm 8$	$19 \pm 9$

## Chapter 8

# SEARCHES FOR ANOMALOUS HIGGS BOSON PRODUCTION

### 8.1 Introduction

The discovery of the standard model (SM) Higgs boson at the LHC [16, 88] presents a unique opportunity to search for physics beyond the SM (BSM) using the Higgs boson as a search tool. Given the small value of the Higgs production cross section in the standard model, any BSM scenario predicting new mechanisms for Higgs boson production can be investigated with dedicated searches, using the known Higgs mass to suppress SM background processes.

This Chapter presents a search of this kind in pp collisions at 13 TeV using data from the CMS detector at the CERN LHC. Events with two photons consistent with a Higgs candidate are selected and categorized according to the  $p_T$  of the Higgs candidate, the presence of additional Higgs to  $b\bar{b}$  or Z to  $b\bar{b}$  candidates, and the estimated resolution of the diphoton pair. Motivated by supersymmetric (SUSY) scenarios, we use the razor variables [85, 196]  $M_R$  and  $R^2$ —extensively discussed and illustrated in Chapter ??—to define search regions that may contain additional events above the SM prediction if a BSM Higgs production mechanism is present. The contribution in the search regions from the non-resonant QCD background is distinguished from a potential BSM Higgs signal using the shape of the diphoton mass distribution. The search uses  $2.3 \text{ fb}^{-1}$  of integrated luminosity collected in 2015 and  $12.9 \text{ fb}^{-1}$  collected in 2016.

In Run 1 of the LHC, a similar CMS analysis [207] reported an excess of  $H \rightarrow \gamma\gamma$  events with  $M_R \approx 400 \text{ GeV}$  and  $R^2 > 0.05$  with a local (global) significance of  $2.9\sigma$  ( $1.6\sigma$ ). Motivated by the Run I result, we consider a SUSY simplified model in which bottom squarks are pair produced and decay to a bottom quark and the next-to-lightest supersymmetric particle (NLSP),  $\tilde{\chi}_2^0$ , with 100% branching ratio. The NLSP subsequently decays to a Higgs boson and the lightest supersymmetric particle (LSP),  $\tilde{\chi}_1^0$ , with 100% branching ratio. We assume that the mass difference between the NLSP and the LSP is 130 GeV, just above the Higgs boson mass. The relevant decay topology in the simplified model is shown in Figure 8.1. The cross section for this simplified model is assumed to be the same as the standard sbottom pair production cross section [60]. Such a signal model is observed to produce event

kinematics consistent with the excess observed in Run I data and is not ruled out by searches in other final states and decay channels. This search is interpreted using the sbottom pair production model as the benchmark, and we derive limits on the production cross section as a function of the sbottom mass and the LSP mass.

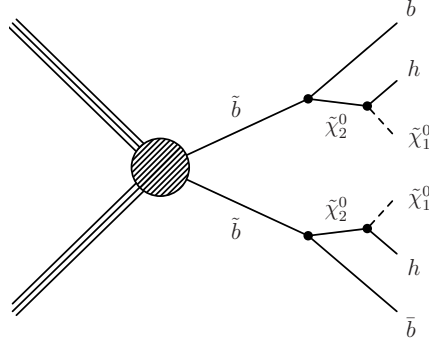


Figure 8.1: Diagram illustrating the SUSY benchmark simplified model of bottom squark decays to a Higgs boson, a b-jet, and the LSP.

## 8.2 Summary of the 8 TeV Results

The first version of the analysis to be presented in this Chapter was carried out by CMS [207] and studied in more detailed in Alex Mott’s thesis [[AlexMott](#)]. Here, a summary of the main results is given as is relevant for the discussions to follow.

The 8 TeV analysis selects events in a very similar fashion to the one presented in this Chapter. It categorizes events based on the Higg candidate  $p_T$ , the photons energy resolution, and the invariant masses of ther possible b-jet pairs – indeed, intended to target an extra Higgs or Z boson on the event. The final results yield that most of the search bins were consisten with the SM expectations, and the results were interpreted as cross section limits on the neutralino/chargino production in the context of SUSY simplified models. The observed significances for all the search bins are shown in Figure 8.2, while the limit on the neutralino/chargino production as a function of the chargino mass is shown in Figure 8.3. Although, most of the search bins were consitent with the SM expectations, an interesting excess of events was obeserved in the most extreme bin – that with the highest  $M_R$  and  $R^2$  boundaries – in the High-Resolution (HighRes) event category, see Figures 8.4 and 8.5, where both photons forming the Higgs cadidate are require to have an energy resolution better than 1.5%. This excess corresponds to a  $2.9\sigma$  ( $1.6\sigma$ ) local (global) significance. Such an excess, despite the limited number of events, is interesting for mainly two reasons: first, it is located at relative high values of  $M_R$  ( $\sim 400$  GeV) and low values of  $R^2$  (below 0.05), see 8.5 for more detail, and therefore suggest a characteristic mass scale and

that they contain relative low  $E_T^{\text{miss}}$  values. second, that the diphoton invariant mass is consistent with that of the SM Higgs boson and therefore any possible model to explain such an excess should at least contain a one SM Higgs boson. The diphoton invariant mass for the events that lie in the bin with the excess are shown in 8.6. The search presented in this Chapter is largely inspired on its 8 TeV counterpart, but with significant differences when it comes to the backgrounds estimation techniques. In addition, the proposed simplified model shown in Figure 8.1 – which is studied in great detail in Chapter ?? – shows some consistency with the excess observed in the 8 TeV CMS result.

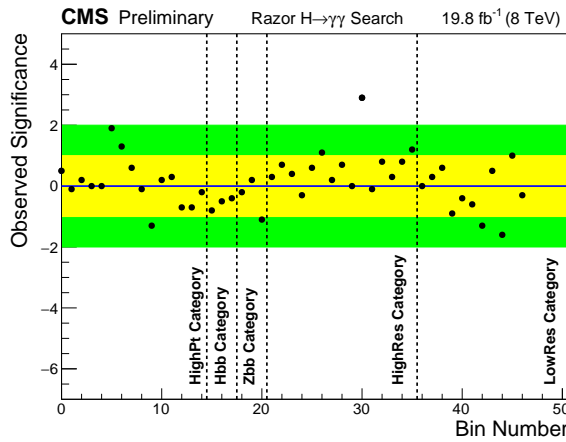


Figure 8.2: Summary of the results in the HighRes category for the 8 TeV version of the analysis.

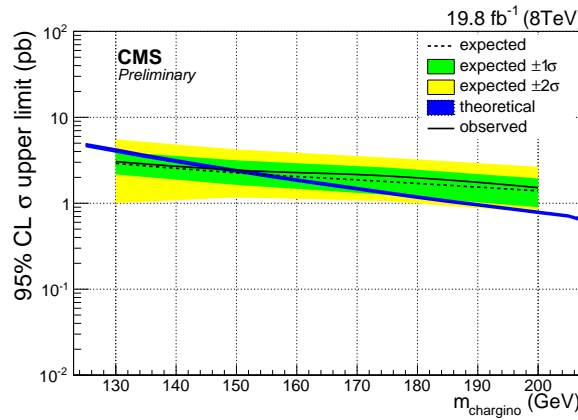


Figure 8.3: Summary of the results in the HighRes category for the 8 TeV version of the analysis.

$M_R$ region	$R^2$ region	observed events	expected background	p-value	significance ( $\sigma$ )
150 - 250	0.00 - 0.05	363	$357.6^{+5.6}_{-5.4}$ (syst.)	0.40	0.3
150 - 250	0.05 - 0.10	149	$139.4^{+5.6}_{-5.4}$ (syst.)	0.23	0.7
150 - 250	0.10 - 0.15	35	$32.5^{+3.1}_{-3.1}$ (syst.)	0.34	0.4
150 - 250	0.15 - 1.00	7	$8.0^{+1.1}_{-1.1}$ (syst.)	0.40	-0.3
250 - 400	0.00 - 0.05	218	$207.9^{+7.0}_{-7.8}$ (syst.)	0.27	0.6
250 - 400	0.05 - 0.10	20	$14.7^{+2.1}_{-2.1}$ (syst.)	0.13	1.1
250 - 400	0.10 - 1.00	3	$2.7^{+0.6}_{-0.6}$ (syst.)	0.43	0.2
400 - 1400	0.00 - 0.05	109	$101.6^{+6.0}_{-6.8}$ (syst.)	0.26	0.7
400 - 1400	0.05 - 1.00	5	$0.5^{+0.4}_{-0.2}$ (syst.)	0.002	2.9
1400 - 3000	0.00 - 1.00	0	$0.9^{+0.3}_{-0.3}$ (syst.)	0.44	-0.1

Figure 8.4: Summary of the results in the HighRes category for the 8 TeV version of the analysis.

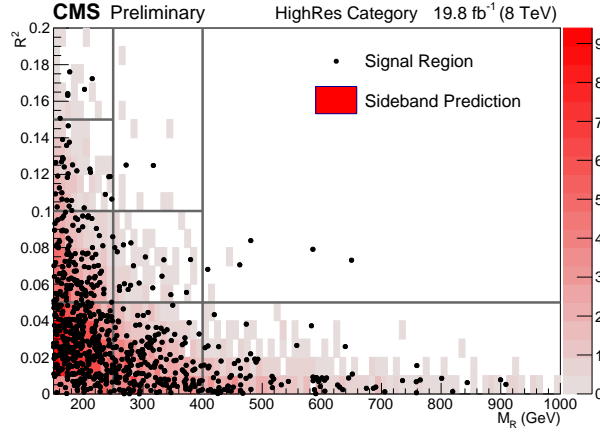


Figure 8.5: Summary of the results in the HighRes category for the 8 TeV version of the analysis.

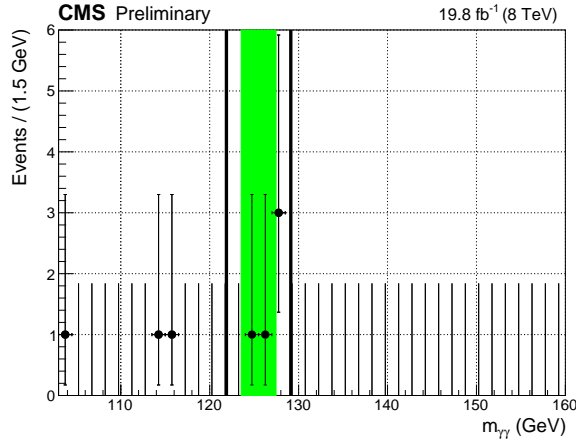


Figure 8.6: Summary of the results in the HighRes category for the 8 TeV version of the analysis.

### 8.3 Object Selection

Photon candidates with  $p_T > 25$  GeV falling in the barrel region ( $|\eta| < 1.4442$ ) are selected if they satisfy identification requirements based on the shower shape in the electromagnetic calorimeter, the hadronic to electromagnetic energy ratio, and

the isolation in a cone around the photon direction [153]. To satisfy the isolation requirement, the sum of the energies of PF candidates near the photon must be smaller than a specified cut value. Isolation cuts are placed separately on energy from charged hadrons, neutral hadrons, and photons. Each isolation sum is corrected for the effect of pileup by subtracting the average energy deposited into the isolation cone estimated using a random sampling of energy density in the event. Photon objects are rejected if they match an electron candidate. The photon identification requirements correspond to a loose working point with an efficiency of about 90%.

The measured energies of the photons are corrected for clustering and local geometric effects using an energy regression trained on Monte Carlo simulation [156]. This regression gives a significant improvement to the energy resolution of the photons and provides an estimate of the uncertainty of the energy measurement. This uncertainty estimate is used in this analysis to categorize events into high and low resolution categories.

Jets are reconstructed using a global event description based on the CMS particle flow (PF) algorithm [99, 97]. Individual particles (PF candidates) are reconstructed by combining the information from the inner tracker, the calorimeters, and the muon system. Charged PF candidates associated to a vertex other than the primary one are considered pileup and are rejected. The remaining particles are clustered into jets, using the FASTJET [69] implementation of the anti- $k_T$  [70] algorithm with the distance parameter  $R = 0.4$ . Jets are required not to overlap with either of the two photons; this requirement is imposed by the condition  $\Delta R = \sqrt{(\Delta\eta)^2 + (\Delta\phi)^2} > 0.5$ . The vector sum of the reconstructed  $p_T$  of the PF particles is used to quantify the missing transverse momentum  $\vec{p}_T^{\text{miss}}$  in the event. Events with detector- and beam-related noise that can mimic event topologies with high energy and large  $E_T^{\text{miss}} = |\vec{p}_T^{\text{miss}}|$  are filtered using dedicated noise reduction algorithms [87, 92, 101].

The combined secondary vertex (CSV) tagging algorithm [185] is used to identify jets originating from the showering and hadronization of b quarks. A loose working point is used which yields a mistag rate that is approximately 10%. Jet pairs are identified as  $b\bar{b}$  candidates if the two jets satisfy the CSV requirement. Among all  $b\bar{b}$  candidates in the event (if there are any), the pair with mass closest to 125 GeV (91.2 GeV) is chosen as a  $H \rightarrow b\bar{b}$  ( $Z \rightarrow b\bar{b}$ ) candidate. Events are not required to contain a  $b\bar{b}$  pair; the presence or absence of a  $H \rightarrow b\bar{b}$  or  $Z \rightarrow b\bar{b}$  candidate with mass in the specified range is used in the event classification procedure described in Section 8.4.

## 8.4 Event Selection and Analysis Strategy

We select events with two photons that satisfy the identification criteria described above. If multiple photon pairs are identified, the pair with the largest scalar sum of the transverse momenta of the photons is chosen as the Higgs candidate. The Higgs candidate must additionally have leading photon  $p_T$  greater than 40 GeV, and diphoton mass between 103 GeV and 160 GeV.

In addition to the diphoton Higgs candidate, we require at least one additional jet with  $p_T > 30$  GeV and  $|\eta| < 3.0$ . The Higgs candidate and all identified jets are clustered into hemispheres according to the Razor *megajet* algorithm[94], and the razor variables [85, 196]  $M_R$  and  $R^2$  are computed as follows:

$$M_R \equiv \sqrt{(|\vec{p}^{j_1}| + |\vec{p}^{j_2}|)^2 - (p_z^{j_1} + p_z^{j_2})^2}, \quad (8.1)$$

$$R^2 \equiv \left( \frac{M_T^R}{M_R} \right)^2, \quad (8.2)$$

where  $\vec{p}$  is the momentum of a hemisphere and  $p_z$  is its longitudinal component, and  $j_1$  and  $j_2$  are used to label the two hemispheres. In the definition of  $R^2$ , the variable  $M_T^R$  is defined as:

$$M_T^R \equiv \sqrt{\frac{E_T^{\text{miss}}(p_T^{j_1} + p_T^{j_2}) - \vec{p}_T^{\text{miss}} \cdot (\vec{p}_T^{j_1} + \vec{p}_T^{j_2})}{2}}. \quad (8.3)$$

The razor variables  $M_R$  and  $R^2$  provide discrimination between SUSY signal models and standard model background processes. SUSY signals typically have large values of  $M_R$  and  $R^2$ , while the standard model background exhibits an exponentially falling spectrum in both variables.

The selected events are categorized into four mutually exclusive categories. An event is categorized as “HighPt” if the  $p_T$  of the selected Higgs candidate is larger than 110 GeV. Otherwise it is categorized as “H( $\gamma\gamma$ )-H/Z(bb)” if the event contains two b-tagged jets whose invariant mass is in the Z mass region between 76 GeV and 106 GeV, or in the Higgs mass region between 110 GeV and 140 GeV. Remaining events are categorized as “HighRes” (“LowRes”) if the mass resolution estimate  $\sigma_M/M$  is less (greater) than 0.85%, where  $\sigma_M$  is computed as  $1/2 \times \sqrt{(\sigma_{E,\gamma 1}/E_{\gamma 1})^2 + (\sigma_{E,\gamma 2}/E_{\gamma 2})^2}$ . The “HighPt” category is intended to isolate events from SUSY signals that produce high- $p_T$  Higgs bosons. The “H( $\gamma\gamma$ )-H/Z(bb)” category is motivated by the fact that many SUSY signal models predict events with two Higgs bosons or a Higgs boson and a Z boson in the final state.

Finally, the ‘‘HighRes’’ and ‘‘LowRes’’ categories are intended to capture other SUSY signals, including compressed models. The categorization procedure is illustrated in Figure 8.7.

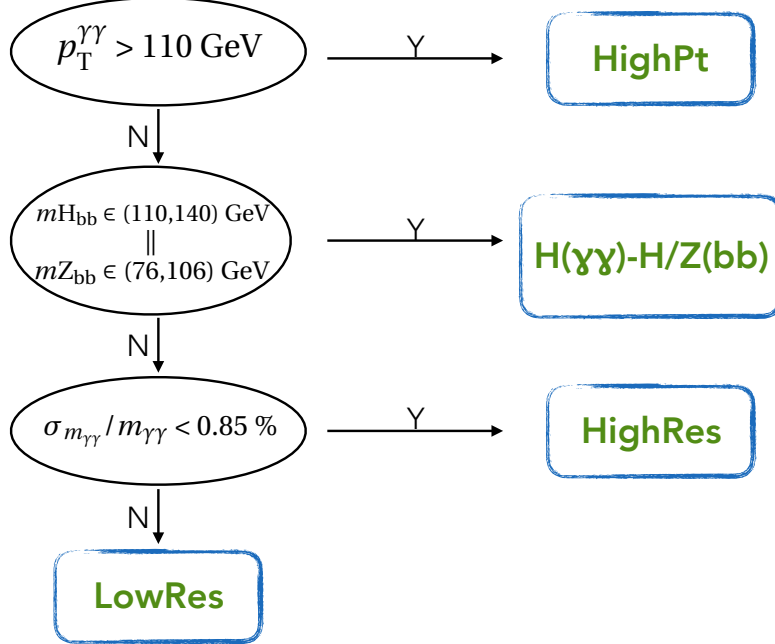


Figure 8.7: Diagram illustrating the event categorization used in the analysis.

Each event category is divided into bins by rectangular cuts on  $M_R$  and  $R^2$ . The binning is chosen via an optimization procedure that uses the sbottom pair production simplified model discussed in Section A.1 as a benchmark model to determine the best bin boundaries. The algorithm begins with a single bin covering the entire  $M_R$ - $R^2$  plane. A division is made in either  $M_R$  or  $R^2$  at the value, which maximizes the expected statistical significance. This process is repeated on each newly created bin, and until convergence is achieved. Each bin returned by the algorithm is treated as a separate analysis search region. This procedure is not performed on the LowRes category; the binning in the LowRes category is instead taken to be the same as that in the HighRes category. The definition of the individual search regions is summarized in Table 8.1.

To illustrate how events from a typical SUSY signal might be distributed in these bins, the distribution of events in the  $M_R$  and  $R^2$  plane for the sbottom pair production signal model discussed in Section A.1 is shown in Figures 8.8 and 8.9 for the HighPt, HighRes, and LowRes categories, respectively.

Table 8.1: A summary of the search region bins in each category is presented. The functional form used to model the non-resonant background is also listed. An exponential function of the form  $e^{-ax}$  is denoted as “singleExp”; a modified exponential function of the form  $e^{-ax^b}$  is denoted as “modExp”; and an N’th order Bernstein polynomial is denoted by “polyN”.

Bin Number	Category	$M_R$ Bin	$R^2$ Bin	Non-Resonant Bkg Model
0	HighPt	600 - $\infty$	0.025 - $\infty$	poly3
1	HighPt	150 - 600	0.130 - $\infty$	singleExp
2	HighPt	1250 - $\infty$	0.000 - 0.025	poly2
3	HighPt	150 - 450	0.000 - 0.130	poly2
4	HighPt	450 - 600	0.000 - 0.035	singleExp
5	HighPt	450 - 600	0.035 - 0.130	singleExp
6	HighPt	600 - 1250	0.000 - 0.015	singleExp
7	HighPt	600 - 1250	0.015 - 0.025	singleExp
8	H( $\gamma\gamma$ )-H/Z(bb)	150 - $\infty$	0.000 - $\infty$	singleExp
9	HighRes	150 - 250	0.000 - 0.175	modExp
10	HighRes	150 - 250	0.175 - $\infty$	singleExp
11	HighRes	250 - $\infty$	0.05 - $\infty$	singleExp
12	HighRes	250 - 600	0.000 - 0.05	modExp
13	HighRes	600 - $\infty$	0.000 - 0.05	singleExp
9	LowRes	150 - 250	0.000 - 0.175	modExp
10	LowRes	150 - 250	0.175 - $\infty$	singleExp
11	LowRes	250 - $\infty$	0.05 - $\infty$	modExp
12	LowRes	250 - 600	0.000 - 0.05	modExp
13	LowRes	600 - $\infty$	0.000 - 0.05	singleExp

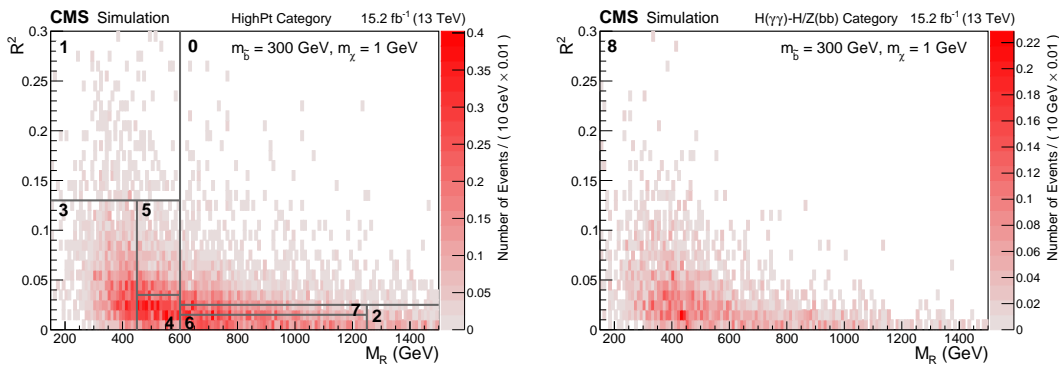


Figure 8.8: Distribution of events in the  $M_R$  and  $R^2$  plane for the HighPt and H( $\gamma\gamma$ )-H/Z(bb) category for sbottom pair production with  $m_{\tilde{b}} = 300$  GeV and  $m_\chi = 1$  GeV. The signal expectation is shown in the color scale and the bin numbers show where each bin is located in the  $M_R$  and  $R^2$  plane.

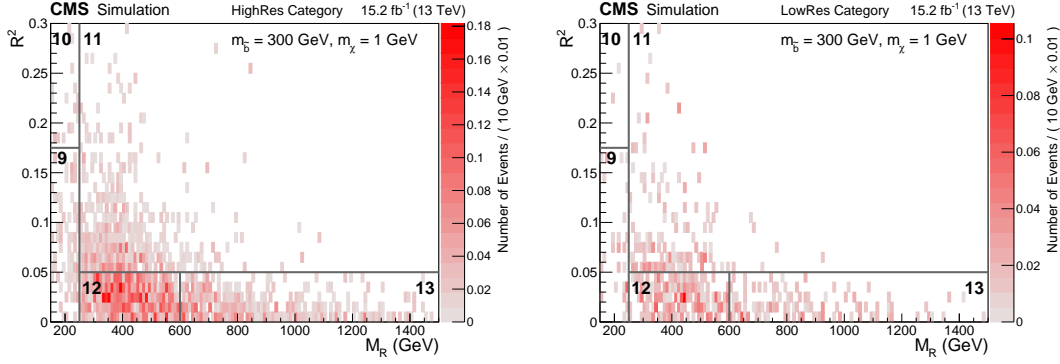


Figure 8.9: Distribution of events in the  $M_R$  and  $R^2$  plane for the HighRes and LowRes categories for sbottom pair production with  $m_{\tilde{b}} = 300$  GeV and  $m_\chi = 1$  GeV. The signal expectation is shown in the color scale and the bin numbers show where each bin is located in the  $M_R$  and  $R^2$  plane.

## 8.5 Background Estimation

Within each search bin, we extract a potential signal by fitting to the diphoton mass spectrum. There are two types of backgrounds: a non-resonant background that is primarily due to QCD production of two photons or one photon and one jet, and a resonant background from standard model Higgs production. The non-resonant background is modeled with the functional form given in Table 8.1 for each individual search region bin, and all parameters of the function are unconstrained in the fit. The functional form model for each search region bin is selected on the basis of its Akaike Information Criterion (AIC) score [31], as well as tests of fit biases for a set of alternative models that all describe the data in the sideband well.

The standard model Higgs background and the SUSY signal are each modeled with a double-sided crystal ball function fit to the diphoton mass distribution obtained from the Monte Carlo simulation. The parameters of each double-sided crystal ball function are held constant in the signal extraction procedure, with the exception of the parameter that determines the location of the peak. This parameter is allowed to float but is restricted via a Gaussian constraint to the region around the Higgs mass. The width of the Gaussian constraint is 1%, corresponding to the systematic uncertainty on the photon energy scale.

The normalization of the standard model Higgs background in each bin is predicted from the Monte Carlo simulation, and is constrained to that value in the fit within uncertainties. Signal yields are also predicted from the Monte Carlo simulation.

Each bin in the HighRes category is fit simultaneously with the corresponding bin

in the LowRes category. The relative SM Higgs and SUSY signal yields in the two categories are constrained according to the simulation prediction. The ratio of the yields in the HighRes and LowRes categories is expected to be independent of the signal model and background process.

Nuisance parameters for various theoretical and instrumental uncertainties that can affect the SM Higgs and signal normalization and are profiled to propagate systematic uncertainties. A more detailed discussion of systematic uncertainties can be found below in Section 8.7. The Monte Carlo simulation predictions for the standard model Higgs background normalization are shown in Table 8.2 for each search region bin.

## 8.6 Non-resonant Background Functional Form Selection: AIC Criterion and Bias Tests

For each signal region – i.e. every  $M_R$ - $R^2$  bin in the search – a functional form is needed to estimate the non-resonant contribution from SM QCD production. This selection process has two steps: 1) the AIC criterion, and 2) the bias test.

The AIC criterion step is used to decide what functions described reasonable well the observed data and therefore describe better the QCD background in each signal region. The AIC criterion, first introduced by Akaike in 1973 [31], is an estimate of the Kullback–Leibler divergence [**KLbook**] – the later is a measure of the distance between two probability density functions. Therefore the AIC criterion is a measure of the distance between the data and a particular probability density function (p.d.f). An advantage over other goodness of fit quantities is that the AIC criterion also accounts for the fact that a function may have move free parameters and thus more flexibility to accomodate the observed data. It is useful to define the AIC score:

$$\text{AIC}_i = -2\log(\mathcal{L}) + 2k - \frac{2k(k+1)}{n-k-1}, \quad (8.4)$$

where  $i$  represents the  $i$ -th p.d.f under study,  $\mathcal{L}$  is the likelihood after the minimization process,  $k$  is the number of free parameters of the p.d.f, and  $n$  is the total numer of observed events. The procedure is as follows: from a set of functions, all AIC scores are computed, then AIC score differences with respect of the minumum AIC score ( $\Delta_i = \text{AIC}_i - \text{AIC}_{\min}$ ) are calculated. The AIC weight, which could be interpreted as the probability that the p.d.f under study is the true p.d.f from were the observed

dataset was drawn, is defined as

$$\omega_i = \frac{e^{-\frac{1}{2}\Delta_i}}{\sum_{j=0}^7 e^{-\frac{1}{2}\Delta_j}}. \quad (8.5)$$

Only p.d.fs with AIC weight larger than 0.1 pass the first step and are then tested for the bias test described below. Table 8.3 shows the full list of p.d.fs used in these studies. Tables 8.4, 8.5, 8.6, and 8.7 summarize four examples of the AIC results obtained for four search regions – one per each category in the analysis –, Figures 8.10, 8.11, 8.12, and 8.13 show the corresponding fits to the observed data. It is of note that the AIC fits are done only to the  $m_{\gamma\gamma} \in \{[103 - 121], [129 - 160]\}$  GeV region.

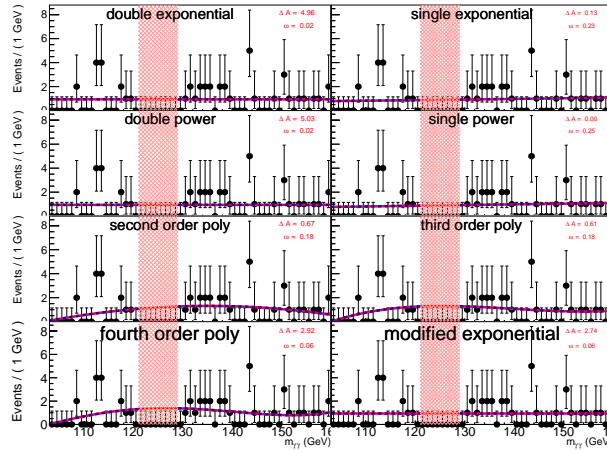


Figure 8.10: sideband fits for the search region: HighPt,  $M_R > 600$  GeV,  $R^2 > 0.025$ .

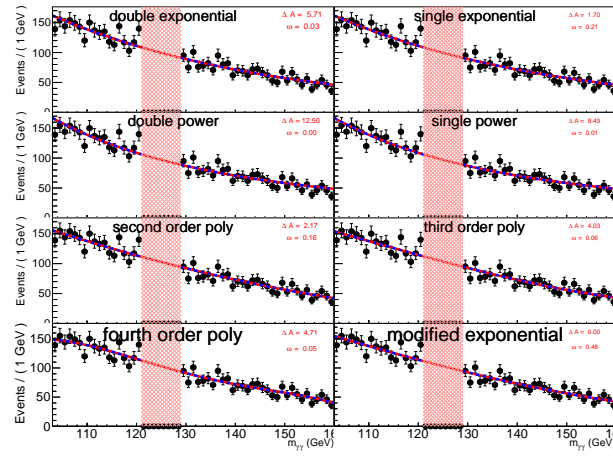


Figure 8.11: sideband fits for the search region: HighRes,  $150 < M_R < 250$  GeV,  $R^2 > 0$

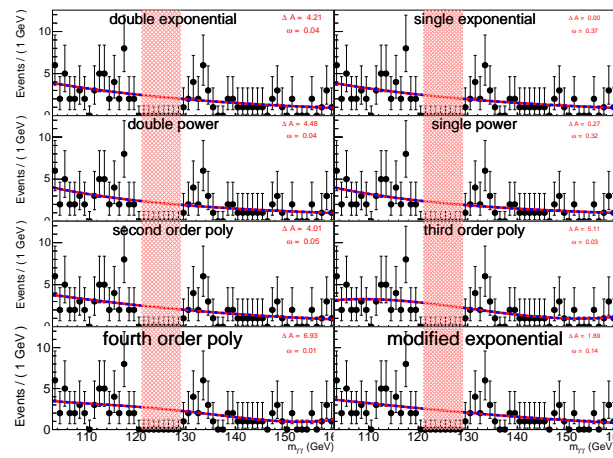


Figure 8.12: Sideband fits for the search region: LowRes,  $150 < M_R < 250$  GeV,  $R^2 > 0.175$ .

Table 8.2: The predicted yields for the standard model Higgs background processes are shown for an integrated luminosity corresponding to  $15.2 \text{ fb}^{-1}$  for each search region considered in this analysis. The contributions from each standard model Higgs process is shown separately, and the total is shown on the rightmost column along with its full uncertainty.

Bin	Category	Expected SM Higgs Yield					Total
		ggH	$t\bar{t}\text{H}$	VBF H	VH	bbH	
0	HighPt	1.09	0.49	0.17	0.25	0.01	$2.0 \pm 0.4$
1	HighPt	0.45	0.22	0.07	0.60	0.00	$1.4 \pm 0.3$
2	HighPt	1.75	0.23	0.89	0.07	0.02	$3.0 \pm 0.6$
3	HighPt	20.82	0.38	4.05	2.36	0.16	$27.7 \pm 8.0$
4	HighPt	6.30	0.20	1.77	0.45	0.06	$8.8 \pm 2.5$
5	HighPt	1.09	0.23	0.18	0.19	0.01	$1.7 \pm 0.4$
6	HighPt	7.15	0.21	2.91	0.28	0.05	$10.7 \pm 2.7$
7	HighPt	1.94	0.19	0.37	0.17	0.01	$2.7 \pm 0.8$
8	$\text{H}(\gamma\gamma)\text{-H/Z(bb)}$	0.35	0.51	0.03	0.10	0.06	$1.0 \pm 0.2$
9	HighRes	27.57	0.10	3.49	1.97	0.43	$33.5 \pm 10.4$
10	HighRes	0.26	0.06	0.04	0.20	0.01	$0.6 \pm 0.1$
11	HighRes	0.94	0.33	0.21	0.19	0.05	$1.7 \pm 0.4$
12	HighRes	16.16	0.31	3.99	0.64	0.39	$21.5 \pm 5.4$
13	HighRes	1.83	0.23	1.25	0.10	0.09	$3.5 \pm 1.0$
9	LowRes	9.55	0.039	1.18	0.72	0.14	$11.6 \pm 3.8$
10	LowRes	0.12	0.02	0.01	0.07	0.00	$0.2 \pm 0.1$
11	LowRes	0.32	0.11	0.06	0.08	0.02	$0.6 \pm 0.2$
12	LowRes	6.02	0.11	1.46	0.24	0.12	$7.9 \pm 2.3$
13	LowRes	0.82	0.09	0.46	0.04	0.03	$1.4 \pm 0.4$

Table 8.3: Full list of p.d.f (function) used in the AIC test.

function name	short name	functional form
single exponential	singleExp	$e^{-\alpha m_{\gamma\gamma}}$
double exponential	doubleExp	$fe^{-\alpha_1 m_{\gamma\gamma}} + (1-f)e^{-\alpha_2 m_{\gamma\gamma}}$
single power law	singlePow	$m_{\gamma\gamma}^{-\alpha}$
double power law	doublePow	$fm_{\gamma\gamma}^{-\alpha_1} + (1-f)m_{\gamma\gamma}^{-\alpha_2}$
modified exponential	modExp	$e^{-\alpha m_{\gamma\gamma}^\beta}$
Bernstein polynomial order 2	poly2	$p_0(1-t)^2 + p_1 2t(1-t) + p_2 t^2$
Bernstein polynomial order 3	poly3	$p_0(1-t)^3 + p_1 3t(1-t)^2 + p_2 3t^2(1-t) + p_3 t^3$
Bernstein polynomial order 4	poly4	$p_0(1-t)^4 + p_1 4t(1-t)^3 + p_2 6t^2(1-t)^2 + p_3 4t^3(1-t) + p_4 t^4$

Table 8.4: AIC results summary for the search region: HighPt,  $M_R > 600 \text{ GeV}$ ,  $R^2 > 0.025$ .

function	#P	$\Delta AIC$	$\omega$	$\omega_{max}/\omega$	status
singlePow	1	0.000	0.247	1.000	0, 3
singleExp	1	0.128	0.232	1.066	0, 3
poly3	4	0.605	0.183	1.353	0, 3
poly2	3	0.673	0.177	1.400	0, 3
modExp	2	2.738	0.063	3.932	0, 3
poly4	5	2.916	0.058	4.297	0, 3
doubleExp	3	4.958	0.021	11.929	0, 3
doublePow	3	5.031	0.020	12.371	0, 3

Table 8.5: AIC results summary for the search region: HighRes,  $150 < M_R < 250 \text{ GeV}$ ,  $R^2 > 0$ .

function	#P	$\Delta AIC$	$\omega$	$\omega_{max}/\omega$	status
modExp	2	0.000	0.484	1.000	1, 2
singleExp	1	1.704	0.206	2.344	0, 3
poly2	3	2.173	0.163	2.964	0, 3
poly3	4	4.028	0.065	7.492	1, 2
poly4	5	4.714	0.046	10.560	0, 3
doubleExp	3	5.708	0.028	17.359	1, 2
singlePow	1	8.492	0.007	69.817	0, 3
doublePow	3	12.496	0.001	517.007	0, 3

Table 8.6: AIC results summary for the search region: LowRes, LowRes,  $150 < M_R < 250 \text{ GeV}$ ,  $R^2 > 0.175$

function	#P	$\Delta AIC$	$\omega$	$\omega_{max}/\omega$	status
singleExp	1	0.000	0.529	1.000	0, 3
modExp	2	1.883	0.206	2.564	1, 2
doubleExp	3	3.646	0.085	6.191	0, 3
singlePow	1	3.698	0.083	6.353	0, 3
poly2	3	4.925	0.045	11.736	0, 3
poly3	4	5.892	0.028	19.029	0, 3
poly4	5	7.657	0.012	45.992	0, 3
doublePow	3	7.703	0.011	47.065	1, 2

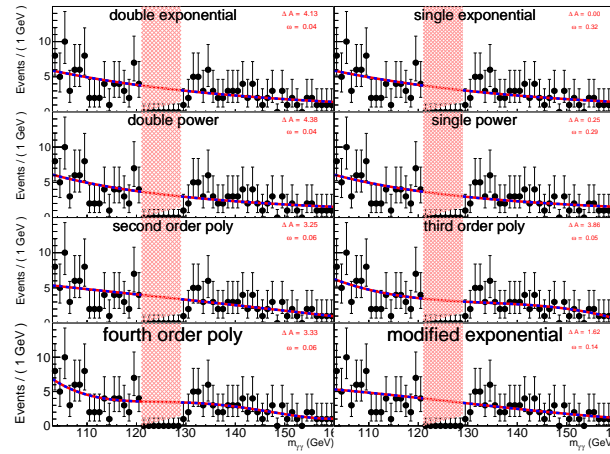


Figure 8.13: Sideband fits for the search region:  $H(\gamma\gamma)-H/Z(bb)$ ,  $M_R > 150 \text{ GeV}$ ,  $R^2 > 0$ .

Table 8.7: AIC results summary for the search region:  $H(\gamma\gamma)-H/Z(bb)$ ,  $M_R > 150 \text{ GeV}$ ,  $R^2 > 0$ .

function	#P	$\Delta AIC$	$\omega$	$\omega_{max}/\omega$	status
singleExp	1	0.000	0.323	1.000	0, 3
singlePow	1	0.247	0.285	1.131	0, 3
modExp	2	1.619	0.144	2.247	1, 2
poly2	3	3.252	0.063	5.083	0, 3
poly4	5	3.334	0.061	5.297	0, 3
poly3	4	3.858	0.047	6.881	0, 3
doubleExp	3	4.134	0.041	7.901	0, 3
doublePow	3	4.382	0.036	8.946	0, 3

The second step is the bias test, where only functions that passed the AIC test are considered. The bias test quantifies the error on the measured signal made when performing a signal-plus-background fit to the entire  $m_{\gamma\gamma}$  region in the final stage of the analysis. By requiring the selected function to have a small bias relative to any of the functions passing the AIC test, the error on the measured signal strength is reduced. In this analysis, the bias is defined relative to the fit uncertainty on the signal, i.e.

$$\delta_s = \frac{\hat{N}_s - N_s}{\sigma_{N_s}}, \quad (8.6)$$

where  $\hat{N}_s$  is the fitted signal,  $N_s$  is the actual value of the signal, and  $\sigma_{N_s}$  is the uncertainty on  $\hat{N}_s$ . The bias estimation is obtained by carrying a large number of pseudo-experiments (toys), each function passing the AIC test will be treated as the parent function from where the data was drawn, then several (10,000) toy datasets will be drawn from it containing the same amount of event as in the real dataset. For each toy dataset a known number of signal event will be injected ( $N_s$ ) and a signal-plus-background fit will be carried out and the bias will be calculated. After this procedure is done, the resulting bias distribution will be fitted with a double-sided crystal ball function, where the most probable value after the fit is taken as an estimate of the bias. Figure 8.14 shows the resulting bias distribution and fit for two different cases. The studies carried out indicate that the most stringent test occurs when the number of injected signal events is small (signal to background ratio or S/B equal to zero) and therefore the results shown here correspond to that case. Table 8.8 shows the bias estimates for one of the search regions, where you can see the relative biases for all possible function passing the AIC test. Finally, the function with the least number of free parameters and having a relative bias smaller than 30% – which yield only an additional error of 5% – is selected as the background model. The final selection for all the signal regions is shown in Table 8.9.

## 8.7 Systematic Uncertainties

The dominant systematic uncertainty is the uncertainty on the prediction of the non-resonant background shape and normalization. These are propagated by profiling the overall normalization and the shape parameters of the non-resonant background functional form.

Sub-dominant systematic uncertainties on the SM Higgs background are propagated through log-normal nuisance parameters, and take into account both theoretical and instrumental effects. The effects considered include missing higher order correc-

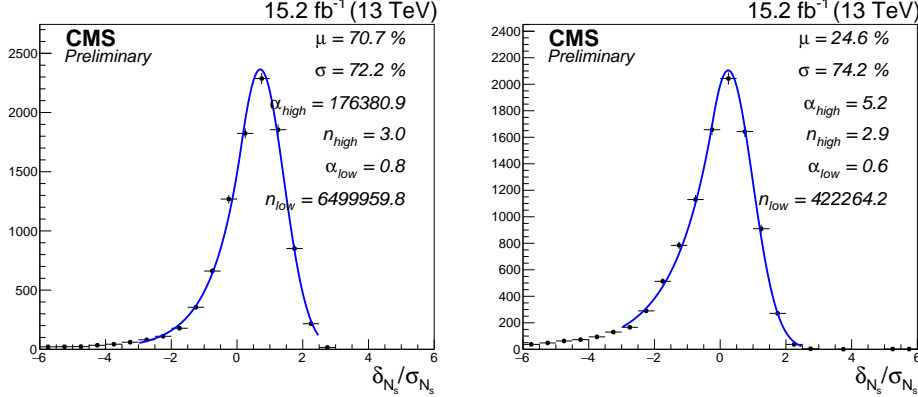


Figure 8.14: Examples of the bias distribution for bin0 ( $\text{HighPt}$ ,  $M_R > 600$ ,  $R^2 > 0.025$ ). Left:  $f_1$  (assumed parent function) = poly3,  $f_2$  (tested function) = singleExp; right:  $f_1$  = poly3,  $f_2$  = poly3. From the left plot we can see that singleExp does not pass the bias test since it has large bias to fit poly3.

Table 8.8: Examples of the bias estimate for different function pairs passing the AIC test for bin0 ( $\text{HighPt}$ ,  $M_R > 600$ ,  $R^2 > 0.025$ ). Functions in the first column are the assumed parent functions ( $f_1$ ), while functions in the first row are the ones being tested ( $f_2$ ). In the first row, the numbers in brackets are the AIC weights.

-	singlePow(0.247)	singleExp(0.232)	poly3(0.183)	poly2(0.177)
singlePow	$(21.3 \pm 1.0)\%$	$(19.3 \pm 1.0)\%$	$(17.8 \pm 1.0)\%$	$(18.5 \pm 1.4)\%$
singleExp	$(22.9 \pm 2.0)\%$	$(18.3 \pm 1.0)\%$	$(7.9 \pm 1.3)\%$	$(18.7 \pm 2.0)\%$
poly3	$(69.9 \pm 1.5)\%$	$(70.7 \pm 0.9)\%$	$(24.6 \pm 1.3)\%$	$(33.5 \pm 1.0)\%$
poly2	$(60.6 \pm 0.9)\%$	$(62.6 \pm 0.9)\%$	$(15.7 \pm 1.9)\%$	$(17.4 \pm 1.4)\%$

tions, parton distribution functions, trigger and selection efficiencies, jet energy scale uncertainties, b-tagging efficiencies, and the uncertainty on the integrated luminosity. The typical size of these effects on the expected limit is summarized in Table 8.10.

The systematic uncertainty on the photon energy scale is implemented as a nuisance parameter that shifts the Higgs peak position, and is Gaussian constrained in the fit to lie within 1% of the nominal Higgs mass peak predicted by the Monte Carlo simulation. There is also a systematic uncertainty on the shape of the  $\sigma_M/M$  distribution, which allows for migration of SM Higgs background and signal events between the HighRes and the LowRes categories.

Table 8.9: List of the selected background functions for different search regions.

Bin	Category	LowMR	HighMR	LowRsq	HighRsq	Function	AIC weight	Max bias / $\sigma_{\text{stat}}$
0	highpt	600	10000	0.025	10.000	poly3	0.183	24.6%
1	highpt	150	600	0.130	10.000	singleExp	0.356	17.7%
2	highpt	1250	10000	0.000	0.025	singleExp	0.359	16.4%
3	highpt	150	450	0.000	0.130	—	—	—%
4	highpt	450	600	0.000	0.035	poly2	0.324	-24.2%
5	highpt	450	600	0.035	0.130	singleExp	0.348	16.1%
6	highpt	600	1250	0.000	0.015	singleExp	0.295	-3.6%
7	highpt	600	1250	0.015	0.025	singleExp	0.344	14.8%
8	hzbb	150	2000	0.00	10.000	singleExp	0.323	4.5%
9	highres	150	250	0.000	0.175	—	—	—%
10	highres	150	250	0.175	10.000	poly2	0.132	16.9%
11	highres	250	10000	0.05	10.000	singlePow	0.237	-19.1%
12	highres	250	600	0.000	0.05	singlePow	0.118	25.7%
13	highres	600	10000	0.000	0.05	singleExp	0.256	-3.4%
14	lowres	150	250	0.000	0.175	singleExp	0.529	-3.4%
15	lowres	150	250	0.175	10.000	singleExp	0.365	7.9%
16	lowres	250	10000	0.05	10.000	singleExp	0.358	-13.9%
17	lowres	250	600	0.000	0.05	—	—	—%
18	lowres	600	10000	0.000	0.05	singleExp	0.364	-9.0%

Table 8.10: Summary of systematic uncertainties and their size.

Uncertainty Source	Size
Luminosity	5.7%
PDFs and QCD Scale Variations	15-30%
Trigger and selection efficiency	3%
Jet energy scale	1-5%
Photon Energy Scale	1%
B-tagging efficiency	4%
$\sigma_M/M$ categorization	4%

## 8.8 Results and Interpretations

The fit results for all search regions using the combination of the 2015 dataset ( $2.3 \text{ fb}^{-1}$ ) and the 2016 dataset ( $12.9 \text{ fb}^{-1}$ ) are shown below. Figures 8.15, 8.16, and 8.17 show the results for the HighPt event category. The results for the  $H(\gamma\gamma)$ - $H/Z(bb)$  category are shown in Figure 8.18. Finally, the results for the HighRes and LowRes categories are shown in Figures 8.19 to 8.23.

The data yields, expected background yields, and best fit signal yields are summarized in Table 8.11 for all search region bins, together with the local statistical significance of the excess for each bin. The observed signal significance is summarized in Figure 8.24 for all statistically independent bins. The bin with the largest significance occurs in the HighPt category with  $M_R > 600 \text{ GeV}$  and  $R^2 > 0.025$ , and has a local significance of  $2.5\sigma$ . Accounting for the number of search region

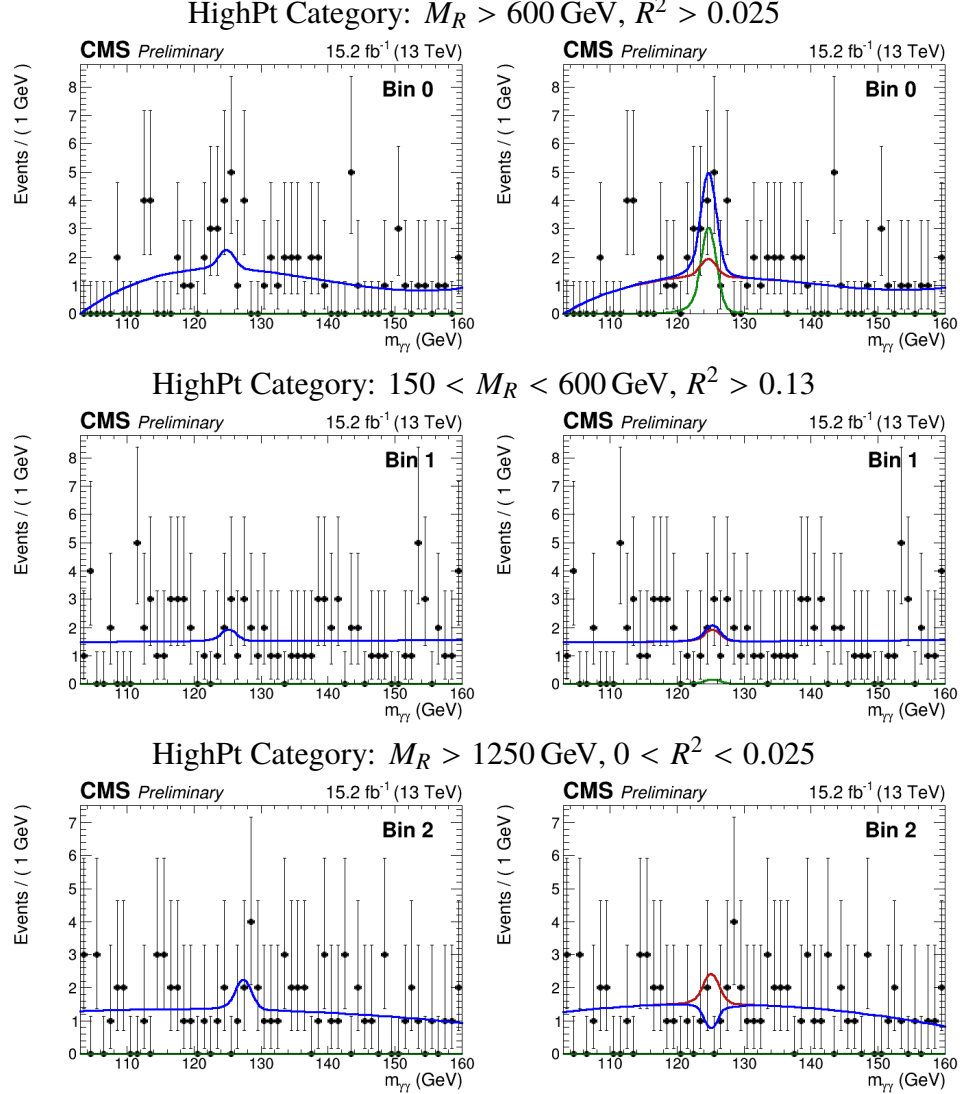


Figure 8.15: The diphoton mass distribution for various search region bins in the HighPt category are shown along with the background-only fit (left) and the signal plus background fit (right). The red curve represents the background prediction; the green curve represents the signal; and the blue curve represents the sum of the signal and background. The definition of the search bin is labeled above each pair of plots.

bins, this corresponds to a global significance of  $1.4\sigma$ .

We interpret these results in terms of limits on the production cross-section times branching ratio for sbottom pair production with a cascade decay to a Higgs boson, a bottom quark, and the LSP. The expected and observed limits on the sbottom pair production cross section is shown in Figure 8.25 as a function of the sbottom mass and the LSP mass. The observe significance is also computed for this simplified

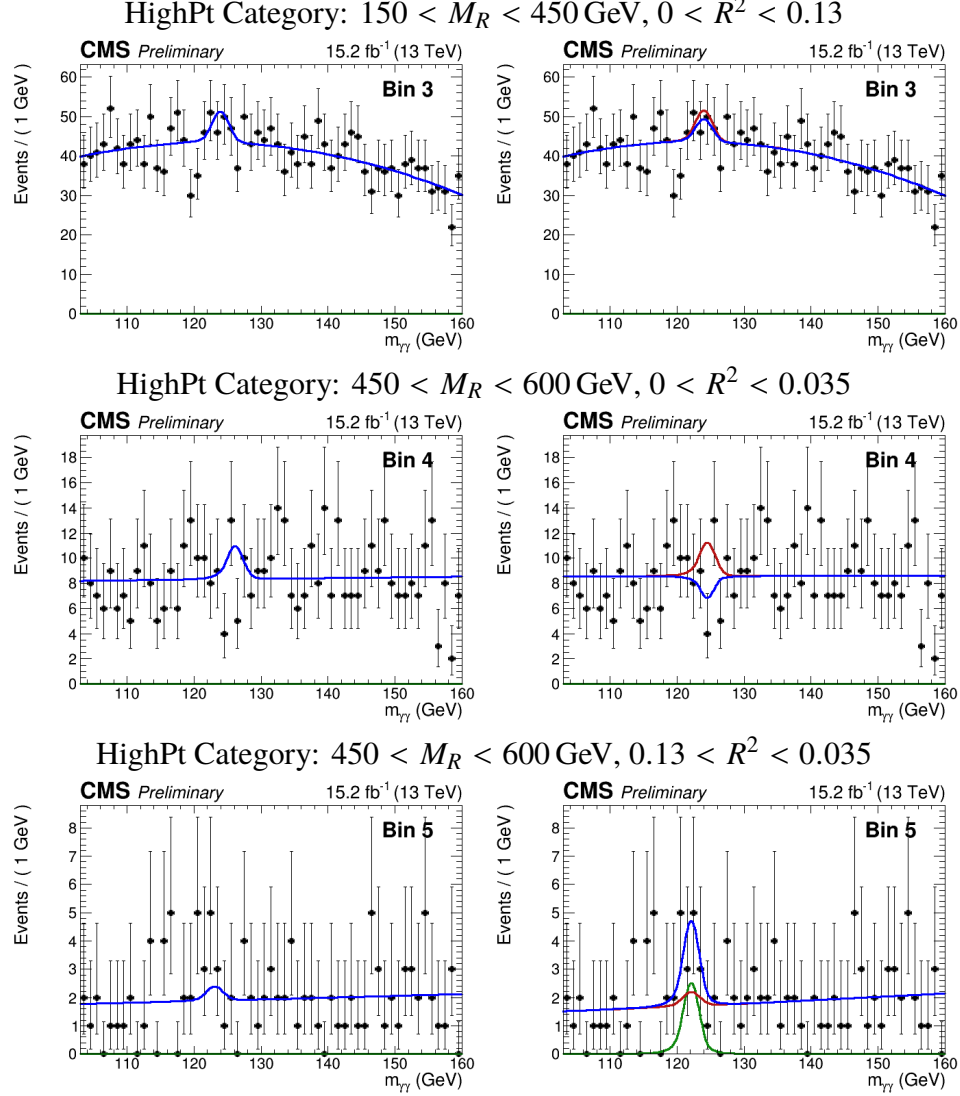


Figure 8.16: The diphoton mass distribution for various search region bins in the HighPt category are shown along with the background-only fit (left) and the signal plus background fit (right). The red curve represents the background prediction; the green curve represents the signal; and the blue curve represents the sum of the signal and background. The definition of the bin is labeled above each pair of plots.

model and shown in Figure 8.26.

## 8.9 Summary

A search for anomalous Higgs boson production through decays of supersymmetric particles is performed with data collected in 2015 and 2016 by the CMS experiment at the CERN LHC. Proton collisions collected at a center-of-mass energy  $\sqrt{s} = 13 \text{ TeV}$  are considered, corresponding to an integrated luminosity of about

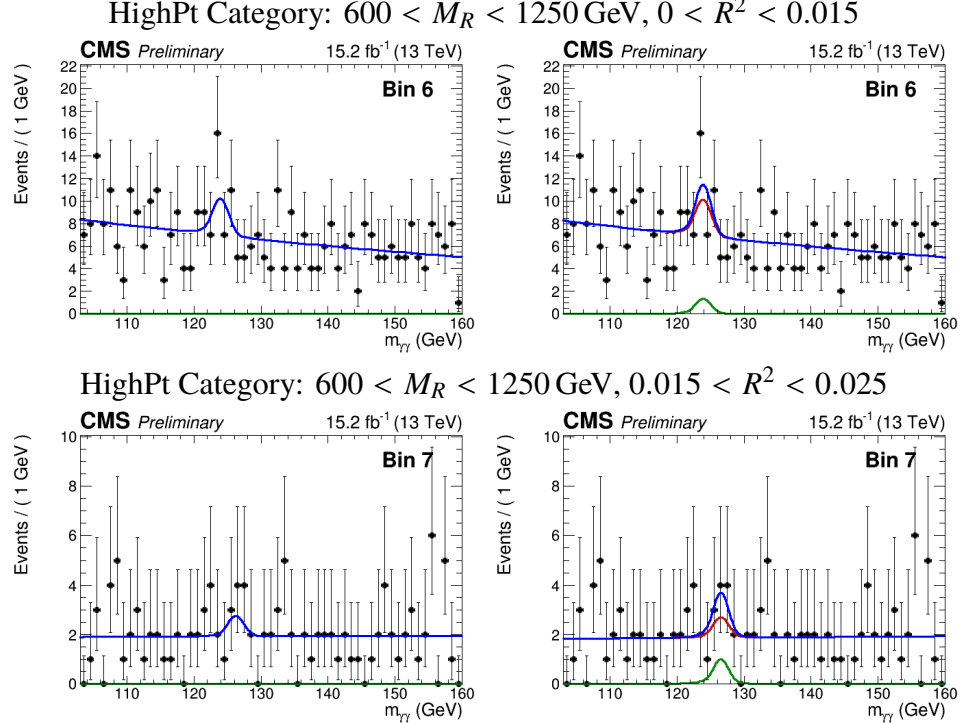


Figure 8.17: The diphoton mass distribution for various search region bins in the HighPt category are shown along with the background-only fit (left) and the signal plus background fit (right). The red curve represents the background prediction; the green curve represents the signal; and the blue curve represents the sum of the signal and background. The definition of the bin is labeled above each pair of plots.

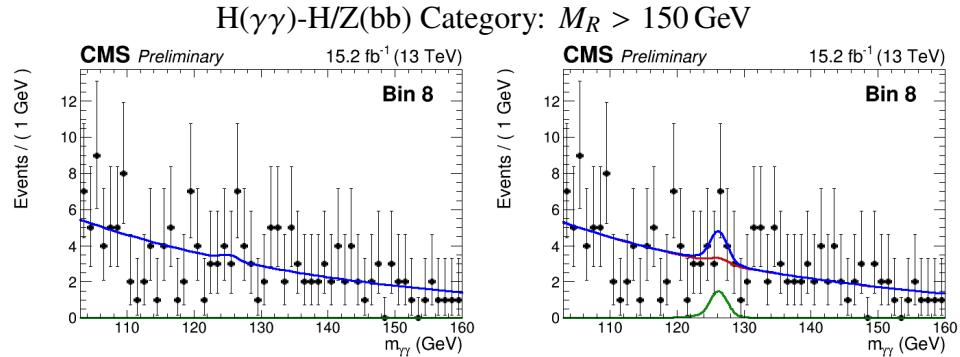


Figure 8.18: The diphoton mass distribution for various search region bins in the H( $\gamma\gamma$ )-H/Z(bb) category are shown along with the background-only fit (left) and the signal plus background fit (right). The red curve represents the background prediction; the green curve represents the signal; and the blue curve represents the sum of the signal and background. The definition of the bin is labeled above each pair of plots.

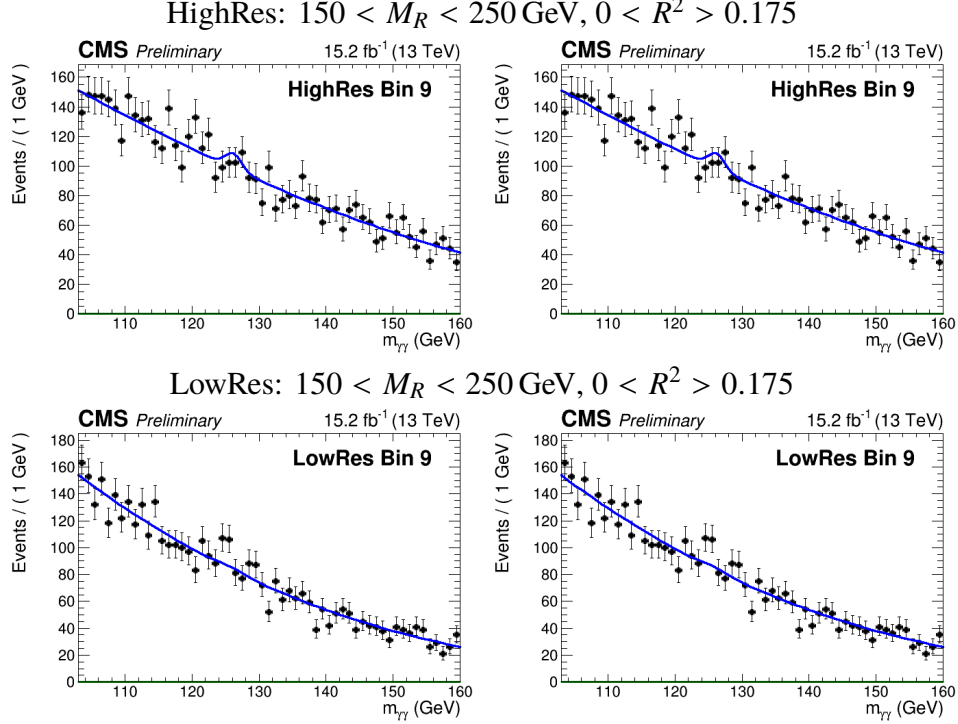


Figure 8.19: The diphoton mass distribution for the search region bin 9 are shown along with the background-only fit (left) and the signal plus background fit (right). The top row shows the HighRes category, while the bottom row shows the LowRes category. The red curve represents the background prediction; the green curve represents the signal; and the blue curve represents the sum of the signal and background. The definition of the bin is labeled above each pair of plots.

$15.2 \text{ fb}^{-1}$  ( $2.3 \text{ fb}^{-1}$  from 2015 and  $12.9 \text{ fb}^{-1}$  from 2016). Higgs boson candidates are reconstructed from pairs of photons in the central part of the detector. The razor variables  $M_R$  and  $R^2$  are used to suppress SM Higgs boson production and other SM processes. The non-resonant background is estimated through a data-driven fit to the diphoton mass distribution using a functional form model selected by a combination of the AIC score and the result of a series of bias tests. The standard model Higgs background is estimated using the Monte Carlo simulation, with systematics on instrumental and theoretical uncertainties propagated. We interpret the results in terms of production cross-section limits on sbottom pair production each decaying to a Higgs boson, a b-quark, and the LSP, and exclude sbottoms with mass below 350 GeV.

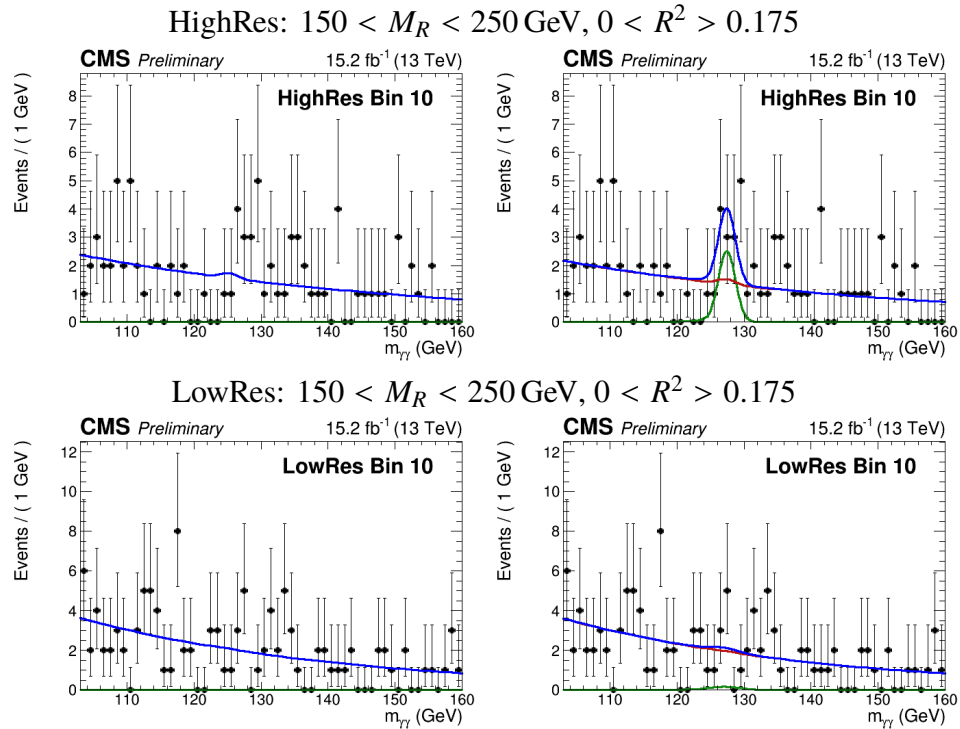


Figure 8.20: The diphoton mass distribution for the search region bin 10 are shown along with the background-only fit (left) and the signal plus background fit (right). The top row shows the HighRes category, while the bottom row shows the LowRes category. The red curve represents the background prediction; the green curve represents the signal; and the blue curve represents the sum of the signal and background. The definition of the bin is labeled above each pair of plots.

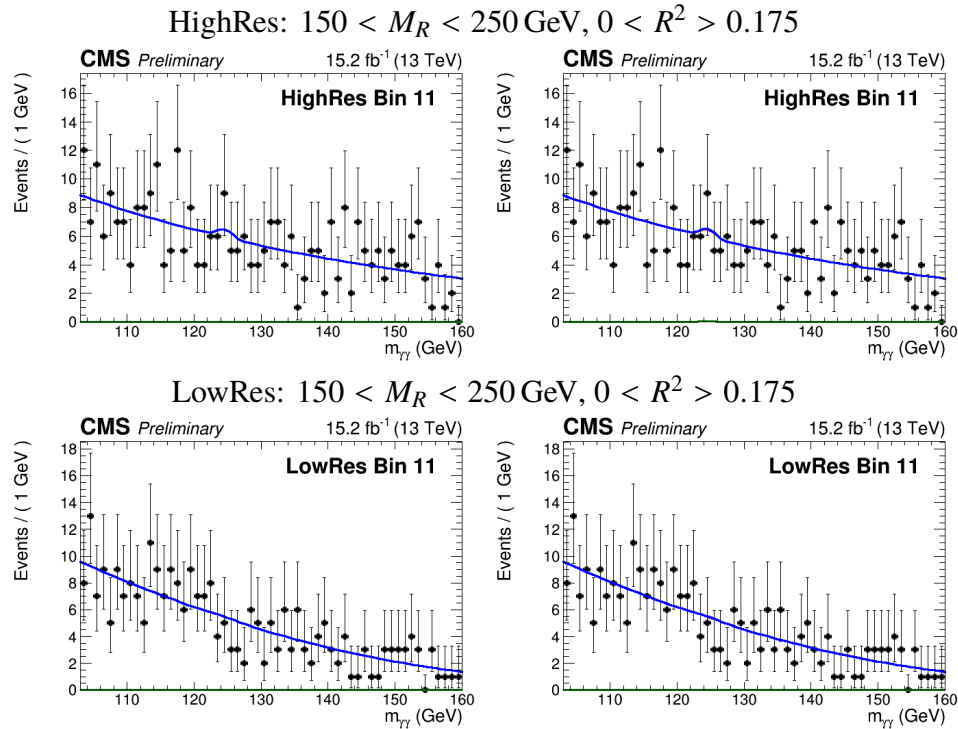


Figure 8.21: The diphoton mass distribution for the search region bin 11 are shown along with the background-only fit (left) and the signal plus background fit (right). The top row shows the HighRes category, while the bottom row shows the LowRes category. The red curve represents the background prediction; the green curve represents the signal; and the blue curve represents the sum of the signal and background. The definition of the bin is labeled above each pair of plots.

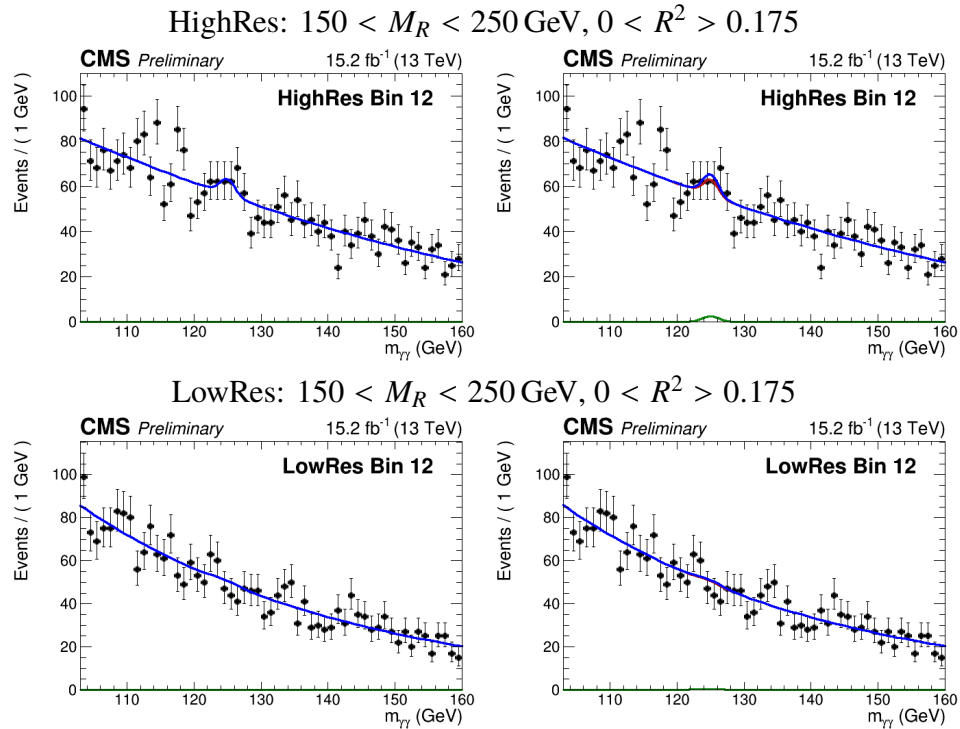


Figure 8.22: The diphoton mass distribution for the search region bin 12 are shown along with the background-only fit (left) and the signal plus background fit (right). The top row shows the HighRes category, while the bottom row shows the LowRes category. The red curve represents the background prediction; the green curve represents the signal; and the blue curve represents the sum of the signal and background. The definition of the bin is labeled above each pair of plots.

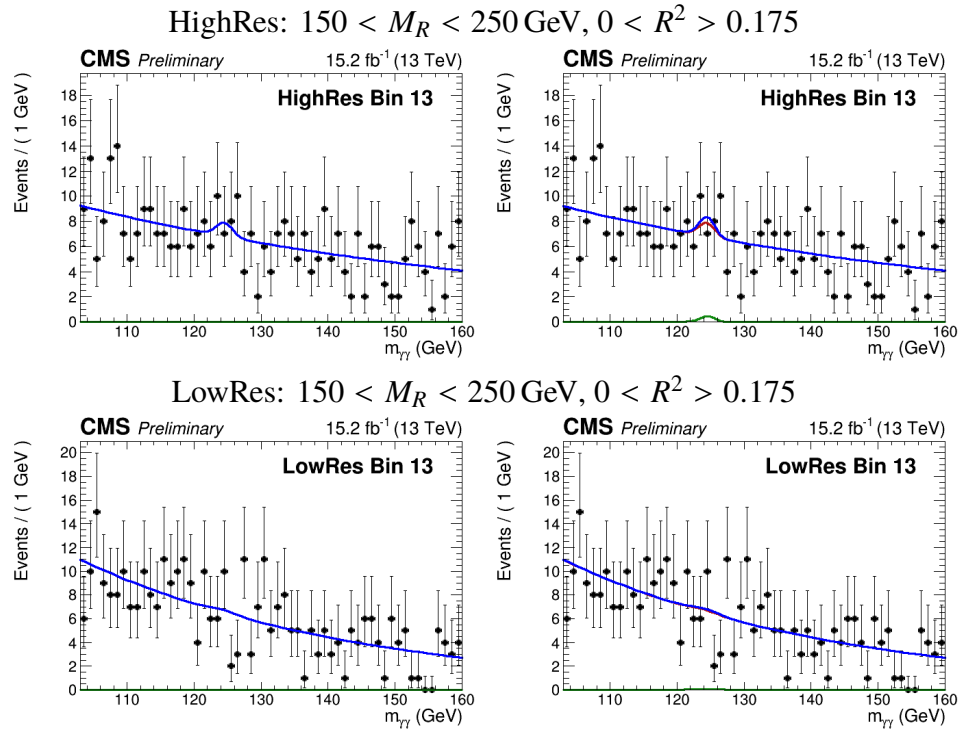


Figure 8.23: The diphoton mass distribution for the search region bin 13 are shown along with the background-only fit (left) and the signal plus background fit (right). The top row shows the HighRes category, while the bottom row shows the LowRes category. The red curve represents the background prediction; the green curve represents the signal; and the blue curve represents the sum of the signal and background. The definition of the bin is labeled above each pair of plots.

Table 8.11: The non-resonant background yields, SM Higgs background yields, best fit signal yields, and observed local significance are shown for the signal plus background fit in each search region bin. The uncertainties include both statistical and systematic components. The non-resonant background yields shown correspond to the yield within the window between 122 GeV and 129 GeV and is intended to better reflect the background under the signal peak. The observed significance for the bins in HighRes and LowRes categories are identical because they are the result of a simultaneous fit. The significance is computed using the profile likelihood, where the sign reflects whether an excess (positive sign) or deficit (negative sign) is observed.

Bin	Category	Yields				Obs. Local Significance
		Non-Resonant Bkg	Exp. SM Higgs	Fitted SM Higgs	Best Fit Signal	
0	HighPt	10.2 ± 1.4	2.0 ± 0.4	2.0 ± 0.7	9.7 ± 5.1	2.5 $\sigma$
1	HighPt	10.5 ± 1.3	1.4 ± 0.3	1.4 ± 0.3	0.5 ± 3.4	0.2 $\sigma$
2	HighPt	10.5 ± 1.6	3.0 ± 0.6	2.9 ± 0.9	-5.2 ± 2.5	-1.4 $\sigma$
3	HighPt	304 ± 16.6	27.7 ± 8.0	27.7 ± 11.2	-7.9 ± 18.1	-0.4 $\sigma$
4	HighPt	60 ± 3.0	8.8 ± 2.5	8.8 ± 3.5	-13.9 ± 6.6	-1.6 $\sigma$
5	HighPt	12.1 ± 1.4	1.7 ± 0.4	1.7 ± 0.6	8.3 ± 4.7	1.9 $\sigma$
6	HighPt	47.6 ± 2.6	10.7 ± 2.7	10.7 ± 3.7	4.1 ± 7.3	0.6 $\sigma$
7	HighPt	13.1 ± 1.4	2.7 ± 0.8	2.7 ± 1.0	3.2 ± 4.1	0.8 $\sigma$
8	H( $\gamma\gamma$ )-H/Z(bb)	21.6 ± 1.8	1.0 ± 0.2	1.0 ± 0.2	5.3 ± 4.6	1.0 $\sigma$
9	HighRes	697 ± 10.6	33.5 ± 10.4	33.2 ± 12.1	0.0 ± 21.4	-0.2 $\sigma$
10	HighRes	9.8 ± 1.2	0.6 ± 0.1	0.6 ± 0.1	8.2 ± 4.1	1.7 $\sigma$
11	HighRes	40.7 ± 2.4	1.7 ± 0.4	1.7 ± 0.6	0.2 ± 5.5	0.0 $\sigma$
12	HighRes	387 ± 14.6	21.5 ± 5.4	21.5 ± 9.1	8.1 ± 14.9	0.5 $\sigma$
13	HighRes	46.8 ± 2.6	3.5 ± 1.0	3.5 ± 1.2	1.3 ± 6.0	0.2 $\sigma$
9	LowRes	591 ± 9	11.6 ± 3.8	11.9 ± 5.1	0.2 ± 10.1	-0.2 $\sigma$
10	LowRes	14.1 ± 1.4	0.2 ± 0.1	0.2 ± 0.1	1.1 ± 0.8	1.7 $\sigma$
11	LowRes	36.6 ± 9.2	0.6 ± 0.3	0.6 ± 0.3	0.1 ± 1.8	0.0 $\sigma$
12	LowRes	341 ± 7	7.9 ± 2.3	7.9 ± 3.5	2.8 ± 5.0	0.5 $\sigma$
13	LowRes	44.3 ± 2.4	1.4 ± 0.4	1.4 ± 0.7	0.5 ± 2.6	0.2 $\sigma$

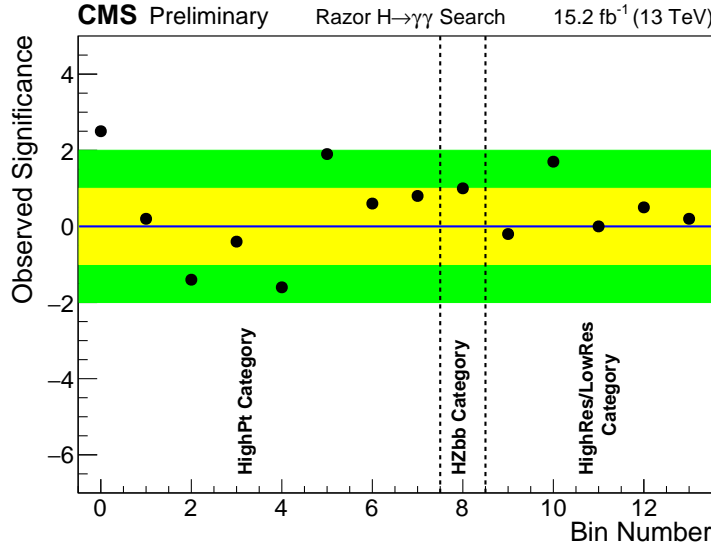


Figure 8.24: The observed significance in units of standard deviations is plotted for each search bin. The significance is computed using the profile likelihood, where the sign reflects whether an excess (positive sign) or deficit (negative sign) is observed. The categories that the bins belong to are labeled at the bottom. The yellow and green bands represent the  $1\sigma$  and  $2\sigma$  regions, respectively.

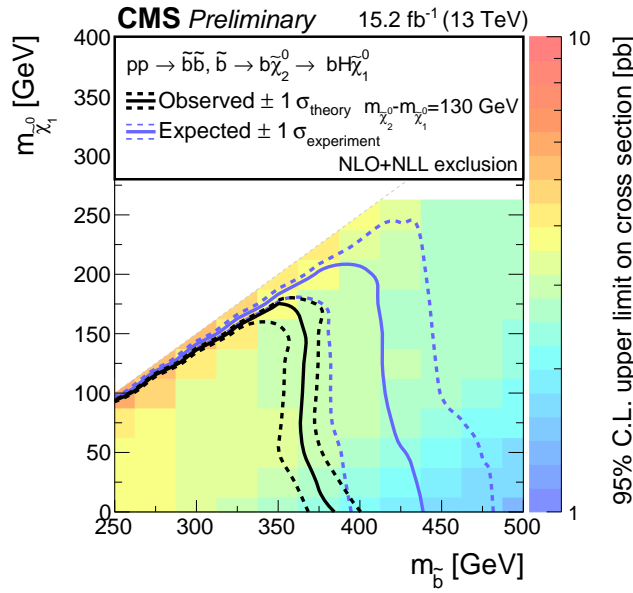


Figure 8.25: The observed 95% confidence level (C.L.) upper limits on the production cross section for sbottom pair production decaying to a bottom quark, a Higgs boson, and the LSP are shown. The solid and dotted black contours represent the observed exclusion region and its  $1\sigma$  bands, while the analogous blue contours represent the expected exclusion region and its  $1\sigma$  bands.

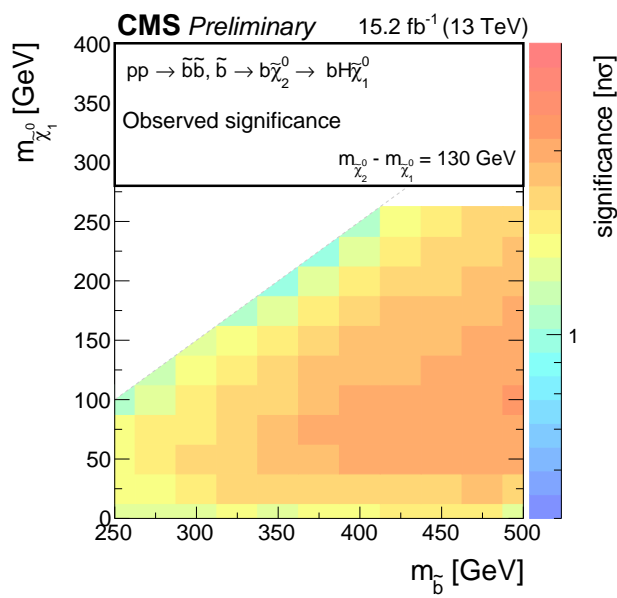


Figure 8.26: The observed significance scan for sbottom pair production decaying to a bottom quark, a Higgs boson, and the LSP is shown.

## **Part IV**

### **Precision Timing Calorimetry**

## C h a p t e r 9

### INTRODUCTION

Calorimeters are a key detector systems in high energy physics experiments ranging from neutrino to particle collider detectors. In particular, electromagnetic (EM) calorimeters are designed to fully contain the energy deposited by electrons, positrons, and photons ( $e/\gamma$ ); as well as to provide position information by means of their granular design. They are usually divided in two types: homogeneous and sampling, homogenous calorimeters are those in which their entire volume is composed of sensitive media, while sampling calorimeters are composed of alternating layers of sensitive and absorber media.

Homogeneous EM calorimeters are usually made out of dense scintillating crystals (BGO, BaF<sub>2</sub>, LYSO, PbWO<sub>4</sub>, among others) or liquid noble gases (Ar, Kr, Xe) and they provide an outstanding energy resolution for  $e/\gamma$ . For example, the CMS EM calorimeter [**cmsECAL**] is composed of PbWO<sub>4</sub> scintillating crystals coupled to avalanche photodiodes and with an energy resolution of

$$\frac{\sigma_E}{E} = \frac{2.8\% \sqrt{\text{GeV}}}{\sqrt{E}} \oplus \frac{12\% \text{ GeV}}{E} \oplus 0.3\%. \quad (9.1)$$

Sampling EM calorimeters use a sensitive medium such as scintillating crystals, liquid noble gases, and silicon, among others to measure the energy the incoming particle; while the absorber medium is a high density material such as lead or tungsten in order to require less volume to completely contain the impinging particle's energy and thus result in a compact design. An example of such an EM calorimeter is the ATLAS lead-liquid argon (LAr) sampling calorimeter with an energy resolution of

$$\frac{\sigma_E}{E} = \frac{10.1\% \sqrt{\text{GeV}}}{\sqrt{E}} \oplus \frac{0.25\% \text{ GeV}}{E} \oplus 0.17\%. \quad (9.2)$$

Particle collider experiments at the LHC such as ATLAS and CMS use EM calorimeters in the  $e/\gamma$  four-momentum and jet energy measurements, particle identification algorithms, trigger systems, and the measurement of the missing transverse energy in each proton-proton collision. Therefore, maintaining the current performance of

the EM calorimeters is critical for the current and future physics measurements of those experiments.

In order to provide the necessary datasets to perform precision measurements of the Higgs couplings, probe rare Higgs processes, study the scattering of longitudinally polarized W bosons, and search for new physics. The high luminosity upgrade of the Large Hadron Collider (HL-LHC) at CERN [169] is expected to provide instantaneous luminosities of  $5 \times 10^{34} \text{ cm}^{-2}\text{s}^{-1}$ . This enhanced data rate will increase the simultaneous interactions per bunch crossing (pileup) from an average of 20-40 to 140-200.

The large amount of pileup foreseen for the HL-LHC will increase the likelihood of confusion in the reconstruction of events of interest, due to the contamination from particles produced in different pileup interactions. The ability to discriminate between jets produced in the events of interests – especially those associated with the vector boson fusion processes – and jets produced by pileup interactions will be degraded, the missing transverse energy resolution will deteriorate, and several other physics objects performance metrics will suffer.

One way to mitigate the detrimental pileup effects, complementary to precision tracking methods, is to perform a time of arrival measurement associated with a particular layer of the calorimeter, allowing for a time assignment for both charged particles and photons. Such a measurement with a precision of about 20 to 30 ps, when unambiguously associated to the corresponding energy measurement, will significantly reduce – approximately a factor of 10 – the inclusion of pileup particles in the reconstruction of the event of interest given that the spread in collision time of pileup interactions is about 200 ps. The association of the time measurement to the energy measurement is crucial, leading to a prototype design that requires the time and energy measurements to be performed in the same sensitive medium. It is in this context that this thesis presents various prototype calorimeters equipped with precision timing capabilities and studies the current limits on their time resolution.

This part of the thesis is organized as follows: section 9.1 provides a brief and general introduction to EM calorimeters, chapter 10 is dedicated to the timing properties of LYSO crystal scintillator based calorimeters, chapter 11 discusses the possibility of a precision timing sampling calorimeter where the sensitive medium is a microchannel plate (MCP) [] chapter 12 discusses the timing capabilities of a sampling calorimeter where the sensitive medium is a 350 microns silicon sensor. finally, chapter ?? summarizes the results and possible improvements as well as

future measurements.

### 9.1 EM Calorimeter Preliminaries

Calorimeters are highly complex instruments and therefore some background is required to understand the subsequent sections in this chapter; this section is intended to provide a short overview of the most important effects – mostly different physical processes in different energy regimes – and the relevant considerations when designing a calorimeter.

#### EM Shower Development

High energy  $e/\gamma$  (with energies above 1 GeV) will develop an EM shower upon entering the calorimeter. The processes involved in the EM shower development are few and well understood. Photons lose energy mostly by photoelectric effect, Compton scattering, or pair production of electrons and positrons. The latter dominates at high energies and it is responsible for the shower development, while photoelectric effect overwhelmingly dominates at low energies (typically below 10 MeV), Figure 9.1 shows the photon cross section as a function of the incoming photon energy in lead. Electrons and positrons lose energy mainly due to two processes, ionization and radiation hereafter referred to as bremsstrahlung, see Figure 9.2. The latter dominates at high energies while the former dominates at low energies. The energy at which these two processes are equally relevant is defined as the critical energy ( $E_c$ ) [**criticalE**], Figure 9.3 shows a graphical representation of this definition.

Empirical functional forms for  $E_c$  can be obtained when a distinction between gaseous and liquid or solid media is made, since there are significant differences in ionization that arise mainly due to the density effect. Figure 9.4 shows the experimental data for  $E_c$  as a function of the atomic number ( $Z$ ) along with the corresponding fits, the functional forms for  $E_c$  are

$$E_c^{gas} = \frac{710 \text{ MeV}}{Z + 0.92}, \quad \text{and} \quad E_c^{solid} = \frac{610 \text{ MeV}}{Z + 1.24}. \quad (9.3)$$

EM showers are then produced when high energy photons (electron/positron) enter the calorimeter media and loses energy by pair production (bremsstrahlung), the subsequently  $e^+/e^-$  pair (high energy photon produced by radiation) loses energy by bremsstrahlung (pair production). The number of particles produced by this multiplicative process increases until a maximum is reached (shower maximum) at the certain depth inside the calorimeter. After this point the newly created particles have low energies and therefore other processes such as photoelectric effect,

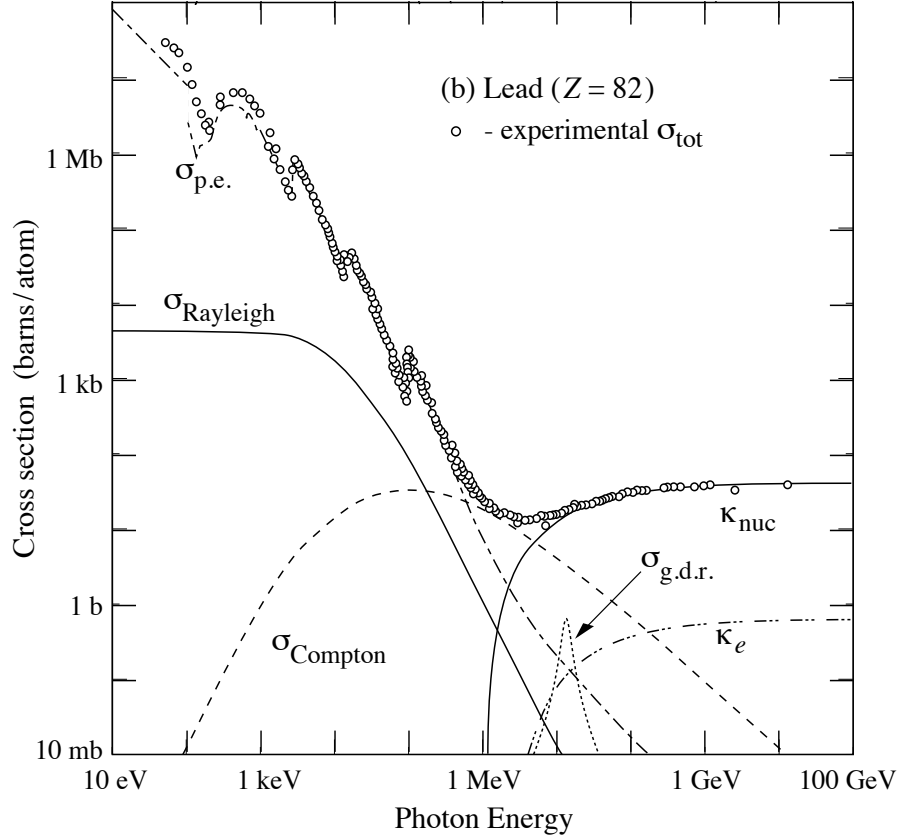


Figure 9.1: Cross section as a function of the incoming photon energy in lead.

Compton scattering, and ionization start to become relevant. The shower profile in the longitudinal direction for a 30 GeV electron in iron is shown in Figure 9.5. The longitudinal shower profile is also a function of the incoming particle energy, Figure 9.5 shows this effect for electrons of different energies in copper.

Shower development is described independently of the calorimeter material by two quantities: the **radiation length** ( $X_0$ ) and the **Molière radius** ( $R_M$ ). The radiation length is the characteristic amount traversed by high energy  $e/\gamma s$  in the longitudinal direction (along the original particle's direction), it is usually measured in  $g\text{cm}^{-2}$ . The quantitative definition is (a) the mean distance over which it and electron loses  $1/e$  of its initial energy, and (b)  $7/9$  of the pair production mean free path for high energy photons.  $X_0$  has been tabulated and calculated by Y. S Tsai [], the analytical expression is the following:

$$\frac{1}{X_0} = 4\alpha r_e^2 \frac{N_A}{A} \left[ Z^2 (L_{\text{rad}} - f(Z)) + Z L'_{\text{rad}} \right], \quad (9.4)$$

where  $\alpha$  is the fine structure constant,  $r_e$  is the classical electron radius,  $N_A$  is

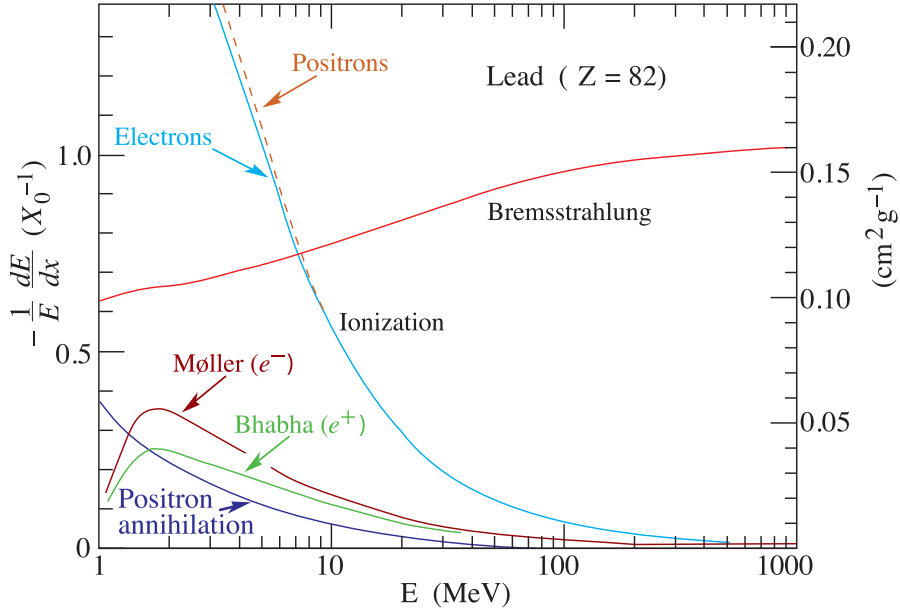


Figure 9.2: Fractional energy loss per radiation length in lead as a function of the electron/positron energy.

Avogadro's number, A is the atomic mass, Z is the atomic number,  $L_{\text{rad}}$  and  $L'_{\text{rad}}$  are shown in Table 9.1, and  $f(Z)$  is an infinite sum, nonetheless for chemical elements up to uranium can be expressed to the 4-decimal place accuracy by

$$f(Z) = (\alpha Z)^2 \left[ (1 + (\alpha Z)^2)^2 + 0.2020 - 0.0369(\alpha Z)^2 + 0.0083(\alpha Z)^4 - 0.0020(\alpha Z)^6 \right]. \quad (9.5)$$

Table 9.1: Tabulated values for  $L_{\text{rad}}$  and  $L'_{\text{rad}}$  from Y. S Tsai.

Element	Z	$L_{\text{rad}}$	$L'_{\text{rad}}$
H	1	5.31	6.144
He	2	4.79	5.621
Li	3	4.74	5.805
Be	4	4.71	5.924
Others	> 4	$\ln(184.15Z^{-1/3})$	$\ln(1194Z^{-2/3})$

The Molière radius is the characteristic size of the shower in the transverse direction and defined as the ratio of the radiation length and the critical energy:

$$R_M = X_0/E_c. \quad (9.6)$$

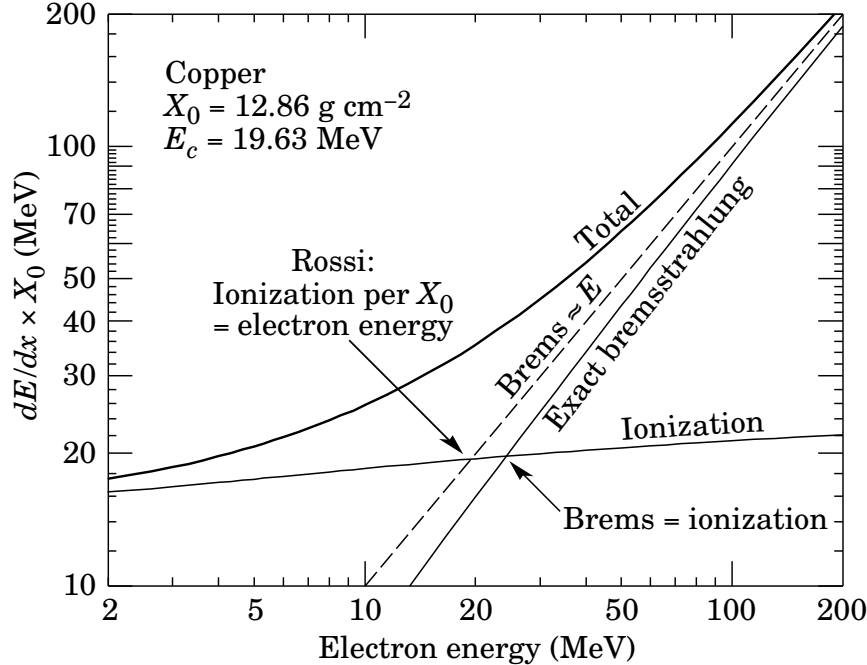


Figure 9.3: Graphical definition of the critical energy ( $E_c$ ). The intersection of the solid lines is the definition used in this thesis. The intersection between the solid (ionization) and dashed line is alternative definition.

The transverse spread of the shower is the result of high energy  $e^\pm$  moving away from the shower axis due to multiple scattering, as well as the isotropic production of low energy electrons and photons. Multiple scattering dominates the lateral evolution in the early stages while isotropic production dominates at the later stages of the shower evolution, after the shower maximum. This two components exhibit a characteristic exponential decay, see Figure 9.7, where the transverse energy density for electron showers in copper is shown.

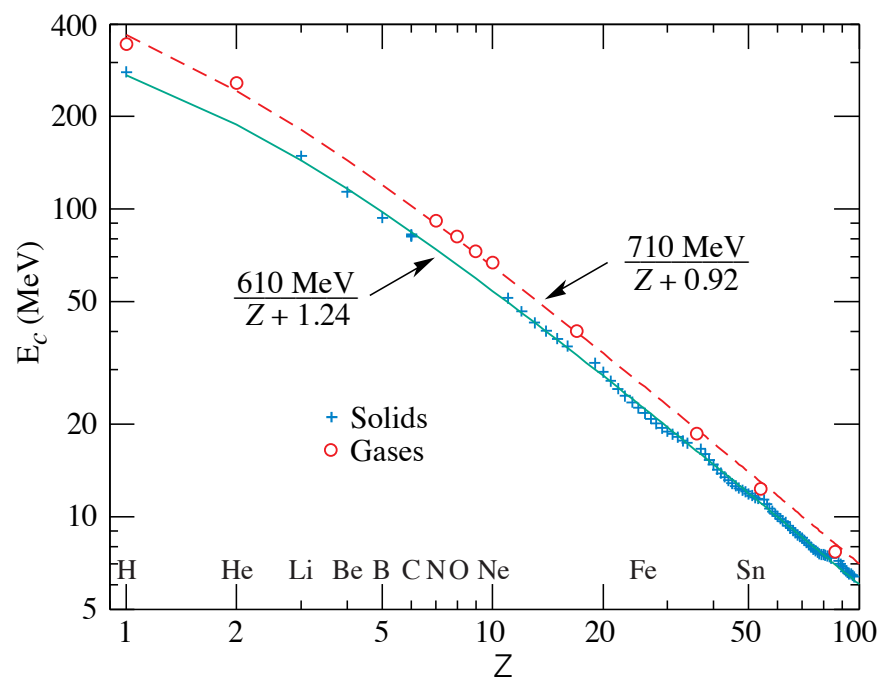


Figure 9.4: Electron critical energy ( $E_c$ ) for the chemical elements. Experimental data is shown for gases (red circles) and solids (magenta crosses). Fits are shown for gases (dashed red line) and solids (solid magenta line)

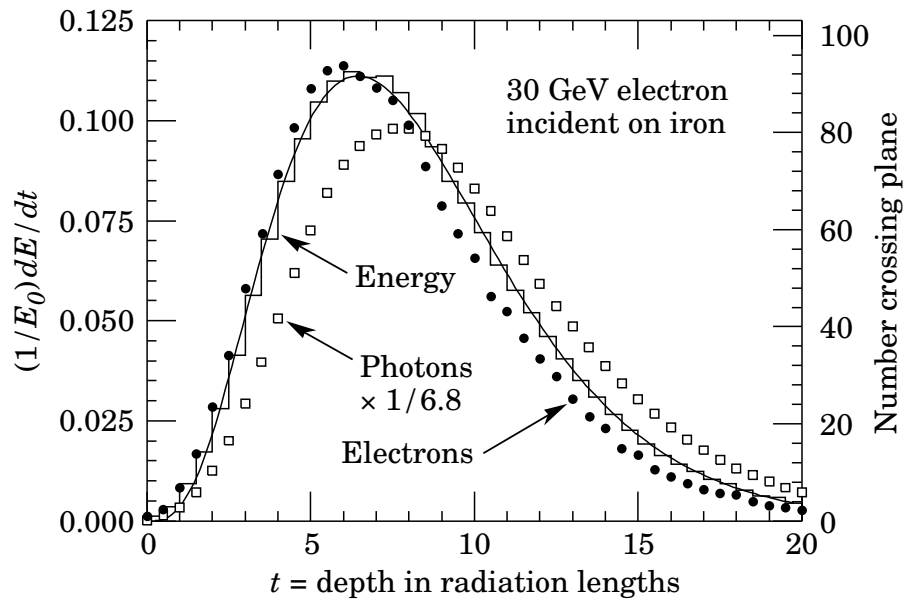


Figure 9.5: Shower profile in the longitudinal direction for a 30 GeV electron in iron from an EGS4 simulation. The solid line histogram shows the fractional energy per radiation length, and the solid line curve is a fit to the distribution using a gamma function. The number of electrons (solid circles) and photons (hollowed squares) with energies larger than 1.5 MeV and crossing planes at  $X_0/2$  intervals (scale on the right) is also shown. The number of photons has been scaled down to have the same area as the number of electrons distribution.

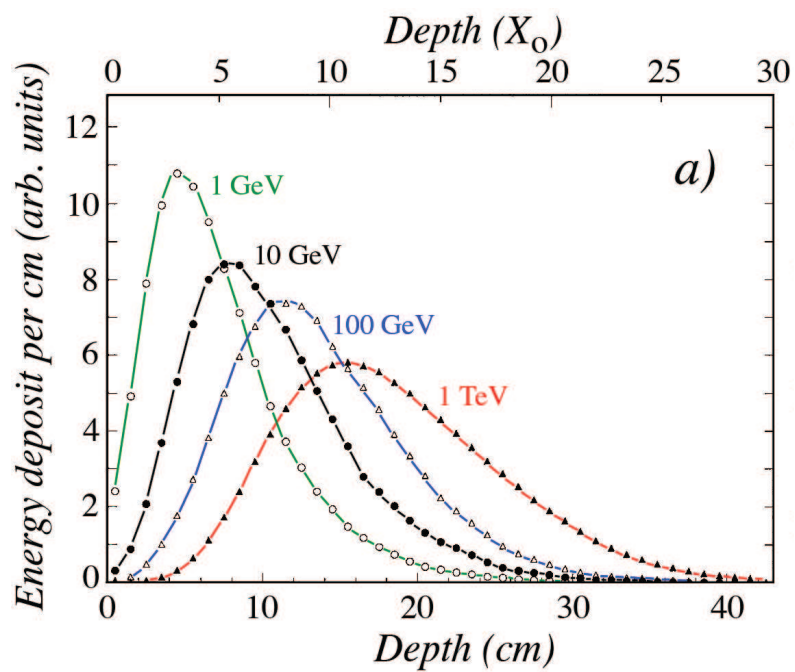


Figure 9.6: Shower profile in the longitudinal direction for electrons in copper. The different curves and points represent different electron energies ranging from 1 GeV-1 TeV.

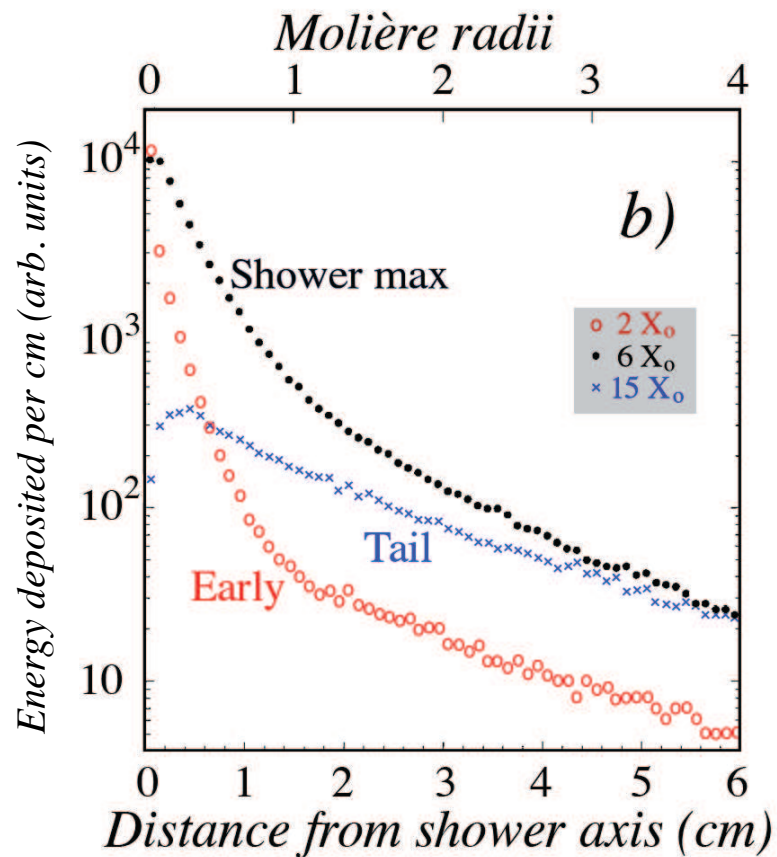


Figure 9.7: Energy deposited per unit length in the transverse direction for 10 GeV electrons in copper. The shower has been sample in three different places; at  $2X_0$  (red circles),  $6X_0$  (black dots), and  $15X_0$  (blue crosses).

**Important Calorimeter Quantities**

xyz

*Chapter 10***LYSO-BASED CALORIMETERS**

This chapter presents studies on measurements of the time of flight (TOF) using sampling calorimeters based on LYSO crystals.

### **10.1 Introduction**

Due to its very high light yield ( $\sim 30$ K photons/MeV) [171], and radiation tolerance [190, 143, 170, 114], LYSO is the active element of one of the options considered for the upgrade of the Compact Muon Solenoid (CMS) detector for the HL-LHC [104].

In Figure 10.1 presents a simplified illustration of the major time scales associated to the timing measurement using a monolithic crystal calorimeter. Upon entering the crystal the photon or electron travels at the speed of light, interacts, and begins to shower, producing scintillation light in the crystal. The time between the entry of the photon into the crystal and the first interaction is denoted by  $t_I$  and for high energy impinging particles it is the shower development time. The time associated with the conversion of the incident photon to scintillation light is denoted by  $t_S$ . The scintillation light travels from the point of interaction to the photodetector at the velocity  $c/\hat{n}$ , where  $\hat{n}$  is the effective index of refraction of the crystal [219]. The time associated with the propagation of the scintillation light to the photodetector is denoted by  $t_P$ . Once the scintillation light reaches the photodetector, the photons are converted into an electrical signal. The time associated with this process is known as the photodetector signal transit time,  $t_T$ . Finally, data acquisition (DAQ) system has a characteristic time constant  $t_D$ . Each of these time intervals will fluctuate or jitter on an event-by-event basis, contributing to the time resolution. Previous studies [197], measured the time resolution at different absorber thickness for electron beams with energies varying from 12 to 32 GeV, and showed that the time of arrival of the front of an electromagnetic shower can be determined with a precision better than 20 ps. The electronic time resolution of the DAQ system was measured to be about 6 ps. Using the same techniques, the time resolution of the MCP-PMT photodetectors used in the studies presented in this paper have been measured to be between 11 ps and 14 ps, depending on the exact device.

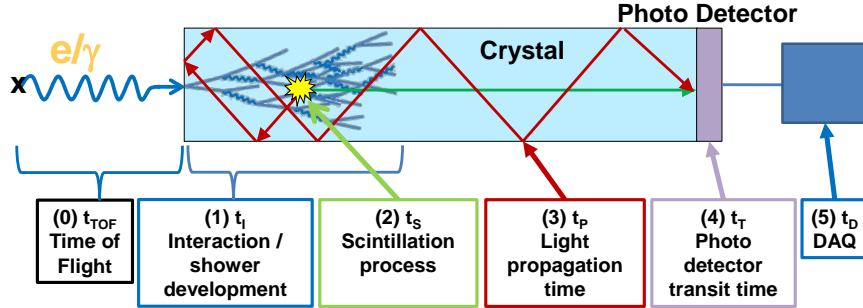


Figure 10.1: Timing measurement schematic breakdown using a monolithic, large scintillating crystal. The incident particle impinges on the crystal face from the left. The characteristic time intervals are discussed in the text.

To characterize the time resolution of an inorganic crystal scintillator calorimeter we study the contributions due to fluctuations in the shower development, scintillation process, and light propagation to the photodetector. We take advantage of the very large number of scintillation photons in a LYSO crystal which result in modest fluctuations associated with the creation and transit of each particular scintillation photon for a LYSO-based detector.

## 10.2 Experimental Setup

A schematic diagram of a typical TOF measurement setup is shown in Figure 10.2. All measurements involve a fast photodetector, typically a micro-channel-plate photo-multiplier-tube (MCP-PMT), which measures the reference timestamp ( $t_0$ ), and a photodetector further downstream that detects the signal associated with the electromagnetic shower and provides a simultaneous energy and time ( $t_1$ ) measurement.

In these studies, two types of MCP-PMT photodetectors are used, one produced by Hamamatsu (model R3809-52) [1], and one produced by Photek (model PMT240) [2]. A DRS4 waveform digitizer V4 evaluation board [195] was used as the primary DAQ system, connected to a laptop via USB interface. The DRS chip contains a switched capacitor array (SCA) with 1024 cells, capable of digitizing eight analog signals with high speed (5 GSPS) and high accuracy (11.5 bit SNR). All experimental beam studies were performed at the Fermilab Test Beam Facility (FTBF), which provided proton beams from the Fermilab Main Injector accelerator at 120 GeV, and secondary electron beams of energies ranging from 4 to 32 GeV. All detector elements were placed inside of a dark box lined with copper foil, providing RF shielding. A  $2 \times 2 \text{ mm}^2$  scintillator was placed inside the box at the upstream extrem-

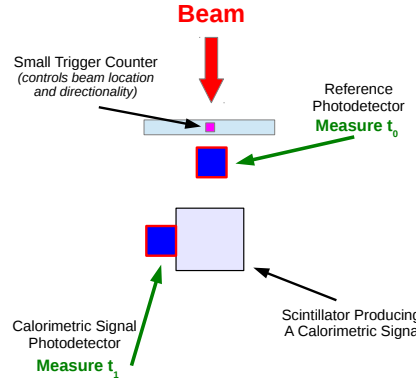


Figure 10.2: The basic schematic diagram of the experimental setup for a typical TOF measurement is shown to illustrate the basic detector elements. One photodetector is used as a time reference and the second measures energy and time simultaneously.

ity and used to trigger the DAQ readout, providing a strict constraint on the location and directionality of the beam particles used in the TOF studies. A differential Cherenkov counter (not shown in the schematic) provided by the FTBF facility and located upstream of our experimental hall, was used for electron identification.

### 10.3 Event Selection and Data Analysis

The primary target is to reconstruct the TOF of beam particles between different detector elements. Different time reconstruction algorithms are used for different detector elements, and all involve the assignment of a timestamp using specific features of each corresponding signal pulse. The signal pulse for the reference time detector is very sharp and symmetric around its maximum amplitude, as shown in Figure 10.3. Hence for the reference detector we determine the time position of the pulse peak by fit a Gaussian function to the peak of the pulse, using three sampling points before the pulse maximum and four sampling points after. The fitted mean parameter of the Gaussian function is assigned as the timestamp  $t_0$ . The signal pulse for the downstream time measurement is the result of scintillation light, and exhibits a fast rising edge and a significantly slower decay. Therefore, we assign the timestamp  $t_1$  using a constant fraction of the rising edge. A linear function is fit to the sampling points between 10% and 60% of the pulse maximum and the timestamp is assigned as the time at which the fitted linear function rises to 20% of the pulse maximum. Examples of fits performed to assign a time stamp from each pulse are shown in Figure 10.4. The impact from the choice of the functional

forms is studied by using a set of alternative functions in the fits, and choosing the one that results in the best time resolution. Among the functions that we tested, the difference between the best and worst performing functions was about 8 psec.

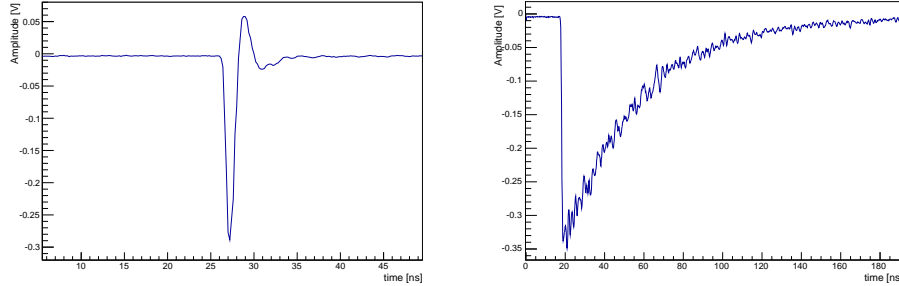


Figure 10.3: Sample pulses as digitized by the DRS4 board. On the left a pulse is shown from the reference Hamamatsu R3809 MCP-PMT, and on the right is a pulse from the Hamamatsu R3809 MCP-PMT optically coupled to a  $(1.7\text{ cm})^3$  LYSO crystal cube recorded using 8 GeV electron beam.

Event selection and pulse cleaning procedures are used to eliminate abnormal pulses in the readout, as described in [197]. Large signals above 500 mV are rejected because they saturate the DRS4 inputs. Only pulses with amplitude larger than 20 mV are used for TOF measurements, in order to reduce the impact of noise from the DRS waveform digitizer DAQ system. Events containing more than one pulse within the 200 ns readout window are not used. Attenuators were used to extend the dynamic range of the DRS4 waveform digitizer in cases when a large fraction of signal pulses are saturated.

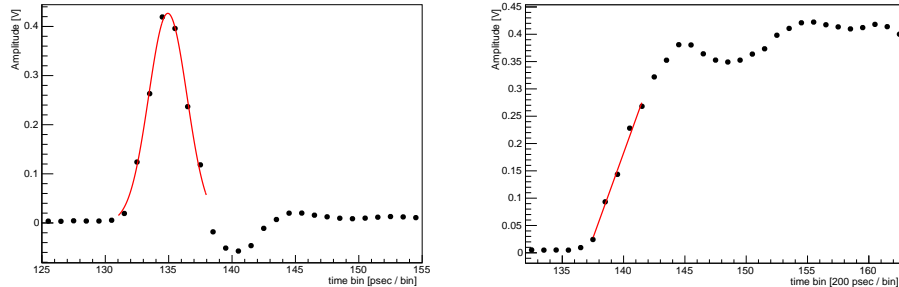


Figure 10.4: Sample fits used to assign timestamps to digitized MCP-PMT pulses. On the left is a pulse from the reference Hamamatsu R3809 MCP-PMT, and on the right is a pulse from the Hamamatsu R3809 MCP-PMT optically coupled to a  $(1.7\text{ cm})^3$  LYSO crystal recorded during an 8 GeV electron run.

#### 10.4 Timing in LYSO-based Calorimeters

The timing measurement in LYSO-based calorimeters is driven by three main factors – other than the intrinsic transit time of the photodetector itself and the DAQ electronics : a) the shower profile fluctuations, b) the scintillation time, and c) the light propagation time. Stochastic processes during the development of an electromagnetic shower affect the time of observed signals, as both the transverse size and the depth of the shower can fluctuate event-by-event. Random processes in the scintillation mechanism and the randomization of the optical paths for the scintillation light affect both the speed of the signal formation and the time jitter. We study these effects using two independent experimental setups.

For a homogeneous crystal calorimeter we are interested in the characterization and optimization of the light propagation time, i.e. the time the scintillation light travels down the length of the crystal. Our setup uses a small LYSO cube with linear dimensions of 17mm as the active scintillation element. The size of this element reduces the effect of the light propagation time and jitter. The LYSO cube is placed behind about  $4.5 X_0$  radiation lengths of lead. Using this LYSO-based sampling calorimeter, we measure the time resolution of electrons.

We also study a shashlik calorimeter composed of alternating layers of tungsten and LYSO, in which scintillation light is extracted through wavelength shifting (WLS) fibers. In this setup, the light propagation time through the fiber is the dominant factor of the timing measurement. We study as a baseline an alternate version of this calorimeter where the light is extracted through direct optical coupling of the photodetectors at the edges of a few LYSO layers to minimize the light propagation time.

#### Timing Studies of the LYSO-based Sampling Calorimeter

We study the combined impact of the shower profile fluctuations, the scintillation mechanism in LYSO, and the light propagation time resolution using a sampling calorimeter with a  $(1.7 \text{ cm})^3$  LYSO cube as active element. The LYSO crystal is wrapped in Tyvek and attached to the Hamamatsu R3809 MCP-PMT (HAMB) with optical coupling [3]. A second Hamamatsu MCP-PMT photodetector (HAMA) is placed upstream of the calorimeter and is used to measure the reference time. A schematic diagram and a photograph of the experimental setup are shown in Figure 10.5.

To ensure that the electron beam is constrained to within a  $2 \times 2 \text{ mm}^2$  region,

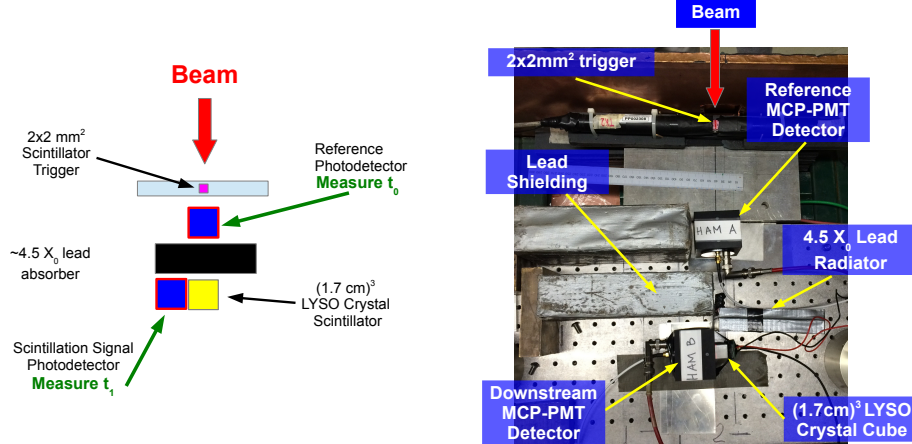


Figure 10.5: A schematic diagram of the experimental setup for the TOF measurement using the LYSO sampling calorimeter is shown on the left, along with a picture of the experimental setup shown on the right.

a plastic scintillator placed upstream and approximately 2 mm by 2 mm in cross sectional area is used to trigger the DAQ readout on the DRS digitizer. Electron events are identified by requiring a signal with amplitude larger than 10 mV in a Cherenkov counter located upstream. Large lead bricks are placed upstream of the Hamamatsu R3809 MCP-PMT (HAMB), out of the path of the beam. These shield the photodetector from stray particles produced in events where an electromagnetic shower occurs upstream of the lead radiator. Such stray shower particles yield very fast signals which can significantly contaminate the scintillation signal. Using the same experimental setup without the LYSO active element in place, we find that stray shower type events yield less than 10% contamination and give a negligible effect on the scintillation signal.

The thickness of the LYSO active element is relatively small and captures only a fraction of the total energy of the electron, but yields a reasonable energy measurement as it is close to the shower maximum.

The TOF measurement is performed using the LYSO sampling calorimeter for electron beams with energies varying from 4 GeV to 32 GeV. The corresponding measured TOF distributions are shown in Figure 10.6. We achieve the best time resolution of 34 ps for electrons with beam energy of 32 GeV.

The time resolution measurement is plotted as a function of the beam energy in Figure 10.15 (left). We fit the result to the sum of a  $1/\sqrt{E}$  term and a constant term of about 11 ps. Given that we measure the contribution to the intrinsic time resolution

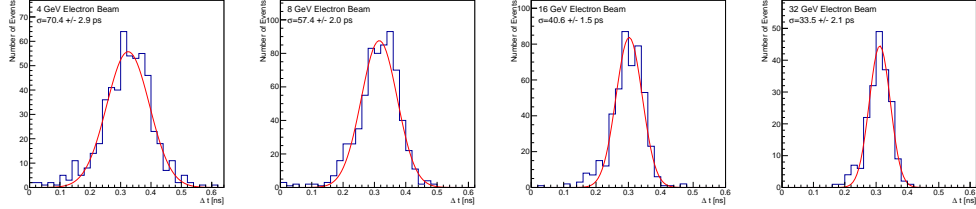


Figure 10.6: TOF distributions for the LYSO cube sampling calorimeter for 4 GeV (top left), 8 GeV (top right), 16 GeV (bottom left), 32 GeV (bottom right) electron beam energy.

of the photodetector and the DAQ electronics to be about 20 ps [197], using the results from the 32 GeV electron beam, we infer that the combined contribution to the time resolution from the shower profile fluctuations, the scintillation mechanism, and the light propagation time inside the LYSO cube is about 27 ps.

### Timing Studies of the LYSO-Tungsten Shashlik Calorimeter

#### Wavelength shifting fibers readout (WLS Y11 & DSB1)

We study the time resolution of a LYSO-tungsten Shashlik calorimeter, one of the proposed choices for the Phase 2 upgrade of the CMS endcap calorimeter system [104]. We compare the time resolution performance for two alternative light propagation schemes.

In our setup the scintillation light is collected by WLS fibers that pass through a set of four holes in the LYSO and tungsten layers. In Figure 10.7, a shashlik cell and the light extraction scheme is illustrated. A schematic diagram and a photograph showing this experimental setup are shown in Figure 10.8. Two MCP-PMTs by Hamamatsu (R3809) are used to collect the scintillation light, while a Photek 240 MCP-PMT is used as a reference time detector.

We compare the signal pulses obtained using two different types of WLS fiber in the same LYSO-tungsten shashlik calorimeter. In Figure 10.9 (a) and (b) and we show the pulse shapes averaged over a few hundred events obtained using DSB1 fibers [34] and Y11 fibers, plotted in blue and red respectively. We find that the rise time of the pulse obtained using the DSB1 fibers, about 2.4 ns, is significantly faster than the rise time of the pulse obtained using the Y11 fibers, which is about 7.1 ns. To optimize the time resolution of this type of calorimeter the DSB1 fiber provides a better choice than Y11 if only this parameter is considered. The signal rise times we observe are comparable to the measured decay times of the corresponding WLS fibers [34].

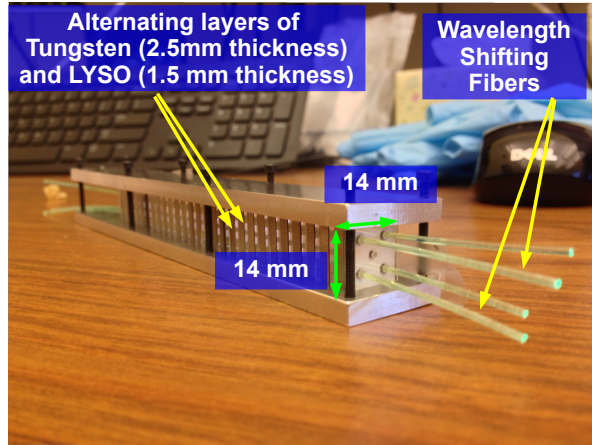


Figure 10.7: The shashlik configuration based upon interleaved W and LYSO layers. Twenty-eight LYSO crystal plates and twenty-seven W plates comprise the module. Four WLS fibers are used to read out the scintillation light from the tiles.

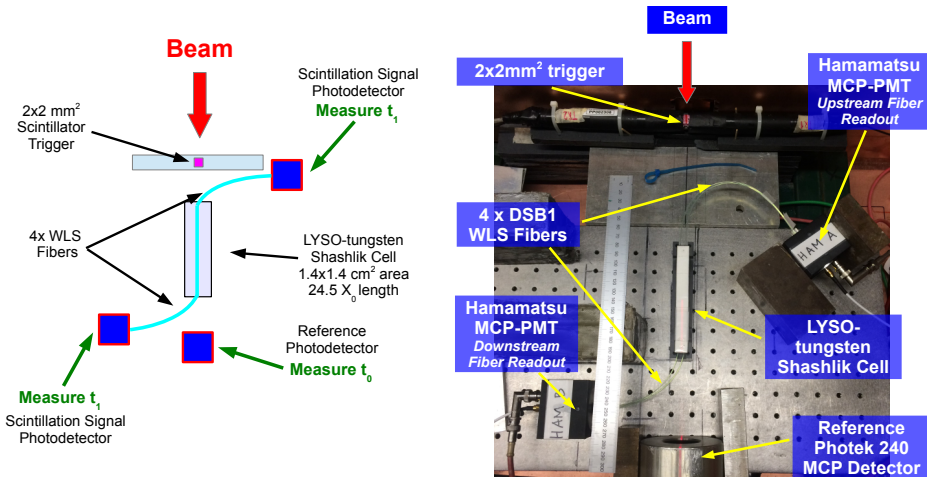


Figure 10.8: A schematic diagram of the experimental setup for the TOF measurement using the LYSO-tungsten shashlik calorimeter with fiber signal extraction, along with a photograph of the experimental setup.

Using the shashlik calorimeter cell with DSB1 fibers, we measure the time resolution for electron beams with energy varying between 4 GeV and 32 GeV. In Figure 10.10 (b) we show the distribution of the pulse integral which is proportional to the total collected charge, for the 32 GeV beam, and observe an energy resolution of about 5% while for the small LYSO cube shown in 10.10 (a), the energy resolution was

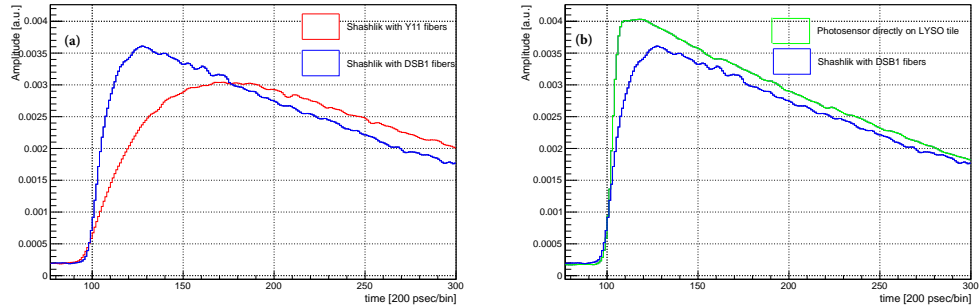


Figure 10.9: (a) Pulse shapes digitized by the DRS4 board and averaged over several hundred events obtained from the LYSO-tungsten shashlik calorimeter with light extracted using DSB1 (blue) and Y11 (red) WLS fibers. (b) DSB1(blue) shashlik average light pulse shape compared with the averaged pulse shape obtained from direct optical coupling of the photodetector to one edge of a LYSO tile in the shashlik calorimeter. (green)

about 20%. For this particular run in the Shashlik setup, no electron identification requirements could be made due to a misconfiguration of the upstream Cherenkov counter, so the background is visible.

TOF distributions, fitted to gaussian functions, are shown in Figure 10.11, and the  $\sigma$  parameter of the gaussian fit is plotted as a function of the beam energy in Figure 10.16. We find that the dependence of the time resolution on beam energy follows a  $1/\sqrt{E}$  functional form, indicating that the current calorimeter setup remains in the photostatistics limited regime. The best time resolution we obtain with this setup is 104 ps. As the measurements are photostatistics limited, the result can be improved in the future if the light collection efficiency is increased.

### **Directly coupled MCP-PMTs to LYSO shashlik plates**

In this setup the MCP-PMT photodetectors are directly coupled to the edges of two adjacent LYSO layers in the shashlik calorimeter and scintillation light is directly transported to the photodetector through the edges of the tile layers. A schematic diagram and corresponding picture of the experimental setup are shown in Figure 10.12. In Figure 10.13, we show a zoomed-in photograph of the exposed LYSO plates from which the scintillation light signal is extracted.

With this setup we invoke an interplay between the light propagation jitter and the limited photostatistics. By placing the photodetectors in direct contact with the edges of two LYSO layers, we minimize the distance the scintillation light travels to reach the photodetectors, and reduce the impact of light propagation jitter on

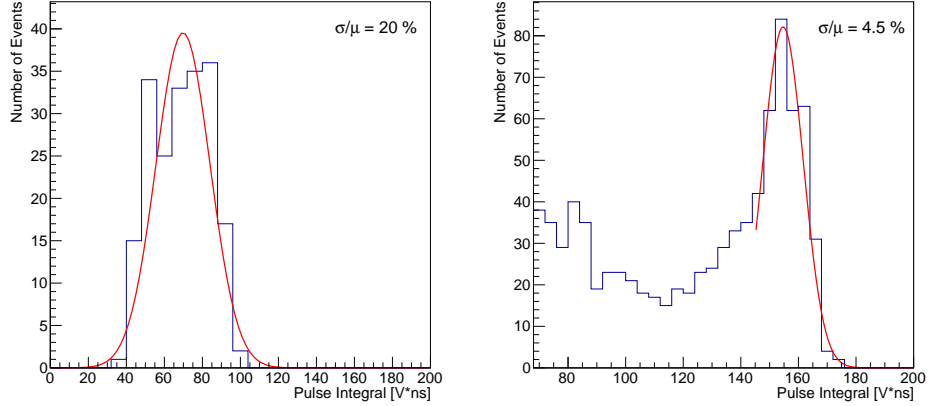


Figure 10.10: (Left) Histogram of the pulse integral which is proportional to the total collected charge is shown for events recorded using the LYSO cube sampling calorimeter for a 32 GeV electron beam. (Right) Histogram of the pulse integral for events recorded using the LYSO-tungsten shashlik calorimeter using DSB1 fibers, for a 32 GeV electron beam. The background is included due to a misconfiguration of the Cherenkov counter.

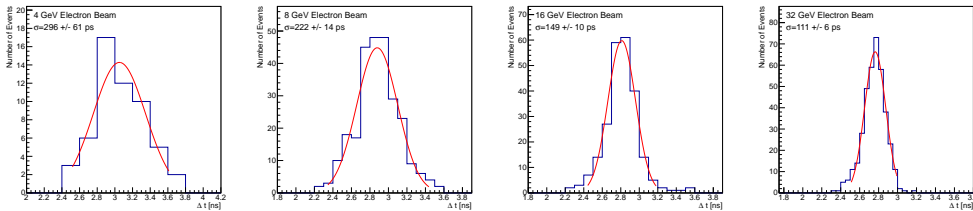


Figure 10.11: TOF distributions for the LYSO-tungsten shashlik calorimeter using DSB1 fibers for electron beams with varying beam energies.

the time measurement resolution. However in this setup we have also reduced the available photostatistics, as we collect light from only a small fraction of the shashlik cell. In Figure 10.14, we show the TOF distributions for electron beams at various energies, fitted to gaussian functions. The width of the best-fit gaussian is plotted as a function of the beam energy in Figure 10.16. The best time resolution that we obtain is about 55 ps, and fitting the result to the sum of a  $1/\sqrt{E}$  term and a constant term, we find a constant term of about 30 ps.

In summary, we find that removing the impact of the wavelength shifting mechanism and minimizing the impact of optical transit does indeed improve the time resolution, but at a cost in photostatistics. Results obtained in this experiment suggest that a LYSO-tungsten shashlik calorimeter with edge readout can likely achieve 30 ps resolution provided some improvement to the light collection efficiency is achieved.

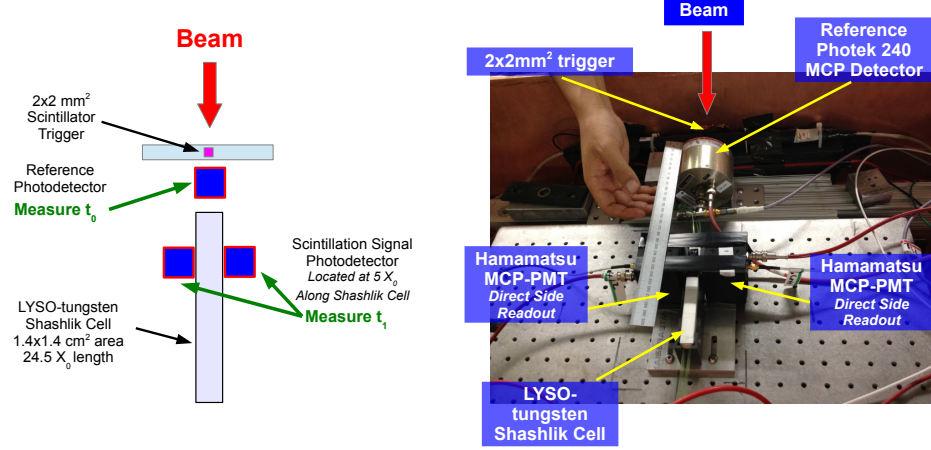


Figure 10.12: A schematic diagram of the experimental setup for the TOF measurement using the LYSO-tungsten shashlik calorimeter with signal extraction from the edges of two LYSO plates, along with a picture of the experimental setup.

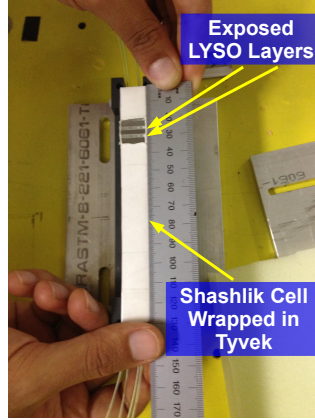


Figure 10.13: A photograph of the two exposed LYSO layers in the shashlik cell. The scintillation light signal is extracted by optically coupling the edges of these two exposed LYSO layers to MCP-PMT photodetectors.

## 10.5 Results Discussion and Summary

This section described studies characterizing the timing performance of LYSO-based calorimeters. Using a  $(1.7 \text{ cm})^3$  LYSO crystal that samples the electromagnetic showers created by electrons of various energies ranging from 4 GeV to 32 GeV at about  $4.5 X_0$ , we infer that the contribution to the time resolution from event-by-event fluctuations of the shower profile, the scintillation process, and the light propagation is less than 30 ps. Studies using different wavelength shifting fibers in a LYSO-tungsten shashlik calorimeter demonstrates that the choice of the fiber affects the timing performance. Besides the absorption and re-emission processes in the fibers, we found that another important factor influencing the timing performance

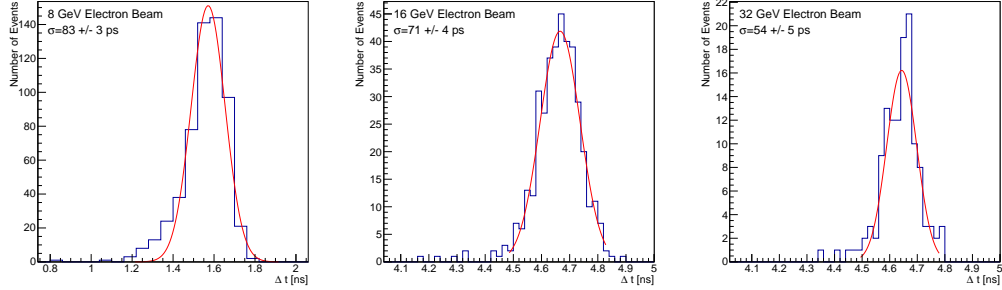


Figure 10.14: TOF distributions for the LYSO-tungsten shashlik calorimeter with signal extracted from the edges of two LYSO layers.

Figure 10.15:

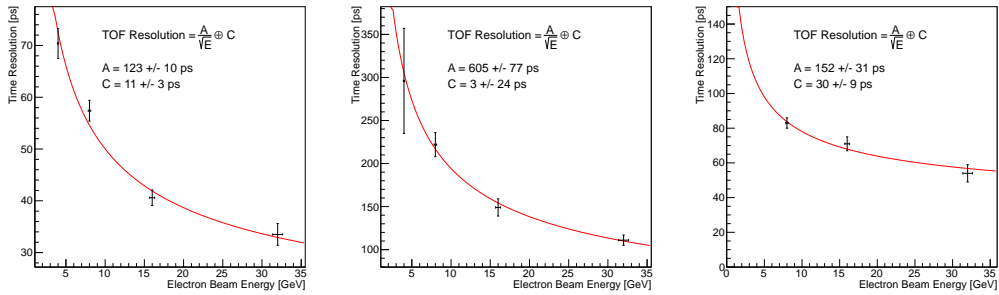


Figure 10.16: Timing resolution measurement as a function of the electron beam energy for (left) the LYSO cube sampling calorimeter (middle) the LYSO-tungsten shashlik calorimeter read-out with DSB1 fibers (right) the LYSO-tungsten shashlik calorimeter read-out directly by optically coupling to the edges of two LYSO layers. In all cases we fit the data with a function of  $1/\sqrt{E}$  and a constant term.

is the light extraction efficiency. Using DSB1 fibers, despite being photostatistics limited, we obtained a best time resolution of about 100 ps. A future development of such a detector will be focused on increasing the light collection efficiency. In a setup where the scintillation light from the LYSO-tungsten shashlik calorimeter is extracted via the edges of two LYSO layers, thereby removing completely the wavelength shifting mechanism and long light propagation distance, we achieve a best time resolution of 55 ps. The result indicates that such a calorimeter design can achieve the 30 ps time resolution benchmark obtained with the LYSO cube provided some improvement to the light collection efficiency.

In comparing results using different light extraction schemes, we find that at a given light yield the time resolution depends significantly on the light propagation

fluctuations. As the light yield increases the dependence on the light propagation fluctuations is reduced. The effect can be seen in the summary Figure 10.17 where we show the dependence of the time resolution on the average pulse height for the shashlik cell with light extracted through the DSB1 fibers and for the sampling calorimeter with the LYSO cube. For the same average pulse height of 500 mV, the LYSO cube time resolution is about half of the shashlik using the DSB1 fibers which have also twice the rise time. As the pulse height increases the time resolution improves. Extrapolating to the regime of very large light yield, we should be able to reach asymptotically the best resolution without limitations from the light propagation fluctuations.

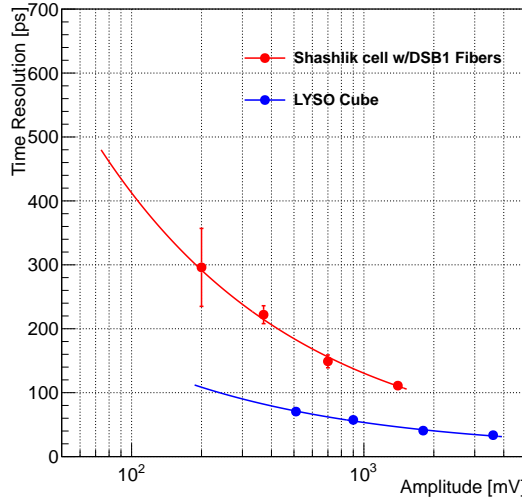


Figure 10.17: Comparison of time resolutions obtained with the  $(1.7 \text{ cm})^3$  LYSO cube (blue), and the LYSO-tungsten shashlik calorimeter with light extracted using DSB1 fibers (red). The x-axis in this figure displays the amplitude of the signal, corrected for the attenuation factors.

In summary, using a LYSO-based calorimeter and different light propagation experimental setups we obtain about 30 ps resolution time measurement for the maximum light yield achieved. As a follow-up we will investigate the time resolution in the limit of very large light yield, and attempt to improve the light collection efficiency in these types of detectors.

## 10.6 Acknowledgements

I would like to thank Erik Ramberg and Sergey Los for their help and support of this work, and Aria Soha and the FTBF test beam facility for the beam delivery and control. We thank Randy Ruchti for providing us with the DSB1 fibers used in the

measurements, and Eileen Hahn for the high quality work in polishing the fibers. We would also like to thank Ewa Skup and Geoff Savage for help with operation of the Cherenkov counters, and to Todd Nobel for organizing and providing supporting equipment at FTBF.

This work is supported by funding from Fermi Research Alliance, LLC under Contract No. DE-AC02-07CH11359 with the United States Department of Energy and from California Institute of Technology High Energy Physics under Contract DE-SC0011925 with the United States Department of Energy.

## HIGH-GRANULARITY MCP-BASED CALORIMETERS

In this chapter another precision timing calorimetric prototype using MCPs as the sensitive medium is studied.

### **11.1 Introduction**

The use of MCPs as the sensitive element of a shower-maximum detector or a calorimeter has been studied in the past [113, 33]. These studies demonstrated the linearity in the multiplicity of secondary shower particles that have energies that the MCP can detect. Such detectors are also a promising option for achieving time measurement precision at the level of a few tens of picoseconds [197, 199, 200, 168]. Moreover, such devices are intrinsically radiation hard and thus would tolerate the harsh radiation environment at future hadron colliders, particularly when operated without the reliance on a photocathode. In reference [200], it has been demonstrated that the intrinsic fluctuations of electromagnetic showers induce jitter on the time measurement that is less than 10 ps, removing one important potential fundamental limitation. A further advantage of MCPs is their capability for highly segmented readout, allowing for the possibility of a highly granular calorimeter with sub-millimeter spatial resolution. Such high-granularity calorimeters have been studied in the context of detector concepts for the ILC [131] and the HL-LHC upgrade of the CMS experiment [68], indicating that such calorimeters have promising potential for substantial improvement in physics reach at the TeV scale. The results in this chapter complement past results [42, 197, 199, 200] with additional studies of the position and time resolution for a calorimeter prototype with highly granular readout.

The studies in this chapter use three different MCP-PMTs:

- Photek 240: the most performant of the three devices, which provides the best time resolution, and excellent uniformity across the detector. The main parameters of the Photek 240 were reported in Ref. [197]. The pore size is 10  $\mu\text{m}$  and the distance from the photocathode to the first amplification stage is 5.3 mm. The Photek 240 has a 41  $\text{mm}^2$  circular sensitive area, and it was operated 4.8 kV high voltage (HV). The gain at this voltage is about  $10^6$ . The

non-uniformity of the time response of the signal is limited to below 3.9 ps across the full sensitive area.

- Photonis XP85011: the anode of this MCP is composed of 64 pads, arranged as an  $8 \times 8$  matrix. The size of each pad is  $6 \times 6 \text{ mm}^2$ . The pore size is  $25 \mu\text{m}$ . The non-uniformity of the time response across the photocathode is 37 ps [197, 200]. The HV applied to the Photonis XP85011 was 2.4 kV, with a corresponding gain of  $10^6$ .
- Photonis XP85012: mostly identical to XP85011, also composed of 64 pixels arranged as an  $8 \times 8$  matrix. Additionally it can be operated in a mode with a reverse voltage applied to photocathode, which enables us to effectively turn off any signals from the photocathode. When operated in this mode, the only signals are directly from secondary shower particles [199].

This chapter reports on the studies of the high-granularity shower-maximum detector prototype that uses the Photonis XP85011 MCP as the active element. As demonstrated in reference [197], due to the fact that the input window is very thin, the signal in this device is dominated by direct detection of secondary shower particles, while Cherenkov photon signals contribute only 30% of the amplitude. The MCP is used to sample the electromagnetic shower induced by a beam of electrons impinging into a tungsten absorber layer that has a thickness of about 4 radiation lengths ( $X_0$ ). The MCP-PMT is read out with a pixelated anode, with square pixels of size  $6 \times 6 \text{ mm}^2$ . The energy of the electromagnetic showers is reconstructed using the total collected charge and the positions are reconstructed using a simple energy-weighting algorithm, described in Section 11.4. Through the use of a high-precision motorized stage, a position scan is performed during beam-tests and the position resolution of the shower-maximum detector is obtained. Finally, the precision of measuring the arrival time of electromagnetic showers with such high-granularity shower-maximum detector is investigated.

This chapter is organized as follows. Section 11.2 gives a description of the experimental setup, Section 11.3 presents the event selection and pulse reconstruction, Section 11.4 and 11.5 the presents the results on position measurements and timing resolutions, respectively.

## 11.2 Experimental Setup

The experiment was performed at the MTEST location of the FTBF using an 8 GeV beam primarily comprised of electrons. A differential Cherenkov counter, located further upstream of the MTEST location, was used to enhance the purity of electrons and to suppress pions, by requiring a signal consistent with the passage of electrons through the device. All other detectors were placed inside a dark box lined with copper foil for electromagnetic shielding. A photograph of the experimental setup within the dark box is shown in Figure 11.1. A scintillator of size 1.7 mm× 2.0 mm optically coupled to two photomultiplier tubes, one on each side, was used to trigger the data acquisition and to constrain the trajectory of the electrons. Downstream from the trigger, a tungsten absorber with a thickness of about 1 cm, equivalent to about  $4 X_0$ , was placed. The Photonis XP85011 MCP-PMT with pixelated readout was set on a high precision motorized stage and placed behind the tungsten absorber. The precision of the motorized stage is about 0.1 mm. To avoid unintended early showers due to interactions with the material of the casing and reference MCP-PMT device, the Photek 240 MCP-PMT was placed behind the Photonis XP85011 MCP-PMT. An external view of the Photonis XP85011 MCP-PMT is shown on the left

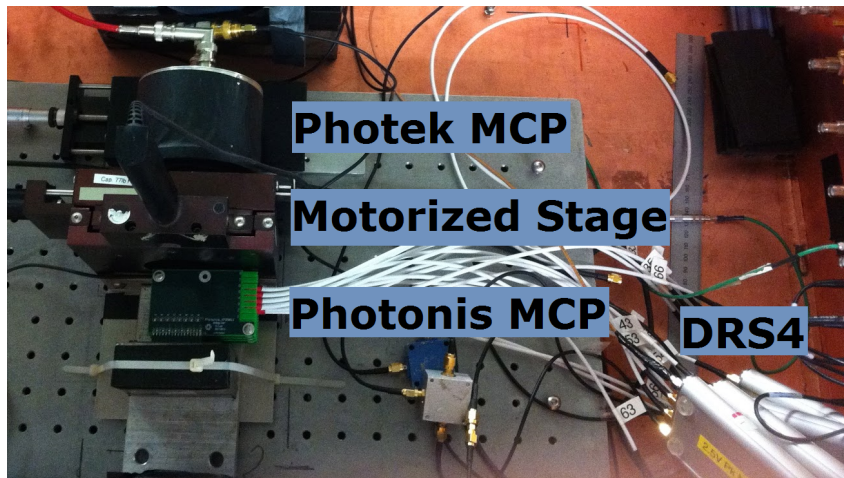


Figure 11.1: The experimental setup inside of the dark box is shown. The beam direction is from the bottom of the photograph to the top. The detector elements shown in the order from upstream to downstream of the beam are: the tungsten absorber, the Photonis XP85011 MCP-PMT located on the motorized stage, and the Photek 240 MCP-PMT used as a time reference detector. The DRS4 waveform digitizers are also shown on the lower right side.

of Figure 11.2, and a schematic diagram is shown on the right. There are a total of 64 pixels arranged in an  $8 \times 8$  square matrix that can be read out individually. Only the nine pixels shown within the red square are used (see Figure 11.2). During the

course of the experiment it was found that the pixel labelled 44 in Figure 11.2 did not function properly and was therefore not used in the analysis of the data. Four DRS4

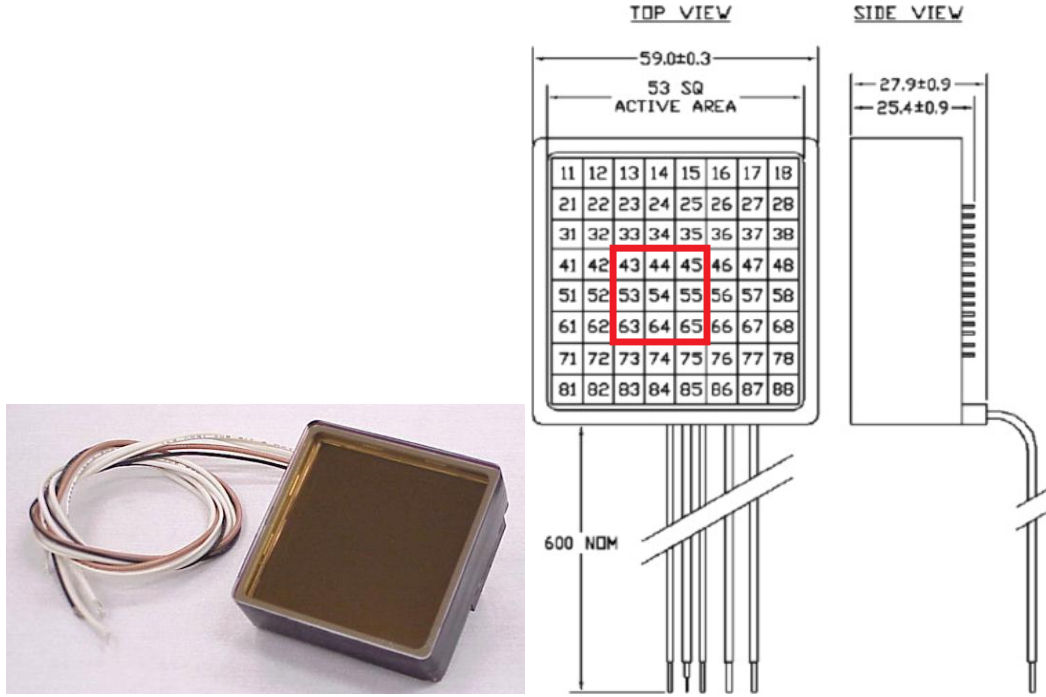


Figure 11.2: The external view of the Photonis XP85011 MCP-PMT is shown on the left, and the schematic diagram is shown on the right. The red square indicates the pixels used for the experiment and data analysis.

high speed waveform digitizers were used to acquire the signals from the Photek 240 MCP-PMT, the cherenkov counter, and the eight operational channels from the Photonis XP85011 MCP-PMT. In order to allow a synchronized readout of four separate DRS4 units we split the signals from the Photek 240 MCP-PMT into four, and connected them to each of the four DRS4 units, thus achieving a “calibration” between the four different units.

### 11.3 Event Selection and Pulse Reconstruction

Reconstruction of the signal pulses and timestamps is performed using the identical methods described in Chapter 10 and other studies [42, 197, 199]. Figure 11.3 shows example pulses from one pixel channel of the Photonis XP85011 MCP-PMT and the Photek 240 MCP-PMT digitized by the DRS4.

The time resolution is measured as the standard deviation of the Gaussian fit to the TOF distribution  $t_0 - t_1$ , where  $t_0$  is the time recorded at the “start” detector, and  $t_1$  is that of the “stop” detector. To assign a time stamp for each signal pulse, we

first determine the time position of the pulse peak. A Gaussian function is fitted to the pulse maximum using three points before the maximum of the pulse peak and four points after the maximum. The mean value of the Gaussian was used as the time stamp for each pulse. A Photek 240 MCP-PMT, whose time resolution was previously measured to be less than 10 ps [199] was used as a “start” signal, while pulses from individual pixels on the Photonis XP85011 MCP-PMT were used as “stop” signals. The integrated charge for each pulse is used as a proxy for the measured energy deposit in each channel, and is computed using four time samples before and after the peak of the pulse. Each time sample is approximately 0.2 ns in time. Events containing pulses above 500 mV in amplitude are rejected as they saturate the DRS4. Only pulses with amplitude larger than 20 mV are used for time measurements, to reduce the impact of the electronics noise in the DRS4. Other event selection and pulse cleaning procedures are used to eliminate abnormal pulses in the readout, as described in [197].

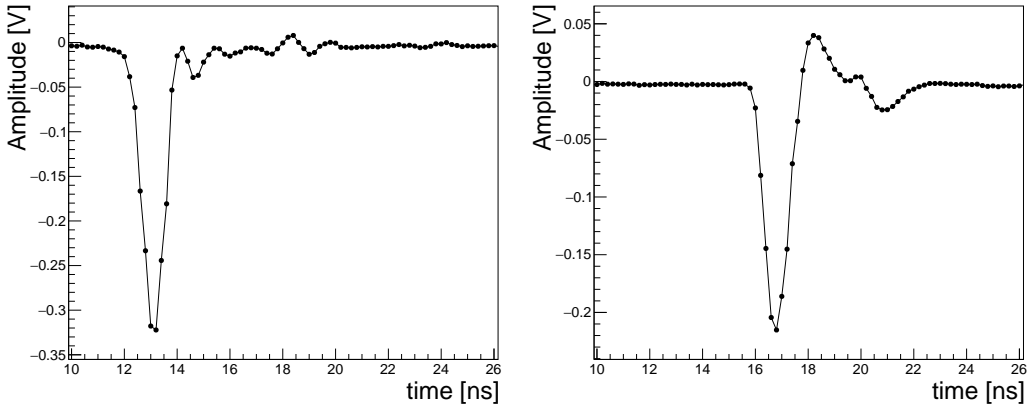


Figure 11.3: Example of a digitized signal from a single Photonis pixel (left) and Photek (right) MCP-PMT following a high-energy electron shower, via DRS4.

#### 11.4 Electromagnetic Shower Position Reconstruction and Resolution

The transverse shape of electromagnetic showers is very well known and has a characteristic width given by the Moliere radius, see Section 9.1. For tungsten, the Moliere radius is about 9 mm and therefore the shower is expected to be contained within two of the pixels in the Photonis XP85011 MCP-PMT. In Figure 11.4 shows the mean charge measured in each of the pixels for one example run where the Photonis MCP-PMT was held in a fixed location approximately centered on the beam. The electron beam has a width of about 1 cm.

Each electron impacting the shower-maximum detector will induce an electromag-

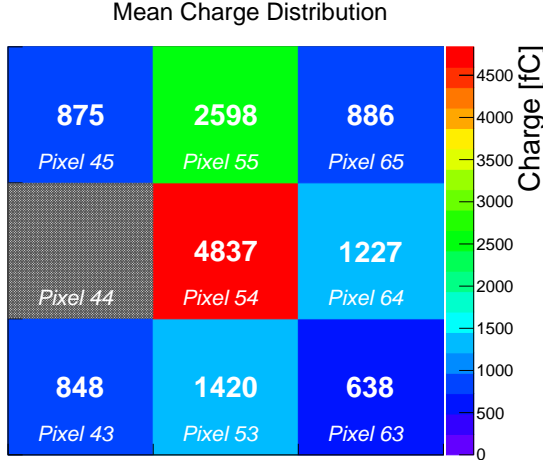


Figure 11.4: The mean charge measured for each pixel for one example run is shown. During this run, the Photonis MCP-PMT was held in the same location. Based on the distribution of the mean charge among the pixels, we can infer that the beam center is located in the upper half of the center pixel. Pixel 44 is not shown as it was found to be not operational.

netic shower, and we define such an occurrence as an event. For each event, the center of the electromagnetic shower ( $\vec{p}$ ) is reconstructed based on the the pixel positions weighted by the corresponding integrated charge as follows:

$$\vec{p} = \frac{\sum_{i \in \text{pixels}} Q_i \vec{p}_i}{\sum_{i \in \text{pixels}} Q_i}, \quad (11.1)$$

where  $i$  labels the individual pixels,  $Q_i$  is the charge collected in pixel  $i$ , and  $\vec{p}_i$  is the vector describing the  $x$  and  $y$  coordinates of the center of pixel  $i$ . The origin of the coordinate system is chosen to be at the lower left corner of the  $3 \times 3$  array of pixels.

Multiple runs were taken; scanning different beam positions relative to the Photonis MCP-PMT by moving the motorized stage. Figure 11.5 shows the distributions of the reconstructed shower positions for three example runs in which the beam was located near the top, center, and bottom of the central pixel. The distributions of the reconstructed  $y$  coordinate for the three corresponding runs are shown together in Figure 11.6. The measured beam-spot is observed to move consistent with the known movement of the motorized stage. In each run, the center of the beam-spot is determined by fitting the measured  $x$  and  $y$  coordinates with a Gaussian function. The data from all runs are combined by considering the measured  $x$  and  $y$  coordinates relative to the center of the beam-spot (see Fig 11.7). We model

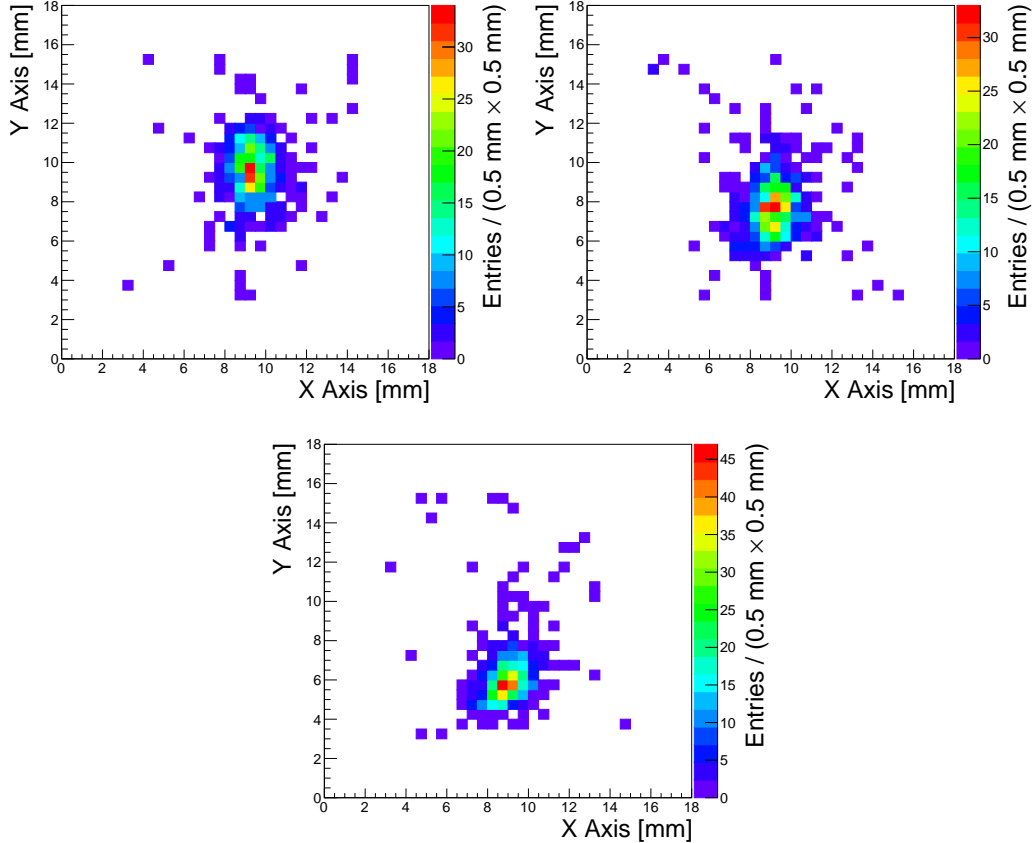


Figure 11.5: The distribution of reconstructed shower positions is shown for three runs with the beam centered near the top, center, and bottom of the central pixel.

the distribution of measured coordinates as a convolution of a flat distribution with width equal to the measured dimensions of the scintillator trigger and a Gaussian resolution function. A maximum likelihood fit is performed on the data using this model, and the position resolution of the detector is measured as the width of the Gaussian resolution function. We measure the position resolution as  $0.55 \pm 0.2 \text{ mm}$  in  $x$ -coordinate, and  $0.91 \pm 0.01 \text{ mm}$  in  $y$ -coordinates.

### 11.5 Electromagnetic Shower Time Resolution

The timestamps of the individual pixels of the Photonis MCP-PMT for each event are reconstructed as described in Section 11.3. The timestamp of the entire electromagnetic shower ( $t$ ) is estimated using the same energy weighting procedure that was used above for the shower position reconstruction, i.e.

$$t = \frac{\sum_{i \in \text{pixels}} Q_i t_i}{\sum_{i \in \text{pixels}} Q_i}, \quad (11.2)$$

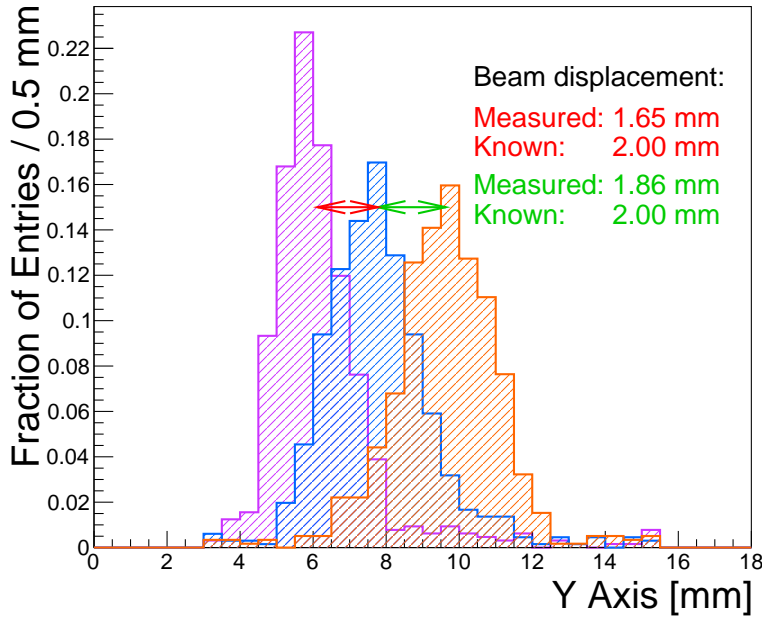


Figure 11.6: The distributions of reconstructed shower position in the  $y$  axis is shown for the three runs corresponding to the distributions shown in Figure 11.5. The measured beam displacements are compared to the known displacements as recorded by the motorized stage.

where  $i$  labels the individual pixels,  $Q_i$  is the charge collected in pixel  $i$ , and  $t_i$  is the reconstructed time-stamp for pixel  $i$ . Alternatively, the time resolution using the single pixel with the highest energy deposit measurement is used. Figure 11.8 shows the time distributions for these two methods of shower time reconstruction.

Figure 11.9 shows the time resolution for electromagnetic showers measured using the two methods described above. The time resolution for the pixel with the largest energy deposit is around 70 ps and 85 ps, depending on the run. Using the energy weighted algorithm improves the time resolution consistently to about 50 ps. The time measurement obtained using the Photonis MCP-PMT typically exhibit a dependence on the pulse amplitude or integrated charge. This dependence is shown on the left of Figure 11.10, and is observed to be approximately the same for all pixels. We perform a correction to the time measurement based on the measured integrated charge, and we verify that the correction does flatten the dependence of the time measurement on the integrated charge as shown on the right panel of Figure 11.10. After performing this time measurement correction, the time resolution measurements improve to about 35 ps and is shown in Figure 11.11. We performed two sets of correction procedures. In one set, labelled as “Self-Calibrated”, an independent

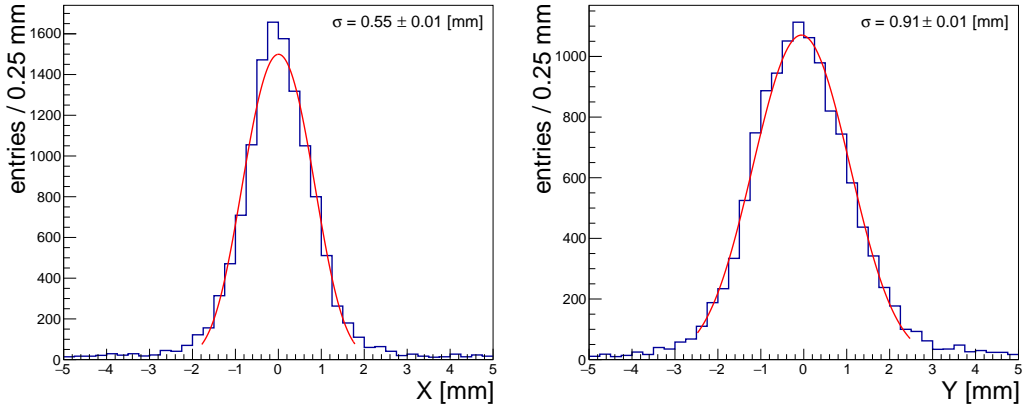


Figure 11.7: The distributions of the measured  $x$  (left) and  $y$  (right) coordinates are shown along with the fit to the resolution model. The position resolution of the EM shower as measured by the MCP-PMT detector is determined from the fit to the resolution model.

correction is derived for each run and for each pixel. In the second set, labelled as “Calibrated”, a single correction is obtained for each pixel from a single run, and this correction is applied to all other runs. Figure 11.11 shows that this single correction is applicable to all other runs without loss of the precision of the measurements.

Finally, the dependence of the electromagnetic shower time resolution on of the number of pixels included in the energy-weighted algorithm is studied. Figure 11.12 shows this dependence for one example run. It is observed that the time resolution improves according to a  $1/\sqrt{N}$  scaling up to about 5–6 pixels, and then becomes flat as more pixels are included. The initial  $1/\sqrt{N}$  scaling is encouraging as it indicates that the time jitter across different pixel channels arise primarily from uncorrelated sources, and that further granularity may improve the time resolution provided that the signal is sufficiently large compared to noise. As the majority of the shower is covered by the pixels closest to the center of the shower—usually 5–6 pixels—, it is not surprising that the time resolution does not further improve by adding the remainder of pixels.

## 11.6 Summary

Studies towards the development of future electromagnetic calorimeters capable of high precision energy and time measurements have been carried out. Such calorimeters should ultimately provide both spatial resolution below the mm level and time resolution of 20 – 30 ps, in order to mitigate the detrimental effects of pileup. A highly granular readout is required to achieve these goals.

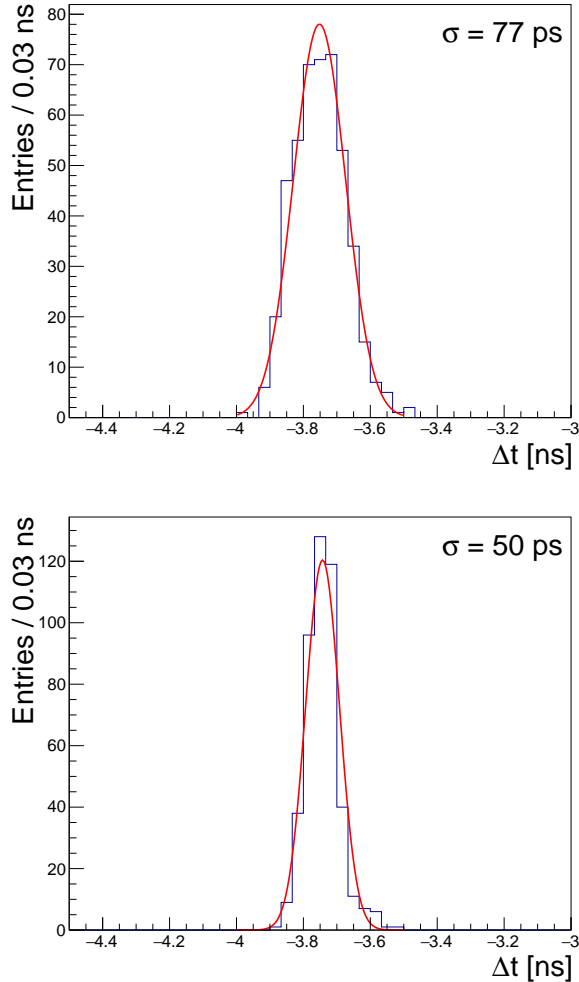


Figure 11.8: The time distributions obtained using the highest energy pixel (left) and the energy weighted algorithm (right) are shown for one example run. The distributions are fitted with Gaussian models, and the width parameter of the Gaussian is displayed on the plot.

This chapter reports the results on position and time resolution measurements of a secondary emission based calorimeter prototype that used the Photonis XP85011 MCP-PMT as the sensitive element. Using a pixelated readout of the MCP-PMT a highly granular information of the shower development in the transverse plane is obtained. Combining the measurements from a  $3 \times 3$ -pixel readout a sub-millimeter position resolution is measured, which far exceeds the 6 mm size of the individual pixels. While the more granular readout degrades the signal to noise for each individual pixel, the proper combination from independent pixels preserves a good time resolution. The measured time resolution improves with the increase in the number of pixels used as  $1/\sqrt{N}$ , and when using all pixels, the time resolution is

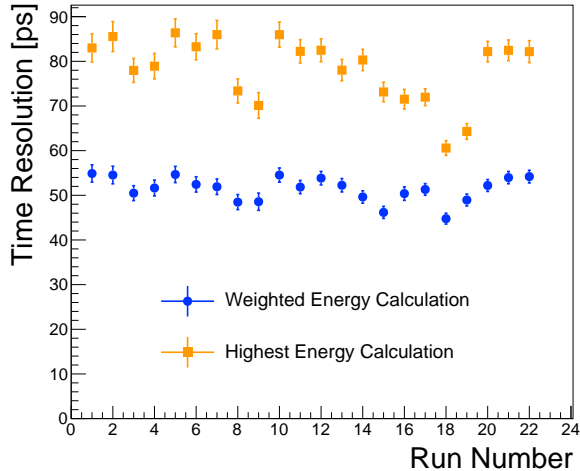


Figure 11.9: Time resolution found for each run. The time-stamp obtained using the energy weighting method yields time resolutions consistently below 60 ps. The time resolution measured using the single pixel with the largest signal is significantly worse.

30 – 40 ps. Future measurements could include larger prototypes with several layers of sensitive material, that will allow the study of the longitudinal development of the showers.

### 11.7 Acknowledgements

I like to thank Erik Ramberg for supporting this work, and Aria Soha and the FTBF test beam facility for the good beam delivery and control. Thanks to Ewa Skup and Geoff Savage for help with operation of Cherenkov counters, and to Todd Nebel for organizing and providing supporting equipment at FTBF.

This work is supported by funding from Fermi Research Alliance, LLC under Contract No. DE-AC02-07CH11359 with the United States Department of Energy, and from California Institute of Technology High Energy Physics under Contract DE-SC0011925 with the United States Department of Energy.

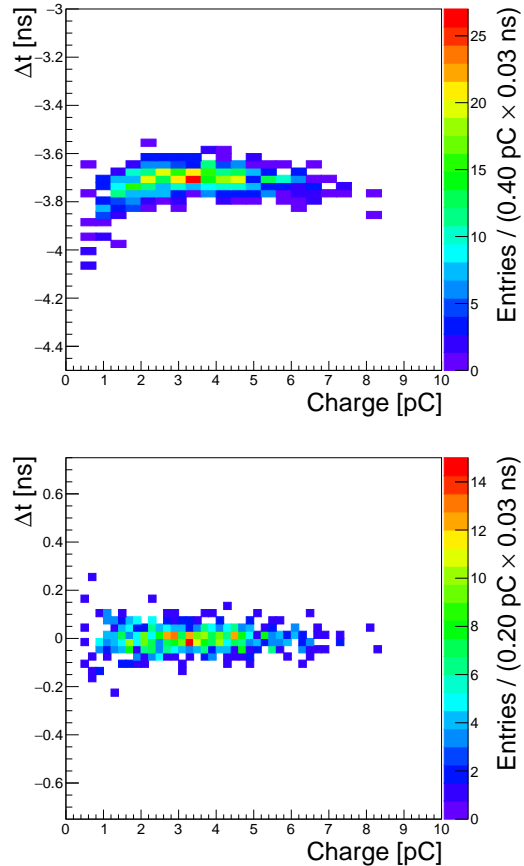


Figure 11.10: The correlation between the time measurement and the measured integrated charge is shown on the left for one example pixel. The same correlation after performing the time measurement correction is shown on the right.

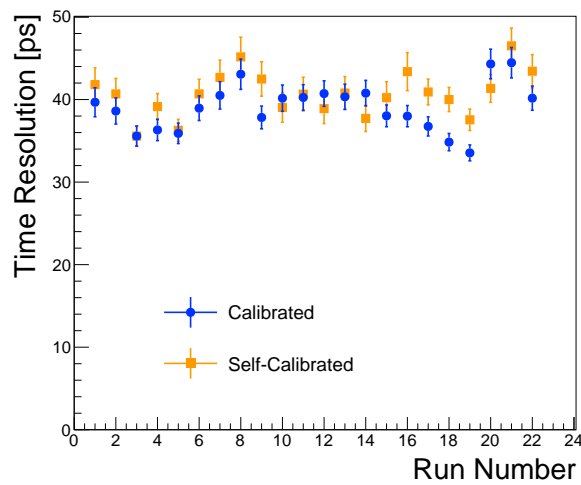


Figure 11.11: The time resolution of the electromagnetic shower for various runs is shown after performing the time measurement correction based on the measured integrated charge.

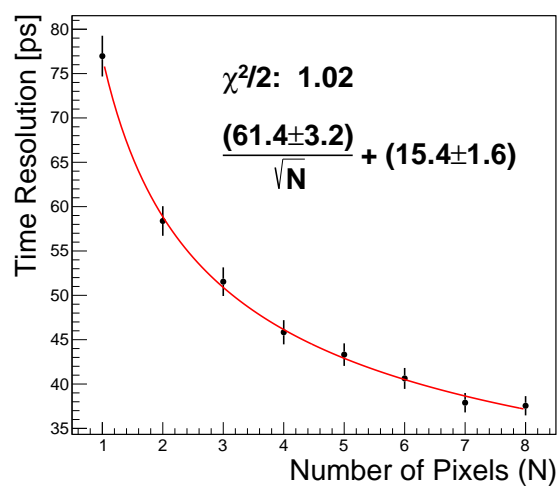


Figure 11.12: The time resolution is plotted as a function of the number of pixels included in the energy-weighted algorithm for one example run.

## SILICON-BASED SAMPLING CALORIMETERS

### 12.1 Introduction

Several alternative options to combine high resolution energy and timing measurements for calorimetry have been reported in Refs. [200, 198, 168, 224, 216] as well as those described in Chapters 10 and 11. This chapter describes the continuation of this program by using a calorimeter prototype employing a  $300\ \mu\text{m}$  thick silicon pad sensor of  $6 \times 6\ \text{mm}^2$  size as the sensitive element. Silicon-based calorimeters have recently become a viable choice for future colliders due to the radiation hardness of silicon, and the ability to construct highly granular detectors [27]. An important example is the forward calorimeter proposed for the CMS Phase 2 Upgrade [68]. We study the timing properties of silicon-based calorimeter using a prototype composed of tungsten absorber and a silicon sensor produced by Hamamatsu [4].

This chapter is organized as follows. General silicon timing properties and bench test results are described in Section 12.2. The test beam setup and experimental apparatus are presented in Section 13.3. The results of the test beam measurements are presented in Section B.7. Finally, Sections 12.5 and 12.6 are devoted to discussion and conclusion, respectively.

### 12.2 General Properties of Silicon Timing and Bench Test Studies

All measurements presented in this chapter were carried out using a silicon sensor produced by Hamamatsu [4]. The thickness of the silicon sensor was measured to be  $325\ \mu\text{m}$ , while its transverse size is  $6 \times 6\ \text{mm}^2$ . The negative bias voltage was applied to the p-side of the silicon. The capacitance of the silicon diode is measured as a function of the bias voltage and shown in Figure 12.1. The silicon is fully depleted above about 120 V.

The electric diagram of the silicon diode connections is presented in left panel of Figure 12.2. Attention was paid to provide good filtering for the bias voltage, to reduce ground loop effects, and to minimize inductive loop for the signal readout. The timing characteristics of the signal pulses are therefore dominated primarily by properties of the silicon sensor rather than the details of the circuit. The silicon diode was placed inside a light-tight box (silicon box) of thickness 1.5 cm, which

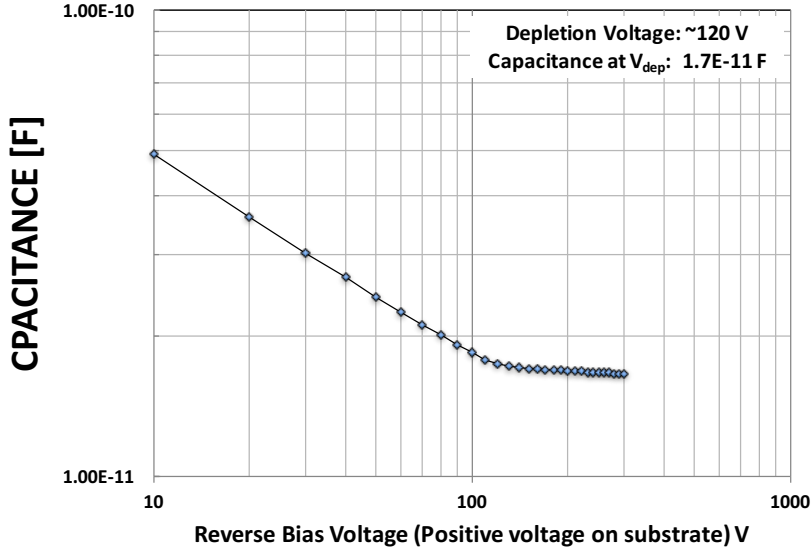


Figure 12.1: The measured capacitance as a function of the applied bias voltage.

also provides electromagnetic shielding. The box is made of 0.2 mm steel. The bias voltage was supplied to the circuitry by a cable with a balun filter, terminated with an SHV connector. The silicon diode output signal was read out through an SMA connector electrically grounded to the box. The dark current was measured at several values of the bias voltage. The maximum value of the dark current was less than 1.0 nA at -500 V, which is the largest bias voltage used in the measurements reported. The silicon box is presented in the right panel of Figure 12.2. Signals

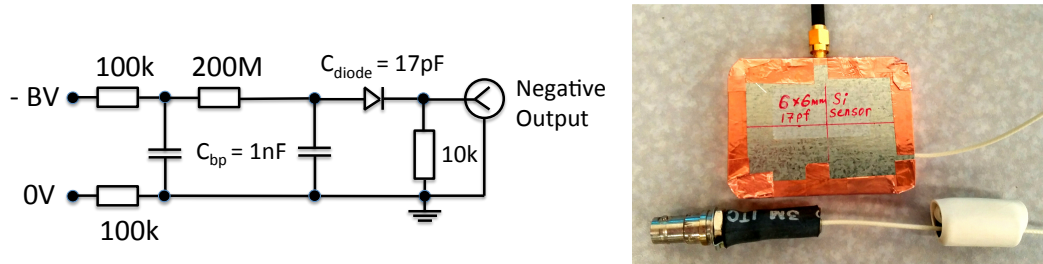


Figure 12.2: The electric diagram for the silicon diode connections (left). External view of the box with silicon diode, and the bias voltage connection is shown below it (right).

from the silicon sensor were amplified by two fast, high-bandwidth pre-amplifiers connected in series. The first amplifier is an ORTEC VT120C pre-amplifier, and the second is a Hamamatsu C5594 amplifier. The combined gain of the two amplifiers in series as a function of the input signal amplitude was measured using a pulse-

generator. Some non-linearities for typical signals produced by the silicon sensor under study were found and corrected.

### 12.3 Test-beam Setup and Experimental Apparatus

Test-beam measurements were carried out at the FTBF which provided a 120 GeV proton beam from the Fermilab Main Injector accelerator , and secondary beams composed of electrons, pions, and muons of energies ranging from 4 GeV to 32 GeV. A simple schematic diagram of the experimental setup is shown in Figure 12.3. A small plastic scintillator of transverse dimensions 1.7 mm×2 mm is used as a trigger counter to initiate the read out of the DAQ system and to select incident beam particles from a small geometric area, allowing us to center the beam particles on the silicon sensor. Next, we place a stack of tungsten absorbers of various thicknesses for measurements of the longitudinal profile of the electromagnetic shower. The silicon pad sensor is located within a metal box covered by copper foil, and is placed immediately downstream of the absorber plates. Finally, a Photek 240 MCP-PMT detector [42, 197, 200, 198] is placed furthest downstream, and serves to provide a very precise reference timestamp. Its precision was previously measured to be less than 10 ps [200]. A photograph showing the various detector components is presented in Figure 12.4. A differential Cherenkov counter is located further upstream of our experimental setup and provides additional particle identification capability. More details of the experimental setup are described in our previous studies using the same experimental facility in references [42, 197, 200, 198] as well as in Chapters 10 and 11.

The DAQ system is based on a CAEN V1742 digitizer board [5], which provides digitized waveforms sampled at 5 GS/s. The metal box containing the silicon sensor was located on a motorized X-Y moving stage allowing us to change the location of the sensor in the plane transverse to the beam at an accuracy better than 0.1 mm. A nominal bias voltage of 500 V was applied to deplete the silicon sensor in most of the studies shown below, unless noted otherwise.

### 12.4 Test Beam Measurements and Results

Measurements were performed in 2015, using the primary 120 GeV proton beam, and secondary electron beam provided for the FTBF. Secondary beams with energies ranging from 4 GeV to 32 GeV were used. Electron purity for those beams ranges between 70% at the lowest energy to about 10% at the highest energy. Stacks of tungsten plates with varying thicknesses were placed immediately upstream of the

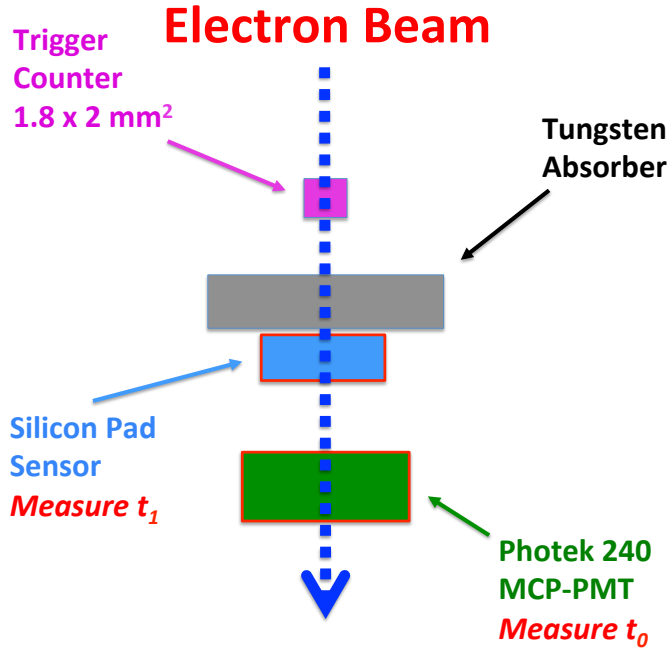


Figure 12.3: A schematic diagram of the test-beam setup is shown. The  $t_0$  and  $t_1$  are defined in Section B.7.

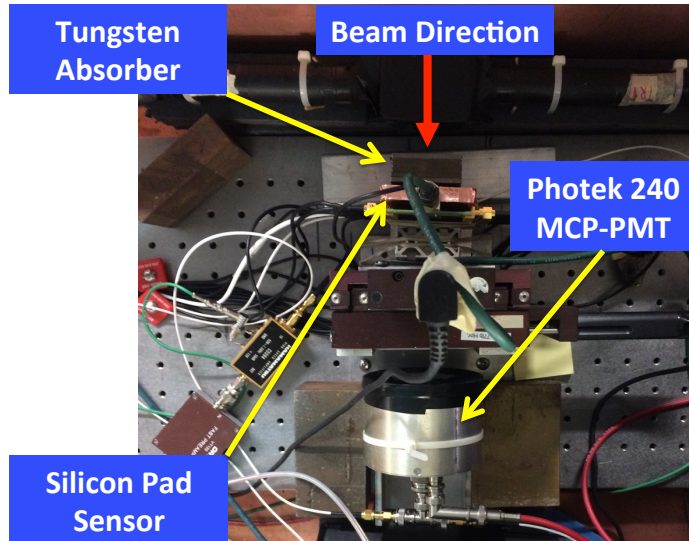


Figure 12.4: Test beam setup.

silicon device in order to measure the response along the longitudinal direction of the electromagnetic shower. The radiation length of tungsten is 3.5 mm, and the Moliere radius is 9.3 mm. The tungsten plate dimensions are sufficient to fully contain the shower in the transverse dimension. Signals from the silicon sensor and the Photek 240 MCP-PMT are read out and digitized by the CAEN V1742 digitizer,

and example signal waveforms are shown in Figure 12.5. The signal pulse in the silicon sensor has a rise time of about 1.5 ns, and a full pulse width of around 7 ns. This rise time is consistent with a time constant of a silicon sensor coupled to a 50 Ohm amplifier.

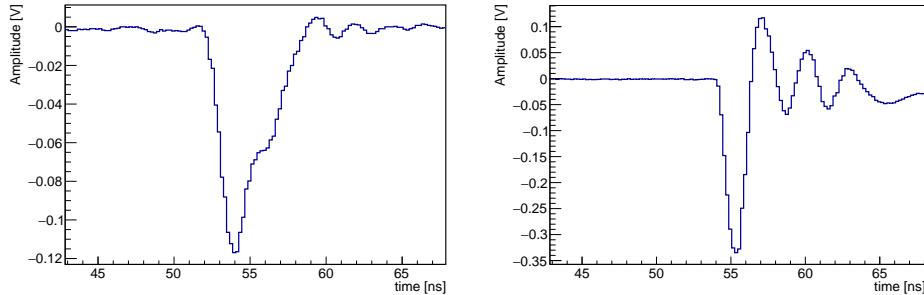


Figure 12.5: Examples of the signal pulse waveform for the silicon sensor (left) and the Photek MCP-PMT (right) digitized by CAEN V1742 digitizer board. The bias voltage applied to the silicon pad sensor is 500 V.

The CAEN digitizer is voltage and time calibrated using the procedure described in Ref. [164]. The total collected charge for each signal pulse is computed by integrating a 10 ns window around the peak of the pulse. The time for the reference Photek MCP-PMT detector is obtained by fitting the peak region of the pulse to a Gaussian function and the mean parameter of the Gaussian is assigned as the timestamp  $t_0$ . The time for signals from the silicon sensor is obtained by performing a linear fit to the rising edge of the pulse and the time at which the pulse reaches 30% of the maximum amplitude is assigned as its timestamp  $t_1$ . The electronic time resolution of the CAEN V1742 digitizer was measured to be  $\sim 4$  ps and neglected on the timing measurements described below.

Electrons were identified by requiring that the signal amplitude of the gas Cherenkov counter provided by the FTBF and the Photek 240 MCP-PMT detector located further downstream of the silicon sensor exceed certain thresholds because electromagnetic showers induced by electrons produce significantly larger signals, while pions produce much smaller signals. After imposing the electron identification requirements the electron purity is between 80% and 90% for all beam conditions. The purity was determined by comparing the calorimetric measurements with those from the Cherenkov detector.

Let's begin by establishing the signal characteristics of a minimum-ionizing particle (MIP) using beams of 120 GeV protons and 8 GeV electrons with no absorbers

upstream of the silicon pad sensor. To separate MIP signals from noise, separate data events with no beam and a random trigger are recorded. The charge distribution for these noise runs is presented in Figure 12.6. As expected, the charge distribution is centered at 0, and the RMS is about 2 fC. Figure 12.7 shows the silicon sensor

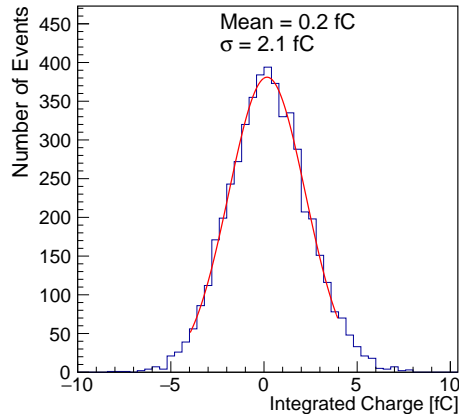


Figure 12.6: The distribution of charge integrated in the silicon sensor is shown for data events with no beam and random trigger.

response to 120 GeV protons and 8 GeV electrons without any absorber. We observe very similar response for these two cases, and measure a mean integrated charge of 4.5 fC and 5.0 fC for proton and electrons, respectively. The measured signals are corrected for the gain of the amplifiers used, and hence is the output charge of the silicon sensor. We expect peak charge of 28,000 and 31,000 electron-hole pairs in a 325  $\mu\text{m}$  thick silicon detector for ionizing particles with Lorentz factor  $\gamma = 120$  (protons) and 16,000 (electrons) [182], which is in a good agreement with the measured values. Having established the absolute scale of the response using single particles, the remaining studies normalize all charge measurements to the 120 GeV proton signal, which hereafter is referred to as  $Q_{\text{MIP}}$ . The response of the silicon sensor to electron beams of various energies after 6 radiation lengths ( $X_0$ ) of tungsten absorber is presented. The silicon sensor is expected to be sensitive to the number of secondary electrons produced within the electromagnetic shower, and therefore its response is expected to scale up with higher incident electron energies. Figure 12.8 shows an example of the integrated charge distribution measured in the silicon sensor after 6 radiation lengths of tungsten, for runs with 32 GeV electrons. The mean and RMS of these distributions as a function of incident electron beam energy are shown in Figure 12.8. The plotted uncertainties represent the RMS of the charge distribution. Since the electron beam profile and purity varies at different

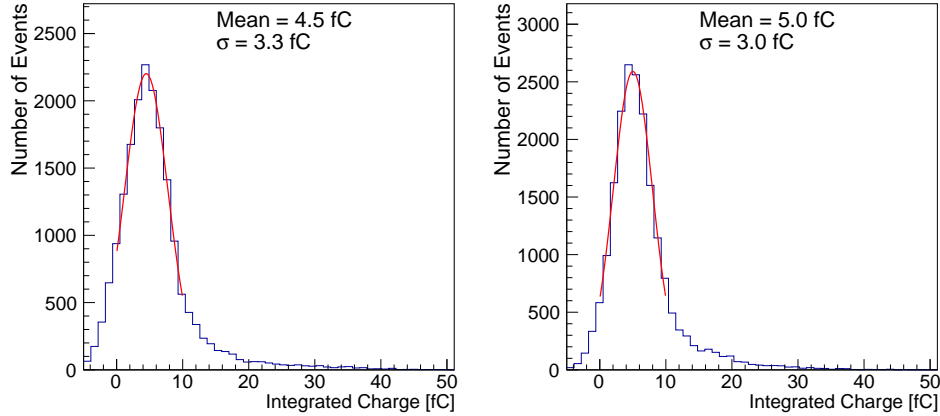


Figure 12.7: The distribution of charge integrated in the silicon sensor is shown for a beam of 120 GeV protons (left) and 8 GeV electrons (right) without any absorber upstream of the silicon sensor. These conditions mimic the response of the silicon sensor to a minimum-ionizing particle. All triggered events were used in these distributions.

beam energies, we collected between 10 and 50 thousand events for each beam energy, in order to ensure sufficiently large data samples. A fairly linear dependence between the measured charge and the incident beam energy is observed, see the right panel of Figure 12.8. The measured time resolution between the silicon sensor

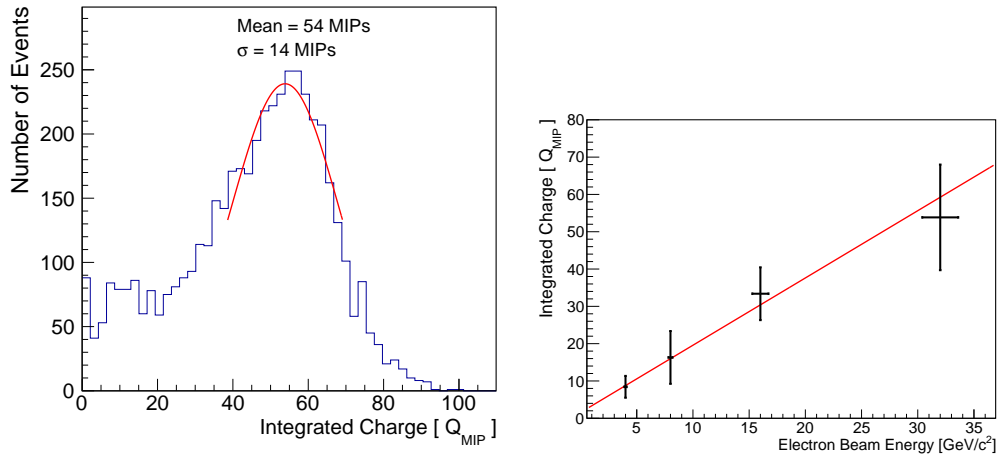


Figure 12.8: Left: An example of the distribution of integrated charge in the silicon sensor for 32 GeV electrons and 6  $X_0$  absorber shown in units of  $Q_{MIP}$ . Right: The integrated charge in the silicon sensor expressed in units of  $Q_{MIP}$  is shown for the same 6  $X_0$  absorber as a function of the electron beam energy. The uncertainty bands show the RMS of the measured charge distribution. The red line is the best fit to a linear function..

and the Photek MCP-PMT, was obtained by measuring the standard deviation of the Gaussian fit to the TOF distribution, i.e.  $\Delta t = t_0 - t_1$ . The later exhibits a systematic dependence on the total charge measured in the silicon detector, as shown on the left panel in Figure 12.9. This dependence on the integrated charge of the amplified signal was reproduced when the output of the pulse-generator was connected to the same amplifiers as used in the measurements. Therefore a correction to  $\Delta t$  for each event using the measured charge in the silicon sensor was applied. This procedure is referred to in the following as *time correction*. The correction is obtained by fitting a second degree polynomial to the profiled distribution of the  $\Delta t$  versus total charge collected in the silicon sensor, as shown in Figure 12.9. The cross-check that the *time correction* flattens the dependence of the time measurement on the integrated charge is shown on the right panel of Figure 12.9. The *time correction* improves the time resolution measurement by 30 – 35%. All time resolution measurements in the rest of this study are performed after such a time correction. An example of a corrected  $\Delta t$  distribution for 32 GeV electrons after 6  $X_0$  is shown on the left panel of Figure 12.10. Other than the electron identification requirements, no additional selection requirements on the amplitude of the signal in the silicon sensor were made. The dependence of the measured time resolution on the beam energy is shown on the right panel of Figure 12.10. The time resolution improves as the beam energy increases, with a time resolution of 23 ps for the 32 GeV electron beam. Furthermore, the response and time resolution of the silicon sensor along the longitudinal direction of the shower development is studied. The integrated charge and the time resolution as a function of the absorber thickness is shown in Figure 12.11, for an 8 GeV electron beam. A typical longitudinal shower profile is observed, consistent with previous studies performed using a secondary emission calorimeter prototype based on MCP's [200], as well as independent studies of silicon-based calorimeter prototypes [178]. The RMS of the integrated charge distribution at each absorber thickness is relatively large, due to the small transverse size of the active element used in the experiment. It is of note that the time resolution improves as the shower develops towards its maximum in the longitudinal direction. Finally, the dependence of the time resolution as a function of the bias voltage applied to deplete the silicon sensor is also studied. The measurements are shown in Figure 12.12 for 16 GeV electrons after 6  $X_0$  of tungsten absorber. As presented in Figure 12.12, the time resolution improves as the bias voltage is increased, which is expected on the basis of increased velocity of electrons and holes in silicon at larger bias voltage.

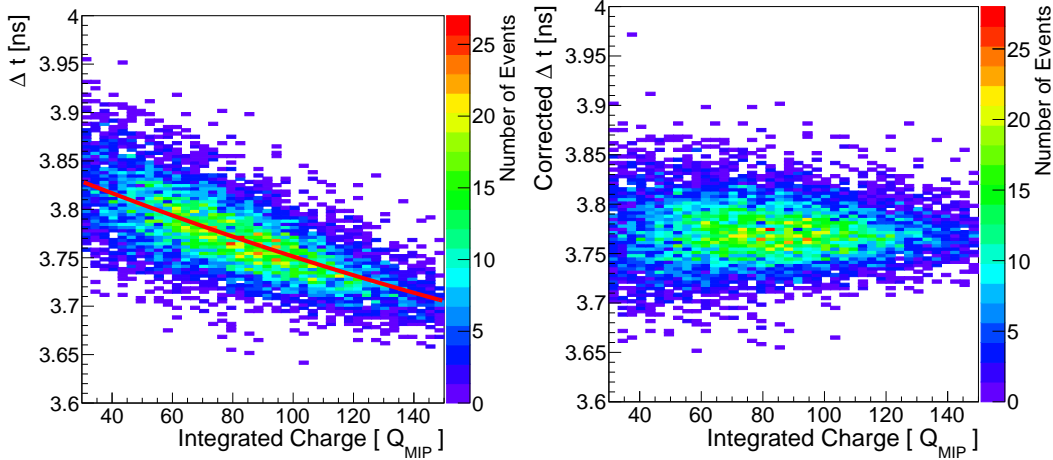


Figure 12.9: The dependence of  $\Delta t$  on the integrated charge in the silicon sensor is shown on the left. The red curve represents the fit to the profile plot of the two dimensional distribution, and is used to correct  $\Delta t$  for this effect. On the right, we show the corresponding two dimensional distribution after performing the correction. A 16 GeV electron beam is used, and the silicon sensor is placed after  $6 X_0$  of tungsten absorber.

## 12.5 Discussion

From Figures 12.6 and 12.7, it is observed that the noise of the prototype calorimetric system is sufficiently low to extract signals from MIPs. Comparing the RMS of the noise distribution with the mean of the MIP signal, a signal-to-noise ratio around 2 to 2.5 is extracted. A rough estimate from Figure 12.7 demonstrates that the efficiency to detect 120 GeV protons and 8 GeV electrons with no absorber present is larger than 80%. The signal distributions for electromagnetic showers are normalized to the MIP response, and a linear response as a function of the beam energy is observed, as shown in Figure 12.10. The measured longitudinal shower profile in, shown in Figure 12.11, is consistent with similar past measurements.

The TOF associated with the detection of electromagnetic showers induced by electrons with energy between 20 GeV and 30 GeV can be measured with a precision better than 25 ps. Results of the measurements reported in Ref. [32] showed that a time resolution below 50 ps could be achieved for signals larger than 10 equivalent MIPs. to achieve this. Taking into account the 13 ps time resolution of the reference Photek MCP-PMT detector measured to electromagnetic showers [200] yields a precision close to 20 ps. Moreover, the time resolution improves with larger electron beam energy, and more generally with larger signal amplitudes. These measurements demonstrate that a calorimeter based on silicon sensors as the

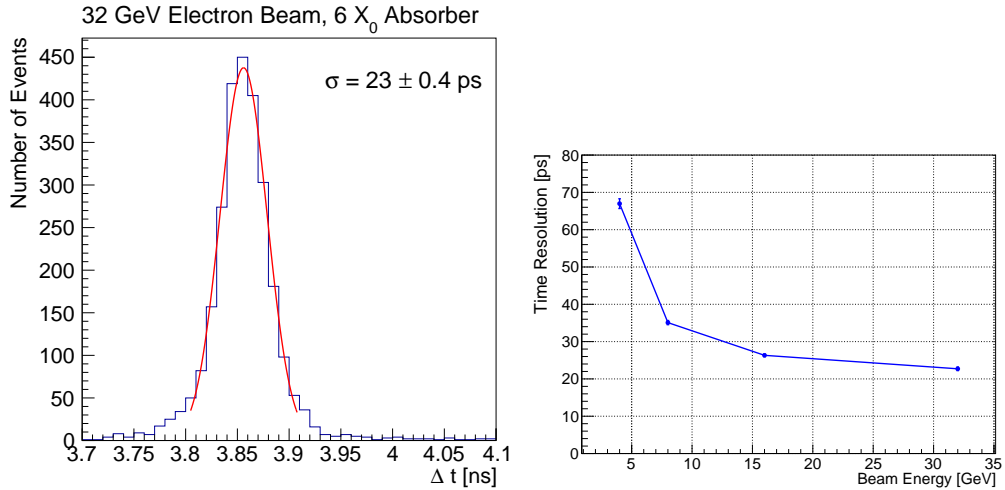


Figure 12.10: Left: The distribution of  $\Delta t$  between the silicon sensor and the Photek MCP-PMT. A 32 GeV electron beam is used, and the silicon sensor is placed after  $6 X_0$  of tungsten absorber. Right: The measured time resolution between the silicon sensor and the Photek MCP-PMT reference is shown as a function of the electron beam energy. The silicon sensor is placed after  $6 X_0$  of tungsten absorber.

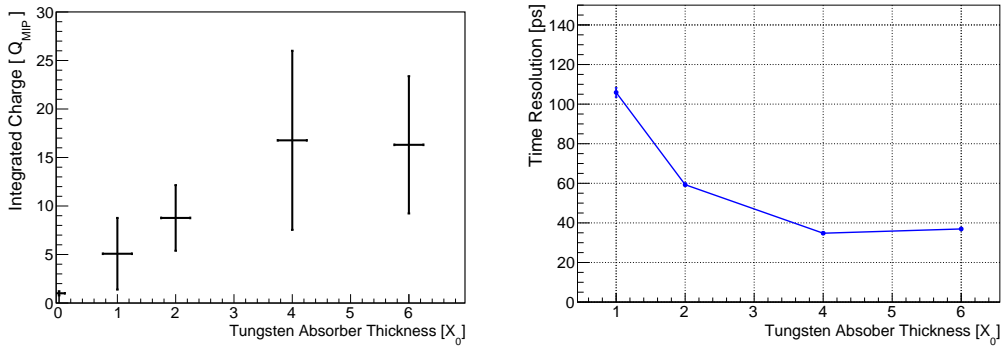


Figure 12.11: On the left, the integrated charge in the silicon sensor expressed in units of  $Q_{\text{MIP}}$  is shown as a function of the absorber (W) thickness measured in units of radiation lengths ( $X_0$ ). The electron beam energy was 8 GeV. The uncertainty bands show the RMS of the measured charge distribution. On the right, the time resolution between the silicon sensor and the Photek MCP-PMT reference is shown as a function of the absorber thickness.

sensitive medium can achieve intrinsic time resolution at the 20 ps level, as long as noise is kept under control. Time jitter arising from intrinsic properties of the silicon sensor is demonstrated to be well below the 20 ps level.

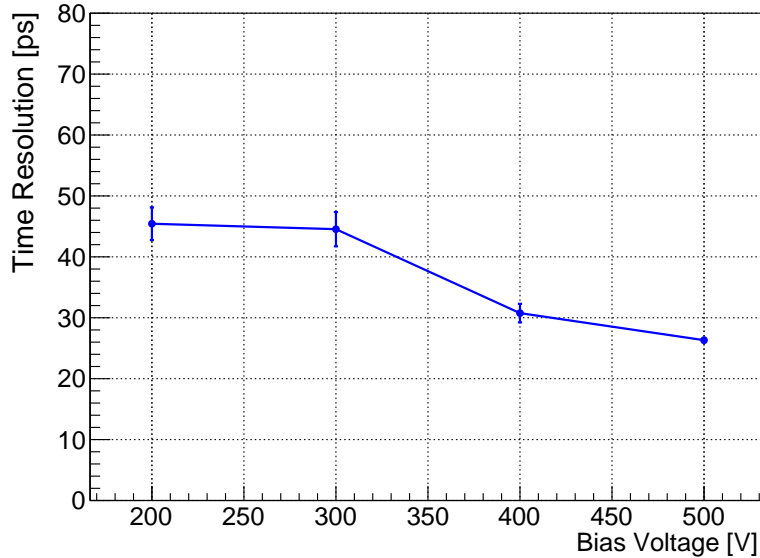


Figure 12.12: The time resolution between the silicon sensor and the Photek MCP-PMT reference is shown as a function of bias voltage applied on the silicon sensor. The electron beam energy was 16 GeV, and the silicon sensor is placed after  $6 X_0$  of tungsten absorber.

## 12.6 Conclusion

The best time resolution of 23 ps for a silicon sensor was achieved with a 32 GeV beam and with the silicon sensor placed after 6 radiation lengths of tungsten absorber. Based on the calibration data for the response of the silicon sensor to MIPs, this measurement corresponds roughly to an average of 54 secondary particles registered from the electromagnetic shower. This results provide a solid ground and further encouragement to use silicon as the sensitive medium in sampling calorimeters, as is planned for example for the CMS Phase 2 upgrade [68], and explicitly demonstrates the opportunity to use silicon for timing measurements in future calorimeters. Further measurements include more realistic prototypes covering larger transverse and longitudinal regions of the electromagnetic shower and increasing the transverse granularity.

## CMS HIGH-GRANULARITY CALORIMETER TIMING LAYER

### 13.1 Introduction

Recent advances in silicon sensors in terms of radiation tolerance, highly granular designs [27], and cost per unit area offers the possibility of their use as the sensitive media in a sampling calorimeter at the HL-LHC. An important example of such a device is the forward calorimeter proposed for the CMS Phase 2 Upgrade [68], where high-granularity silicon sensors and tungsten/copper absorber layers are interleaved. As described in Chapter 12, silicon-based shower maximum detectors have extremely good precision timing capabilities – achieving a TOF resolution of 25 ps for 32 GeV electron induced shower – which could be used to reduce the detrimental effects of the high pileup environment foreseen for the HL-LHC. This chapter presents recent studies on the intrinsic timing properties of the silicon sensors to be used by the proposed CMS high-granularity calorimeter (HGC).

This chapter is organized as follows. General properties of the HGC silicon sensor are described in Section 13.2. The test beam setup and experimental apparatus are presented in Section 13.3. The results of the test beam measurements are presented in Section 13.4. Finally, Section 13.5 is devoted to discussion and conclusions.

### 13.2 General Properties of Silicon Timing and Bench Test Studies

All measurements presented in this chapter were carried out using a silicon sensor identical to that of the CMS HGC. The silicon sensor thickness is  $300\mu\text{m}$  and it is comprised of 128 hexagonal pixels with 1 cm maximal diameter. The left and right panels of Figure 13.1 show a schematic with 7 pixels and a full CAD schematic of the sensor, respectively. The silicon sensor was wire-bonded to a printed circuit board (PCB) where 25 pixels were implemented with an independent analog readout. The PCB provided amplification for all the 25 implemented pixels and was optimized for timing measurement, this final HGC timing layer is shown in Figure 13.2. The silicon sensor was operated with a bias voltage of  $-300\text{ V}$  and the measured total current was  $170\text{ }\mu\text{A}$ .

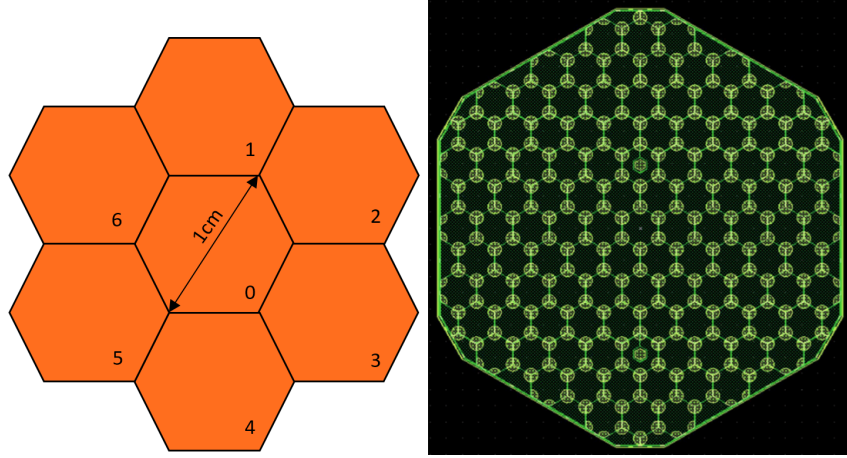


Figure 13.1: An HGC sensor schematic geometry with 7 pixels (left), and a CAD schematic of the entire sensor (right) are shown.

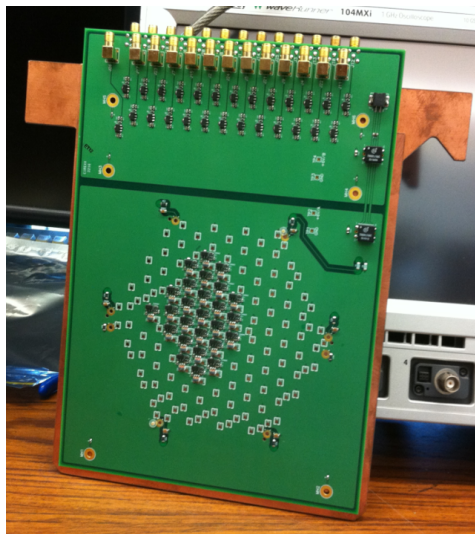


Figure 13.2: The implemented HGC timing layer is shown. 25 pixels with full analog electronics were implemented. The silicon sensor is at the back of the PCB.

### 13.3 Test-beam Setup and Experimental Apparatus

Test-beam measurements were carried out at the FTBF which provided a 120 GeV proton beam from the Fermilab Main Injector accelerator , and secondary beams composed of electrons, pions, and muons of energies ranging from 4 GeV to 32 GeV. A simple schematic diagram of the experimental setup is shown in Figure 13.3. A small plastic scintillator of transverse dimensions 1.7 mm×2 mm is used as a trigger counter to initiate the read out of the DAQ system and to select incident beam particles from a small geometric area, allowing us to center the beam particles on the HGC timing layer. Next, we place a stack of either tungsten or lead absorbers of var-

ious thicknesses for measurements of the longitudinal profile of the electromagnetic shower. The HGC timing layer is located immediately downstream of the absorber plates. Finally, a Photek 240 MCP-PMT detector [42, 197, 200, 198] is placed furthest downstream, and serves to provide a very precise reference timestamp; Its precision has been previously measured to be less than 10 ps [200]. A photograph showing the various detector components is presented in Figure 13.4. More details of the experimental setup are described in our previous studies using the same experimental facility in references [42, 197, 200, 198] as well as in Chapters 10 and 11. The DAQ system is based on a CAEN V1742 digitizer board [5], which

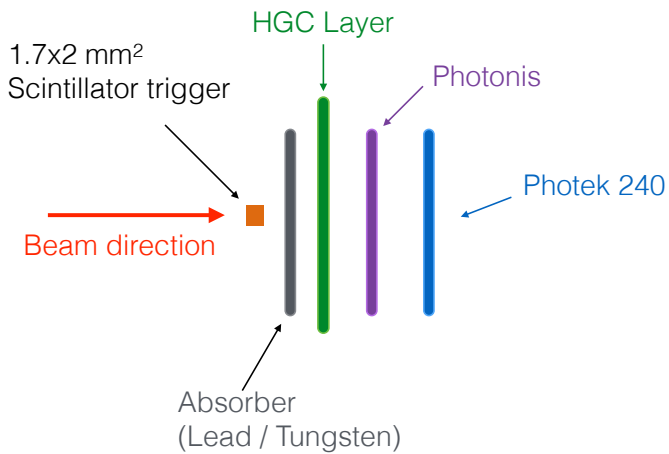


Figure 13.3: A schematic diagram of the test-beam setup is shown. The  $t_0$  and  $t_1$  are defined in Section B.7.

provides digitized waveforms sampled at 5 GS/s. The HGC timing layer was not electromagnetically shielded and therefore some electronic pickup noise was detected and accounted for during the offline analysis. A nominal bias voltage of  $-300$  V was applied to deplete the silicon sensor in all of the studies shown below.

### 13.4 Test Beam Measurement, Data Analysis, and Results

Measurements were performed in June 2016, using the primary 120 GeV proton beam, and secondary electron beam provided for the FTBF. Secondary beams with energies ranging from 4 GeV to 32 GeV were used. As discussed in Chapter 12, the electron purity for those beams ranges between 70% at the lowest energy to about 10% at the highest energy. Stacks of either tungsten or lead plates with varying thicknesses were placed immediately upstream of the HGC timing layer in order to measure the response along the longitudinal direction of the electromagnetic shower, although most of the results presented below correspond to  $6X_0$  of lead.

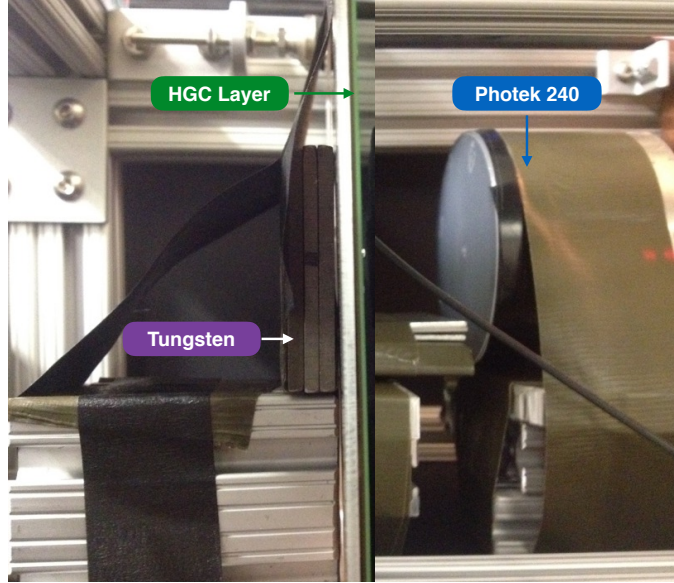


Figure 13.4: HGC timing layer test beam setup.

Signals from the HGC timing layer (25 pixels were implemented and read out) and the Photek 240 MCP-PMT are read out and digitized by the CAEN V1742 digitizer; representative signal waveforms for one of the 25 silicon pixels and the Photek 240 are shown in the left and right panel of Figure 13.5, respectively. The silicon signal pulse has a rise time of about 2 ns, and a full pulse width of around 7 ns. This rise time is consistent with a time constant of a silicon sensor coupled to a 50 Ohm amplifier.

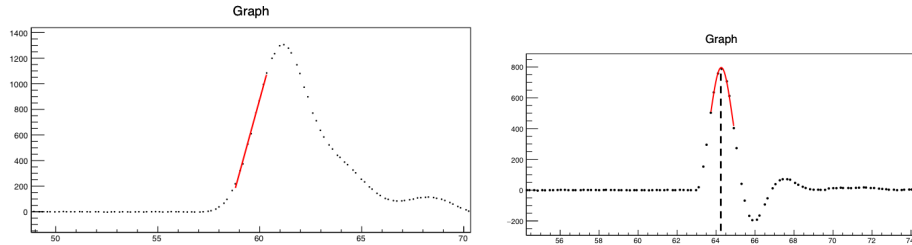


Figure 13.5: Examples of the signal pulse waveform for one of the pixels of the HGC timing layer (left) and the Photek MCP-PMT (right) digitized by CAEN V1742 digitizer board. The bias voltage applied to the HGC silicon sensor is  $-300$  V.

The CAEN digitizer is voltage and time calibrated using the procedure described in Ref. [164]. The total collected charge for each signal pulse is computed by integrating a 10 ns window around the peak of the pulse. The time for the reference Photek 240 MCP-PMT detector is obtained by fitting the peak region of the pulse

to a Gaussian function and the mean parameter of the Gaussian is assigned as the timestamp  $t_0$ , see the right panel of Figure 13.6. The time for signals from each pixel in the HGC layer is obtained by performing a linear fit to the rising edge of the pulse and the time at which the pulse reaches 45% of the maximum amplitude is assigned as its timestamp  $t_1$ , see the left panel of Figure 13.6. The electronic time resolution of the CAEN V1742 digitizer was measured to be  $\sim 4$  ps and neglected on the timing measurements described below.

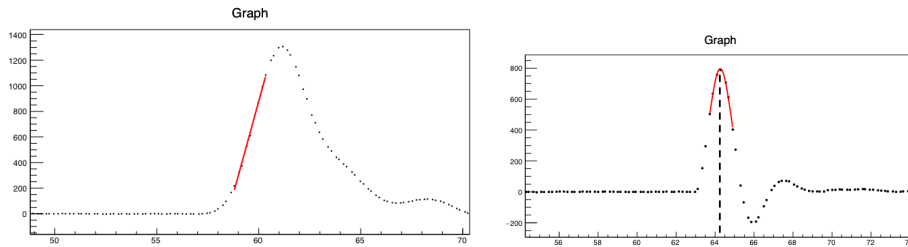


Figure 13.6: Examples of the timestamps extraction for a pulse waveform in one the pixels of the HGC timing layer (left) and the Photek 240 MCP-PMT (right) digitized by CAEN V1742 digitizer board. The timestamp on the HGC pixel is extracted by intersecting the linear fit (solid red line) with the horizontal line corresponding to 45% of the pulse maximum. The timestamp for the Photek 240 is the mean parameter of the Gaussian fit (solid blue line).

Electrons were identified by requiring that the signal amplitude of the Photek 240 MCP-PMT detector, located downstream of the HGC timing layer, exceeds certain thresholds because electromagnetic showers induced by electrons produce significantly larger signals, while pions produce much smaller signals. This procedure has been measured to provide electron purities between 80% and 90% for all beam conditions, see Chapter 12.

### Intrinsic HGC TOF resolution

Let's now examine the intrinsic timing capabilities of the HGC layer. The HGC timing layer was positioned just downstream of  $6X_0$  of lead and showering electrons were selected by requiring the signal amplitude and integrated charge in the Photek 240 MCP-PMT to be above a certain threshold. Figure 13.7 shows two examples of transverse shower profile measured by the HGC layer, where the color palette represents the integrated charge in each pixel. As observed in Figure 13.7 most of the activity is concentrated in the central and the 6 neighbouring pixels – these 7 pixel are more clearly represented in the left panel of Figure 13.1 – and therefore the studies in this chapter just include these pixels. It is of note that the central pixel could

fluctuate in an event-by-event basis. The TOF for each of the considered pixels in the

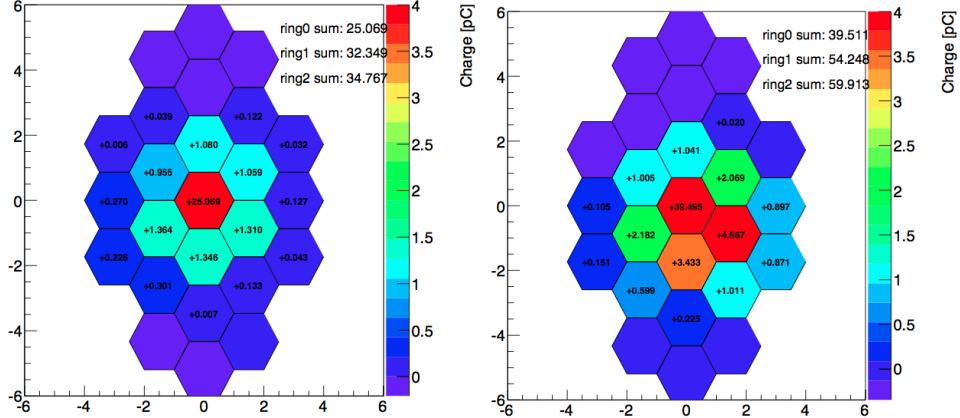


Figure 13.7: Examples of the shower transverse profile sampled by the HGC layer for a 32 GeV (left) and 16 GeV (right) electron beam. There is  $6X_0$  of tungsten right upstream of the HGC layer.

HGC layer with respect to the Photek 240 MCP-PMT, i.e.  $\Delta t = t_1 - t_0$ , is calculated. Subsequently, the information from all the pixels is combined by weighting the individual times with the corresponding charge deposited in the following fashion:

$$\Delta t_{HGC} = \frac{\sum_{i=0}^6 \text{charge}_i \times \Delta t_i}{\sum_{i=0}^6 \text{charge}_i}, \quad (13.1)$$

where  $\Delta t_{HGC}$  is the combined HGC layer TOF,  $\text{charge}_i$  is the charge deposited in the  $i$ -th pixel, and  $\Delta t_i$  is the  $i$ -th pixel TOF. The TOF distributions for the pixels with highest and second highest charge are shown in the left and right panel of Figure 13.8, respectively. The TOF distributions of the HGC layer ( $\Delta t_{HGC}$ ) is shown in the left panel of Figure 13.9, while an alternative method for combining the HGC pixels – using the most probable value (mpv) of the deposited charge distribution in each pixel as the weight, see Eq. 13.1. These weights are constant throughout an entire run. – is shown in the right panel of Figure 13.9. It is of note that the default and the alternative (mpv) algorithms yield very similar results with an outstanding time resolution of about 15 ps for an electron beam of 32 GeV.

Comparing Figure 13.8 (left panel) and Figure 13.9, it is observed that the TOF resolution of the central pixel is already close the final time resolution of the entire HGC layer. This suggests that pixels combination does not provide a significant improvement to the overall TOF resolution. Figure 13.10 shows the HGC TOF

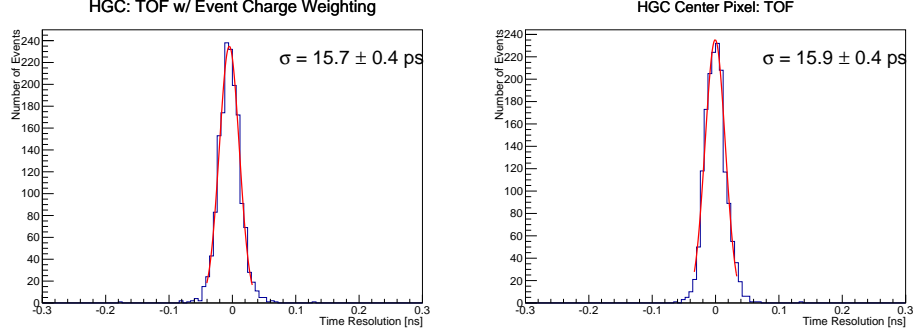


Figure 13.8: TOF distributions for (left) the pixel with the highest and (right) the the pixel with the second highest charge in the HGC layer using a 32 GeV electron beam and  $6X_0$  of tungsten. The TOF resolutions are estimated by the standard deviation parameter of the Gaussian fit (red solid curve) to the TOF distribution.

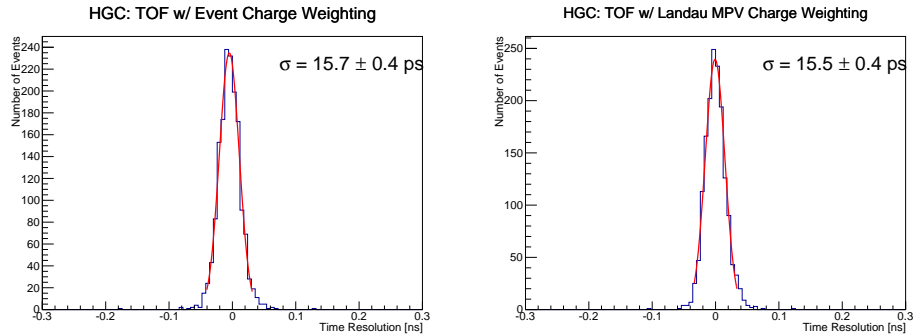


Figure 13.9: TOF distributions of the HGC layer using a 32 GeV electron beam and  $6X_0$  of tungsten, where the pixels are combined with (left) the default algorithm and (right) the mpv of the charge distribution as the weight. The TOF resolutions are estimated by the standard deviation parameter of the Gaussian fit (red solid curve) to the TOF distribution .

resolution as a function of the pixels combined at different separations between the tungsten absorber and the HGC layer, where it is observed that the TOF resolution is not significantly improved as a function of the added pixels for any of the separations. Despite the small improvement, it is observed that the larger the distance between the absorber and the HGC layer the larger is the relative improvement in the time resolution as more pixels are added, this is consistent with the fact that showers are more spread for the runs with more separation. Thus, it is convenient to define a quantity related to the transverse shower spread, to achieve this we use the ratio of the charge in the central pixel and the total charge in the 7 pixels as proxy to the transverse shower profile:

$$R_7 = \frac{\text{charge}_0}{\sum_{i=0}^6 \text{charge}_i}, \quad (13.2)$$

where  $\text{charge}_i$  is the charge deposited in the  $i$ -th pixel, with the zeroth being the central pixel. The  $R_7$  distribution is shown in Figure 13.11.

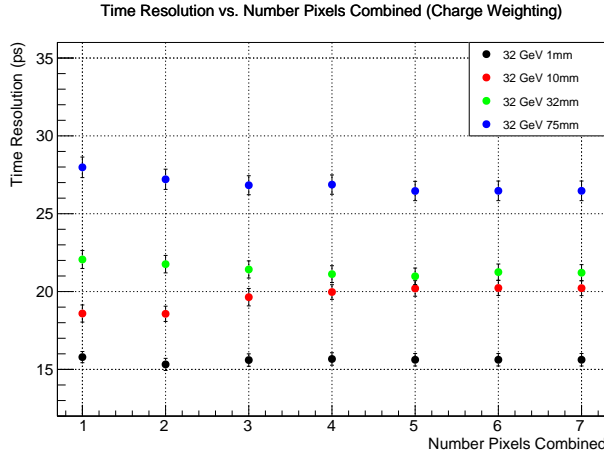


Figure 13.10: HGC layer TOF resolution as a function of the number of pixels combined. The distance between the absorber and the HGC layer was varied to sample the shower at different location.

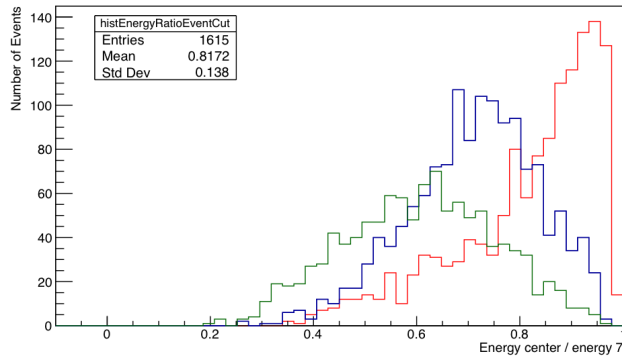


Figure 13.11:  $R_7$  distribution for different separations between the HGC layer and the  $6X_0$  of tungsten.

Finally, the dependence of the time resolution as a function of the beam energy is studied. Electron beams with energies of 8, 16, and 32 GeV were used, the separation between the absorber and the HGC layer was 1 mm. The results are summarized in Figure 13.12, the functional form  $A/\sqrt{E} + B$  was used to fit the data points. It is observed that the functional form does not fit well the data and thus more beam

energy points are needed to better constrain the floating parameters. Nevertheless, the best time resolution measured was found to be around 15 ps for a 32 GeV electron beam.

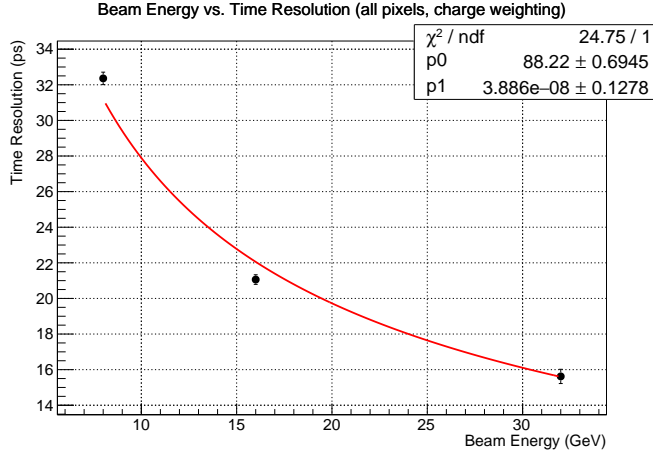


Figure 13.12: HGC layer TOF resolution as a function of the beam energy using  $6X_0$  of tungsten. The functional form  $A/\sqrt{E} + B$  was fitted to the data points (red solid curve).

### Combining Two Timing Layers

Combining the timing information of multiple HGC layers could improve the final TOF resolution of the calorimeter to em showers. The measurements presented in this chapter lack of an identical second HGC layer, but as shown in Chapter 11 the Photonis MCP-PMT located downstream of the HGC layer could be used as an additional timing measurement. To obtain the final TOF measurement (two-layer combination) the HGC layer and the Photonis MCP-PMT are combined with an equal weight. Figure 13.13 shows the TOF distribution for the Photonis MCP-PMT and the final two-layer combination in the left and right panels, respectively.

### Emulation of SKIROC2 Readout

The HGC proposed for the Phase 2 Upgrade of the CMS electromagnetic calorimeter uses a front-end electronics readout based on the *SKIROC2* chip, which has been preliminary shown to have around 50 ps jitter[68]. In order to simulate the effect of having a *SKIROC2* readout, the studies just presented above are now repeated with all the measured timestamps randomly smeared by 50 ps. Each timestamp – this includes all the HGC layer pixels, the Photonis MCP-PMT, and the reference Photek

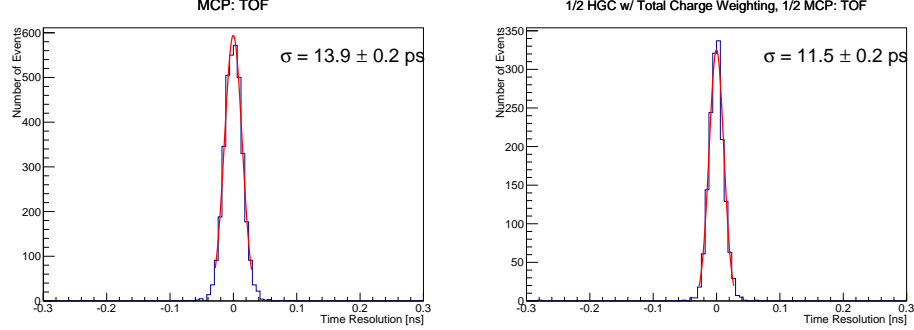


Figure 13.13: TOF distributions for (left) the Photonis MCP-PMT and (right) the final two-layer combination using a 32 GeV electron beam and  $6X_0$  of tungsten. The TOF resolutions are estimated by the standard deviation parameter of the Gaussian fit (red solid curve) to the TOF distribution .

240 MCP-PMT. – is smeared by adding a random number drawn from a Gaussian p.d.f with a mean and a width of 0 and 50 ps, respectively.

Figure 13.14 shows the TOF distributions after smearing for the pixels with highest and second highest charge in the left and right panel, respectively. The  $\Delta t_{HGC}$  distribution and the two-layer combination TOF distribution are shown in the left and right panel of Figure 13.15. Here, pixels and layer are all combined with the same weight. The HGC time resolution improves from that of the central pixel only, this could be explain since the dominance of the central pixels has been diluted by the 50 ps Gaussian smearing. The HGC time resolution as a function of the number of pixels combined is shown in Figure 13.16.

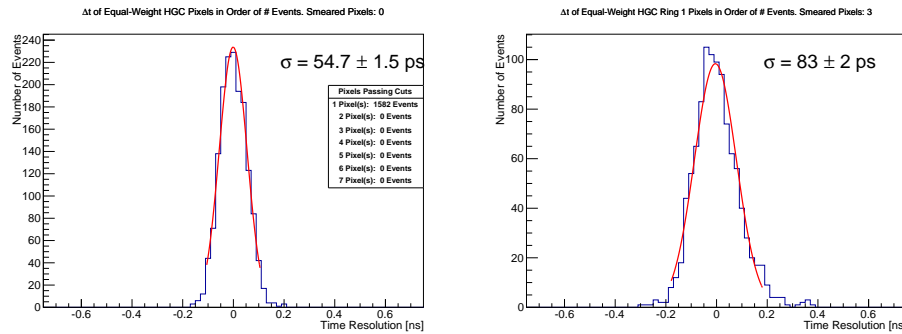


Figure 13.14: TOF distributions after a 50 ps Gaussian smearing for (left) the pixel with the highest and (right) the the pixel with the second highest charge in the HGC layer using a 32 GeV electron beam and  $6X_0$  of tungsten. The TOF resolutions are estimated by the standard deviation parameter of the Gaussian fit (red solid curve) to the TOF distribution.

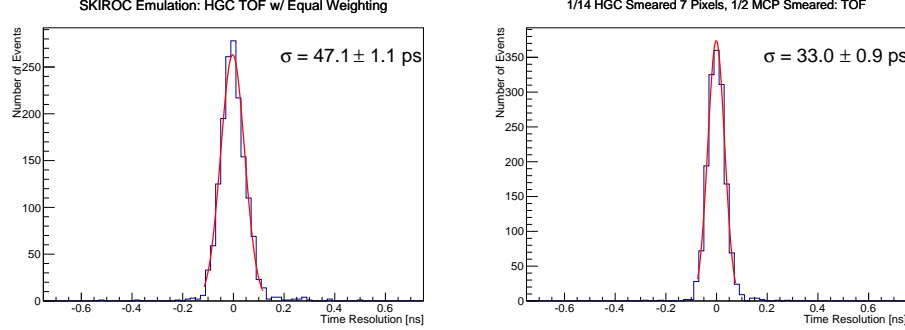


Figure 13.15: TOF distributions after a 50 ps Gaussian smearing for (left) the HGC layer and (right) the final two-layer combination using a 32 GeV electron beam and  $6X_0$  of tungsten. The TOF resolutions are estimated by the standard deviation parameter of the Gaussian fit (red solid curve) to the TOF distribution.

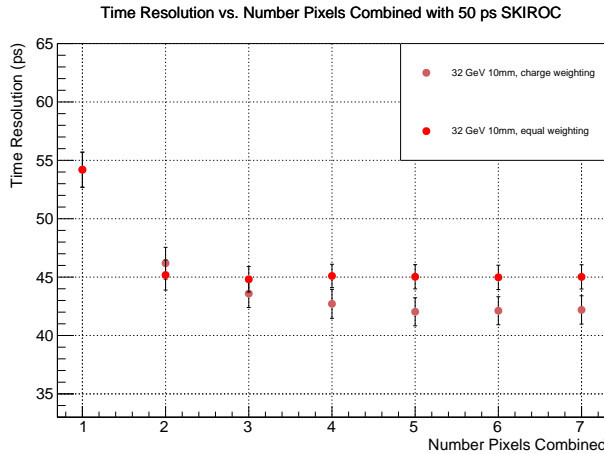


Figure 13.16: HGC layer TOF resolution after a 50 ps Gaussian smearing as a function of the number of pixels combined.

Finally, the dependence of the TOF resolution is studied after the 50 ps smearing was applied. The results are summarized in Figure 13.17. It is of note that the final two-layer combination time resolution for a 32 GeV electron beam is around 30 ps and meets the requirements needed to reject pileup at the HL-LHC (30 ps is equivalent to 1 cm resolution in the collision axis).

### 13.5 Conclusions

The first timing studies on the HGC were carried out; the studies were done on a single HGC layer implemented with 25 pixels, each with an independent analog readout and then digitized by the CAEN V1742 digitizer. The HGC layer was placed right downstream of  $6X_0$  of tungsten absorber. The selected em shower events

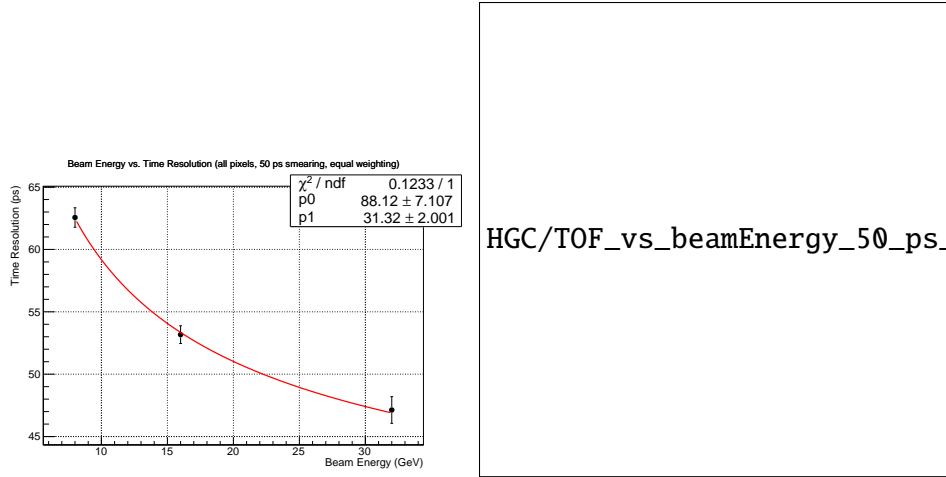


Figure 13.17: TOF distributions as a function of the beam energy after a 50 ps Gaussian smearing for (left) the HGC layer and (right) the final two-layer combination using  $6X_0$  of tungsten. The functional form  $A/\sqrt{E} + B$  was fitted to the data points (red solid curve).

showed a transverse spread that was contained in the inner most pixels with the central pixel containig most of the energy of the shower. As expected, the total charge deposited in the 7 HGC pixels showed a linear relationship with respect to the electron beam energy. The HGC time-of-flight resolution was obtained by combining the 7 inner pixels and found to be around 15 ps, which was close to that of the central pixel alone; suggesting, that sampling the shower at place with more transverse spread could improve the timing performance, provided large signal to noise ratios in the 7 inner pixels. The combination of two timing layers was also studied, the results suggest that adding additional timing layers improves the timing performance as expected from two uncorrelated measurements. Finally, the effect of the *SKIROC2* readout was studied by smearing each timestamp measurement by a Gaussian with 50 ps width. The HGC layer time resolution and the final two-layer combination were measured to be about 45 ps and 30 ps, respetively. These studies suggest that the desirable time-of-flight resolution for the proposed CMS high-granularity calorimeter are in principle well within reach.

## **Part V**

### **Summary and Conclusions**

### 13.6 Conclusion

Write your conclusion here.

[You can have chapters that were published as part of your thesis. The text style of the body should be single column, as it was submitted to the publisher, not formatted as the publisher did.]

## BIBLIOGRAPHY

- [1] In: (). <http://www.hamamatsu.com/resources/pdf/etd/R3809U-50 TPMH1067E09.pdf>.
- [2] In: (). [http://www.photek.com/pdf/datasheets/detectors/DS006\\_Photomultipliers.pdf](http://www.photek.com/pdf/datasheets/detectors/DS006_Photomultipliers.pdf).
- [3] In: (). <http://www.ellsworth.com/dow-corning-q2-3067-optical-couplant-453g-bottle>.
- [4] In: (). [https://www.hamamatsu.com/resources/pdf/ssd/e10\\_handbook\\_for\\_high\\_energy.pdf](https://www.hamamatsu.com/resources/pdf/ssd/e10_handbook_for_high_energy.pdf).
- [5] In: (). <http://www.caen.it/csite/CaenProd.jsp?parent=11&idmod=661>.
- [6] Morad Aaboud et al. “Search for resonances in diphoton events at  $\sqrt{s} = 13$  TeV with the ATLAS detector”. In: *JHEP* 09 (2016), p. 001. doi: [10.1007/JHEP09\(2016\)001](https://doi.org/10.1007/JHEP09(2016)001). arXiv: [1606.03833 \[hep-ex\]](https://arxiv.org/abs/1606.03833).
- [7] G. Aad et al. “Search for dark matter in events with heavy quarks and missing transverse momentum in pp collisions with the ATLAS detector”. In: *Eur. Phys. J. C* 75 (2015), p. 92. doi: [10.1140/epjc/s10052-015-3306-z](https://doi.org/10.1140/epjc/s10052-015-3306-z). arXiv: [1410.4031 \[hep-ex\]](https://arxiv.org/abs/1410.4031).
- [8] G. Aad et al. “Search for dilepton resonances in pp collisions at  $\sqrt{s} = 7$  TeV with the ATLAS detector”. In: *Phys. Rev. Lett.* 107 (2011), p. 272002. doi: [10.1103/PhysRevLett.107.272002](https://doi.org/10.1103/PhysRevLett.107.272002). arXiv: [1108.1582 \[hep-ex\]](https://arxiv.org/abs/1108.1582).
- [9] G. Aad et al. “Search for extra dimensions in diphoton events using proton-proton collisions recorded at  $\sqrt{s} = 7$  TeV with the ATLAS detector at the LHC”. In: *New J. Phys.* 15 (2013), p. 043007. doi: [10.1088/1367-2630/15/4/043007](https://doi.org/10.1088/1367-2630/15/4/043007). arXiv: [1210.8389 \[hep-ex\]](https://arxiv.org/abs/1210.8389).
- [10] G. Aad et al. “Search for high-mass dilepton resonances in pp collisions at  $\sqrt{s} = 8$  TeV with the ATLAS detector”. In: *Phys. Rev. D* 90 (2014), p. 052005. doi: [10.1103/PhysRevD.90.052005](https://doi.org/10.1103/PhysRevD.90.052005). arXiv: [1405.4123 \[hep-ex\]](https://arxiv.org/abs/1405.4123).
- [11] G. Aad et al. “Search for high-mass diphoton resonances in pp collisions at  $\sqrt{s} = 8$  TeV with the ATLAS detector”. In: *Phys. Rev. D* 92 (2015), p. 032004. doi: [10.1103/PhysRevD.92.032004](https://doi.org/10.1103/PhysRevD.92.032004). arXiv: [1504.05511 \[hep-ex\]](https://arxiv.org/abs/1504.05511).
- [12] G. Aad et al. “Search for new phenomena in the WW to  $\ell\nu\ell'\nu'$  final state in pp collisions at  $\sqrt{s} = 7$  TeV with the ATLAS detector”. In: *Phys. Lett. B* 718 (2013), p. 860. doi: [10.1016/j.physletb.2012.11.040](https://doi.org/10.1016/j.physletb.2012.11.040). arXiv: [1208.2880 \[hep-ex\]](https://arxiv.org/abs/1208.2880).

- [13] G. Aad et al. “Search for resonant diboson production in the  $WW/WZ \rightarrow \ell\nu jj$  decay channels with the ATLAS detector at  $\sqrt{s} = 7$  TeV”. In: *Phys. Rev. D* 87 (2013), p. 112006. doi: [10.1103/PhysRevD.87.112006](https://doi.org/10.1103/PhysRevD.87.112006). arXiv: [1305.0125 \[hep-ex\]](https://arxiv.org/abs/1305.0125).
- [14] G. Aad et al. “Search for Scalar Diphoton Resonances in the Mass Range 65–600 GeV with the ATLAS Detector in  $pp$  Collision Data at  $\sqrt{s} = 8$  TeV”. In: *Phys. Rev. Lett.* 113 (2014), p. 171801. doi: [10.1103/PhysRevLett.113.171801](https://doi.org/10.1103/PhysRevLett.113.171801). arXiv: [1407.6583 \[hep-ex\]](https://arxiv.org/abs/1407.6583).
- [15] Georges Aad et al. “Combined Measurement of the Higgs Boson Mass in  $pp$  Collisions at  $\sqrt{s} = 7$  and 8 TeV with the ATLAS and CMS Experiments”. In: *Phys. Rev. Lett.* 114 (2015), p. 191803. doi: [10.1103/PhysRevLett.114.191803](https://doi.org/10.1103/PhysRevLett.114.191803). arXiv: [1503.07589 \[hep-ex\]](https://arxiv.org/abs/1503.07589).
- [16] Georges Aad et al. “Observation of a new particle in the search for the Standard Model Higgs boson with the ATLAS detector at the LHC”. In: *Phys. Lett. B* 716 (2012), p. 1. doi: [10.1016/j.physletb.2012.08.020](https://doi.org/10.1016/j.physletb.2012.08.020). arXiv: [1207.7214 \[hep-ex\]](https://arxiv.org/abs/1207.7214).
- [17] Georges Aad et al. “Observation of a new particle in the search for the Standard Model Higgs boson with the ATLAS detector at the LHC”. In: *Phys. Lett. B* 716 (2012), pp. 1–29. doi: [10.1016/j.physletb.2012.08.020](https://doi.org/10.1016/j.physletb.2012.08.020). arXiv: [1207.7214 \[hep-ex\]](https://arxiv.org/abs/1207.7214).
- [18] Georges Aad et al. “Search for dark matter in events with a hadronically decaying W or Z boson and missing transverse momentum in  $pp$  collisions at  $\sqrt{s} = 8$  TeV with the ATLAS detector”. In: *Phys. Rev. Lett.* 112 (2014), p. 041802. doi: [10.1103/PhysRevLett.112.041802](https://doi.org/10.1103/PhysRevLett.112.041802). arXiv: [1309.4017 \[hep-ex\]](https://arxiv.org/abs/1309.4017).
- [19] Georges Aad et al. “Search for dark matter in events with a Z boson and missing transverse momentum in  $pp$  collisions at  $\sqrt{s} = 8$  TeV with the ATLAS detector”. In: *Phys. Rev. D* 90 (2014), p. 012004. doi: [10.1103/PhysRevD.90.012004](https://doi.org/10.1103/PhysRevD.90.012004). arXiv: [1404.0051 \[hep-ex\]](https://arxiv.org/abs/1404.0051).
- [20] Georges Aad et al. “Search for Dark Matter in Events with Missing Transverse Momentum and a Higgs Boson Decaying to Two Photons in  $pp$  Collisions at  $\sqrt{s} = 8$  TeV with the ATLAS Detector”. In: *Phys. Rev. Lett.* 115 (2015), p. 131801. doi: [10.1103/PhysRevLett.115.131801](https://doi.org/10.1103/PhysRevLett.115.131801). arXiv: [1506.01081 \[hep-ex\]](https://arxiv.org/abs/1506.01081).
- [21] Georges Aad et al. “Search for dark matter produced in association with a Higgs boson decaying to two bottom quarks in  $pp$  collisions at  $\sqrt{s} = 8$  TeV with the ATLAS detector”. 2015.
- [22] Georges Aad et al. “Search for new particles in events with one lepton and missing transverse momentum in  $pp$  collisions at  $\sqrt{s} = 8$  TeV with the ATLAS detector”. In: *JHEP* 09 (2014), p. 037. doi: [10.1007/JHEP09\(2014\)037](https://doi.org/10.1007/JHEP09(2014)037). arXiv: [1407.7494 \[hep-ex\]](https://arxiv.org/abs/1407.7494).

- [23] Georges Aad et al. “Search for new phenomena in events with a photon and missing transverse momentum in pp collisions at  $\sqrt{s} = 8$  TeV with the ATLAS detector”. In: *Phys. Rev. D* 91 (2015). [Erratum: *Phys. Rev. D* 92 (2015) 059903], p. 012008. doi: [10.1103/PhysRevD.92.059903](https://doi.org/10.1103/PhysRevD.92.059903), [10.1103/PhysRevD.91.012008](https://doi.org/10.1103/PhysRevD.91.012008). arXiv: [1411.1559](https://arxiv.org/abs/1411.1559) [hep-ex].
- [24] Georges Aad et al. “Search for new phenomena with the monojet and missing transverse momentum signature using the ATLAS detector in  $\sqrt{s} = 7$  TeV proton-proton collisions”. In: *Phys. Lett. B* 705 (2011), p. 294. doi: [10.1016/j.physletb.2011.10.006](https://doi.org/10.1016/j.physletb.2011.10.006). arXiv: [1106.5327](https://arxiv.org/abs/1106.5327) [hep-ex].
- [25] Georges Aad et al. “Search for supersymmetry in events containing a same-flavour opposite-sign dilepton pair, jets, and large missing transverse momentum in  $\sqrt{s} = 8$  TeV pp collisions with the ATLAS detector”. In: *Eur. Phys. J. C*75.7 (2015). [Erratum: *Eur. Phys. J.*C75,no.10,463(2015)], p. 318. doi: [10.1140/epjc/s10052-015-3661-9](https://doi.org/10.1140/epjc/s10052-015-3661-9), [10.1140/epjc/s10052-015-3518-2](https://doi.org/10.1140/epjc/s10052-015-3518-2). arXiv: [1503.03290](https://arxiv.org/abs/1503.03290) [hep-ex].
- [26] P. A. R. Ade et al. “Planck 2013 results. XVI. Cosmological parameters”. In: *Astron. Astrophys.* 571 (2014), A16. doi: [10.1051/0004-6361/201321591](https://doi.org/10.1051/0004-6361/201321591). arXiv: [1303.5076](https://arxiv.org/abs/1303.5076) [astro-ph.CO].
- [27] C. Adloff et al. “Tests of a particle flow algorithm with CALICE test beam data”. In: *JINST* 6 (2011), P07005. doi: [10.1088/1748-0221/6/07/P07005](https://doi.org/10.1088/1748-0221/6/07/P07005). arXiv: [1105.3417](https://arxiv.org/abs/1105.3417) [physics.ins-det].
- [28] S. Agostinelli et al. “GEANT4 — a simulation toolkit”. In: *Nucl. Instrum. Meth. A* 506 (2003), p. 250. doi: [10.1016/S0168-9002\(03\)01368-8](https://doi.org/10.1016/S0168-9002(03)01368-8).
- [29] S. Agostinelli et al. “GEANT4: a simulation toolkit”. In: *Nucl. Instrum. Meth. A* 506 (2003), p. 250. doi: [10.1016/S0168-9002\(03\)01368-8](https://doi.org/10.1016/S0168-9002(03)01368-8).
- [30] Prateek Agrawal et al. “Flavored Dark Matter and the Galactic Center Gamma-Ray Excess”. In: *Phys. Rev. D* 90 (2014), p. 063512. doi: [10.1103/PhysRevD.90.063512](https://doi.org/10.1103/PhysRevD.90.063512). arXiv: [1404.1373](https://arxiv.org/abs/1404.1373) [hep-ph].
- [31] H. Akaike. “A new look at the statistical model identification”. In: *IEEE Transactions on Automatic Control* 19-6 (1974), pp. 716–723. doi: [10.1109/TAC.1974.1100705](https://doi.org/10.1109/TAC.1974.1100705).
- [32] Nural Akchurin et al. “On the timing performance of thin planar silicon sensors”. In preparation, for submission to the *Nucl. Instrum. Meth. A*.
- [33] A. Albayrak-Yetkin et al. “Secondary Emission Calorimetry: Fast and Radiation Hard”. In: (2013). arXiv: [1307.8051](https://arxiv.org/abs/1307.8051) [physics.ins-det]. URL: <https://inspirehep.net/record/1245371/files/arXiv:1307.8051.pdf>.

- [34] M. Albrecht, K. Andert, P. Anselmino, et al. “Scintillators and Wave-length Shifters for the Detection of Ionizing Radiation”. In: *Proceedings of the 8th Conference on astroparticle, particle and space physics, detectors and medical physics applications* (2003), pp. 502–511. doi: [10.1142/9789812702708\\_0074](https://doi.org/10.1142/9789812702708_0074).
- [35] Sergey Alekhin et al. “The PDF4LHC Working Group Interim Report”. 2011.
- [36] Ben Allanach, Are R. Raklev, and Anders Kvellestad. “Interpreting a CMS excess in  $lljj + \text{missing-transverse-momentum}$  with the golden cascade of the minimal supersymmetric standard model”. In: *Phys. Rev.* D91.11 (2015), p. 115022. doi: [10.1103/PhysRevD.91.115022](https://doi.org/10.1103/PhysRevD.91.115022). arXiv: [1409.3532](https://arxiv.org/abs/1409.3532) [hep-ph].
- [37] Ben Allanach, Are Raklev, and Anders Kvellestad. “Consistency of the recent ATLAS  $Z + E_T^{\text{miss}}$  excess in a simplified GGM model”. In: *Phys. Rev.* D91 (2015), p. 095016. doi: [10.1103/PhysRevD.91.095016](https://doi.org/10.1103/PhysRevD.91.095016). arXiv: [1504.02752](https://arxiv.org/abs/1504.02752) [hep-ph].
- [38] Johan Alwall et al. “MadGraph5: going beyond”. In: *JHEP* 06 (2011), p. 128. doi: [10.1007/JHEP06\(2011\)128](https://doi.org/10.1007/JHEP06(2011)128). arXiv: [1106.0522](https://arxiv.org/abs/1106.0522) [hep-ph].
- [39] J. Alwall et al. “The automated computation of tree-level and next-to-leading order differential cross sections, and their matching to parton shower simulations”. In: *JHEP* 07 (2014), p. 079. doi: [10.1007/JHEP07\(2014\)079](https://doi.org/10.1007/JHEP07(2014)079). arXiv: [1405.0301](https://arxiv.org/abs/1405.0301) [hep-ph].
- [40] C. Amole et al. “Dark Matter Search Results from the PICO-2L  $\text{C}_3\text{F}_8$  Bubble Chamber”. In: *Phys. Rev. Lett.* 114 (2015), p. 231302. doi: [10.1103/PhysRevLett.114.231302](https://doi.org/10.1103/PhysRevLett.114.231302). arXiv: [1503.00008](https://arxiv.org/abs/1503.00008) [astro-ph.CO].
- [41] “An Indirect Search for WIMPs in the Sun using 3109.6 Days of Upward-going Muons in Super-Kamiokande”. In: *Astrophys. J.* 742 (78 2011), p. 78. doi: [10.1088/0004-637X/742/2/78](https://doi.org/10.1088/0004-637X/742/2/78). arXiv: [1108.3384](https://arxiv.org/abs/1108.3384).
- [42] D. Anderson et al. “On Timing Properties of LYSO-Based Calorimeters”. In: *Nucl. Instrum. Meth. A* 794 (2015), pp. 7–14. doi: [10.1016/j.nima.2015.04.013](https://doi.org/10.1016/j.nima.2015.04.013).
- [43] G. Angloher et al. “Results on light dark matter particles with a low-threshold CRESST-II detector”. 2015.
- [44] G. Angloher et al. “Results on low mass WIMPs using an upgraded CRESST-II detector”. In: *Eur. Phys. J. C* 74 (2014), p. 3184. doi: [10.1140/epjc/s10052-014-3184-9](https://doi.org/10.1140/epjc/s10052-014-3184-9). arXiv: [1407.3146](https://arxiv.org/abs/1407.3146) [astro-ph.CO].
- [45] E. Aprile et al. “Limits on spin-dependent WIMP-nucleon cross sections from 225 live days of XENON100 data”. In: *Phys. Rev. Lett.* 111 (2013), p. 021301. doi: [10.1103/PhysRevLett.111.021301](https://doi.org/10.1103/PhysRevLett.111.021301). arXiv: [1301.6620](https://arxiv.org/abs/1301.6620) [astro-ph.CO].

- [46] S. Archambault et al. “Constraints on Low-Mass WIMP Interactions on  ${}^{19}F$  from PICASSO”. In: *Phys. Lett. B* 711 (2012), p. 153. doi: [10.1016/j.physletb.2012.03.078](https://doi.org/10.1016/j.physletb.2012.03.078). arXiv: [1202.1240](https://arxiv.org/abs/1202.1240) [hep-ex].
- [47] ATLAS Collaboration. *Procedure for the LHC Higgs boson search combination in summer 2011*. Tech. rep. ATL-PHYS-PUB-2011-011. 2011. URL: <https://cds.cern.ch/record/1375842>.
- [48] Yang Bai, Patrick J. Fox, and Roni Harnik. “The Tevatron at the Frontier of Dark Matter Direct Detection”. In: *JHEP* 12 (2010), p. 048. doi: [10.1007/JHEP12\(2010\)048](https://doi.org/10.1007/JHEP12(2010)048). arXiv: [1005.3797](https://arxiv.org/abs/1005.3797) [hep-ph].
- [49] R. D. Ball et al. “Parton distributions with LHC data”. In: *Nucl. Phys. B* 867 (2013), p. 244. doi: [10.1016/j.nuclphysb.2012.10.003](https://doi.org/10.1016/j.nuclphysb.2012.10.003). arXiv: [1207.1303](https://arxiv.org/abs/1207.1303) [hep-ph].
- [50] Richard D. Ball et al. “Parton distributions for the LHC Run II”. In: *JHEP* 04 (2015), p. 040. doi: [10.1007/JHEP04\(2015\)040](https://doi.org/10.1007/JHEP04(2015)040). arXiv: [1410.8849](https://arxiv.org/abs/1410.8849) [hep-ph].
- [51] Richard D. Ball et al. “Parton distributions with QED corrections”. In: *Nucl. Phys. B* 877 (2013), pp. 290–320. doi: [10.1016/j.nuclphysb.2013.10.010](https://doi.org/10.1016/j.nuclphysb.2013.10.010). arXiv: [1308.0598](https://arxiv.org/abs/1308.0598) [hep-ph].
- [52] Riccardo Barbieri and G. F. Giudice. “Upper Bounds on Supersymmetric Particle Masses”. In: *Nucl. Phys. B* 306 (1988), p. 63. doi: [10.1016/0550-3213\(88\)90171-X](https://doi.org/10.1016/0550-3213(88)90171-X).
- [53] James M. Bardeen et al. “The Statistics of Peaks of Gaussian Random Fields”. In: *Astrophys. J.* 304 (1986), p. 15. doi: [10.1086/164143](https://doi.org/10.1086/164143).
- [54] W. Beenakker et al. “Soft-gluon resummation for squark and gluino hadroproduction”. In: *JHEP* 12 (2009), p. 041. doi: [10.1088/1126-6708/2009/12/041](https://doi.org/10.1088/1126-6708/2009/12/041). arXiv: [0909.4418](https://arxiv.org/abs/0909.4418) [hep-ph].
- [55] W. Beenakker et al. “Squark and gluino hadroproduction”. In: *Int. J. Mod. Phys. A* 26 (2011), p. 2637. doi: [10.1142/S0217751X11053560](https://doi.org/10.1142/S0217751X11053560). arXiv: [1105.1110](https://arxiv.org/abs/1105.1110) [hep-ph].
- [56] W. Beenakker et al. “Squark and gluino production at hadron colliders”. In: *Nucl. Phys. B* 492 (1997), p. 51. doi: [10.1016/S0550-3213\(97\)80027-2](https://doi.org/10.1016/S0550-3213(97)80027-2). arXiv: [hep-ph/9610490](https://arxiv.org/abs/hep-ph/9610490) [hep-ph].
- [57] Maria Beltrán et al. “Maverick dark matter at colliders”. English. In: *JHEP* 09, 37 (2010), p. 037. doi: [10.1007/JHEP09\(2010\)037](https://doi.org/10.1007/JHEP09(2010)037). arXiv: [1002.4137](https://arxiv.org/abs/1002.4137). URL: [http://dx.doi.org/10.1007/JHEP09\(2010\)037](http://dx.doi.org/10.1007/JHEP09(2010)037).
- [58] P. de Bernardis et al. “A flat Universe from high resolution maps of the cosmic microwave background radiation”. In: *Nature* 404 (2000), p. 955. doi: [10.1038/35010035](https://doi.org/10.1038/35010035). arXiv: [astro-ph/0004404](https://arxiv.org/abs/astro-ph/0004404) [astro-ph].

- [59] P. S. Bhupal Dev and Apostolos Pilaftsis. “Maximally symmetric two Higgs doublet model with natural standard model alignment”. In: *JHEP* 12 (2014). [Erratum: DOI10.1007/JHEP11(2015)147], p. 024. doi: 10.1007/JHEP12(2014)024. arXiv: 1408.3405 [hep-ph].
- [60] Christoph Borschensky et al. “Squark and gluino production cross sections in pp collisions at  $\sqrt{s} = 13, 14, 33$  and  $100$  TeV”. In: *Eur. Phys. J.* C74.12 (2014), p. 3174. doi: 10.1140/epjc/s10052-014-3174-y. arXiv: 1407.5066 [hep-ph].
- [61] Michiel Botje et al. “The PDF4LHC Working Group Interim Recommendations”. 2011.
- [62] D Bourilkov, R C Group, and M R Whalley. “LHAPDF: PDF use from the Tevatron to the LHC”. In: *TeV4LHC Workshop - 4th meeting Batavia, Illinois, October 20-22, 2005*. 2006. arXiv: hep-ph/0605240 [hep-ph].
- [63] G. C. Branco et al. “Theory and phenomenology of two-Higgs-doublet models”. In: *Phys. Rep.* 516 (2012), p. 1. doi: 10.1016/j.physrep.2012.02.002. arXiv: 1106.0034 [hep-ph].
- [64] O. Buchmueller, Matthew J. Dolan, and Christopher McCabe. “Beyond Effective Field Theory for Dark Matter Searches at the LHC”. In: *JHEP* 01 (2014), p. 025. doi: 10.1007/JHEP01(2014)025. arXiv: 1308.6799 [hep-ph].
- [65] Giorgio Busoni et al. “On the Validity of the Effective Field Theory for Dark Matter Searches at the LHC”. In: *Phys. Lett. B* 728 (2014), p. 412. doi: 10.1016/j.physletb.2013.11.069. arXiv: 1307.2253 [hep-ph].
- [66] Giorgio Busoni et al. “On the Validity of the Effective Field Theory for Dark Matter Searches at the LHC, Part II: Complete Analysis for the  $s$ -channel”. In: *JCAP* 06 (2014), p. 060. doi: 10.1088/1475-7516/2014/06/060. arXiv: 1402.1275 [hep-ph].
- [67] Giorgio Busoni et al. “On the Validity of the Effective Field Theory for Dark Matter Searches at the LHC Part III: Analysis for the  $t$ -channel”. In: *JCAP* 09 (2014), p. 022. doi: 10.1088/1475-7516/2014/09/022. arXiv: 1405.3101 [hep-ph].
- [68] J Butler et al. *Technical Proposal for the Phase-II Upgrade of the CMS Detector*. Tech. rep. CERN-LHCC-2015-010. LHCC-P-008. Geneva: CERN, June 2015. url: <https://cds.cern.ch/record/2020886>.
- [69] Matteo Cacciari, Gavin P. Salam, and Gregory Soyez. “FastJet user manual”. In: *Eur. Phys. J. C* 72 (2012), p. 1896. doi: 10.1140/epjc/s10052-012-1896-2. arXiv: 1111.6097 [hep-ph].
- [70] Matteo Cacciari, Gavin P. Salam, and Gregory Soyez. “The anti- $k_T$  jet clustering algorithm”. In: *JHEP* 04 (2008), p. 063. doi: 10.1088/1126-6708/2008/04/063. arXiv: 0802.1189 [hep-ph].

- [71] Junjie Cao et al. “Explanation of the ATLAS Z-Peaked Excess in the NMSSM”. In: *JHEP* 06 (2015), p. 152. doi: [10.1007/JHEP06\(2015\)152](https://doi.org/10.1007/JHEP06(2015)152). arXiv: [1504.07869](https://arxiv.org/abs/1504.07869) [hep-ph].
- [72] R. G. Carlberg and H. M. P. Couchman. “Mergers and bias in a cold dark matter cosmology”. In: *Astrophys. J.* 340 (1989), p. 47. doi: [10.1086/167375](https://doi.org/10.1086/167375).
- [73] Stefano Carrazza. “Towards an unbiased determination of parton distributions with QED corrections”. In: *Proceedings, 48th Rencontres de Moriond on QCD and High Energy Interactions*. 2013, pp. 357–360. arXiv: [1305.4179](https://arxiv.org/abs/1305.4179) [hep-ph]. URL: <http://inspirehep.net/record/1234242/files/arXiv:1305.4179.pdf>.
- [74] Stefano Carrazza. “Towards the determination of the photon parton distribution function constrained by LHC data”. In: *PoS DIS2013* (2013), p. 279. arXiv: [1307.1131](https://arxiv.org/abs/1307.1131) [hep-ph].
- [75] Renyue Cen. “Decaying cold dark matter model and small-scale power”. In: *Astrophys. J.* 546 (2001), pp. L77–L80. doi: [10.1086/318861](https://doi.org/10.1086/318861). arXiv: [astro-ph/0005206](https://arxiv.org/abs/astro-ph/0005206) [astro-ph].
- [76] S. Chatrchyan et al. “Measurement of differential cross sections for the production of a pair of isolated photons in  $pp$  collisions at  $\sqrt{s} = 7$  TeV”. In: *Eur. Phys. J. C* 74 (2014), p. 3129. doi: [10.1140/epjc/s10052-014-3129-3](https://doi.org/10.1140/epjc/s10052-014-3129-3). arXiv: [1405.7225](https://arxiv.org/abs/1405.7225) [hep-ex].
- [77] S. Chatrchyan et al. “Performance of the CMS missing transverse momentum reconstruction in  $pp$  data at  $\sqrt{s} = 8$  TeV”. In: *JINST* 10 (2015), p. 2006. doi: [10.1088/1748-0221/10/02/P02006](https://doi.org/10.1088/1748-0221/10/02/P02006). arXiv: [1411.0511](https://arxiv.org/abs/1411.0511) [hep-ex]. URL: <http://stacks.iop.org/1748-0221/10/i=02/a=P02006>.
- [78] S. Chatrchyan et al. “Search for a narrow spin-2 resonance decaying to a pair of Z vector bosons in the semileptonic final state”. In: *Phys. Lett. B* 718 (2013), p. 1208. doi: [10.1016/j.physletb.2012.11.063](https://doi.org/10.1016/j.physletb.2012.11.063). arXiv: [1209.3807](https://arxiv.org/abs/1209.3807) [hep-ex].
- [79] S. Chatrchyan et al. “Search for exotic resonances decaying into WZ/ZZ in  $pp$  collisions at  $\sqrt{s} = 7$  TeV”. In: *JHEP* 02 (2013), p. 036. doi: [10.1007/JHEP02\(2013\)036](https://doi.org/10.1007/JHEP02(2013)036). arXiv: [1211.5779](https://arxiv.org/abs/1211.5779) [hep-ex].
- [80] S. Chatrchyan et al. “Search for heavy narrow dilepton resonances in  $pp$  collisions at  $\sqrt{s} = 7$  TeV and  $\sqrt{s} = 8$  TeV”. In: *Phys. Lett. B* 720 (2013), p. 63. doi: [10.1016/j.physletb.2013.02.003](https://doi.org/10.1016/j.physletb.2013.02.003). arXiv: [1212.6175](https://arxiv.org/abs/1212.6175) [hep-ex].
- [81] S. Chatrchyan et al. “Search for narrow resonances using the dijet mass spectrum in  $pp$  collisions at  $\sqrt{s} = 8$  TeV”. In: *Phys. Rev. D* 87 (2013), p. 114015. doi: [10.1103/PhysRevD.87.114015](https://doi.org/10.1103/PhysRevD.87.114015). arXiv: [1302.4794](https://arxiv.org/abs/1302.4794) [hep-ex].

- [82] S. Chatrchyan et al. “Search for signatures of extra dimensions in the diphoton mass spectrum at the Large Hadron Collider”. In: *Phys. Rev. Lett.* 108 (2012), p. 111801. doi: [10.1103/PhysRevLett.108.111801](https://doi.org/10.1103/PhysRevLett.108.111801). arXiv: [1112.0688 \[hep-ex\]](https://arxiv.org/abs/1112.0688).
- [83] S. Chatrchyan et al. “The CMS experiment at the CERN LHC”. In: *JINST* 3 (2008), S08004. doi: [10.1088/1748-0221/3/08/S08004](https://doi.org/10.1088/1748-0221/3/08/S08004).
- [84] Serguei Chatrchyan et al. “Identification of b-quark jets with the CMS experiment”. In: *JINST* 8 (2013), p. 4013. doi: [10.1088/1748-0221/8/04/P04013](https://doi.org/10.1088/1748-0221/8/04/P04013). arXiv: [1211.4462 \[hep-ex\]](https://arxiv.org/abs/1211.4462).
- [85] Serguei Chatrchyan et al. “Inclusive search for squarks and gluinos in pp collisions at  $\sqrt{s} = 7$  TeV”. In: *Phys. Rev. D* 85 (2012), p. 012004. doi: [10.1103/PhysRevD.85.012004](https://doi.org/10.1103/PhysRevD.85.012004). arXiv: [1107.1279 \[hep-ex\]](https://arxiv.org/abs/1107.1279).
- [86] Serguei Chatrchyan et al. “Measurement of the properties of a Higgs boson in the four-lepton final state”. In: *Phys. Rev. D* 89.9 (2014), p. 092007. doi: [10.1103/PhysRevD.89.092007](https://doi.org/10.1103/PhysRevD.89.092007). arXiv: [1312.5353 \[hep-ex\]](https://arxiv.org/abs/1312.5353).
- [87] Serguei Chatrchyan et al. “Missing transverse energy performance of the CMS detector”. In: *JINST* 6 (2011), P09001. doi: [10.1088/1748-0221/6/09/P09001](https://doi.org/10.1088/1748-0221/6/09/P09001). arXiv: [1106.5048 \[physics.ins-det\]](https://arxiv.org/abs/1106.5048).
- [88] Serguei Chatrchyan et al. “Observation of a new boson at a mass of 125 GeV with the CMS experiment at the LHC”. In: *Phys. Lett. B* 716 (2012), p. 30. doi: [10.1016/j.physletb.2012.08.021](https://doi.org/10.1016/j.physletb.2012.08.021). arXiv: [1207.7235 \[hep-ex\]](https://arxiv.org/abs/1207.7235).
- [89] Serguei Chatrchyan et al. “Observation of a new boson at a mass of 125 GeV with the CMS experiment at the LHC”. In: *Phys. Lett. B* 716 (2012), pp. 30–61. doi: [10.1016/j.physletb.2012.08.021](https://doi.org/10.1016/j.physletb.2012.08.021). arXiv: [1207.7235 \[hep-ex\]](https://arxiv.org/abs/1207.7235).
- [90] Serguei Chatrchyan et al. “Search for dark matter and large extra dimensions in monojet events in pp collisions at  $\sqrt{s} = 7$  TeV”. In: *JHEP* 09 (2012), p. 094. doi: [10.1007/JHEP09\(2012\)094](https://doi.org/10.1007/JHEP09(2012)094). arXiv: [1206.5663 \[hep-ex\]](https://arxiv.org/abs/1206.5663).
- [91] Serguei Chatrchyan et al. “Search for dark matter, extra dimensions, and unparticles in monojet events in proton-proton collisions  $\sqrt{s} = 8$  TeV”. In: *Euro. Phys. J. C* 75 (2015), p. 235. doi: [10.1140/epjc/s10052-015-3451-4](https://doi.org/10.1140/epjc/s10052-015-3451-4). arXiv: [1408.3583 \[hep-ex\]](https://arxiv.org/abs/1408.3583).
- [92] Serguei Chatrchyan et al. “Search for New Physics in the Multijet and Missing Transverse Momentum Final State in Proton-Proton Collisions at  $\sqrt{s} = 7$  TeV”. In: *Phys. Rev. Lett.* 109 (2012), p. 171803. doi: [10.1103/PhysRevLett.109.171803](https://doi.org/10.1103/PhysRevLett.109.171803). arXiv: [1207.1898 \[hep-ex\]](https://arxiv.org/abs/1207.1898).
- [93] Serguei Chatrchyan et al. “Search for supersymmetry with razor variables in pp collisions at  $\sqrt{s} = 7$  TeV”. In: *Phys. Rev. D* 90 (2014), p. 112001. doi: [10.1103/PhysRevD.90.112001](https://doi.org/10.1103/PhysRevD.90.112001). arXiv: [1405.3961 \[hep-ex\]](https://arxiv.org/abs/1405.3961).

- [94] Serguei Chatrchyan et al. “Search for supersymmetry with razor variables in pp collisions at  $\sqrt{s} = 7$  TeV”. In: *Phys. Rev. D* 90 (2014), p. 112001. doi: [10.1103/PhysRevD.90.112001](https://doi.org/10.1103/PhysRevD.90.112001). arXiv: [1405.3961](https://arxiv.org/abs/1405.3961) [hep-ex].
- [95] Douglas Clowe et al. “A direct empirical proof of the existence of dark matter”. In: *Astrophys. J.* 648 (2006), p. L109. doi: [10.1086/508162](https://doi.org/10.1086/508162). arXiv: [astro-ph/0608407](https://arxiv.org/abs/astro-ph/0608407) [astro-ph].
- [96] CMS Collaboration. *Commissioning of the Particle-flow Event Reconstruction with the first LHC collisions recorded in the CMS detector*. CMS Physics Analysis Summary CMS-PAS-PFT-10-001. 2010. URL: <https://cds.cern.ch/record/1247373>.
- [97] CMS Collaboration. *Commissioning of the particle-flow event reconstruction with the first LHC collisions recorded in the CMS detector*. CMS Physics Analysis Summary CMS-PAS-PFT-10-011. 2010. URL: <http://cdsweb.cern.ch/record/1247373>.
- [98] CMS Collaboration. *Data Parking and Data Scouting at the CMS Experiment*. CMS Physics Analysis Summary CMS-DP-2012-022. 2012. URL: <http://cdsweb.cern.ch/record/1247373>.
- [99] CMS Collaboration. *Particle-flow event reconstruction in CMS and performance for jets, taus, and  $E_T^{\text{miss}}$* . CMS Physics Analysis Summary CMS-PAS-PFT-09-001. 2009. URL: <http://cdsweb.cern.ch/record/1194487>.
- [100] CMS Collaboration. *Particle-flow event reconstruction in CMS and performance for jets, taus, and  $E_T^{\text{miss}}$* . CMS Physics Analysis Summary CMS-PAS-PFT-09-001. 2009. URL: <http://cdsweb.cern.ch/record/1194487>.
- [101] CMS Collaboration. *Performance of the missing transverse energy reconstruction by the CMS experiment in  $\sqrt{s} = 8$  TeV pp data*. CMS Physics Analysis Summary CMS-PAS-JME-13-003. 2013. URL: <http://cds.cern.ch/record/1966665>.
- [102] CMS Collaboration. *Procedure for the LHC Higgs boson search combination in Summer 2011*. Tech. rep. CMS-NOTE-2011-005. 2011. URL: <https://cds.cern.ch/record/1379837>.
- [103] CMS Luminosity Measurement for the 2015 Data Taking Period. CMS Physics Analysis Summary CMS-PAS-LUM-15-001. 2016. URL: <https://cds.cern.ch/record/2138682>.
- [104] D Contardo and J Spalding. *CMS Phase 2 Upgrade: Preliminary Plan and Cost Estimate*. Tech. rep. CERN-RRB-2013-124. Geneva: CERN, Oct. 2013.
- [105] Glen Cowan et al. “Asymptotic formulae for likelihood-based tests of new physics”. In: *Eur. Phys. J. C* 71 (2011). [Erratum: DOI10.1140/epjc/s10052-013-2501-z], p. 1554. doi: [10.1140/epjc/s10052-011-1554-0](https://doi.org/10.1140/epjc/s10052-011-1554-0). arXiv: [1007.1727](https://arxiv.org/abs/1007.1727) [physics.data-an].

- [106] Nathaniel Craig, Jamison Galloway, and Scott Thomas. “Searching for signs of the second Higgs doublet”. 2013.
- [107] Richard H. Cyburt. “Primordial nucleosynthesis for the new cosmology: Determining uncertainties and examining concordance”. In: *Phys. Rev. D* 70 (2 July 2004), p. 023505. doi: [10.1103/PhysRevD.70.023505](https://doi.org/10.1103/PhysRevD.70.023505). URL: <http://link.aps.org/doi/10.1103/PhysRevD.70.023505>.
- [108] Richard H. Cyburt. “Primordial nucleosynthesis for the new cosmology: Determining uncertainties and examining concordance”. In: *Phys. Rev. D* 70 (2 July 2004), p. 023505. doi: [10.1103/PhysRevD.70.023505](https://doi.org/10.1103/PhysRevD.70.023505). URL: <http://link.aps.org/doi/10.1103/PhysRevD.70.023505>.
- [109] Michal Czakon and Alexander Mitov. “Top++: a program for the calculation of the top-pair cross-section at hadron colliders”. In: *Comp. Phys. Commun.* 185 (2014), p. 2930. doi: [10.1016/j.cpc.2014.06.021](https://doi.org/10.1016/j.cpc.2014.06.021). arXiv: 1112.5675 [hep-ph].
- [110] “Dark Matter Results from 100 Live Days of XENON100 Data”. In: *Phys. Rev. Lett.* 107 (13 2011), p. 131302. doi: [10.1103/PhysRevLett.107.131302](https://doi.org/10.1103/PhysRevLett.107.131302). arXiv: 1104.2549.
- [111] “Dark Matter Search Results from the CDMS II Experiment”. In: *Science* 86 (5 2012), p. 052001. doi: [10.1126/science.1186112](https://doi.org/10.1126/science.1186112).
- [112] H. Davoudiasl, J. L. Hewett, and T. G. Rizzo. “Phenomenology of the Randall-Sundrum Gauge Hierarchy Model”. In: *Phys. Rev. Lett.* 84 (2000), p. 2080. doi: [10.1103/PhysRevLett.84.2080](https://doi.org/10.1103/PhysRevLett.84.2080). arXiv: hep-ph/9909255 [hep-ph].
- [113] A. A. Derevshchikov et al. *On possibility to make a new type of calorimeter: Radiation resistant and fast*. Tech. rep. IFVE-90-99. Protvino, Russia: IHEP, 1990. URL: <http://ccdb5fs.kek.jp/cgi-bin/img/allpdf?199010441>.
- [114] G. Dissertori, D. Luckey, Nessi-Tedaldi, et al. “Results on damage induced by high-energy protons in LYSO calorimeter crystals”. In: *NIM A* 745 (2014) 1-6 (). doi: [10.1016/j.nima.2014.02.003](https://doi.org/10.1016/j.nima.2014.02.003). arXiv: 1309.3872 [physics.ins-det].
- [115] Ulrich Ellwanger. “Possible explanation of excess events in the search for jets, missing transverse momentum and a Z boson in pp collisions”. In: *Eur. Phys. J. C* 75.8 (2015), p. 367. doi: [10.1140/epjc/s10052-015-3591-6](https://doi.org/10.1140/epjc/s10052-015-3591-6). arXiv: 1504.02244 [hep-ph].
- [116] F. Englert and R. Brout. “Broken Symmetry and the Mass of Gauge Vector Mesons”. In: *Phys. Rev. Lett.* 13 (9 Aug. 1964), pp. 321–323. doi: [10.1103/PhysRevLett.13.321](https://doi.org/10.1103/PhysRevLett.13.321). URL: <http://link.aps.org/doi/10.1103/PhysRevLett.13.321>.

- [117] J. de Favereau et al. “DELPHES 3, A modular framework for fast simulation of a generic collider experiment”. In: *JHEP* 02 (2014), p. 057. doi: [10.1007/JHEP02\(2014\)057](https://doi.org/10.1007/JHEP02(2014)057). arXiv: [1307.6346 \[hep-ex\]](https://arxiv.org/abs/1307.6346).
- [118] Pierre Fayet. “Supergauge Invariant Extension of the Higgs Mechanism and a Model for the Electron and its Neutrino”. In: *Nucl. Phys. B* 90 (1975), p. 104. doi: [10.1016/0550-3213\(75\)90636-7](https://doi.org/10.1016/0550-3213(75)90636-7).
- [119] Rick Field. “Early LHC Underlying Event Data - Findings and Surprises”. In: *Hadron collider physics. Proceedings, 22nd Conference, HCP 2010, Toronto, Canada, August 23-27, 2010*. arXiv: [1010.3558 \[hep-ph\]](https://arxiv.org/abs/1010.3558). URL: <http://inspirehep.net/record/873443/files/arXiv:1010.3558.pdf>.
- [120] “Final Analysis and Results of the Phase II SIMPLE Dark Matter Search”. In: *Phys. Rev. Lett.* 108 (2012), p. 201302. doi: [10.1103/PhysRevLett.108.201302](https://doi.org/10.1103/PhysRevLett.108.201302). arXiv: [1106.3014](https://arxiv.org/abs/1106.3014).
- [121] “First dark matter search results from a 4-kg CF<sub>3</sub>I bubble chamber operated in a deep underground site”. In: *Phys. Rev. D* 86 (5 2012), p. 052001. doi: [10.1103/PhysRevD.86.052001](https://doi.org/10.1103/PhysRevD.86.052001). arXiv: [1204.3094](https://arxiv.org/abs/1204.3094).
- [122] “First Results from the LUX Dark Matter Experiment at the Sanford Underground Research Facility”. In: *Phys. Rev. Lett.* 112 (9 2014), p. 091303. doi: [10.1103/PhysRevLett.112.091303](https://doi.org/10.1103/PhysRevLett.112.091303). arXiv: [1310.8214](https://arxiv.org/abs/1310.8214).
- [123] Patrick J. Fox et al. “Missing energy signatures of dark matter at the LHC”. In: *Phys. Rev. D* 85 (5 2012), p. 056011. doi: [10.1103/PhysRevD.85.056011](https://doi.org/10.1103/PhysRevD.85.056011). arXiv: [1109.4398](https://arxiv.org/abs/1109.4398). URL: <http://link.aps.org/doi/10.1103/PhysRevD.85.056011>.
- [124] Patrick J. Fox et al. “Taking a razor to dark matter parameter space at the LHC”. In: *Phys. Rev. D* 86 (2012), p. 015010. doi: [10.1103/PhysRevD.86.015010](https://doi.org/10.1103/PhysRevD.86.015010). arXiv: [1203.1662 \[hep-ph\]](https://arxiv.org/abs/1203.1662).
- [125] Alexander Friedland et al. “Probing Nonstandard Standard Model Backgrounds with LHC Monojets”. In: *Phys. Lett. B* 714 (2012), p. 267. doi: [10.1016/j.physletb.2012.06.078](https://doi.org/10.1016/j.physletb.2012.06.078). arXiv: [1111.5331 \[hep-ph\]](https://arxiv.org/abs/1111.5331).
- [126] Ryan Gavin et al. “FEWZ 2.0: A code for hadronic Z production at next-to-next-to-leading order”. 2010.
- [127] Ryan Gavin et al. “W physics at the LHC with FEWZ 2.1”. 2012.
- [128] T. Gleisberg et al. “Event generation with SHERPA 1.1”. In: *JHEP* 02 (2009), p. 007. doi: [10.1088/1126-6708/2009/02/007](https://doi.org/10.1088/1126-6708/2009/02/007). arXiv: [0811.4622 \[hep-ph\]](https://arxiv.org/abs/0811.4622).
- [129] Yu. A. Golfand and E. P. Likhtman. “Extension of the algebra of Poincare group generators and violation of p invariance”. In: *JETP Lett.* 13 (1971), p. 323.

- [130] Jessica Goodman et al. “Constraints on Dark Matter from Colliders”. In: *Phys. Rev. D* 82 (2010), p. 116010. doi: [10.1103/PhysRevD.82.116010](https://doi.org/10.1103/PhysRevD.82.116010). arXiv: [1008.1783](https://arxiv.org/abs/1008.1783) [hep-ph].
- [131] Denis Grondin and Daniel Jeans. “Next Generation CALICE Electromagnetic Calorimeter”. In: *International Linear Collider Workshop 2010 (LCWS10 & ILC10) Beijing, China, March 26-30, 2010*. 2010. arXiv: [1006.4313](https://arxiv.org/abs/1006.4313) [physics.ins-det]. URL: <http://inspirehep.net/record/859118/files/arXiv:1006.4313.pdf>.
- [132] G. S. Guralnik, C. R. Hagen, and T. W. B. Kibble. “Global Conservation Laws and Massless Particles”. In: *Phys. Rev. Lett.* 13 (20 Nov. 1964), pp. 585–587. doi: [10.1103/PhysRevLett.13.585](https://doi.org/10.1103/PhysRevLett.13.585). URL: <http://link.aps.org/doi/10.1103/PhysRevLett.13.585>.
- [133] Peter W. Higgs. “Broken Symmetries and the Masses of Gauge Bosons”. In: *Phys. Rev. Lett.* 13 (16 Oct. 1964), pp. 508–509. doi: [10.1103/PhysRevLett.13.508](https://doi.org/10.1103/PhysRevLett.13.508). URL: <http://link.aps.org/doi/10.1103/PhysRevLett.13.508>.
- [134] Peter W. Higgs. “Spontaneous Symmetry Breakdown without Massless Bosons”. In: *Phys. Rev.* 145 (4 May 1966), pp. 1156–1163. doi: [10.1103/PhysRev.145.1156](https://doi.org/10.1103/PhysRev.145.1156). URL: <http://link.aps.org/doi/10.1103/PhysRev.145.1156>.
- [135] P.W. Higgs. “Broken symmetries, massless particles and gauge fields”. In: *Physics Letters* 12.2 (1964), pp. 132–133. ISSN: 0031-9163. doi: [http://dx.doi.org/10.1016/0031-9163\(64\)91136-9](http://dx.doi.org/10.1016/0031-9163(64)91136-9). URL: <http://www.sciencedirect.com/science/article/pii/0031916364911369>.
- [136] Stefan Hoeche et al. “Matching parton showers and matrix elements”. 2006.
- [137] G.’t Hooft. “Renormalizable Lagrangians for massive Yang-Mills fields”. In: *Nuclear Physics B* 35.1 (1971), pp. 167–188. ISSN: 0550-3213. doi: [http://dx.doi.org/10.1016/0550-3213\(71\)90139-8](http://dx.doi.org/10.1016/0550-3213(71)90139-8). URL: <http://www.sciencedirect.com/science/article/pii/0550321371901398>.
- [138] Dan Hooper and Lisa Goodenough. “Dark Matter Annihilation in The Galactic Center As Seen by the Fermi Gamma Ray Space Telescope”. In: *Phys. Lett. B* 697 (2011), p. 412. doi: [10.1016/j.physletb.2011.02.029](https://doi.org/10.1016/j.physletb.2011.02.029). arXiv: [1010.2752](https://arxiv.org/abs/1010.2752) [hep-ph].
- [139] Peisi Huang and Carlos E. M. Wagner. “CMS kinematic edge from sbottoms”. In: *Phys. Rev. D* 91.1 (2015), p. 015014. doi: [10.1103/PhysRevD.91.015014](https://doi.org/10.1103/PhysRevD.91.015014). arXiv: [1410.4998](https://arxiv.org/abs/1410.4998) [hep-ph].
- [140] H. C. van de Hulst, E. Raimond, and H. van Woerden. “Rotation and Density Distribution of the Andromeda Nebula Derived from Observations of the 21 cm line”. In: *Bull. Astr. Inst. Netherlands* 14 (1957), p. 1.

- [141] *Inclusive search for supersymmetry using the razor variables at sqrt(s) = 13 TeV*. Tech. rep. CMS-PAS-SUS-15-004. Geneva: CERN, 2015. URL: <https://cds.cern.ch/record/2114815>.
- [142] *Inclusive search for supersymmetry using the razor variables at sqrt(s) = 13 TeV*. Tech. rep. CMS-PAS-SUS-15-004. Geneva: CERN, 2015. URL: <https://cds.cern.ch/record/2114815>.
- [143] J. Chen, R. Mao, L. Zhang, and R. Zhu. “Gamma-Ray Induced Radiation Damage in Large Size LSO and LYSO Crystal Samples”. In: *IEEE Transactions on Nuclear Science* 54.4 (Aug. 2007), pp. 1319–1326. ISSN: 0018-9499. doi: [10.1109/TNS.2007.902370](https://doi.org/10.1109/TNS.2007.902370).
- [144] T. Junk. “Confidence level computation for combining searches with small statistics”. In: *Nucl. Instrum. Meth. A* 434 (1999), p. 435. doi: [10.1016/S0168-9002\(99\)00498-2](https://doi.org/10.1016/S0168-9002(99)00498-2). arXiv: [hep-ex/9902006](https://arxiv.org/abs/hep-ex/9902006) [hep-ex].
- [145] V. Khachatryan et al. “Performance of photon reconstruction and identification with the CMS detector in proton-proton collisions at  $\sqrt{s} = 8 \text{ TeV}$ ”. In: *JINST* 10 (2015), P08010. doi: [10.1088/1748-0221/10/08/P08010](https://doi.org/10.1088/1748-0221/10/08/P08010). arXiv: [1502.02702](https://arxiv.org/abs/1502.02702) [physics.ins-det].
- [146] V. Khachatryan et al. “Search for diphoton resonances in the mass range from 150 to 850 GeV in  $pp$  collisions at  $\sqrt{s} = 8 \text{ TeV}$ ”. In: *Phys. Lett. B* 750 (2015), p. 494. doi: [10.1016/j.physletb.2015.09.062](https://doi.org/10.1016/j.physletb.2015.09.062). arXiv: [1506.02301](https://arxiv.org/abs/1506.02301) [hep-ex].
- [147] V. Khachatryan et al. “Search for massive resonances in dijet systems containing jets tagged as  $W$  or  $Z$  boson decays in  $pp$  collisions at  $\sqrt{s} = 8 \text{ TeV}$ ”. In: *JHEP* 08 (2014), p. 173. doi: [10.1007/JHEP08\(2014\)173](https://doi.org/10.1007/JHEP08(2014)173). arXiv: [1405.1994](https://arxiv.org/abs/1405.1994) [hep-ex].
- [148] V. Khachatryan. “Search for Monotop Signatures in Proton-Proton Collisions at  $\sqrt{s} = 8 \text{ TeV}$ ”. In: *Phys. Rev. Lett.* 114 (10 2015), p. 101801. doi: [10.1103/PhysRevLett.114.101801](https://doi.org/10.1103/PhysRevLett.114.101801). arXiv: [1410.1149](https://arxiv.org/abs/1410.1149). URL: <http://link.aps.org/doi/10.1103/PhysRevLett.114.101801>.
- [149] V. Khachatryan et al. “Search for narrow resonances decaying to dijets in proton-proton collisions at  $\sqrt{s} = 13 \text{ TeV}$ ”. In: *Phys. Rev. Lett.* 116 (2016), p. 071801. doi: [10.1103/PhysRevLett.116.071801](https://doi.org/10.1103/PhysRevLett.116.071801). arXiv: [1512.01224](https://arxiv.org/abs/1512.01224) [hep-ex].
- [150] V. Khachatryan et al. “Search for physics beyond the standard model in dilepton mass spectra in proton-proton collisions at  $\sqrt{s} = 8 \text{ TeV}$ ”. In: *JHEP* 04 (2015), p. 025. doi: [10.1007/JHEP04\(2015\)025](https://doi.org/10.1007/JHEP04(2015)025). arXiv: [1412.6302](https://arxiv.org/abs/1412.6302) [hep-ex].
- [151] V. Khachatryan et al. “Search for resonances and quantum black holes using dijet mass spectra in proton-proton collisions at  $\sqrt{s} = 8 \text{ TeV}$ ”. In: *Phys. Rev. D* 91 (2015), p. 052009. doi: [10.1103/PhysRevD.91.052009](https://doi.org/10.1103/PhysRevD.91.052009). arXiv: [1501.04198](https://arxiv.org/abs/1501.04198) [hep-ex].

- [152] Vardan Khachatryan et al. “Event generator tunes obtained from underlying event and multiparton scattering measurements”. In: *Eur. Phys. J. C* 76 (2016), p. 155. doi: [10.1140/epjc/s10052-016-3988-x](https://doi.org/10.1140/epjc/s10052-016-3988-x). arXiv: [1512.00815](https://arxiv.org/abs/1512.00815) [hep-ex].
- [153] Vardan Khachatryan et al. “Observation of the diphoton decay of the Higgs boson and measurement of its properties”. In: *Eur. Phys. J. C* 74 (2014), p. 3076. doi: [10.1140/epjc/s10052-014-3076-z](https://doi.org/10.1140/epjc/s10052-014-3076-z). arXiv: [1407.0558](https://arxiv.org/abs/1407.0558) [hep-ex].
- [154] Vardan Khachatryan et al. “Observation of the diphoton decay of the Higgs boson and measurement of its properties”. In: *Eur. Phys. J. C* 74.10 (2014), p. 3076. doi: [10.1140/epjc/s10052-014-3076-z](https://doi.org/10.1140/epjc/s10052-014-3076-z). arXiv: [1407.0558](https://arxiv.org/abs/1407.0558) [hep-ex].
- [155] Vardan Khachatryan et al. “Performance of electron reconstruction and selection with the CMS detector in proton-proton collisions at  $\sqrt{s} = 8$  TeV”. In: *JINST* 10 (2015), P06005. doi: [10.1088/1748-0221/10/06/P06005](https://doi.org/10.1088/1748-0221/10/06/P06005). arXiv: [1502.02701](https://arxiv.org/abs/1502.02701) [physics.ins-det].
- [156] Vardan Khachatryan et al. “Performance of Photon Reconstruction and Identification with the CMS Detector in Proton-Proton Collisions at  $\sqrt{s} = 8$  TeV”. In: *JINST* 10.08 (2015), P08010. doi: [10.1088/1748-0221/10/08/P08010](https://doi.org/10.1088/1748-0221/10/08/P08010). arXiv: [1502.02702](https://arxiv.org/abs/1502.02702) [physics.ins-det].
- [157] Vardan Khachatryan et al. “Performance of Photon Reconstruction and Identification with the CMS Detector in Proton-Proton Collisions at  $\sqrt{s} = 8$  TeV”. In: *JINST* 10.08 (2015), P08010. doi: [10.1088/1748-0221/10/08/P08010](https://doi.org/10.1088/1748-0221/10/08/P08010). arXiv: [1502.02702](https://arxiv.org/abs/1502.02702) [physics.ins-det].
- [158] Vardan Khachatryan et al. “Search for narrow resonances in dijet final states at  $\sqrt{s} = 8$  TeV with the novel CMS technique of data scouting”. In: *Phys. Rev. Lett.* 117 (2016), p. 031802. doi: [10.1103/PhysRevLett.117.031802](https://doi.org/10.1103/PhysRevLett.117.031802). arXiv: [1604.08907](https://arxiv.org/abs/1604.08907) [hep-ex].
- [159] Vardan Khachatryan et al. “Search for new phenomena in monophoton final states in proton-proton collisions at  $\sqrt{s} = 8$  TeV”. 2014.
- [160] Vardan Khachatryan et al. “Search for physics beyond the standard model in final states with a lepton and missing transverse energy in proton-proton collisions at  $\sqrt{s} = 8$  TeV”. In: *Phys. Rev. D* 91 (2015), p. 092005. doi: [10.1103/PhysRevD.91.092005](https://doi.org/10.1103/PhysRevD.91.092005). arXiv: [1408.2745](https://arxiv.org/abs/1408.2745) [hep-ex].
- [161] Vardan Khachatryan et al. “Search for resonant production of high-mass photon pairs in proton-proton collisions at  $\sqrt{s} = 8$  and 13 TeV”. In: *Phys. Rev. Lett.* 117 (2016), p. 051802. doi: [10.1103/PhysRevLett.117.051802](https://doi.org/10.1103/PhysRevLett.117.051802). arXiv: [1606.04093](https://arxiv.org/abs/1606.04093) [hep-ex].

- [162] Vardan Khachatryan et al. “Search for Supersymmetry Using Razor Variables in Events with  $b$ -Tagged Jets in  $pp$  Collisions at  $\sqrt{s} = 8$  TeV”. In: *Phys. Rev.* D91 (2015), p. 052018. doi: [10.1103/PhysRevD.91.052018](https://doi.org/10.1103/PhysRevD.91.052018). arXiv: [1502.00300](https://arxiv.org/abs/1502.00300) [hep-ex].
- [163] T. W. B. Kibble. “Symmetry Breaking in Non-Abelian Gauge Theories”. In: *Phys. Rev.* 155 (5 Mar. 1967), pp. 1554–1561. doi: [10.1103/PhysRev.155.1554](https://doi.org/10.1103/PhysRev.155.1554). URL: <http://link.aps.org/doi/10.1103/PhysRev.155.1554>.
- [164] H. Kim et al. “A new time calibration method for switched-capacitor-array-based waveform samplers”. In: *Nucl. Instrum. Meth. A* 767 (2014), pp. 67–74. ISSN: 0168-9002. doi: <http://dx.doi.org/10.1016/j.nima.2014.08.025>. URL: <http://www.sciencedirect.com/science/article/pii/S016890021400953X>.
- [165] Archil Kobakhidze et al. “ATLAS Z-peaked excess in the MSSM with a light sbottom or stop”. In: *Phys. Rev.* D92.7 (2015), p. 075008. doi: [10.1103/PhysRevD.92.075008](https://doi.org/10.1103/PhysRevD.92.075008). arXiv: [1504.04390](https://arxiv.org/abs/1504.04390) [hep-ph].
- [166] A. Kulesza and L. Motyka. “Soft gluon resummation for the production of gluino-gluino and squark-antisquark pairs at the LHC”. In: *Phys. Rev. D* 80 (2009), p. 095004. doi: [10.1103/PhysRevD.80.095004](https://doi.org/10.1103/PhysRevD.80.095004). arXiv: [0905.4749](https://arxiv.org/abs/0905.4749) [hep-ph].
- [167] A. Kulesza and L. Motyka. “Threshold Resummation for Squark-Antisquark and Gluino-Pair Production at the LHC”. In: *Phys. Rev. Lett.* 102 (2009), p. 111802. doi: [10.1103/PhysRevLett.102.111802](https://doi.org/10.1103/PhysRevLett.102.111802). arXiv: [0807.2405](https://arxiv.org/abs/0807.2405) [hep-ph].
- [168] L. Brianza, F. Cavallari, D. Del Re, S. Gelli, A. Ghezzi, C. Gotti, P. Govoni, C. Jorda Lopez, A. Martelli, B. Marzocchi, P. Meridiani, G. Organtini, R. Paramatti, L. Pernie, S. Pigazzini, S. Rahatlou, C. Rovelli, F. Santanastasio, T. Tabarelli de Fatis, N. Trevisani. “Response of microchannel plates to single particles and to electromagnetic showers”. In: *Nucl. Instrum. Meth. A* 797 (2015), pp. 216–221. ISSN: 0168-9002. doi: <http://dx.doi.org/10.1016/j.nima.2015.06.057>. URL: <http://www.sciencedirect.com/science/article/pii/S0168900215008074>.
- [169] L. Rossi, and O. Brüning. *High Luminosity Large Hadron Collider A description for the European Strategy Preparatory Group*. Tech. rep. CERN-ATS-2012-236. Geneva: CERN, Aug. 2012.
- [170] L. Zhang, R. Mao, and R. Zhu. “Effects of neutron irradiations in various crystal samples of large size for future crystal calorimeter”. In: *Nuclear Science Symposium Conference Record (NSS/MIC), 2009 IEEE*. Oct. 2009, pp. 2041–2044. doi: [10.1109/NSSMIC.2009.5402125](https://doi.org/10.1109/NSSMIC.2009.5402125).

- [171] L. Zhang, R. Mao, F. Yang, and R. Zhu. “LSO/LYSO Crystals for Calorimeters in Future HEP Experiments”. In: *IEEE Transactions on Nuclear Science* 61.1 (Feb. 2014), pp. 483–488. ISSN: 0018-9499.
- [172] Hung-Liang Lai et al. “New parton distributions for collider physics”. In: *Phys. Rev. D* 82 (2010), p. 074024. doi: [10.1103/PhysRevD.82.074024](https://doi.org/10.1103/PhysRevD.82.074024). arXiv: [1007.2241](https://arxiv.org/abs/1007.2241) [hep-ph].
- [173] L. D. Landau. “On the angular momentum of a system of two photons”. In: *Dokl. Akad. Nauk SSSR* 60 (1948), p. 207. doi: [10.1016/B978-0-08-010586-4.50070-5](https://doi.org/10.1016/B978-0-08-010586-4.50070-5).
- [174] LHC Higgs Combination Group. *Procedure for the LHC Higgs boson search combination in Summer 2011*. Tech. rep. CMS-NOTE-2011-005, ATL-PHYS-PUB-2011-11. 2011. URL: <https://cds.cern.ch/record/1379837>.
- [175] Tongyan Lin, Edward W. Kolb, and Lian-Tao Wang. “Probing dark matter couplings to top and bottom quarks at the LHC”. In: *Phys. Rev. D* 88 (2013), p. 063510. doi: [10.1103/PhysRevD.88.063510](https://doi.org/10.1103/PhysRevD.88.063510). arXiv: [1303.6638](https://arxiv.org/abs/1303.6638) [hep-ph].
- [176] A. D. Martin et al. “Parton distributions for the LHC”. In: *Eur. Phys. J. C* 63 (2009), p. 189. doi: [10.1140/epjc/s10052-009-1072-5](https://doi.org/10.1140/epjc/s10052-009-1072-5). arXiv: [0901.0002](https://arxiv.org/abs/0901.0002).
- [177] A. D. Martin et al. “Update of parton distributions at NNLO”. In: *Phys. Lett. B* 652 (2007), p. 292. doi: [10.1016/j.physletb.2007.07.040](https://doi.org/10.1016/j.physletb.2007.07.040). arXiv: [0706.0459](https://arxiv.org/abs/0706.0459) [hep-ph].
- [178] Sanjib Muhuri et al. “Test and characterization of a prototype silicon-tungsten electromagnetic calorimeter”. In: *Nucl. Instrum. Meth. A* 764 (2014), pp. 24–29. ISSN: 0168-9002. doi: <http://dx.doi.org/10.1016/j.nima.2014.07.019>. URL: <http://www.sciencedirect.com/science/article/pii/S0168900214008614>.
- [179] “Multiyear search for dark matter annihilations in the Sun with the AMANDA-II and IceCube detectors”. In: *Phys. Rev. D* 85 (4 2012), p. 042002. doi: [10.1103/PhysRevD.85.042002](https://doi.org/10.1103/PhysRevD.85.042002). arXiv: [1112.1840](https://arxiv.org/abs/1112.1840).
- [180] Pavel M. Nadolsky et al. “Implications of CTEQ global analysis for collider observables”. In: *Phys. Rev. D* 78 (2008), p. 013004. doi: [10.1103/PhysRevD.78.013004](https://doi.org/10.1103/PhysRevD.78.013004). arXiv: [0802.0007](https://arxiv.org/abs/0802.0007) [hep-ph].
- [181] J. F. Navarro, C. S. Frenk, and S. D. M. White. “The Structure of Cold Dark Matter Halos”. In: 462 (May 1996), p. 563. doi: [10.1086/177173](https://doi.org/10.1086/177173). eprint: [astro-ph/9508025](https://arxiv.org/abs/astro-ph/9508025).
- [182] K. A. Olive et al. “Review of Particle Physics”. In: *Chin. Phys. C* 38 (2014), p. 090001. doi: [10.1088/1674-1137/38/9/090001](https://doi.org/10.1088/1674-1137/38/9/090001).

- [183] Michele Papucci, Joshua T. Ruderman, and Andreas Weiler. “Natural SUSY Endures”. In: *JHEP* 09 (2012), p. 035. doi: [10.1007/JHEP09\(2012\)035](https://doi.org/10.1007/JHEP09(2012)035). arXiv: [1110.6926](https://arxiv.org/abs/1110.6926) [hep-ph].
- [184] Michele Papucci, Alessandro Vichi, and Kathryn M. Zurek. “Monojet versus the rest of the world I:  $t$ -channel models”. In: *JHEP* 11 (2014), p. 024. doi: [10.1007/JHEP11\(2014\)024](https://doi.org/10.1007/JHEP11(2014)024). arXiv: [1402.2285](https://arxiv.org/abs/1402.2285) [hep-ph].
- [185] *Performance of b tagging at  $\sqrt{s} = 8 \text{ TeV}$  in multijet,  $t\bar{t}$  and boosted topology events*. CMS Physics Analysis Summary CMS-PAS-BTV-13-001. 2013. URL: <http://cds.cern.ch/record/1581306>.
- [186] M. Persic, P. Salucci, and F. Stel. “The universal rotation curve of spiral galaxies - I. The dark matter connection”. In: 281 (July 1996), pp. 27–47. doi: [10.1093/mnras/281.1.27](https://doi.org/10.1093/mnras/281.1.27). eprint: [astro-ph/9506004](https://arxiv.org/abs/astro-ph/9506004).
- [187] *Phenomenological MSSM interpretation of CMS results at  $\sqrt{s} = 7$  and 8 TeV*. Tech. rep. CMS-PAS-SUS-15-010. Geneva: CERN, 2015. URL: <http://cds.cern.ch/record/2063744>.
- [188] Planck Collaboration. “Planck 2015 results”. In: *AA* 594 (2016), A13. doi: [10.1051/0004-6361/201525830](https://doi.org/10.1051/0004-6361/201525830). URL: <http://dx.doi.org/10.1051/0004-6361/201525830>.
- [189] J. Pumplin et al. “New generation of parton distributions with uncertainties from global QCD analysis”. In: *JHEP* 07 (2002), p. 012. doi: [10.1088/1126-6708/2002/07/012](https://doi.org/10.1088/1126-6708/2002/07/012). arXiv: [hep-ph/0201195](https://arxiv.org/abs/hep-ph/0201195) [hep-ph].
- [190] R. Mao, L. Zhang, and R. Zhu. “Gamma ray induced radiation damage in PWO and LSO/LYSO crystals”. In: *Nuclear Science Symposium Conference Record (NSS/MIC), 2009 IEEE*. Oct. 2009, pp. 2045–2049. doi: [10.1109/NSSMIC.2009.5402126](https://doi.org/10.1109/NSSMIC.2009.5402126).
- [191] Pierre Ramond. “Dual theory for free fermions”. In: *Phys. Rev. D* 3 (1971), p. 2415. doi: [10.1103/PhysRevD.3.2415](https://doi.org/10.1103/PhysRevD.3.2415).
- [192] L. Randall and R. Sundrum. “A large mass hierarchy from a small extra dimension”. In: *Phys. Rev. Lett.* 83 (1999), p. 3370. doi: [10.1103/PhysRevLett.83.3370](https://doi.org/10.1103/PhysRevLett.83.3370). arXiv: [hep-ph/9905221](https://arxiv.org/abs/hep-ph/9905221) [hep-ph].
- [193] Lisa Randall and Raman Sundrum. “An alternative to compactification”. In: *Phys. Rev. Lett.* 83 (1999), p. 4690. doi: [10.1103/PhysRevLett.83.4690](https://doi.org/10.1103/PhysRevLett.83.4690). arXiv: [hep-th/9906064](https://arxiv.org/abs/hep-th/9906064) [hep-th].
- [194] A. L. Read. “Presentation of search results: the  $CL_s$  technique”. In: *J. Phys. G* 28 (2002), p. 2693. doi: [10.1088/0954-3899/28/10/313](https://doi.org/10.1088/0954-3899/28/10/313).
- [195] S. Ritt, R. Dinapoli, and U. Hartmann. “Application of the DRS chip for fast waveform digitizing”. In: *NIM A* 623 (2010) 486-488 () .
- [196] C. Rogan. “Kinematics for new dynamics at the LHC”. CALT-68-2790. 2010.

- [197] A. Ronzhin et al. “Development of a new fast shower maximum detector based on microchannel plates photomultipliers (MCP-PMT) as an active element”. In: *Nucl. Instrum. Meth. A* 759 (2014), pp. 65–73. ISSN: 0168-9002. doi: <http://dx.doi.org/10.1016/j.nima.2014.05.039>. URL: <http://www.sciencedirect.com/science/article/pii/S016890021400566X>.
- [198] A. Ronzhin et al. “Direct tests of micro channel plates as the active element of a new shower maximum detector”. In: *Nucl. Instrum. Meth. A* 795 (2015), pp. 52–57. ISSN: 0168-9002. doi: <http://dx.doi.org/10.1016/j.nima.2015.05.029>. URL: <http://www.sciencedirect.com/science/article/pii/S0168900215006610>.
- [199] A. Ronzhin et al. “Direct tests of micro channel plates as the active element of a new shower maximum detector”. In: *Nucl. Instrum. Meth. A* 795 (2015), pp. 52–57. doi: <10.1016/j.nima.2015.05.029>.
- [200] A. Ronzhin et al. “Study of the timing performance of micro-channel plate photomultiplier for use as an active layer in a shower maximum detector”. In: *Nucl. Instrum. Meth. A* 795 (2015), pp. 288–292. ISSN: 0168-9002. doi: <http://dx.doi.org/10.1016/j.nima.2015.06.006>. URL: <http://www.sciencedirect.com/science/article/pii/S0168900215007500>.
- [201] V. C. Rubin and W. K. Ford Jr. “Rotation of the Andromeda Nebula from a Spectroscopic Survey of Emission Regions”. In: 159 (Feb. 1970), p. 379. doi: <10.1086/150317>.
- [202] V.C. Rubin, N. Thonnard, and W.K. Ford Jr. “Rotational properties of 21 SC galaxies with a large range of luminosities and radii, from NGC 4605/R = 4 kpc to UGC 2885/R = 122 kpc”. In: *Astrophys. J.* 238 (1980), p. 471. doi: <10.1086/158003>.
- [203] “Search for Low-Mass Weakly Interacting Massive Particles Using Voltage-Assisted Calorimetric Ionization Detection in the SuperCDMS Experiment”. In: *Phys. Rev. Lett.* 112 (4 2014), p. 041302. doi: <10.1103/PhysRevLett.112.041302>. arXiv: <1309.3259>.
- [204] *Search for physics beyond the standard model in events with two opposite-sign same-flavor leptons, jets, and missing transverse energy in pp collisions at  $\sqrt{s} = 8 \text{ TeV}$* . Tech. rep. CMS-PAS-SUS-12-019. Geneva: CERN, 2014. URL: <http://cds.cern.ch/record/1751493>.
- [205] “Search for supersymmetry using razor variables in events with b-tagged jets in pp collisions at  $\sqrt{s} = 8 \text{ TeV}$ ”. In: *Phys. Rev. D* 91 (5 2015), p. 052018. doi: <10.1103/PhysRevD.91.052018>. arXiv: <1502.00300>. URL: <http://link.aps.org/doi/10.1103/PhysRevD.91.052018>.

- [206] *Search for SUSY in Events with a Higgs Decaying to Two Photons Using the Razor Variables*. Tech. rep. CMS-PAS-SUS-16-012. Geneva: CERN, 2016. URL: <https://cds.cern.ch/record/2205153>.
- [207] *Search for SUSY with Higgs in the diphoton final state using the razor variables*. CMS Physics Analysis Summary CMS-PAS-SUS-14-017. 2014. URL: <http://cds.cern.ch/record/2047472>.
- [208] *Search for SUSY with Higgs in the diphoton final state using the razor variables*. Tech. rep. CMS-PAS-SUS-14-017. Geneva: CERN, 2015. URL: <https://cds.cern.ch/record/2047472>.
- [209] “Search for the production of dark matter in association with top-quark pairs in the single-lepton final state in proton-proton collisions at  $\sqrt{s} = 8$  TeV”. In: *JHEP* 06 (2015), p. 121. doi: [10.1007/JHEP06\(2015\)121](https://doi.org/10.1007/JHEP06(2015)121). arXiv: [1402.2285 \[hep-ph\]](https://arxiv.org/abs/1402.2285).
- [210] Torbjorn Sjostrand, Stephen Mrenna, and Peter Z. Skands. “PYTHIA 6.4 Physics and Manual”. In: *JHEP* 05 (2006), p. 026. doi: [10.1088/1126-6708/2006/05/026](https://doi.org/10.1088/1126-6708/2006/05/026). arXiv: [hep-ph/0603175 \[hep-ph\]](https://arxiv.org/abs/hep-ph/0603175).
- [211] Torbjorn Sjöstrand, Stephen Mrenna, and Peters Skands. “PYTHIA 6.4 physics and manual”. In: *JHEP* 05 (2006), p. 026. doi: [10.1088/1126-6708/2006/05/026](https://doi.org/10.1088/1126-6708/2006/05/026). arXiv: [hep-ph/0603175 \[hep-ph\]](https://arxiv.org/abs/hep-ph/0603175).
- [212] Torbjörn Sjöstrand et al. “An Introduction to PYTHIA 8.2”. In: *Comput. Phys. Commun.* 191 (2015), pp. 159–177. doi: [10.1016/j.cpc.2015.01.024](https://doi.org/10.1016/j.cpc.2015.01.024). arXiv: [1410.3012 \[hep-ph\]](https://arxiv.org/abs/1410.3012).
- [213] T. Sjöstrand et al. “An Introduction to PYTHIA 8.2”. In: *Comput. Phys. Commun.* 191 (2015), p. 159. doi: [10.1016/j.cpc.2015.01.024](https://doi.org/10.1016/j.cpc.2015.01.024). arXiv: [1410.3012 \[hep-ph\]](https://arxiv.org/abs/1410.3012).
- [214] George F. Smoot et al. “Structure in the COBE differential microwave radiometer first year maps”. In: *Astrophys. J.* 396 (1992), p. L1. doi: [10.1086/186504](https://doi.org/10.1086/186504).
- [215] D.N. Spergel et al. “Wilkinson Microwave Anisotropy Probe (WMAP) three year results: implications for cosmology”. In: *Astrophys. J. Suppl.* 170 (2007), p. 377. doi: [10.1086/513700](https://doi.org/10.1086/513700). arXiv: [astro-ph/0603449 \[astro-ph\]](https://arxiv.org/abs/astro-ph/0603449).
- [216] Maria Spiropulu. “Precision Timing Calorimetry”. CPAD Instrumentation Frontier Meeting, October 2015.
- [217] Volker Springel et al. “Simulating the joint evolution of quasars, galaxies and their large-scale distribution”. In: *Nature* 435 (2005), p. 629. doi: [10.1038/nature03597](https://doi.org/10.1038/nature03597). arXiv: [astro-ph/0504097 \[astro-ph\]](https://arxiv.org/abs/astro-ph/0504097).
- [218] D. V. Volkov and V. P. Akulov. “Possible universal neutrino interaction”. In: *JETP Lett.* 16 (1972), p. 438.

- [219] W. W. Moses and S. E. Derenzo. “Prospects for Time-of-Flight PET using LSO Scintillator”. In: *IEEE Transactions on Nuclear Science* 46.3 (June 1999), pp. 474–478. ISSN: 0018-9499. doi: [10.1109/TNS.2007.902370](https://doi.org/10.1109/TNS.2007.902370).
- [220] Ann Miao Wang. “New Physics Models in the Diphoton Final State at CMS”. DOI [10.7907/Z9CC0XMN](https://doi.org/10.7907/Z9CC0XMN). <http://resolver.caltech.edu/CaltechTHESIS:01152016-102117113>. Senior Thesis (Major). 1200 E. California Blvd., Pasadena, CA 91125, USA: California Institute of Technology, 2015. doi: [10.7907/Z9CC0XMN](https://doi.org/10.7907/Z9CC0XMN). URL: <http://resolver.caltech.edu/CaltechTHESIS:01152016-102117113>.
- [221] Steven Weinberg. “A Model of Leptons”. In: *Phys. Rev. Lett.* 19 (21 Nov. 1967), pp. 1264–1266. doi: [10.1103/PhysRevLett.19.1264](https://doi.org/10.1103/PhysRevLett.19.1264). URL: <http://link.aps.org/doi/10.1103/PhysRevLett.19.1264>.
- [222] J. Wess and B. Zumino. “Supergauge transformations in four-dimensions”. In: *Nucl. Phys. B* 70 (1974), p. 39. doi: [10.1016/0550-3213\(74\)90355-1](https://doi.org/10.1016/0550-3213(74)90355-1).
- [223] Simon D.M. White et al. “Clusters, filaments, and voids in a universe dominated by cold dark matter”. In: *Astrophys. J.* 313 (1987), p. 505. doi: [10.1086/164990](https://doi.org/10.1086/164990).
- [224] Si Xie. “New Developments in Secondary Emission Calorimeters”. CPAD Instrumentation Frontier Meeting, October 2015.
- [225] C. N. Yang. “Selection Rules for the Dematerialization of a Particle into Two Photons”. In: *Phys. Rev.* 77 (1950), p. 242. doi: [10.1103/PhysRev.77.242](https://doi.org/10.1103/PhysRev.77.242).
- [226] F. Zwicky. “On the Masses of Nebulae and of Clusters of Nebulae”. In: 86 (Oct. 1937), p. 217. doi: [10.1086/143864](https://doi.org/10.1086/143864).
- [227] F. Zwicky. “On the Masses of Nebulae and of Clusters of Nebulae”. In: *Astrophys. J.* 86 (1937), p. 217. doi: [10.1086/143864](https://doi.org/10.1086/143864).
- [228] F. Zwicky. “Republication of: The redshift of extragalactic nebulae”. In: *General Relativity and Gravitation* 41.1 (2009), pp. 207–224. ISSN: 1572-9532. doi: [10.1007/s10714-008-0707-4](https://doi.org/10.1007/s10714-008-0707-4). URL: <http://dx.doi.org/10.1007/s10714-008-0707-4>.

## A p p e n d i x A

# SEARCH FOR MASSIVE RESONANCES DECAYING INTO TWO PHOTONS

### A.1 Introduction

The standard model (SM) of particle physics has been highly successful in describing physical phenomena but it is widely considered to be an incomplete theory because of various shortcomings. In particular, the SM suffers from the so-called hierarchy problem [52], which refers to the large difference between the Higgs boson mass of 125 GeV [15] and the highest energy scale up to which the SM must be valid. Many extensions to the SM have been proposed to address the hierarchy problem, including theories with additional space-like dimensions [192] and models with extended Higgs boson sectors [63]. Some of these extensions predict new resonances that decay to a diphoton final state. For example, the Randall–Sundrum (RS) approach [192, 193] to extra dimensions postulates massive excitations of spin-2 gravitons that can decay to two photons. The simplest extension of the SM Higgs boson sector consists of the addition of a doublet of complex scalar fields. In such models [106], some of these additional scalar resonances can decay to a photon pair [59]. According to the Landau–Yang theorem, the spin of a resonance decaying to two photons can only be zero or an integer larger than one [173, 225].

Recently, the ATLAS and CMS Collaborations at the CERN LHC presented results on searches for high-mass diphoton resonances in proton-proton ( $pp$ ) collisions at a center-of-mass energy of 13 TeV [6, 161]. The results were based on data collected in 2015, corresponding to integrated luminosities of approximately  $3\text{ fb}^{-1}$  per experiment. The CMS results included a combined analysis with  $pp$  collision data at  $\sqrt{s} = 8\text{ TeV}$  collected in 2012 [146] corresponding to an integrated luminosity of  $19.7\text{ fb}^{-1}$ . Both collaborations reported the observation of a moderate excess of events compared to SM expectations, compatible with the production of a new resonance with a mass around 750 GeV.

In this Letter, we report on an updated search for spin-0 resonances and RS gravitons produced in  $pp$  collisions and decaying to two photons. The data were collected in 2016 with the CMS detector at  $\sqrt{s} = 13\text{ TeV}$  and correspond to an integrated luminosity of  $12.9\text{ fb}^{-1}$ . The analysis procedures are very similar to those presented

in Ref. [161] for the 2015 data. A combined analysis of the 8 TeV data set of Ref. [146], the 13 TeV data set of Ref. [161], and the 13 TeV data set examined here is performed to improve the sensitivity of the results. Earlier LHC searches for RS gravitons are presented in Refs. [11, 9, 10, 8, 12, 13, 146, 82, 150, 80, 149, 81, 158, 151, 147, 79, 78], and for spin-0 particles decaying to two photons in Refs. [14, 146]. These earlier searches are based on  $pp$  collisions at either  $\sqrt{s} = 7$  or 8 TeV.

## A.2 The CMS detector

The central feature of the CMS apparatus is a superconducting solenoid of 6 m internal diameter, providing a magnetic field of 3.8 T. Within the solenoid volume are a silicon pixel and strip tracker, a lead tungstate crystal electromagnetic calorimeter (ECAL), and a brass and scintillator hadron calorimeter (HCAL). The tracking detectors cover the pseudorapidity range  $|\eta| < 2.5$ . The ECAL and HCAL, each composed of a barrel and two endcap sections, cover  $|\eta| < 3.0$ , with the boundary between the barrel and endcaps at around  $|\eta| = 1.5$ . Forward calorimeters extend the coverage to  $|\eta| < 5.0$ . The ECAL consists of 75 848 lead tungstate crystals. The barrel section has a granularity  $\Delta\eta \times \Delta\phi = 0.0174 \times 0.0174$ , with  $\phi$  the azimuthal angle, while the endcap sections have a granularity that coarsens progressively up to  $\Delta\eta \times \Delta\phi = 0.05 \times 0.05$ . Preshower detectors consisting of two planes of silicon sensors interleaved with a total of  $3X_0$  of lead are located in front of the endcap sections. Muons are measured within  $|\eta| < 2.4$  by gas-ionization detectors embedded in the steel flux-return yoke outside the solenoid. A more detailed description of the CMS detector, together with a definition of the coordinate system and the relevant kinematic variables, can be found in Ref. [83].

In the barrel section of the ECAL, for photons with energies on the scale of tens of GeV, an energy resolution of about 1% is achieved for unconverted photons and for photons that convert “late”, i.e., just before entering the ECAL. The remaining barrel photons have an energy resolution of about 1.3% up to  $|\eta| = 1.0$ , rising to about 2.5% for  $|\eta| = 1.4$ . In the endcaps, the corresponding resolution for unconverted and late-converting photons is about 2.5%, while the remaining endcap photons have a resolution between 3 and 4% [145].

The particle-flow algorithm [100, 96] reconstructs and identifies each individual particle with an optimised combination of information from the various elements of the CMS detector. Particle candidates are classified as either muons, electrons, photons,  $\tau$  leptons, charged hadrons, or neutral hadrons.

A two-stage trigger system selects events of interest for the analysis. The level-1 trigger, composed of custom hardware processors, selects events at a maximum readout rate of about 100 kHz using information from the calorimeters and muon detectors. The high-level trigger software algorithms use the full event information to reduce the event rate to less than 1 kHz before data storage.

### A.3 Event simulation

The **PYTHIA** 8.2 [213] event generator with NNPDF2.3 [49] parton distribution functions (PDFs) is used to produce simulated signal samples of spin-0 and spin-2 resonances decaying to two photons. The samples are generated at leading order (LO), with values of the resonance mass  $m_X$  in the range  $0.5 < m_X < 4.5$  TeV. Three values of the relative width  $\Gamma_X/m_X$  are used as benchmarks:  $1.4 \times 10^{-4}$ ,  $1.4 \times 10^{-2}$ , and  $5.6 \times 10^{-2}$ , where  $\Gamma_X$  is the width of the resonance. These relative widths correspond, respectively, to resonances much narrower than, comparable to, and significantly wider than the detector resolution. In the context of the RS graviton model, for which  $\Gamma_X/m_X = 1.4 \tilde{k}^2$  [112], the relative widths correspond to the dimensionless coupling parameter  $\tilde{k} = 0.01, 0.1$ , and  $0.2$ . The scalar resonances are produced through gluon-gluon fusion, and RS graviton resonances through both gluon-gluon fusion and quark-antiquark annihilation. In the RS model, the first mechanism accounts for approximately 90% of the production cross section.

The SM background mostly arises from the direct production of two photons, the production of  $\gamma$ +jets events in which jet fragments are misidentified as photons, and the production of multijet events with misidentified jet fragments. These backgrounds are simulated with the **SHERPA** 2.1 [128], **MADGRAPH5\_aMC@NLO** 2.2 [39] (interfaced with **PYTHIA** 8.2 for parton showering and hadronization), and **PYTHIA** 8.2 generators, respectively, using the CT10NLO [172], NNPDF3.0 [50], and NNPDF2.3 PDF sets, again respectively. The **PYTHIA** tune CUETP8M1 [152] is used.

For both the signal and background samples, the detector response is simulated using the **GEANT4** package [28]. The simulated samples incorporate additional  $pp$  interactions within the same or a nearby bunch crossing (pileup) and are weighted to reproduce the measured distribution of the number of interactions per bunch crossing.

#### A.4 Event selection and diphoton mass spectrum

The trigger requirements, photon identification criteria, and event selection procedures are described in Ref. [161]. Some details are given below. Energy deposits in the ECAL compatible with the shower shape expected for a photon are clustered together to define a photon candidate. Variations in the crystal transparency during the data collection period are corrected for using a dedicated monitoring system, and the single-channel response is equalized based on collision data [145]. A multivariate regression technique [145] is used to correct the photon energy for the incomplete containment of the shower in the clustered crystals, the shower losses for photons that convert before reaching the calorimeter, and the effects of pileup. The interaction vertex is selected using the algorithm described in Ref. [153], which combines information on the correlation between the diphoton system and the recoiling tracks, the average transverse momentum ( $p_T$ ) of the recoiling tracks, and, when available, directional information from reconstructed photon conversions. For resonances with a mass above 500 GeV, the fraction of events in which the interaction vertex is correctly assigned is approximately 90%. For each photon candidate, the transverse size of the electromagnetic cluster in the  $\eta$  coordinate must be compatible with that expected for a photon from a hard interaction, and the ratio of the associated energy in the HCAL to the photon energy must be less than 0.05.

Photon candidates are required to have  $p_T > 75$  GeV and to appear within  $|\eta| < 2.5$ . Candidates in the transition region between the barrel and endcap detectors ( $1.44 < |\eta| < 1.57$ ), where the acceptance is difficult to model, are rejected. Photon candidates associated with electron tracks that are incompatible with conversion tracks are rejected. Photon candidates are required to be isolated. There are two isolation criteria, both of which are imposed: i) the sum of the scalar  $p_T$  of charged hadron candidates from the interaction vertex that lie within a cone of radius  $R = \sqrt{(\Delta\eta)^2 + (\Delta\phi)^2} = 0.3$  around the photon candidate must be less than 5 GeV, where charged hadrons identified as conversion tracks associated with the photon candidate are excluded; ii) the pileup-corrected sum of the scalar  $p_T$  of additional photon candidates within this same cone must be less than 2.5 GeV.

The identification and trigger efficiencies are measured as functions of photon  $p_T$  using data events containing a Z boson decaying to a  $\mu^+ \mu^-$  pair in association with a photon, or to an  $e^+ e^-$  pair [145]. The efficiency of the photon selection procedure in the kinematic range considered in the analysis is above 90 and 85% for candidates in the barrel and endcap regions, respectively. The ratio between the efficiencies

measured in data and simulation is found to be lower than 1 by 3.5% for photons in the barrel region and by 6.5% for photons in the endcap region. No significant  $p_T$  dependence of the efficiency ratios is observed, and a  $p_T$ -independent correction is applied to the normalization of the simulated event samples to account for this difference.

The photon candidates in an event are grouped into all possible pairs. At least one photon candidate in the pair must have  $|\eta| < 1.44$ , i.e., lie in the barrel. Photon pairs are divided into two categories. The first category, denoted “EBEB”, contains pairs for which both candidates lie in the barrel. For the second category, denoted “EBEE”, one candidate lies in the barrel and the other in an endcap. The invariant mass  $m_{\gamma\gamma}$  of the pair must satisfy  $m_{\gamma\gamma} > 230 \text{ GeV}$  for EBEB candidates and  $m_{\gamma\gamma} > 330 \text{ GeV}$  for EBEE candidates. The fraction of events in which more than one photon pair satisfies the selection criteria is approximately 1%. In these cases, only the pair with the largest scalar sum of photon  $p_T$  is retained.

The selection efficiency for signal events varies between 50 and 70%, depending on the signal hypothesis. Because of the different angular distribution of the decay products, the kinematic acceptance for the RS graviton resonances is lower than for scalar resonances. For  $m_X < 1 \text{ TeV}$  the difference is approximately 20%. The two acceptances are similar for  $m_X > 3 \text{ TeV}$ .

The event selection procedure described above was finalized on the basis of studies with simulated signal and background event samples prior to inspection of the data in the search region of the diphoton invariant mass distribution, which is defined as  $m_{\gamma\gamma} > 500 \text{ GeV}$ .

A total of 6284 (2791) photon pairs are selected in the EBEB (EBEE) category. Of these, 461 (800) pairs have an invariant mass above 500 GeV. According to simulation, the direct production of two photons accounts, respectively, for 90 and 80% of the background events selected in the EBEB and EBEE categories. This prediction is tested in data using the method described in Ref. [76].

The diphoton invariant mass distribution of the selected events is shown in Fig. A.1, for both the EBEB and EBEE categories. We perform an independent maximum likelihood fit to the data in each category using the function

$$f(m_{\gamma\gamma}) = m_{\gamma\gamma}^{a+b \log(m_{\gamma\gamma})}. \quad (\text{A.1})$$

This parametric form is chosen to model the background in the hypothesis tests discussed below. The results of the fits are shown in Fig. A.1.

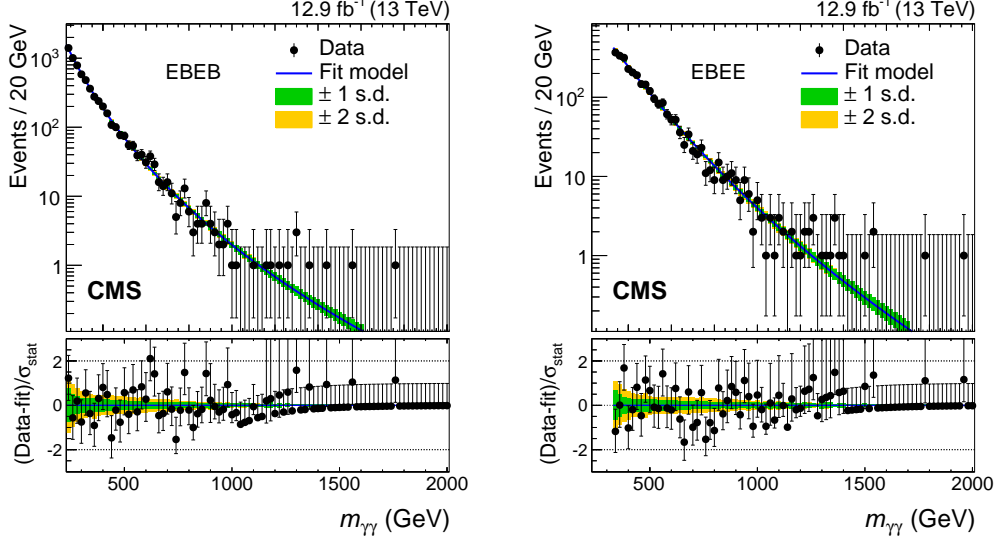


Figure A.1: The observed invariant mass spectra  $m_{\gamma\gamma}$  for selected events in the (left) EBEB and (right) EBEE categories. There are no selected events with  $m_{\gamma\gamma} > 2000$  GeV. The solid lines and the shaded bands show the results of likelihood fits to the data together with the associated 1 and 2 standard deviation uncertainty bands. The ratio of the difference between the data and the fit to the statistical uncertainty in the data is given in the lower plots.

### A.5 Likelihood fit

A simultaneous fit to the invariant mass spectra of events in the EBEB and EBEE event categories is performed to determine the compatibility of the data with the background-only and the signal+background hypotheses. The test statistic is based on the profile likelihood ratio:

$$q(\mu) = -2 \log \frac{L(\mu S + B | \hat{\vec{\theta}}_\mu)}{L(\hat{\mu} S + B | \hat{\vec{\theta}})}, \quad (\text{A.2})$$

where  $S$  and  $B$  represent the probability density functions for resonant diphoton production and for the SM background, respectively. The parameter  $\mu$  is the so-called signal strength, while  $\vec{\theta}$  represents the nuisance parameters of the model, used to account for systematic uncertainties. The  $\hat{x}$  notation indicates the best fit value of the parameter  $x$  for any  $y$  value, while  $\hat{x}_y$  denotes the best fit value of  $x$  for a fixed value  $y$ .

To set upper limits on the rate of resonant diphoton production, the modified frequentist method known as  $\text{CL}_s$  [144, 194] is used, following the prescription described in Ref. [174]. The compatibility of the observation with the background-only hypothesis is evaluated by computing the background-only  $p$ -value. The latter is defined

as the probability, in the background-only hypothesis, for  $q(0)$  to exceed the value observed in data. This quantity, the “local  $p$ -value”  $p_0$ , does not take into account the fact that many signal hypotheses are tested.

Asymptotic formulas [105] are used in the calculations of exclusion limits and local  $p$ -values. The accuracy of the asymptotic approximation in the estimation of exclusion limits and significance is studied, using pseudo-experiments, for a subset of the hypothesis tests and is found to be about 10%.

The signal shape in  $m_{\gamma\gamma}$  is determined from the convolution of the intrinsic shape of the resonance and the CMS detector response to photons. The intrinsic shape is taken from the PYTHIA 8.2 generator. A grid of mass points with 125 GeV spacing, in the range 500–4500 GeV, is used. The resulting shapes are interpolated to intermediate points using a parametric description of the distribution. The detector response is determined using fully simulated signal samples of small intrinsic width, corrected through Gaussian smearing to agree with measurements based on  $Z \rightarrow e^+e^-$  data. Nine uniformly spaced mass hypotheses in the range 500–4500 GeV are employed. The signal mass resolution, quantified through the ratio of the full width at half maximum of the distribution, divided by 2.35, to the peak position, is approximately 1.0 and 1.5% for the EBEB and EBEE categories, respectively. The signal normalization coefficients are proportional to the product of the kinematic acceptance and the signal efficiency within the acceptance region. These are computed, for each category, in simulated samples and interpolated to intermediate points using quadratic functions of  $m_X$  and  $\Gamma_X/m_X$ .

The background shape in  $m_{\gamma\gamma}$  is described by the parametric function given by Eq. (A.1). The values of the parameters  $a$  and  $b$  are determined in the fit to data, with separate values for the EBEB and EBEE categories, and are treated as unconstrained nuisance parameters in the hypothesis tests.

The accuracy of the background parameterization is assessed using simulation and is quantified by studying the difference between the true and predicted numbers of background events in several  $m_{\gamma\gamma}$  intervals in the search region. The relative widths of the intervals, defined by  $2(x_1 - x_2)/(x_1 + x_2)$  with  $x_1$  and  $x_2$  the lower and upper bin edges, range between 2 and 15%. Pseudo-experiments are drawn from the mass spectrum predicted by the simulation and are fit with the chosen background model. The total number of events in each pseudo-experiment is taken from a Poisson distribution whose mean is set equal to the observation in data. For each interval, the distribution of the pull variable, defined as the difference between the

true and predicted numbers of events divided by the estimated statistical uncertainty, is constructed. If the absolute value of the median of this distribution is found to be above 0.5 in an interval, an additional uncertainty is assigned to the background parametrization. A modified pull distribution is then constructed, increasing the statistical uncertainty in the fit by an extra term, denoted the “bias term”. The bias term is parametrized as a smooth function of  $m_{\gamma\gamma}$ , which is tuned in such a manner that the absolute value of the median of the modified pull distribution is less than 0.5 in all intervals. The amplitude of the bias term function is comparable to that of the 1 standard deviation bands in Fig. A.1. This additional uncertainty is included in the likelihood function by adding to the background model a component having the same shape as the signal. The normalization coefficient of this component is constrained to have a Gaussian distribution of mean zero, with a width equal to the integral of the bias term function over the full width at half maximum of the tested signal shape. The inclusion of this additional component has the effect of avoiding falsely positive or falsely negative tests that could be induced by a mismodeling of the background shape, and it reduces the sensitivity of the analysis by at most 10%.

### A.6 Systematic uncertainties

The impact of systematic uncertainties in this analysis is smaller than that of the statistical uncertainties. The parametric background model has no associated systematic uncertainties except for the bias term uncertainty described in the previous section. Since the background shape coefficients  $a$  and  $b$  [Eq. (A.1)] are treated as unconstrained nuisance parameters, the associated uncertainties are statistical in nature.

The systematic uncertainties in the signal normalization associated with the integrated luminosity, the selection efficiency, and the PDFs are 6.2, 6.0, and 6.0%, respectively. The uncertainty in the integrated luminosity is estimated from beam scans performed in August 2016, utilizing the methods of Ref. [103]. The uncertainty associated with the PDFs is evaluated by comparing the overall selection efficiency obtained with the CT10 [172], MSTW08 [176], and NNPDF2.3 [49] PDF sets and taking the largest deviation over all tested signal hypotheses. A 1% uncertainty is associated with the level of knowledge of the energy scale and accounts for the uncertainty in the energy scale at the Z boson peak and its extrapolation to higher masses. A 10% uncertainty is assigned to the knowledge of the photon energy resolution, corresponding to the uncertainty in the estimated additional Gaussian smearing determined at the Z boson peak.

### A.7 Results for the 2016 data

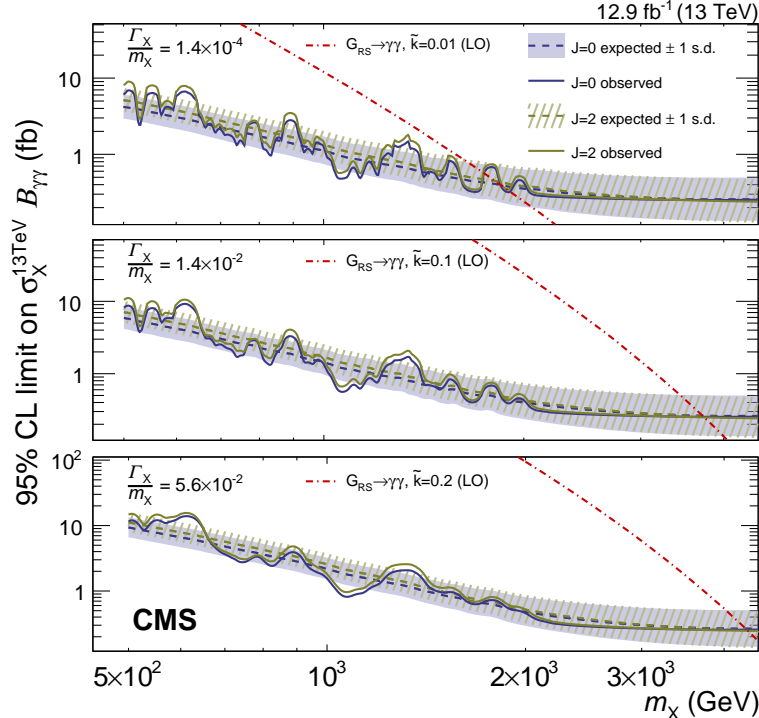


Figure A.2: The 95% CL upper limits on the production of diphoton resonances as a function of the resonance mass  $m_X$ , from the analysis of data collected in 2016. Exclusion limits for the scalar and RS graviton signals are given by the grey (darker) and green (lighter) curves, respectively. The observed limits are shown by the solid lines, while the median expected limits are given by the dashed lines together with their associated 1 standard deviation uncertainty bands. The leading-order production cross section for diphoton resonances in the RS graviton model is shown for three values of the dimensionless coupling parameter  $\tilde{k}$  together with the exclusion upper limits calculated for the corresponding three values of the width relative to the mass,  $\Gamma_X/m_X$ . Shown are the results for (upper) a narrow width, (middle) an intermediate-width, and (lower) a broad resonance.

The observed and expected 95% confidence level (CL) upper limits on the product of the production cross section ( $\sigma_X^{13\text{TeV}}$ ) and branching fraction to two photons ( $B_{\gamma\gamma}$ ) for scalar and RS graviton resonances are shown in Fig. A.2. Using the LO cross sections from PYTHIA 8.2, RS gravitons with masses below 1.75, 3.75, and 4.35 TeV are excluded for  $\tilde{k} = 0.01$ , 0.1, and 0.2, respectively, corresponding to  $\Gamma_X/m_X = 1.4 \times 10^{-4}$ ,  $1.4 \times 10^{-2}$ , and  $5.6 \times 10^{-2}$ .

The value of  $p_0$  for different signal hypotheses is shown in Fig. A.3. The largest excess is observed for  $m_X \approx 620$  GeV, and has a local significance of approximately

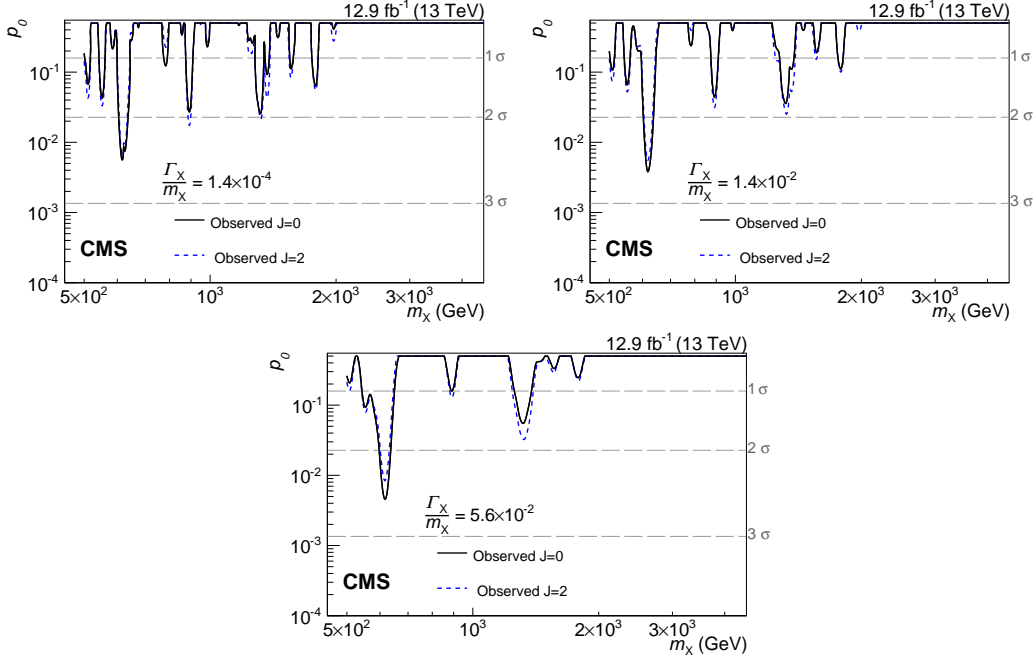


Figure A.3: Observed background-only  $p$ -values for resonances with (upper left)  $\Gamma_X/m_X = 1.4 \times 10^{-4}$ , (upper right)  $1.4 \times 10^{-2}$ , and (bottom)  $5.6 \times 10^{-2}$  as a function of the resonance mass  $m_X$ , from the analysis of data collected in 2016. The solid black and dashed blue lines correspond to spin-0 and spin-2 resonances, respectively.

2.4 and 2.7 standard deviations for narrow spin-0 and RS graviton signal hypotheses, respectively. After taking into account the effect of searching for several signal hypotheses, i.e., searching over a range of widths and masses, the significance of the excess is reduced to less than one standard deviation. No excess is observed in the proximity of  $m_X = 750$  GeV.

### A.8 Combination with the 2012 and 2015 data

The results obtained for the 2016 data are combined statistically with those obtained for the data discussed in Ref. [161], namely  $19.7\text{ fb}^{-1}$  of proton-proton collisions recorded at  $\sqrt{s} = 8\text{ TeV}$  in 2012 [146] and  $3.3\text{ fb}^{-1}$  recorded at  $\sqrt{s} = 13\text{ TeV}$  in 2015. For a portion of the 2015 data ( $0.6\text{ fb}^{-1}$ ), the CMS magnet was off (0 T), while for the rest of the 2015 data and for all of the 2012 and 2016 data, the magnet was at its operational field strength (3.8 T). The analysis of the 0 T data from 2015 is described in Ref. [161].

The procedure followed for the combined analysis of 8 and 13 TeV data is the same as in Ref. [161]. The ratio of the 8 to the 13 TeV production cross section

is computed using `PYTHIA` 8.2, for the two types of signal hypotheses considered: scalar resonances and RS graviton resonances. The cross section ratio decreases from 0.27 and 0.29 at  $m_X = 500 \text{ GeV}$  to 0.03 and 0.04 at  $m_X = 4 \text{ TeV}$ , for the scalar and RS graviton resonance hypotheses, respectively.

Exclusion limits are set on the 13 TeV production cross section for both models, and background-only  $p$ -values are computed for the signal hypotheses.

The correlation model between the systematic uncertainties associated with 8 and 13 TeV data is described in Ref. [161]. It assumes all uncertainties to be uncorrelated except for those related to the knowledge of the photon energy scale, which are taken to have a linear correlation of 0.5, and those related to the knowledge of the PDFs, which are taken to be fully correlated. For the combination of the two 13 TeV data sets, the background shape and the associated bias term uncertainties are assumed to be fully correlated between the corresponding categories of the 2015 (3.8 T) and 2016 data. Independent background normalization coefficients are used for the two data sets. The uncertainty in the signal selection efficiency is taken to be uncorrelated between the 2015 and 2016 data. The uncertainty in the knowledge of the integrated luminosity is treated as follows: a 2.3% uncertainty, corresponding to the knowledge of the absolute luminosity scale calibration determined with beam scans, is taken to be fully correlated between the 2015 (3.8 T) and 2016 data, and additional uncertainties of 1.5 and 5.8%, corresponding to the uncertainty in extrapolating the scale calibration to the data collection conditions, are applied, again respectively. Finally, the photon energy scale uncertainties are taken to be fully correlated between the two data sets.

Figure A.4 shows the observed and expected 95% CL upper limits on the 13 TeV production cross section of the different signal hypotheses obtained with the combined analysis of the 13 TeV data recorded in 2015 and 2016. The upper limits on the production of scalar resonances decaying to two photons range from about 10 to 0.2 fb, for resonance masses between 0.5 and 4.5 TeV. Compared to the 2016 data alone, the sensitivity is improved by approximately 10 and 20% at the high and low end of the  $m_X$  search region, respectively. Using the LO cross sections from `PYTHIA` 8.2, RS gravitons with masses below 3.85 and 4.45 TeV are excluded for  $\tilde{k} = 0.1$  and 0.2, respectively. For  $\tilde{k} = 0.01$ , graviton masses below 1.95 TeV are excluded, except for the region between 1.75 and 1.85 TeV.

The observed  $p_0$  for  $\Gamma_X/m_X = 1.4 \times 10^{-4}$  and  $5.6 \times 10^{-2}$  obtained with the combined analysis of the 2015 and 2016 data is shown in Fig. A.5. The largest excess is

observed for  $m_X \approx 1.3$  TeV and has a local significance of about 2.2 standard deviations, corresponding to less than 1 standard deviation after accounting for the effect of searching for several signal hypotheses. For  $m_X = 750$  GeV, the 2.9 standard deviation local significance excess observed in the 2015 data is reduced to 0.8 standard deviations.

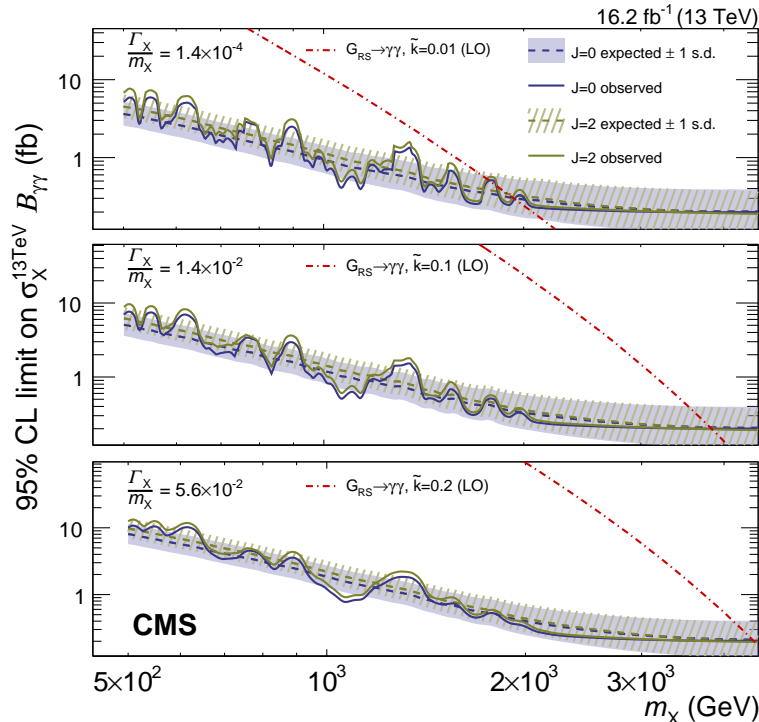


Figure A.4: The 95% CL upper limits on the production of diphoton resonances as a function of the resonance mass  $m_X$ , from the combined analysis of data collected in 2015 and in 2016. Exclusion limits for the scalar and RS graviton signals are given by the grey (darker) and green (lighter) curves, respectively. The observed limits are shown by the solid lines, while the median expected limits are given by the dashed lines together with their associated 1 standard deviation uncertainty bands. The leading-order production cross section for diphoton resonances in the RS graviton model is shown for three values of the dimensionless coupling parameter  $\tilde{k}$  together with the exclusion upper limits calculated for the corresponding three values of the width relative to the mass,  $\Gamma_X/m_X$ . Shown are the results for (upper) a narrow width, (middle) an intermediate-width, and (lower) a broad resonance.

The observed and expected 95% CL upper limits on the 13 TeV signal production cross sections obtained through a combined analysis of the 8 TeV data from 2012 and the 13 TeV data from 2015 and 2016 are shown in Fig. A.6. Compared to the combined 13 TeV data, the analysis sensitivity improves by about 10% at the low

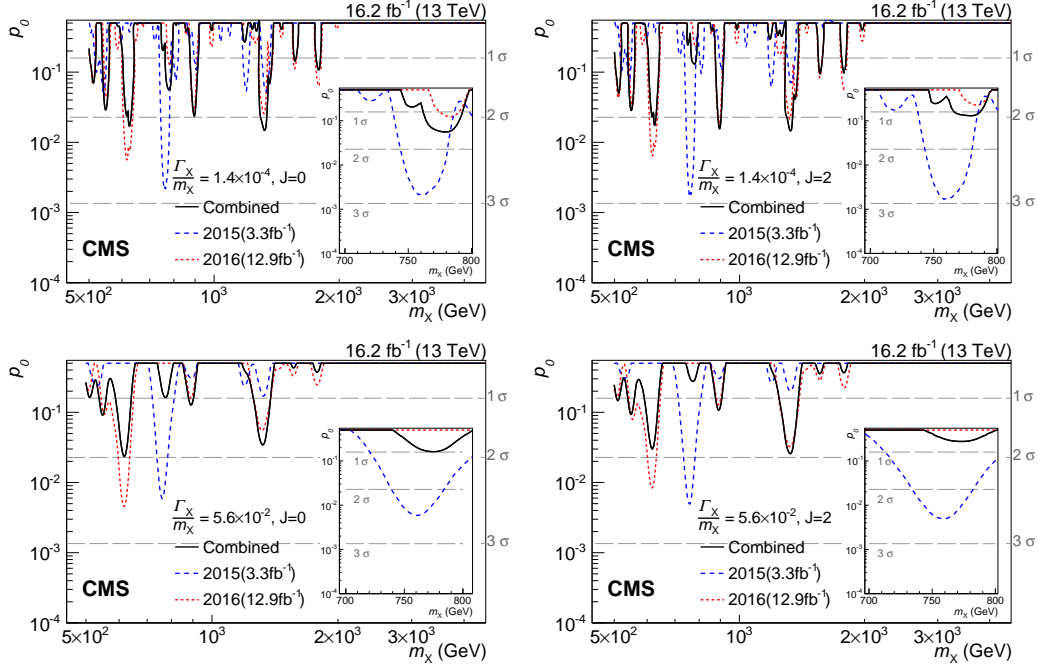


Figure A.5: Observed background-only  $p$ -values for resonances with (upper)  $\Gamma_X/m_X = 1.4 \times 10^{-4}$  and (lower)  $5.6 \times 10^{-2}$  as a function of the resonance mass  $m_X$ , from the combined analysis of data recorded in 2015 and 2016. The results obtained for the two individual data sets are also shown. The curves corresponding to the scalar and RS graviton hypotheses are shown in left and right columns, respectively. The insets show an expanded region around  $m_X = 750$  GeV.

end of the  $m_X$  range, while the improvement is negligible at the higher end of the range. Thus the lower limits on the mass of RS gravitons obtained by combining the 8 and 13 TeV data coincide with those obtained with the 13 TeV data alone.

The observed  $p_0$  for  $\Gamma_X/m_X = 1.4 \times 10^{-4}$  and  $5.6 \times 10^{-2}$  obtained with the combined 8 and 13 TeV analysis is shown in Fig. A.7. The largest excess, observed for  $m_X \approx 0.9$  TeV, has a local significance of about 2.2 standard deviations, corresponding to less than 1 standard deviation overall. For  $m_X = 750$  GeV, the 3.4 standard deviation local significance excess reported in Ref. [161] is reduced to about 1.9 standard deviations.

### A.9 Summary

A search for the resonant production of high-mass photon pairs has been presented. The analysis is based on a sample of proton-proton collisions collected by the CMS experiment in 2016 at  $\sqrt{s} = 13$  TeV, corresponding to an integrated luminosity of  $12.9 \text{ fb}^{-1}$ . Events containing two photon candidates with transverse momenta

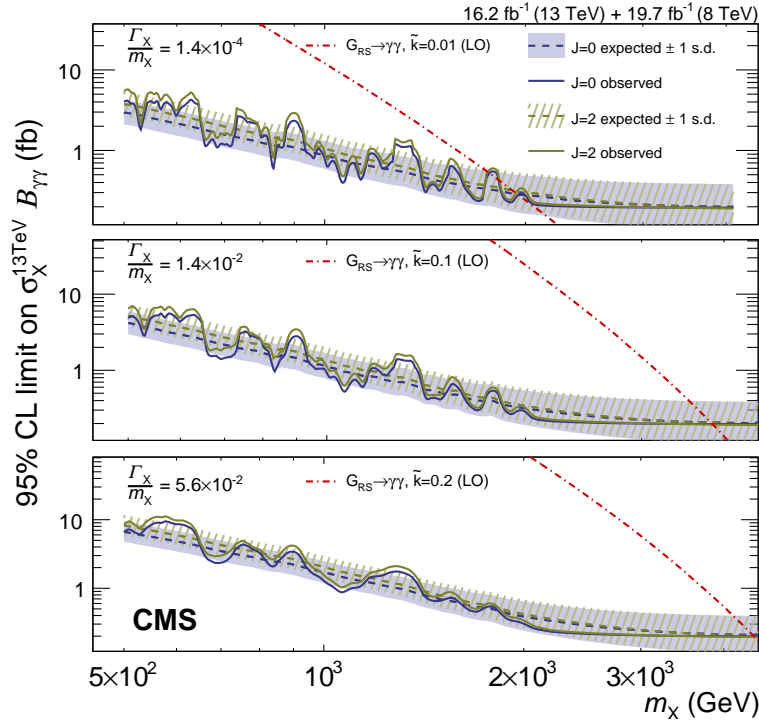


Figure A.6: The 95% CL upper limits on the production of diphoton resonances as a function of the resonance mass  $m_X$ , from the combined analysis of the 8 and 13 TeV data. The 8 TeV results are scaled by the ratio of the 8 to 13 TeV cross sections. Exclusion limits for the scalar and RS graviton signals are given by the grey (darker) and green (lighter) curves, respectively. The observed limits are shown by the solid lines, while the median expected limits are given by the dashed lines together with their associated 1 standard deviation uncertainty bands. The leading-order production cross section for diphoton resonances in the RS graviton model is shown for three values of the dimensionless coupling parameter  $\tilde{k}$  together with the exclusion upper limits calculated for the corresponding three values of the width relative to the mass,  $\Gamma_X/m_X$ . Shown are the results for (upper) a narrow width, (middle) an intermediate-width, and (lower) a broad resonance.

above 75 GeV are selected. The diphoton mass spectrum above 500 GeV is examined for evidence of the production of high-mass spin-0 and spin-2 resonances.

Limits on the production of scalar resonances and Randall–Sundrum gravitons in the range  $0.5 < m_X < 4.5$  TeV and  $1.4 \times 10^{-4} < \Gamma_X/m_X < 5.6 \times 10^{-2}$  are determined using the modified frequentist approach, where  $m_X$  and  $\Gamma_X$  are the resonance mass and width, respectively. The results obtained with the 2016 data set are combined statistically with those obtained in 2012 and 2015, corresponding to integrated luminosities of  $19.7$  and  $3.3$   $\text{fb}^{-1}$  of data recorded at  $\sqrt{s} = 8$  and 13 TeV, respectively.

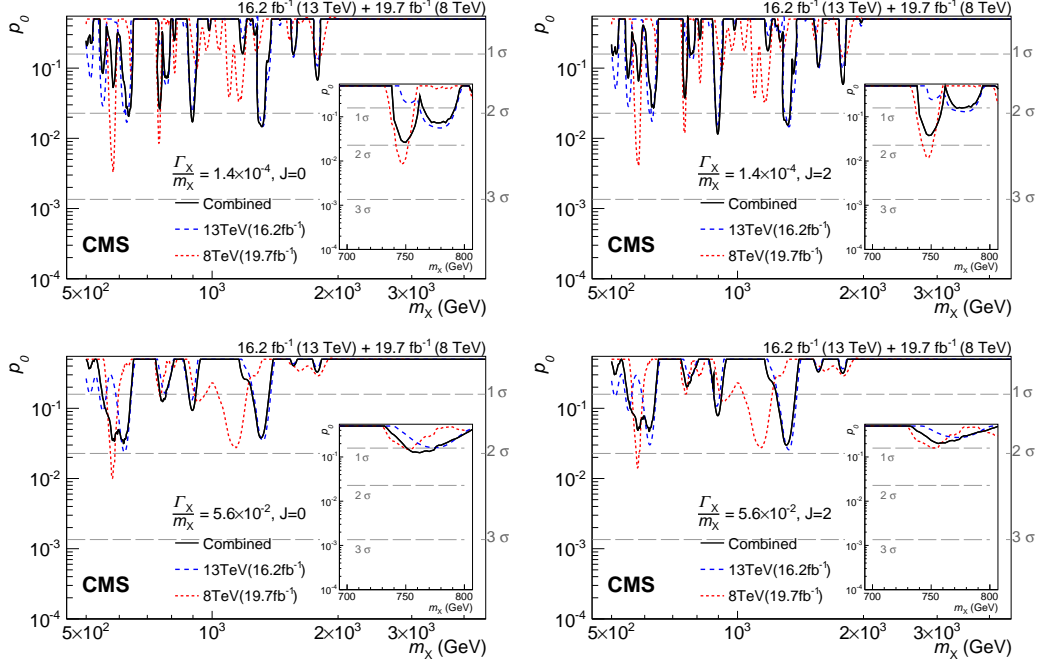


Figure A.7: Observed background-only  $p$ -values for resonances with (upper)  $\Gamma_X/m_X = 1.4 \times 10^{-4}$  and (lower)  $5.6 \times 10^{-2}$  as a function of the resonance mass  $m_X$ , from the combined analysis of the 8 and 13 TeV data. The results obtained for the two individual center-of-mass energies are also shown. The curves corresponding to the scalar and RS graviton hypotheses are shown in left and right columns, respectively. The insets show an expanded region around  $m_X = 750$  GeV.

No significant excess is observed above the predictions of the standard model. Using the leading-order cross sections, Randall–Sundrum gravitons with masses below 3.85 and 4.45 TeV are excluded for values of the dimensionless coupling parameter  $\tilde{k} = 0.1$  and 0.2, respectively. For  $\tilde{k} = 0.01$ , graviton masses below 1.95 TeV are excluded, except for the region between 1.75 and 1.85 TeV. These are the most stringent limits on Randall–Sundrum graviton production to date.

## A p p e n d i x   B

# PHENOMENOLOGY OF ANAMALOUS HIGGS PRODUCTION IN SUPERSYMMETRIC MODELS

### B.1 Introduction

The ATLAS and CMS collaborations intensively searched for SUSY production in the data collected at a center-of-mass energy  $\sqrt{s} = 8 \text{ TeV}$  in 2012. A large part of the searches focused on SUSY models with conserved R-parity, for which the lightest SUSY particle (LSP) is stable. The LHC is particularly sensitive to the production of SUSY partners charged under QCD (squarks and gluinos), given the large production cross section in proton collisions. Given the strong bounds on generic SUSY models derived with  $\sqrt{s} = 7 \text{ TeV}$  data, ATLAS and CMS moved the focus of their SUSY searches to the so-called *natural* SUSY models [183]. In its minimal realization, a natural SUSY spectrum is composed of the minimum set of SUSY partners needed to protect the mass of the Higgs (H) boson from quantum corrections: a gluino, one bottom squark, two top squarks, and three higgsinos (two neutral and one charged). This SUSY scenario results in events with multiple top and bottom quarks, produced in association with missing transverse energy  $E_T^{\text{miss}}$ . No evidence for the production of such particles was found, pushing the allowed mass range for gluinos and top squarks above  $\sim 1600 \text{ GeV}$  and  $\sim 700 \text{ GeV}$ , respectively, for a low-mass neutralino LSP and largely independent of the top squark and gluino branching ratios (see for instance Ref. [162, 142]).

In a few cases, a data yield above the expected background was observed for certain signal regions, for example, in the case of the *edge* dilepton analysis by CMS [204] and the SUSY search in Z+jets events by ATLAS [25]. These excesses correspond to, respectively,  $\sim 2.4\sigma$  and  $\sim 3.0\sigma$  of local significance, which are reduced after accounting for the look-elsewhere effect (LEE). Several interpretations of these results were given in the literature [139, 36, 37, 71, 115, 165], mainly related to the electroweak production of SUSY particles with long decay chains.

Here we discuss another interesting excess, observed in a search for electroweak SUSY partners in  $H(\gamma\gamma)+ \geq 1 \text{ jet}$  events by the CMS collaboration performed at 8 TeV [208]. The analysis uses the diphoton invariant mass  $m_{\gamma\gamma}$  to select events with a H-like candidate. The nonresonant (mostly QCD diphoton production) and

resonant (standard model  $H(\gamma\gamma)$  production) backgrounds are estimated using the  $m_{\gamma\gamma}$  sidebands in data and the Monte Carlo simulation, respectively. The background prediction is performed as a function of the razor variables  $M_R$  and  $R^2$  in five mutually exclusive *boxes*, targeting different final states: high- $p_T$   $H(\gamma\gamma)$  (HighPt box),  $H(\gamma\gamma) + H(b\bar{b})$  (Hbb box),  $H(\gamma\gamma) + Z(b\bar{b})$  (Zbb box), and low- $p_T$   $H(\gamma\gamma)$  with high- and low-resolution photons (HighRes and LowRes boxes, respectively). Five events are observed in one ( $M_R, R^2$ ) bin of the HighRes box, compared to less than one expected background event. This corresponds to a local significance of  $2.9\sigma$ , reduced to  $1.6\sigma$  after the LEE.

In this paper, we discuss a possible interpretation of this search in terms of SUSY models with light quarks. We emulate this CMS analysis to derive bounds on squark production. Since the analysis does not require or veto jets originating from b-quarks (b-jets), the results apply to bottom-squark production in natural SUSY models.

Recently, an updated search was performed with data collected at 13 TeV [206], which exhibits a similar excess of  $2.5\sigma$  local significance, reduced to  $1.4\sigma$  after the LEE. Model B proposed in this paper was also used for the interpretation of the results.

## B.2 Benchmark signal models

We consider two simplified models with bottom squark pair production, both resulting in a  $H+jets$  final state.

In the first model, hereafter referred to as model A, we consider the asymmetric production of a  $\tilde{b}_2\tilde{b}_1$  pair, where  $\tilde{b}_2$  and  $\tilde{b}_1$  are the heaviest and the lightest bottom squarks, respectively. The  $\tilde{b}_2$  decays to  $b\tilde{\chi}_2^0$ , with  $\tilde{\chi}_2^0 \rightarrow H\tilde{\chi}_1^0$ . The lightest neutralino  $\tilde{\chi}_1^0$  is assumed to be the LSP. The  $\tilde{b}_1$ , close in mass to the LSP, decays to  $b\tilde{\chi}_1^0$ . All the other SUSY partners are assumed to be too heavy to be produced at the LHC and are ignored in this analysis. This model represents a new mechanism for the production of  $H + 2b$ -jets + invisible, with one of the associated b-jets typically having low momentum.

In the second model, hereafter referred to as model B [220], two bottom squarks  $\tilde{b}_1\tilde{b}_1$  are produced, each decaying as  $\tilde{b}_1 \rightarrow b\tilde{\chi}_2^0$ . The  $\tilde{\chi}_2^0$  then decays to  $H\tilde{\chi}_1^0$ , the  $\tilde{\chi}_1^0$  being the LSP. As for model A, the other SUSY partners are ignored. This simplified model corresponds to a final state consisting of  $2H + 2b$ -jets + invisible.

The mass spectrum for each model is shown in Fig. B.1. We fix the  $\tilde{\chi}_2^0$  and  $\tilde{\chi}_1^0$  masses to 230 GeV and 100 GeV, respectively. In model A, we fix the  $\tilde{b}_1$  mass to

130 GeV as varying its mass in between the limits of the  $\tilde{\chi}_1^0$  and  $\tilde{\chi}_2^0$  masses has little effect. Finally, we scan the  $\tilde{b}_2$  ( $\tilde{b}_1$ ) mass between 250 GeV and 800 GeV for model A (B). These assumptions do not limit the conclusions derived on the squark production cross section. In fact, the analysis is sensitive to mass differences and not to the absolute mass of SUSY partners. On the other hand, the chosen LSP and NLSP masses does play a role when the cross section limits are translated in terms of mass exclusion bounds.

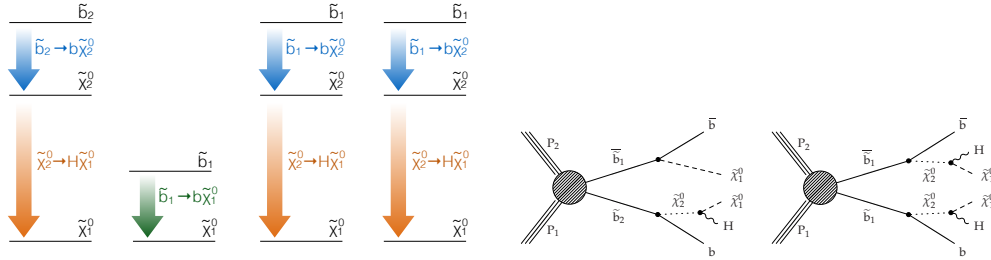


Figure B.1: Pictorial representation of the decay chains and event topologies associated with model A (left) and model B (right), as described in the text.

### B.3 Event generation and detector simulation

The study is performed using samples of Monte Carlo events. The event generation is performed in PYTHIA 8.210 [210, 212]. The default parton density function set is NNPDF 2.3 QCD+QED LO (with  $\alpha_s(m_Z) = 0.130$ ) [51, 74, 73]. Fast simulation of the CMS detector is performed in DELPHES 3.3.2 [117]. The default description of CMS as provided in the release is used, except for a modification to the photon isolation and efficiency, described in the next section. Jet clustering is performed using FASTJET 3.1.3 [69]. As in CMS, the anti- $k_T$  jet clustering algorithm is used with jet-size parameter  $R = 0.5$  [70].

### B.4 Emulation of the CMS search

The emulated event selection is summarized as follows,

- Events with two isolated photons with  $p_T > 25$  GeV and  $|\eta| < 1.44$  are selected. As in Ref. [157], the photon isolation variables,  $I_\gamma$ ,  $I_n$ , and  $I_\pi$ , are computed by summing the transverse momenta of photons, neutral hadrons, and charged hadrons, respectively, inside an isolation cone of radius  $\Delta R = 0.3$  around the selected photon. The photon isolation requirements on these variables are shown in Tab B.1. An additional photon selection efficiency

Table B.1: Photon isolation requirements, as in Ref [157]. The photon isolation variables,  $I_\gamma$ ,  $I_n$ , and  $I_\pi$ , are computed by summing the transverse momenta of photons, neutral hadrons, and charged hadrons, respectively, inside an isolation cone of radius  $\Delta R = 0.3$  around the selected photon.

$I_\gamma$	barrel	$1.3 \text{ GeV} + 0.005 p_T^\gamma$
	endcap	—
$I_n$	barrel	$3.5 \text{ GeV} + 0.04 p_T^\gamma$
	endcap	$2.9 \text{ GeV} + 0.04 p_T^\gamma$
$I_\pi$	barrel	$2.6 \text{ GeV}$
	endcap	$2.3 \text{ GeV}$

is applied in **DELPHES** such that isolated photons with  $p_T < 10 \text{ GeV}$  ( $p_T \geq 10 \text{ GeV}$ ) are randomly selected with 94% (98%) efficiency.

- Events with one H candidate with  $p_T > 20 \text{ GeV}$  are selected. A pair of selected photons is considered an H candidate if at least one photon has  $p_T > 40 \text{ GeV}$  and the diphoton mass  $m_{\gamma\gamma} > 100 \text{ GeV}$ . If the event contains more than one H candidate, the one with the highest scalar sum  $p_T$  of the two photons is selected.
- Jets are reconstructed using the **FASTJET** [69] implementation of the anti- $k_T$  [70] algorithm with jet radius parameter  $R = 0.5$ .
- Events with at least one jet with  $p_T > 30 \text{ GeV}$  and  $|\eta| < 3.0$  are selected.
- An emulation of the “medium” requirement (mistag probability of 1% and b-tag efficiency of  $\sim 68\%$ ) of the combined secondary vertex (CSV) b-tagging algorithm is used to identify b-jets [185].
- A  $b\bar{b}$  candidate pair is identified if both jets satisfy the medium requirement of the b-tagging algorithm (note: the CMS analysis requires only one to satisfy the medium requirement, while both are required to satisfy the loose requirement).
- The  $b\bar{b}$  candidate pair with the mass closest to  $125 \text{ GeV}$  or  $91.2 \text{ GeV}$  is chosen as the  $H \rightarrow b\bar{b}$  or  $Z \rightarrow b\bar{b}$  candidate, respectively.
- The razor variable  $M_R$ , calculated from two megajets [94] is required to be greater than  $150 \text{ GeV}$ . All possible combinations of the reconstructed jets and the  $H(\gamma\gamma)$  candidate are clustered to form megajets. The pair of megajets that

minimizes the sum in quadrature of the invariant masses of the two megajets is selected.

After this baseline selection, events are categorized according to the following requirements,

- **HighPt**: all events with an  $H \rightarrow \gamma\gamma$  candidate with  $p_T > 110$  GeV.
- **Hbb**: remaining events with a  $H \rightarrow b\bar{b}$  candidate with mass  $110 \geq m_{b\bar{b}} \geq 140$  GeV.
- **Zbb**: remaining events with a  $Z \rightarrow b\bar{b}$  candidate with mass  $76 \geq m_{b\bar{b}} \geq 106$  GeV.
- **HighRes**: 70% of remaining events after the Zbb selection (emulating the efficiency of the “high-resolution photon” selection).
- **LowRes**: all remaining events.

We assume the breakdown of events between the **HighRes** box and **LowRes** box is 70%-to-30% after the Zbb selection. This is based on the following observations: (i) CMS categorizes events in the **HighRes** box if both photons in the event satisfy  $\sigma_E/E < 0.015$ , where  $\sigma_E/E$  is the estimated relative energy resolution, and categorizes events in the **LowRes** box otherwise, (ii) CMS observes a similar 70%-to-30% breakdown for both SM Higgs production and electroweak SUSY processes in Monte Carlo simulation [208], and (iii) we expect this breakdown to be model-independent assuming both photons are real and come from the decay of a Higgs boson, as it is based on the properties of such photons detected in CMS and not on the details of the model.

Finally, the search region selection is as follows,

- The search region in the  $m_{\gamma\gamma}$  distribution is defined by  $(125 - 2\sigma_{\text{eff}}, 126 + 2\sigma_{\text{eff}})$  in each event category, where  $\sigma_{\text{eff}}$  is defined such that  $\sim 68\%$  of Higgs boson events fall in an interval of  $\pm\sigma_{\text{eff}}$  around the nominal  $m_H$  value. Following this procedure using our generated and simulated signal samples, we derive  $\sigma_{\text{eff}}$  to be 3.8 GeV in the **HighPt** box and 2.2 GeV in the **HighRes** and **LowRes** boxes. For the **Hbb** and **Zbb** boxes, due to the low number of selected signal events, we use the overall average value of 2.8 GeV.

We note that these  $\sigma_{\text{eff}}$  values are larger than the corresponding ones in Ref. [208]. This is due to the larger width observed for the diphoton mass distribution in Higgs boson events simulated and reconstructed with **DELPHES**, compared to official CMS software. This implies the effective diphoton mass resolution when using **DELPHES** is larger than in the real CMS detector. We attempt to account for this with a modification explained in Sec. B.6.

## B.5 Bayesian Statistical Interpretation

We model the likelihood according to a Poisson density, considering the expected background yield (with associated uncertainty), the expected signal yield (for a given signal cross section), and the observed yield. The background uncertainty is modeled with a gamma density. The background yields and the corresponding uncertainties are taken from the tables provided in Ref. [208]. To take into account systematic uncertainties on the signal, we assign a 30% uncertainty (assuming a log-normal density) on the signal strength, a multiplicative factor modifying the signal cross section. We then derive the posterior density for the signal cross section  $\sigma$  as:

$$p(\sigma|\text{data}) \propto \mathcal{L}(\text{data}|\sigma)p_0(\sigma), \quad (\text{B.1})$$

where  $\mathcal{L}(\text{data}|\sigma)$  is the likelihood and  $p_0(\sigma)$  is the prior density taken to be uniform. The likelihood is then

$$\begin{aligned} \mathcal{L}(\text{data}|\sigma) &= \int_0^\infty d\mu \ln(\mu|\bar{\mu}, \delta\mu) \\ &\times \prod_{i=0}^{n_{\text{bins}}} \int_0^\infty db_i \text{Poisson}(n_i|L\mu\sigma\epsilon_i + b_i) \\ &\times \Gamma(b_i|\bar{b}_i, \delta b_i), \end{aligned} \quad (\text{B.2})$$

where the product runs over the number of bins  $n_{\text{bins}}$ ;  $n_i$  is the observed yield in the  $i^{\text{th}}$  bin,  $L$  is the integrated luminosity,  $b_i$  is the assumed value of the background yield in the  $i^{\text{th}}$  bin and  $\bar{b}_i \pm \delta b_i$  is its expected value and the associated uncertainty;  $\epsilon_i$  is the nominal value of the signal efficiency times acceptance in the  $i^{\text{th}}$  bin;  $\mu$  is the signal strength, a nuisance parameter modifying the signal cross section (nominally equal to  $\bar{\mu} = 1$  with a  $\delta\mu = 30\%$  uncertainty);  $\ln(x|m, \delta)$  is the log-normal distribution for  $x$ , parameterized such that  $\log(m)$  is the mean and  $\log(1 + m\delta)$  is the standard deviation of the log of the distribution;  $\Gamma(x|m, \delta)$  is the gamma distribution for  $x$ , parameterized such that  $m$  is the mode and  $\delta^2$  is the variance of the distribution. The 95% credibility level (CL) upper limit on the signal cross section  $\sigma_{\text{up}}$  is obtained

from the posterior, such that

$$\frac{\int_0^{\sigma_{\text{up}}} d\sigma p(\sigma|\text{data})}{\int_0^\infty d\sigma p(\sigma|\text{data})} = 0.95. \quad (\text{B.4})$$

We also utilize a signal significance measure defined by

$$Z(\sigma) = \text{sign}[\log B_{10}(\text{data}, \sigma)] \sqrt{2|\log B_{10}(\text{data}, \sigma)|}, \quad (\text{B.5})$$

where

$$B_{10}(\text{data}, \sigma) = \frac{\mathcal{L}(\text{data}|\sigma, H_1)}{\mathcal{L}(\text{data}|H_0)} \quad (\text{B.6})$$

is the *local* Bayes factor for the data for a given signal cross section  $\sigma$ , and  $\mathcal{L}(\text{data}|\sigma, H_1)$  and  $\mathcal{L}(\text{data}|H_0)$  are the likelihoods for the signal-plus-background ( $H_1$ ) and background-only ( $H_0$ ) hypotheses, respectively. As described in Ref. [187], this measured is a signed Bayesian analog of the frequentist “n-sigma.” For each signal model with specified masses, we scan the signal cross section  $\sigma$  to find the maximum significance, which occurs at the mode of the posterior.

## B.6 Correction and Validation

As explained above, we find differences in the performance of the emulated CMS detector and the real CMS detector, e.g. the larger diphoton mass resolution. To take into account this and other differences in the detector simulation and reconstruction performed by `DELPHES` and official CMS software, we conservatively double the background uncertainties in each bin reported by CMS in Ref. [208] when evaluating the likelihood in Eqn. B.3. We find this conservative approach better reproduces the observed and expected limits on a benchmark simplified model.

To validate our emulation result, we produced 95% CL limits on the production cross section of an electroweak simplified model of  $\tilde{\chi}_1^\pm \tilde{\chi}_2^0$  production, followed by the decays  $\tilde{\chi}_1^\pm \rightarrow W^\pm \tilde{\chi}_1^0$ ,  $\tilde{\chi}_2^0 \rightarrow H \tilde{\chi}_1^0$ . For this model, CMS provided the 95% confidence level upper limits on the cross section assuming an LSP mass of  $m_{\tilde{\chi}_1^0} = 1 \text{ GeV}$  and equal chargino and second neutralino masses,  $m_{\tilde{\chi}_1^\pm} = m_{\tilde{\chi}_2^0}$ . The comparison between our result and the CMS result for this model is shown in figure B.2 as a function of  $m_{\tilde{\chi}_1^\pm}$ .

## B.7 Results

Figures B.3-B.5 contain the results of the reinterpretation of the CMS data for both models. To show how well signal model A agrees with the excess observed

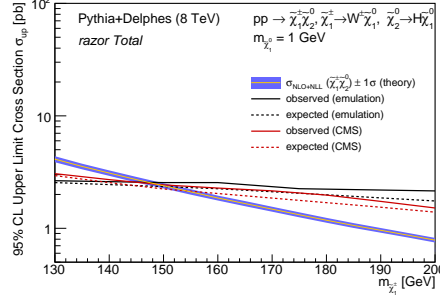


Figure B.2: Comparison between the CMS result (red) and our emulation (black). Note, this scan assumes  $m_{\tilde{\chi}_1^0} = 1 \text{ GeV}$  and  $m_{\tilde{\chi}_1^\pm} = m_{\tilde{\chi}_2^\pm}$ .

by CMS, Fig. B.3 (top) displays the expected SM background distribution and uncertainty taken from the CMS result compared to the distribution of the signal events for  $m_{\tilde{b}_2} = 500 \text{ GeV}$  and  $m_{\tilde{b}_2} = 800 \text{ GeV}$ , with other mass parameters set as  $m_{\tilde{b}_2} = 130 \text{ GeV}$ ,  $m_{\tilde{\chi}_2^0} = 230 \text{ GeV}$ , and  $m_{\tilde{\chi}_1^0} = 100 \text{ GeV}$ . The bin numbers correspond to the order of the signal regions in the yield tables in Ref. [208] and are reproduced in Tab. B.2. The normalization for each signal model is taken from the mode (i.e.

Table B.2: HighRes bin numbering scheme as in Ref. [208].

Bin	$M_R$ range	$R^2$ range
0	[150, 250]	[0.00, 0.05]
1	[150, 250]	[0.05, 0.10]
2	[150, 250]	[0.10, 0.15]
3	[150, 250]	[0.15, 1.00]
4	[250, 400]	[0.00, 0.05]
5	[250, 400]	[0.05, 0.10]
6	[250, 400]	[0.10, 1.00]
7	[400, 1400]	[0.00, 0.05]
8	[400, 1400]	[0.05, 1.00]
9	[1400, 3000]	[0.00, 1.00]

“best-fit”) signal cross section of the posterior density in the HighRes box. Fig. B.4 (top), shows the 95% CL combined upper limit on the cross section for model A. Finally, Fig. B.5 (top) shows the maximum significance  $Z$  as well as the best fit signal cross section for model A as a function of  $m_{\tilde{b}_2}$ .

The bottom of Fig. B.3-B.5 are the analogous results for model B. The chosen model B mass points in Fig. B.3 are  $m_{\tilde{b}_1} = 500 \text{ GeV}$  or  $m_{\tilde{b}_1} = 800 \text{ GeV}$ ,  $m_{\tilde{\chi}_2^0} = 230 \text{ GeV}$ , and  $m_{\tilde{\chi}_1^0} = 100 \text{ GeV}$ . The limit and significance scans in Fig. B.4 and B.5 are performed as a function of the  $\tilde{b}_1$  mass. For model B, we also compare both the

excluded cross section at 95% CL and the best-fit cross section as a function of the  $\tilde{b}_1$  mass to the NLO+NLL predicted cross section at  $\sqrt{s} = 8$  TeV [56, 167, 166, 54, 55, 60]. We find the 8 TeV data excludes bottom squark pair production below  $m_{\tilde{b}_1} = 330$  GeV for the chosen neutralino masses of  $m_{\tilde{\chi}_2^0} = 230$  GeV and  $m_{\tilde{\chi}_1^0} = 100$  GeV. More interestingly, the largest combined significance is  $1.8\sigma$  for  $m_{\tilde{b}_1} = 500$  GeV and the best-fit cross section is 0.4 pb, which is of the same order of magnitude as the predicted cross section.

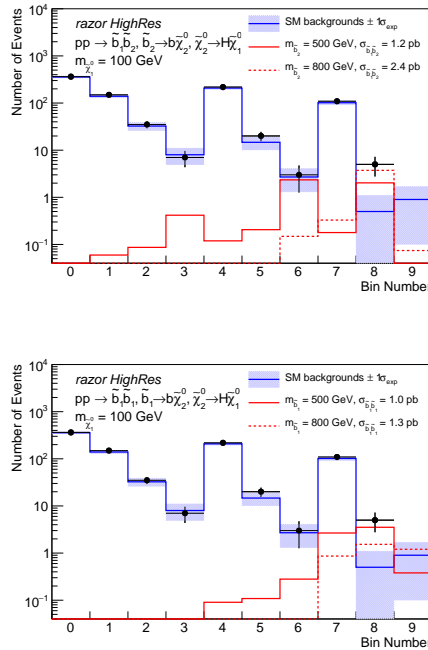


Figure B.3: (Top) The expected background and uncertainty (multiplied by a factor of two as explained in the text) compared to the best-fit signal distribution in the HighRes box for two particular mass points,  $m_{\tilde{b}_2} = 500$  GeV and  $m_{\tilde{b}_2} = 800$  GeV, in model A. (Bottom) The expected background and uncertainty (multiplied by a factor of two as explained in the text) compared to the best-fit signal distribution in the HighRes box for two particular mass points,  $m_{\tilde{b}_1} = 500$  GeV and  $m_{\tilde{b}_1} = 800$  GeV, in model B. The bin numbers correspond to the order of the signal regions in the yield tables in Ref. [208] and are reproduced in Tab. B.2.

## B.8 Discussion and summary

In this paper, we proposed two simplified models of bottom squark pair production for use in the interpretation of an excess observed by CMS in a search for SUSY in H+jets events using razor variables at  $\sqrt{s} = 8$  TeV [208]. In model A, we considered the asymmetric production of a  $\tilde{b}_2\tilde{b}_1$  pair, with the  $\tilde{b}_1 \rightarrow \tilde{\chi}_1^0$ ,  $\tilde{b}_2 \rightarrow b\tilde{\chi}_2^0$ ,

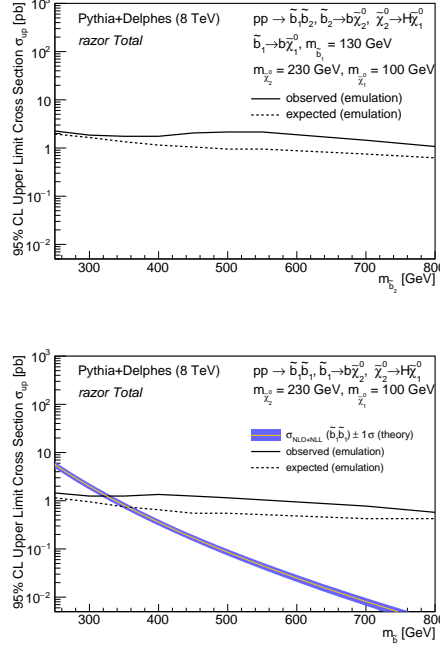


Figure B.4: (Top) The 95% CL upper limit on the cross section on  $\tilde{b}_1 \tilde{b}_2$  production in model A as a function of  $m_{\tilde{b}_2}$  (black). (Bottom) The 95% CL upper limit on the cross section on  $\tilde{b}_1 \tilde{b}_1$  production in model B as a function of  $m_{\tilde{b}_1}$  (black) compared to the NLO+NLL predicted cross section (yellow). Note, these scans assume  $m_{\tilde{\chi}_1^0} = 100 \text{ GeV}$ ,  $m_{\tilde{\chi}_2^0} = 230 \text{ GeV}$ , and for model A  $m_{\tilde{b}_1} = 130 \text{ GeV}$ .

and  $\tilde{\chi}_2^0 \rightarrow H \tilde{\chi}_1^0$ , where  $\tilde{\chi}_1^0$  is a neutralino LSP and we fix the mass splitting  $m_{\tilde{\chi}_2^0} - m_{\tilde{\chi}_1^0} = 130 \text{ GeV}$ . In model B, we considered the symmetric production of a  $\tilde{b}_1 \tilde{b}_1$  pair, with  $\tilde{b}_1 \rightarrow b \tilde{\chi}_2^0$ ,  $\tilde{\chi}_2^0 \rightarrow H \tilde{\chi}_1^0$ , and  $m_{\tilde{\chi}_2^0} - m_{\tilde{\chi}_1^0} = 130 \text{ GeV}$ .

We scanned the bottom squark masses for a fixed LSP mass of  $m_{\tilde{\chi}_1^0} = 100 \text{ GeV}$  for both models and quantified the agreement with the data. We found the excess observed in data is broadly consistent with both models, with the largest signal significance being  $1.8\sigma$  corresponding to model B with  $m_{\tilde{b}_1} = 500 \text{ GeV}$ ,  $m_{\tilde{\chi}_2^0} = 230 \text{ GeV}$ , and  $m_{\tilde{\chi}_1^0} = 100 \text{ GeV}$ . Following this study, model B used by the CMS collaboration to interpret the results of the updated 13 TeV search for SUSY in the same channel [206], which also exhibits an excess possibly consistent with the model.

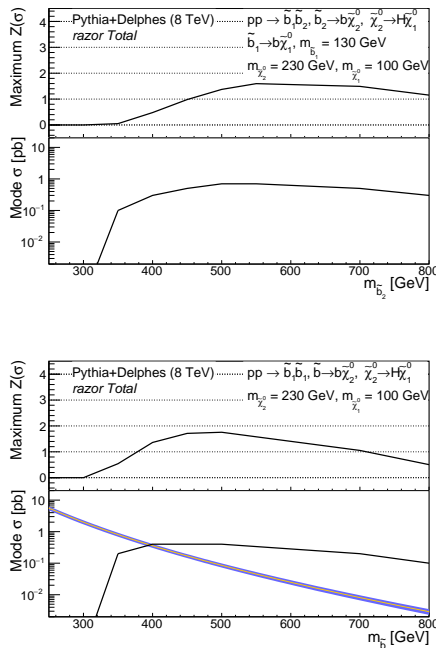


Figure B.5: (Top) The maximum significance  $Z(\sigma)$  for a given  $m_{\tilde{b}_2}$  in the top panel and the “best fit” signal cross section  $\sigma$  in the bottom panel for model A. (Bottom) The maximum significance  $Z(\sigma)$  for a given  $m_{\tilde{b}_1}$  in the top panel and the “best fit” signal cross section  $\sigma$  in the bottom panel for model B. Note, these scans assume  $m_{\tilde{\chi}_1^0} = 100$  GeV,  $m_{\tilde{\chi}_2^0} = 230$  GeV, and for model A  $m_{\tilde{b}_1} = 130$  GeV.

